Measurement of the photon asymmetry for the $\mathrm{p}\,(\overrightarrow{\gamma}, \mathrm{K}^{+})\,\Lambda^{0}$ reaction at CLAS from 1.6 to $2.0\ \mathrm{GeV}$

Joseph James Melone

Presented as a Thesis for the Degree of Doctor of Philosophy

Nuclear Physics Group
Department of Physics and Astronomy
University of Glasgow

Abstract

For the $\mathrm{p}\,(\overrightarrow{\gamma}, \mathrm{K}^+)\,\Lambda^0$ reaction, polarisation observables were measured using linearly polarised photons in CLAS, during the G8a experiment in the summer of 2001. Using the CEBAF accelerator facility in Virginia, USA, an incident electron beam energy of 5.7 GeV was achieved. The electron beam then passed into the newly commissioned Coherent Bremsstrahlung Facility, producing a beam of linearly polarised photons. For the purpose of this thesis the polarised photon beam, of energy 1.6 GeV < $E_{\overrightarrow{\gamma}}$ < 2.0 GeV, then collided with a fixed liquid hydrogen target. The CLAS detector was used to detect several charged particles that were the signature of the decay channels chosen for this experiment. For the analysis presented here, the decay particles of K^+, proton and π^- which are produced from the decay of a K^+ and a Λ^0, are analysed in terms of azimuthal distributions to extract a value for the photon asymmetry.

This value can be calculated over a range of polar angles in the centre-of-mass frame of the $\mathrm{K}^+\Lambda^0$ reaction. The polar angle is defined in terms of the direction of the K^+ in the centre-of-mass frame of the reaction, and the results are presented in 4 variable-width bins over the range of 20 degrees to 130 degrees. The quality of these measurements vindicates the choice of apparatus for the G8a experiment.

A proof-of-principle experiment, the fact that the existing data set for this reaction have been extended in terms of the polar angle range by a factor of two by the G8a experiment shows that using linearly polarised photons at CLAS is indeed an effective way of investigating the polarisation observables for a variety of charged-particle final states.

These measurements are then compared with the tree-level isobar model of Janssen, which takes account of the effect of N^* resonance exchange on the kaon photoproduction propagator of Adelseck et.al. The model of Janssen incorporates a genetic algorithm approach to finding the most likely resonance contributions to the propagator, using the previous experimental measurements made of the $\mathrm{K}^+\Lambda^0$ polarisation observables at SAPHIR and CLAS.

This comparison suggests the presence of a resonance with mass $\sim 1900\,\mathrm{MeV/c^2}$, which is also indicated by previous cross-section data produced from SAPHIR and CLAS. Furthermore the identification of the quantum numbers of the resonance, made possible by considering the relevant polarisation observables, indicates that the N^* resonance in question may be the controversial "missing" $\mathrm{D}_{13}(1895)$ resonance.

The question of the existence of the “missing” resonances is of fundamental importance to the understanding of Nuclear Physics at intermediate energies, and the G8a data set has already shown that this experimental approach is has been successful in obtaining new data and extending our understanding of associated strangeness production.

As a continuation of this work, the G8b experiment will run in 2005, providing much increased statistics of a very high quality, and thereby enabling further studies in this important field.

Declaration

The data presented in this thesis were obtained as part of the G8a collaboration at the U.S. Department of Energy facility Jefferson Laboratory, in Virginia, USA, and the Nuclear Physics Group of the University of Glasgow. I participated fully in the preparation and execution of the experiment. The analysis of the experimental data is my own work. This thesis was composed by myself.

Joseph J. Melone

March 2005.

Acknowledgements

After the long task of putting this thesis together, I'd like to take a moment to thank all those people who saw me through. Thanks to Prof. Rosner for giving me the initial opportunity to take up this study. I'm in massive debt to the excellent supervision of Dr. Jim Kellie and the expert assistance of Dr. Ken Livingston without whom it would have been impossible to undertake this project. The work (and help) of Dr. Dave Ireland has also been vital in putting together the final analysis and results shown in this thesis, as have suggestions on error analysis by Prof. Robert Owens.

It wouldn't have been possible to even start this thesis without the hard work of all the members of the G8a collaboration at JLab, and I would particularly like to thank Prof. Juan Carlos Sanabria for his efforts with the data calibration and advice for data analysis.

All of the members of the Glasgow NPE group have been a great source of inspiration, and whenever problems with work have arisen, being part of such a sociable group has really helped me keep perspective.

A special thanks goes to Chris and David who, as my fellow ex-pats in Virginia, helped me through many tough days and nights at JLab. Not to mention numerous invaluable coffee sessions which were the epitome of scientific endeavour... Andreas "The German" deserves much praise as well for the many rants that kept us all sane!

I'd also really like to thank Dr. Val O'Shea for giving me an employment opportunity at a time when it was much needed, and my brother John who assisted me in the job while thesis corrections were being done. Finally I'd like to thank all my family for their inexhaustible support, especially my mum and dad who tolerated me getting in their road about the house while putting food on the table and providing essential financial backing while I was writing up, and Lynn, for showing infinite patience and moral support, especially while I was working abroad. You've all been great!

Contents

List of Figures

List of Tables

Chapter 1

Introduction

Current investigations into the nature of matter concern themselves with the dynamical properties of matter at the atomic level. This entails looking in detail at what the atom is made of, and while the orbiting electrons and their dynamics are well-understood, the real challenge is to understand the properties of the atomic nucleus. Opinion on what takes place at the sub-atomic level has changed vastly as the field of atomic physics has developed into nuclear physics. At the time of Rutherford [1] the nucleus was thought to consist of a mixture of protons and neutrons, collectively known as nucleons, randomly distributed throughout the nucleus. This perspective has shifted considerably, with point-like fractionally charged particles called quarks now believed to be the elementary components of nucleons.

Every particle observed thus far in the universe interacts by mediation of the four fundamental forces. The effects of gravity are only measurable for extremely large systems of atoms, and the electro-magnetic force is unified with the weak force to describe the interactions of charged particles and the decay of unstable atomic and nucleon states. Every particle which can be identified as a hadron interacts via the strong force, and hadrons are defined as systems of multiple quarks. Baryons are hadrons containing three quarks, and mesons are hadrons consisting of a quark-antiquark $\langle q\overline{q}\rangle$ pair. Leptons are fundamental particles with no detectable substructure, and although they never experience the effects of the strong force, they normally interact through the electro-magnetic and weak forces. The overall classification of quarks and leptons, which are fermions obeying the Pauli Exclusion Principle, and the force-carrying bosons, is achieved by the highly successful Standard Model of Particle Physics.

1.1 Standard Model

The Standard Model of Particle Physics is a theoretical framework classifying all elementary particles and their interactions. Some elementary particles have half-integer quantum mechanical spin and are known as fermions. There are two classes of fermions, quarks and leptons. Quarks come in six different flavours: up, down, strange, charm, bottom and top in order of mass. Leptons are similarly grouped with three fundamental particles: the electron, muon, and tau, with corresponding neutrinos $(\nu_e,\, \nu_\mu,\, \nu_\tau)$. The e, μ and τ are all equally negatively charged, the neutrinos carry no charge, while the quarks are all fractionally charged with $q_u = q_c = q_t = +\frac{2}{3}q_e$ and $q_d = q_s = q_b = -\frac{1}{3}q_e$. All these particles have corresponding anti-particles which have opposite electric charge and magnetic moment.

From a theoretical perspective, the Standard Model is a quantum field theory, and is based on the gauge symmetry of $SU(3)_C \times SU(2)_L \times U(1)_Y$. The electromagnetic and weak forces are unified to create an electroweak interaction governed by the symmetry $SU(2)_L \times U(1)_Y$, and has four fundamental bosons associated with it. These are the $W^\pm$, Z^0 and the photon. Here the $SU(2)_L$ component relates to the symmetric states of the W and Z bosons, and therefore represents the weak force. The $U(1)_Y$ component is representative of the photon, a massless boson which carries the electromagnetic part of the electroweak unified force. The strong force has the extra symmetry based on colour exchange, $SU(3)_C$, and this gives rise to eight colour variants of the strong force-carrying boson, which is called the gluon. Gluons are massless and electrically neutral. At present there exists no quantum field theory representing the force of gravity hence this is not included in the Standard Model.

1.2 Quantum Chromodynamics

Quantum Chromodynamics (QCD) is the theory of quark interactions at the sub-nucleonic scale, and involves the extra degrees of freedom of colour exchange. Being a quantum field theory the QCD Lagrangian, which describes the energy states and dynamics of the nucleon system, is composed of individual quark fields and the strong potential in which they move. Such quark fields are massless and have the added ingredient of being gauge invariant under colour exchange, which is a core requirement of QCD to allow renormalisation. Renormalisation is the process by which the infinities generated by having a point-like charged particle interact with a quantum field are cancelled out. The ability to carry out this process depends on the symmetric properties of the

fundamental QCD Lagrangian.

Important aspects of this theory include quark confinement, asymptotic freedom and chiral symmetry. Quark confinement relates to the fact that the quark-quark potential in the Standard Model increases with separation distance. This is also linked to the symmetric property of colour-neutrality which implies that every observed hadron must be colour-neutral, as required by the experimental fact that no isolated quarks have ever been observed. In the high-energy regime the quark mass is small relative to the strength of the gluon interaction, so a perturbative expansion of the interaction coupling allows the behaviour of the nucleon to be accurately described. However, at low energies, the quark mass is a much more important part of the Lagrangian, and due to the relative strength of the strong coupling constant ($\alpha_s \simeq 1$), a perturbative solution for the modified interaction is no longer a possibility. At these energies the quarks are asymptotically free. In short, the whole nucleon system is extremely tightly bound at high energy and asymptotically approaches a free state at low energy.

Current theory suggests that the strong force is embodied by the exchange of gluons and, due to the quantum nature of the vacuum, quarks and gluons must always be virtually present. The "vacuum state" of the nucleon is not completely empty but exists as a quark-gluon condensate with non-zero energy. Therefore the tightly bound energetic systems of quarks which comprise nucleons are surrounded by what has been coined as the quark sea. It follows logically that there should be interaction between this sea of virtual quarks and the valence quarks of the nucleon, and properties such as mass and angular momentum of the overall nucleon system are linked to this concept. However, since the fluctuations of the quark-gluon condensate are intrinsically random and complex, interactions between the valence quarks and the QCD vacuum are highly chaotic in nature so accurate predictions of mass and momentum from this physical picture alone are impossible.

Chiral symmetry invokes the concept of left or right-handedness, which is related to the concept of helicity. Helicity may be defined as the alignment of particle spin with the direction of travel, and for chiral symmetry to be observed, this property must be conserved.. In the high-energy limit where the quark masses are insignificant relative to the strong force, this chiral symmetry can be approximated if the valence quark mass is assumed to be zero. It is however important to note the difference between the chirally symmetric QCD Lagrangian and the broken symmetry that exists in nature, especially at low energies. Whether or not the valence quarks are actually massless is an important question, but of fundamental importance is the understanding that the QCD Lagrangian has the chiral symmetry of its pure form broken either spontaneously

by the presence of a non-zero valence quark mass or by dynamic interaction of the valence quarks with the QCD vacuum state. Under the conditions of broken chiral symmetry, naked valence quarks are believed to be "cloaked" by their interactions with the quark-gluon condensate, and the mass of a so-called constituent quark results from the energy of this dynamic system.

Fig 1.1 refers to this idea; the distribution of gluon exchange, proceeding via mutual interaction in the vacuum, is shown to make up a large part of the total energy inside the proton and therefore is the major contributor to its mass. Some attempts to calculate the non-perturbative dynamics of the quark-gluon condensate have been successful, and these have been based on a computational method called Lattice QCD. This approach utilises a discrete space-time framework to allow finite calculations of the quantum field strength inside the nucleon. From such calculations, the visualisation shown in Fig 1.1 is based on Lattice calculations of the QCD Lagrangian vacuum state.

1.3 Constituent Quark Model

To develop a model which allows a prediction of the possible nucleon states at low energy, a phenomenological concept called the Constituent Quark Model [3] is used. This consists of assuming the valence quarks to be effective degrees of freedom within the nucleon, which take on a much greater mass than the perturbative QCD quarks previously mentioned. By assuming that the behaviour of this nucleon state can be modelled by a simple harmonic oscillator and that the three valence quarks can move independently, a spectrum of possible baryon states can be built up which displays the $SU(6)XO(3)$ symmetry when limiting the number of quark flavours to N_f =3. This symmetry reflects the structure of the model, which has a symmetric group of three quark flavours ($SU(3)$), two spin states ($SU(2)$), and ($O(3)$) representing the orbital motion of the quarks.

Isgur et al. [3] have made extensive predictions for the number of nucleon states to be expected, including the stable ground state baryons (such as the proton and neutron) and the higher energy resonant states with their corresponding mass and quantum numbers. The most extensive data has been compiled from examining the $\gamma + N \rightarrow N^*/\Delta \rightarrow N + \pi$ reaction. Surprisingly, not all the predicted resonances have yet been found. The implications are that either the basic baryon quark model is incorrect in its assumption of three internal degrees of freedom always present in the nucleon, or else the missing resonant states do not couple to the pion photoproduction channel.

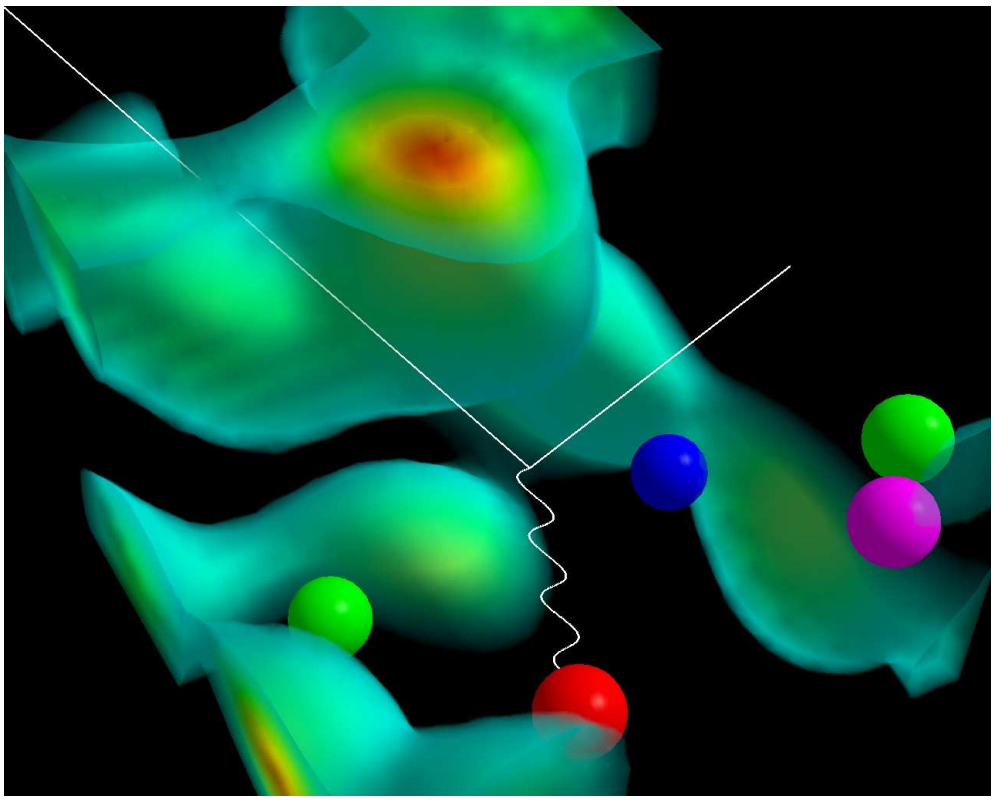

Figure 1.1: *An artist's representation of the modern proton concept, based on lattice QCD calculations of gluon exchange in the vacuum [2]. Here 97% of the proton mass comes from the gluon field, with just 3% residing in the valence quarks. Red, blue and green are the valence quarks here, with a virtual pion forming to the right of the picture (shown as a green and magenta pair). A electron interacts with a quark here by way of exchanging a virtual photon (shown as a wavy line).*

The constituent quark model works well in the low-energy region (centre-of-mass energy $W < 2\,GeV$). With current high-energy experiments investigating QCD in the perturbative regime, some QCD-based models have been developed to try and bridge the gap between the high-energy and low-energy dynamics of the baryon. One particular model which is currently being investigated as a low-energy alternative to the original quark model is the Diquark Model [4–6]. Some important aspects of this model are reduced hadronic degrees of freedom in the nucleon, and an asymptotic tendency at high energy towards the three-quark dynamical system. The concept of the diquark-quark model is that one quark remains free to interact as the sole valence quark while the other two quarks form a pseudo-elementary particle analogous to a meson (see Fig 1.2). The reasons for postulating this model are based on the discrepancies between the number of nucleon resonances predicted by the constituent quark

model and the numbers yielded so far by experiment. The electromagnetic form factors of the proton and neutron measured at high energies also indicate experimentally the existence of the diquark structure.

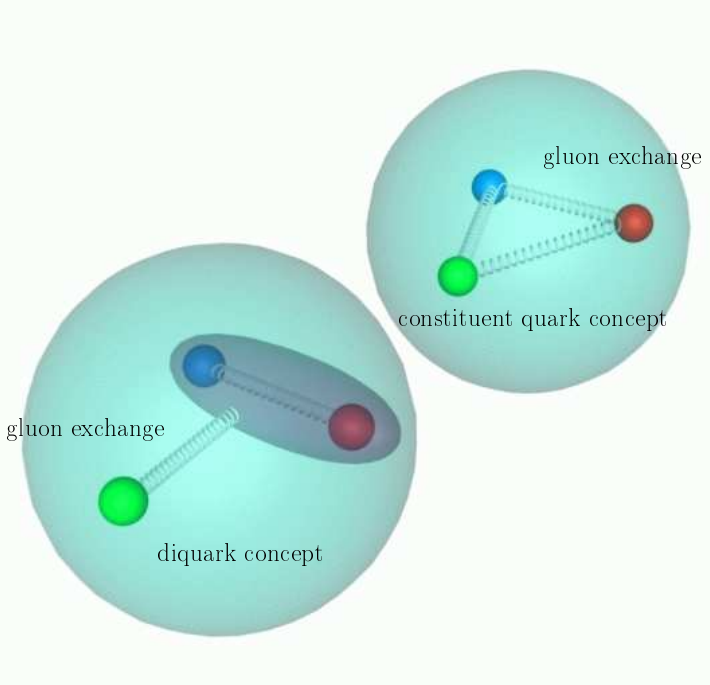

Figure 1.2: *Diquark interpretation compared with the more widely used Constituent Quark Model interpretation. Shown here is an illustration of the theoretical concept of limited degrees of freedom. The figure showing the Diquark concept has an effective pion interacting with a single valence quark, illustrating the reduced degrees of freedom compared with the Constituent Quark Model.*

Further experimental developments in the last few years [7] have indicated that more exotic baryons may exist than currently catered for in the Standard Model. Here the theoretical framework of the diquark model has been instrumental in obtaining a theoretical prediction of the Θ^+ pentaquark $(uudd\overline{s})$ which is in agreement with the current experimentally measured mass of 1540 MeV [8, 9].

Recent theoretical work using the Constituent Model as a foundation [3, 10–12] has shown that decays involving strange mesons and baryons are a possible avenue for investigating these predicted "missing" resonances of the quark model. Strange mesons and baryons are those which contain one or more strange quarks. The amount of strangeness in a reaction is always conserved so this means that in the case where a photon strikes a proton, the initial strangeness is zero, hence the reaction products must have zero overall strangeness. Usually this strangeness conservation is maintained by

the production of a strange baryon such as the Λ or Σ with quark content $(\mathrm{u}, \mathrm{d}, \mathrm{s}))$ and a strange meson, most likely a kaon with quark content $(\mathrm{u}, \overline{\mathrm{s}})$. The recent quark model calculations indicate the strong possibility that resonances may decay via the strange channel and not the more usual channels such as pion photoproduction as has been widely assumed. This makes the study of strange decays extremely suitable for extending the current investigation of the properties of N^* resonances, and the potential also exists for investigating the properties of the postulated "missing" resonances.

1.4 Motivation

It is clearly of major interest to nuclear physicists to clear up the question of which quark model approximates reality best, since the choice of models to calculate the properties of resonances will be important for future understanding of the nucleus. Of paramount importance is the establishment of a suitable bridging model between the low energy non-perturbative quark model and the high energy QCD Lagrangian approach. The recent emergence of new accelerator facilities such as CEBAF [13] and SPring-8 [14] has sparked interest once more in the study of baryon spectroscopy. The pursuit of an accurate model of excited baryonic states is now being realised since polarised beams of electrons and photons can be used which unlock more information about the resonant states that have been verified to exist. In the region of interest (W ~ 2 GeV), the baryon spectrum consists of a multitude of overlapping resonant states, making the process of isolating them by cross-section or missing mass techniques impractical. A more accurate technique is to isolate the resonant state by looking at the polarisation information that would be generated in theory by each candidate, and then identify the physical state by comparison with the prediction. A further possible confirmation is then to perform a partial-wave analysis [15] of the suspected resonance identified in this way to confirm the quantum numbers of the state.

With this aim in mind, G8a was the first of a series of experiments planned to use the newly installed Coherent Bremsstrahlung facility which produces linearly polarised photons using a diamond radiator. This experiment was the commissioning run for the new facility, and is aimed at studying the polarisation information available from specific reactions. The reaction studied in this thesis was that of $\overrightarrow{\gamma} + \mathrm{p} \rightarrow \mathrm{K}^+ + \Lambda^0$, and with an experimental setup consisting of a polarised photon beam ranging in energy from $1.8\,\mathrm{GeV} \rightarrow 2.3\,\mathrm{GeV}$ incident on a liquid hydrogen target, the photon asymmetry was studied. In Chapters 3 and 4 the experimental setup used for the G8a experiment is discussed in detail, as are the detector calibration procedures that the author

participated in. Chapter 5 deals with the software techniques used for identifying the components of the $K\Lambda$ reaction, and in Chapter 6 the final data set is analysed. These results are compared with theoretical calculations over the same energy range in Chapter 7, and the relevant quantities for this comparison are introduced next in Chapter 2, along with the basic theory of $K\Lambda$ photoproduction.

Chapter 2

Theory

2.1 Introduction

The results of the analysis, presented in Chapter 6, are to be compared with a range of theoretical predictions of properties of the $\overrightarrow{\gamma} + \mathrm{p} \rightarrow \mathrm{K}^{+} + \Lambda^{0}$ reaction. As mentioned in Chapter 1, the most interesting predictions for the purpose of this thesis involve the polarisation information available from the reaction. These polarisation information components are called observables, since they should be experimentally accessible through interactions involving a polarised photon or electron beam. Fig 2.1 shows a possible quark flow diagram for this reaction, and the polarisation information, which has components defined in Table 2.4 in this chapter, have been calculated to be highly sensitive to the presence of N^{*} resonances.

Much of the interest in these N^{*} states has been generated by a recent quark model calculation [16] which strongly predicted that it should be possible for some undiscovered N^{*} resonances to couple to a strange decay. This makes the study of polarisation observables extremely attractive, not only through reactions involving ρ , ϕ or ω meson photoproduction [17–19] but also through the photoproduction of strangeness [20].

2.2 Baryon spectroscopy

In order to understand the low-energy dynamics of the nucleon, the current approach is to try to predict the various excited states of the nucleon and compare with experimental data. This reflects the problems encountered when trying to make QCD-based predictions in the energy region where the strong interaction can no longer be approximated by perturbation theory. These problems call for a phenomenological approach

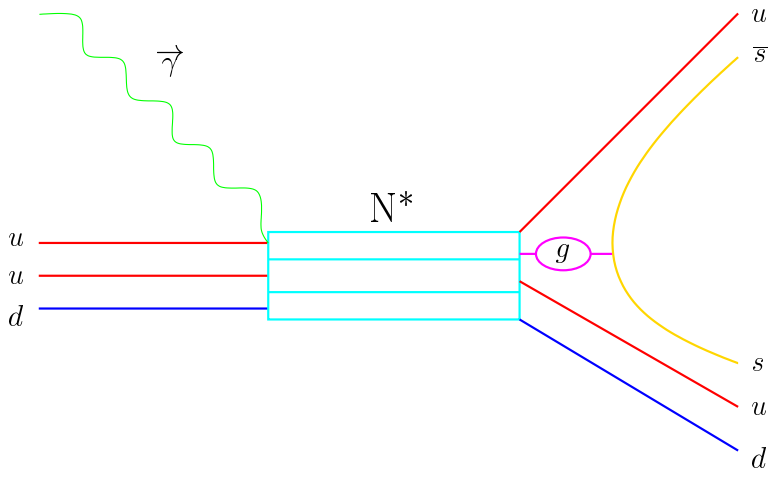

Figure 2.1: *Quark flow diagram for a possible strange decay. The coupling of an N^* resonance to the production of the $K\Lambda$ system is predicted to be observable, particularly when looking at angular variations in CLAS which can reveal the presence of the so-called polarisation observables(See Table 2.4).*

which has the appropriate degrees of freedom to model the system being studied. One of the first methods developed was the Constituent Quark Model [10], which treats the problem by assuming three constituent quarks independently interact in a nuclear potential. This avoids the difficulties inherent in the QCD Lagrangian, and in fact adopts an Effective Lagrangian to describe the energy states of the system. Utilising the properties of $SU(6) \times O(3)$ symmetry to estimate the number of possible states and a quantum harmonic oscillator to generate states with different charge, parity and angular momentum, this model tries to generate a realistic spectrum of baryon resonances.

The quantum number spin plays an important role in determining the individual characteristics of the nucleon. The total angular momentum J, the orbital angular momentum L and the total spin S are vital components for determining the state of the nucleon and they are related by the form $J = L + S$. When defining the total angular momentum J of the nucleon the projection of the sum S_z of individual quark spins for a given nucleon onto the z-axis (helicity axis) sums with the projection of angular momentum L_z to define this unique state for a given nucleon. The quantum number J_z is the projection of J onto the z(helicity) axis, as shown in Fig 2.2, and results from the sum $J_z = L_z + S_z$. Every quark has a quantum-mechanical spin of $\frac{1}{2}\hbar$, but the relative direction of this spin vector (whether parallel or anti-parallel) to the helicity axis of the nucleon system is what defines the spin of the nucleon.

Although the older concept of isospin is completely unrelated to quantum spin,

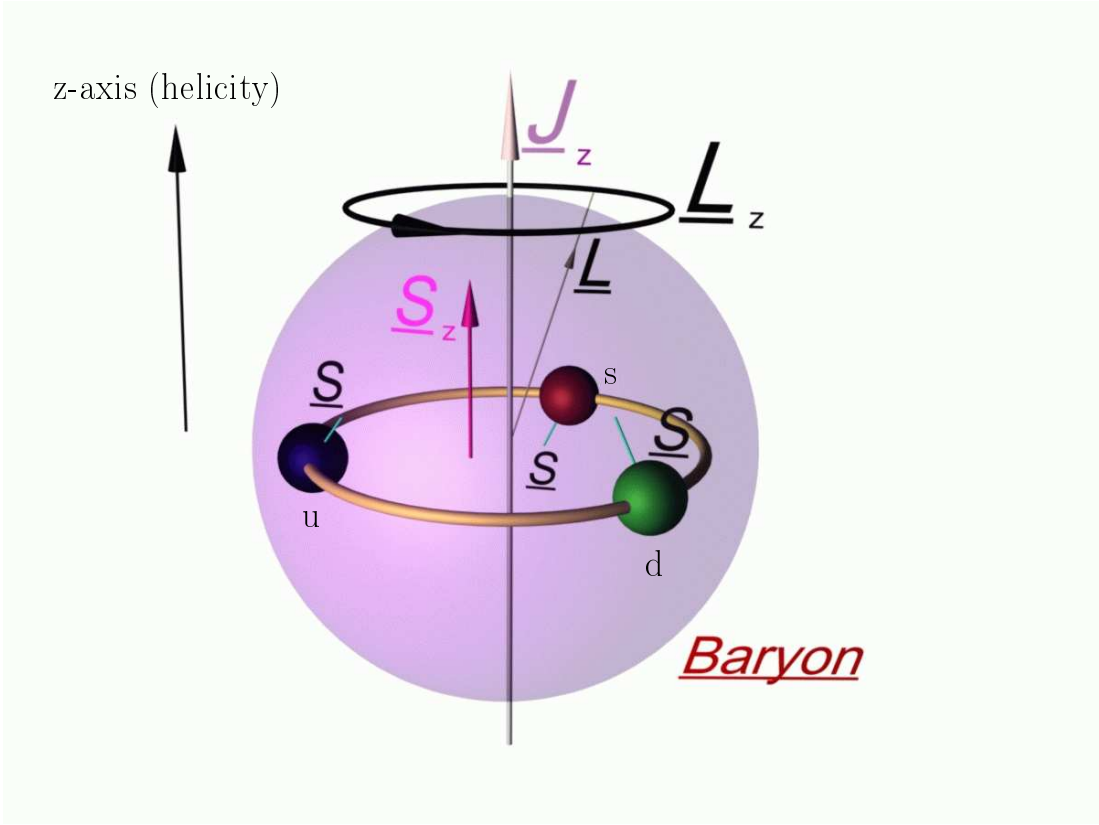

Figure 2.2: *The general properties of the quark model of a nucleon. The orbital angular momentum L contributes to the overall momentum carried by the nucleon, labelled J. The intrinsic spin S_z is the total sum of all the spins carried by the individual quarks with quantum spin $S = \frac{1}{2}$, projected along the helicity axis (z). The projection of the orbital angular momentum L_z is also along the helicity axis.*
Quantum mechanics defines the quantum number J_z as a label for the total angular momentum state of the nucleon, with the property $J_z = L_z + S_z$, where the helicity of the nucleon defines the axis (z). The nucleon also possesses isospin, which is a property linked to its charge state, although not to the quantum number spin as the name suggests. Shown here is the Λ^0 which has an isospin of 0. N^* particles have isospin $I = \frac{1}{2}$ since they occur in charge states of either 0 or +1.

it is also useful for classifying nucleon states. For example the proton and neutron are examples of two particles which are identical except for a different I_3 component, where I_3 is the third component of an isospin vector in a hypothetical space. The concept of isospin was originally introduced to account for the fact the the proton and neutron have nearly equal mass while the proton has positive charge and the neutron is neutral. Using the I_3 component of the isospin is therefore convenient for classifying and grouping together nucleons and mesons with similar mass and differing charge states. The lightest two quarks also have non-zero isospin since the u and d quarks form an isospin multiplet, where the u quark has $\mathrm{I}_3 = +\frac{1}{2}$ and the d quark has $\mathrm{I}_3 = -\frac{1}{2}$, on account of their similar masses.

The constituent quark model predicts various excited states for baryons, taking into account the possible permutations of quark mass, spin and charge as shown in Fig 2.2. These excited resonant states are distinguished into two families, those that are part of the isospin doublet with $\mathrm{I} = \frac{1}{2}$ which are known as N^* resonances ,and those that are part of the isospin $\mathrm{I} = \frac{3}{2}$ quadruplet which are termed as Δ resonances. Resonances are typically labelled according to the orbital angular momentum L of their decay daughter particles which are typically a nucleon plus a pion or other pseudoscalar meson. This is notated on the basis of levels or shells. S, P, D and F correspond to $\mathrm{L} = 0,\ 1,\ 2,\ 3$ respectively, and I and J are also included in this notation. A typical N^* resonance may be labelled $\mathrm{P}_{11}(938)$, where $\mathrm{L} = 1$, $\mathrm{I} = \frac{1}{2}$, and $\mathrm{J} = \frac{1}{2}$, which is the N^* ground state, the proton. Strictly speaking, the proton does not undergo a decay which allows the classification as P_{11} state using the above notation. However, many experiments involving elastic scattering of pions from the nucleon, denoted as $\pi + \mathrm{p} \rightarrow \pi + \mathrm{p}$, have shown that the cross-section at low incident pion scattering energies is dominated by p-wave scattering [21]. This indicates that the proton has orbital angular momentum of L=1.

An outstanding issue for the Constituent Quark Model is the fact that some of the resonances predicted by the model have not yet been observed. Although the experimental approach has been limited thus far to pion photoproduction, there are two possible theoretical interpretations of this state of affairs.

One is the conclusion that a different mechanism may be at work inside a nucleon undergoing excitation. The quarks may not all be free to interact, and this has led to the postulation of two quarks existing as a pre-meson inside the nucleon, analogous to the pre-α particle postulated by Gamow [22] in the accepted theory of $\alpha-$decay. This approach is known as the Diquark Model [4–6] and the predictions of resonance mass, charge and spin are modified from the constituent model by removing the extra degree

of freedom inside the nucleon as shown in Fig 1.2. Table 2.1 shows the divergence between the Constituent Quark Model and the Diquark Model, where the resonances predicted in accordance with the limited degrees of freedom of the Diquark Model have all been experimentally verified.

N^*	Particle Data Group Star Rating	SU(6) × O(3) super-multiplet
$P_{11}(938)$	****	$(56,\ 0^+)$
$S_{11}(1535)$	****	$(70,\ 1^-)$
$S_{11}(1650)$	****	$(70,\ 1^-)$
$D_{13}(1520)$	****	$(70,\ 1^-)$
$D_{13}(1700)$	****	$(70,\ 1^-)$
$D_{15}(1675)$	***	$(70,\ 1^-)$
$P_{11}(1520)$	****	$(56,\ 0^+)$
$P_{11}(1710)$	***	$(70,\ 0^+)$
$P_{11}(1880)$		$(70,\ 2^+)$
$P_{11}(1975)$		$(20,\ 1^+)$
$P_{13}(1720)$	****	$(56,\ 2^+)$
$P_{13}(1870)$	*	$(70,\ 0^+)$
$P_{13}(1910)$		$(70,\ 2^+)$
$P_{13}(1950)$		$(70,\ 2^+)$
$P_{13}(2030)$		$(20,\ 1^+)$
$F_{15}(1680)$	****	$(56,\ 2^+)$
$F_{15}(2000)$	**	$(70,\ 2^+)$
$F_{15}(1995)$		$(70,\ 2^+)$
$F_{17}(1990)$	**	$(70,\ 2^+)$

Table 2.1: The QCD-based resonance predictions from the model of Cutkosky [23]. The states shown in red are consistent with the predictions of the diquark model. SU(3) states are notated here as (r, N^P) where *r* is the symmetry representation, *N* is the harmonic oscillator mode used in the model to calculate the properties of the state, and *P* is parity. The star rating is the standard notation used by the Particle Data Group [24] for showing the experimental certainty of the existence of resonant states.

The other conclusion to be drawn is that not all resonances will couple strongly to the pion decay channel. Mart and Bennhold [11], along with Janssen et al. [25], have made quark-model calculations showing the possibility of the existence of one of these "missing" resonances coupling to the $K\Lambda$ channel. The data from the most recent experiments [26, 27] were fitted using a modification of the kaon photoproduction propagator devised by Thom [28]. This formalism, developed by Adelseck [29], allows the inclusion of extra resonant terms to vary the strength of the $K\Lambda$ coupling constants [30]. The differential cross-section for $K\Lambda$ photoproduction could only be

fitted properly by including the $\mathrm{D}_{13}(1895)$ missing resonance. However many other groups have pointed out that this does not conclusively prove the existence of the D_{13}. Another paper by Mart et al. [12] points out that an excellent way of determining the existence of such a resonance in the strange channel is to look at the polarisation observables of the reaction. Their calculation of the photon asymmetry, defined later in Section 2.5, does indeed indicate a viable method for testing the contributions of resonant terms in the overall interaction. Janssen et al. [31] have gone further by including a whole series of missing resonances using the Adelseck approach. While there are multiple predictions from this model for each polarisation observable, comparing these calculations with data is essential to constrain the parameters of the model.

Each of the several ongoing experimental investigations of the polarisation observables [32, 33] will further reduce the uncertainty regarding which N^* resonances make a contribution to the $\overrightarrow{\gamma} + \mathrm{p} \rightarrow \mathrm{K}^+ + \Lambda^0$ reaction. Measuring one polarisation observable automatically reduces the possible range of values for the other observables. This method of comparing experimental data with a model prediction then subsequently refining the parameters of the model promises to make it possible to discriminate between the constituent and diquark models. Furthermore, it will provide valuable information on the previously unknown coupling constants for strangeness photoproduction.

2.3 Previous calculations and measurements

The most recent experiments measuring the photoproduction of strangeness have been carried out by the SAPHIR collaboration at Bonn and the CLAS collaboration at Jefferson Lab. In the case of the SAPHIR results [27], the differential cross-section at photon energies ranging from 0.9 to 2.0 GeV was measured, while the G1c experiment [34] at CLAS repeated the differential cross-section measurement. In addition the Λ recoil polarisation [see Section 2.5] was measured for $\mathrm{E}_\gamma = 0.9$ to 2.3 GeV. The G1c measurement was recently extended by the SAPHIR collaboration over the energy range of $\mathrm{E}_\gamma = 0.9$ to 2.6 GeV [35].

The SAPHIR data in Fig 2.3 shows an interesting feature with an invariant mass W of around $1900\ \mathrm{MeV}$ which has been interpreted in the past as evidence pointing to the existence of a "missing" $\mathrm{D}_{13}(1895)$ resonance. Despite normalisation problems during the G1c experiment which are estimated to have artificially increased the value of the $\mathrm{K}\Lambda$ cross-section, the data from the G1c experiment support the SAPHIR results with confirmation of the presence of this structure, both in the total cross-section of Fig 2.3

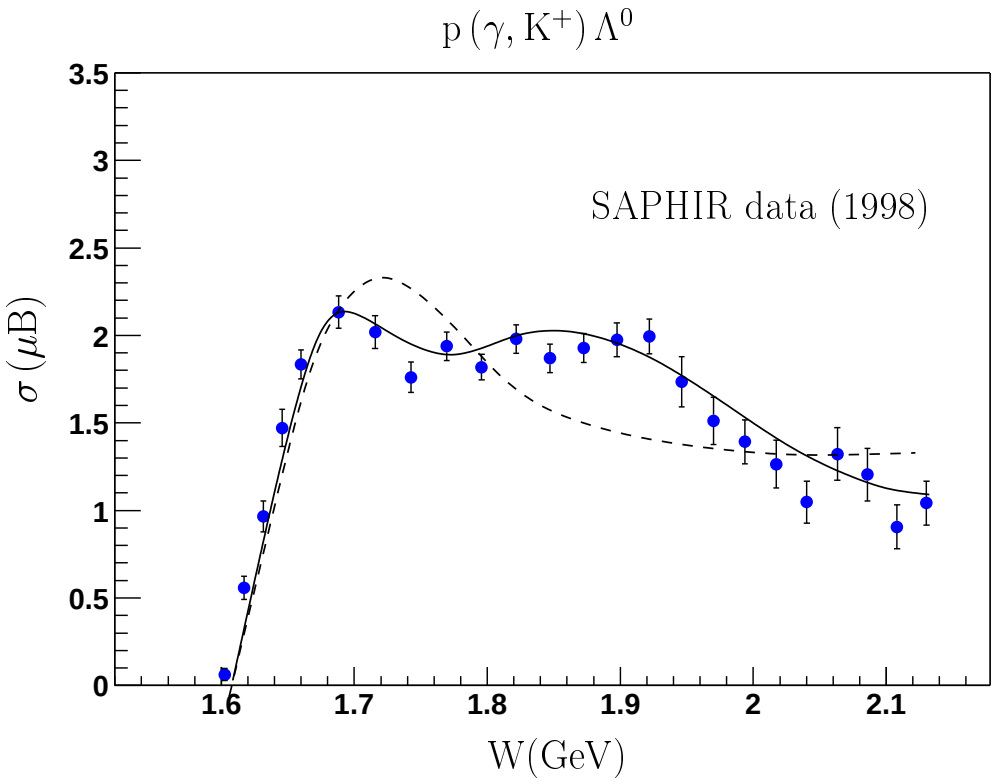

Figure 2.3: *The total cross-section of p($\vec{\gamma}$,K^+)Λ^0 measured by the SAPHIR collaboration. The solid line shows a fit (of the type described in Section 2.4.3) to the data including the $D_{13}(1895)$ resonance in a constituent quark model calculation [11]. The dashed line shows the same calculation made without the D_{13}.*

and the differential cross-section of Fig 2.4.

Bennhold et al. performed a fit to the SAPHIR data based on the isobar phenomenological approach discussed in Section 2.4.3, and found the best fit to the data was given by including the "missing" D_{13} from the constituent quark model calculations of Capstick et al. [16] in their model. There exist a number of candidate resonances with $\mathrm{W} \simeq 1900\,\mathrm{MeV}$ which have a two-star rating from the Particle Data Group [24], including the $\mathrm{S}_{11}(1945)$, $\mathrm{P}_{13}(1950)$ and the $\mathrm{P}_{11}(1975)$. Capstick et al. [16] calculate that the $\mathrm{D}_{13}(1895)$ should have the strongest photoproduction and strange decay coupling, hence the emphasis on the D_{13} by Bennhold. The difference found between two calculations with and without the "missing" D_{13} resonance is shown for the differential cross-section in Fig 2.5. Here the contribution of the D_{13} plays a significant role in shaping the differential cross-section. At the top of Fig 2.5 there appears to be no structure at 1900 MeV other than a continuous curve from the threshold peak to the increasing contribution of the Born terms to the calculation. However, this situation is not repeated when the D_{13} is added into the recipe for calculating the differential cross-section.

At the bottom of Fig 2.5, the previously smooth curve at 1900 MeV is now broken by a distinct peak which is clearly observable over the entire angular range of the differential cross-section, further adding interest to the measurements made at SAPHIR [27, 35] and CLAS [34]. Clearly, if there is a peak in the cross-section of the $\mathrm{K}\Lambda$ channel at around 1900 MeV that is seen over the entire angular coverage of detectors like CLAS and ELSA, this is strong evidence that a N^{*} resonance is coupling to the strange decay in this case. Moreover, as Capstick and others [11, 12, 16, 36] have shown, this resonance is likely to fall into the category of being one of the "missing" resonances shown in Table 2.3. If the resonance that has been clearly suggested by previous $\mathrm{K}\Lambda$ cross-section measurements is in fact the $\mathrm{D}_{13}(1895)$, then this would be a very important discovery, with strong implications about the validity of the Constituent Quark Model as opposed to the Diquark Model.

However the most recent work by Janssen et al. [31] shows that the structure at ~1900 MeV is explainable by other means. In particular other resonances, discussed later and listed in Tables 2.2 and 2.3, may couple to the reaction strongly in this area, and the only way to disentangle their contribution to the reaction is to do a thorough calculation of the effect of each resonance on the polarisation observables of the reaction. At the present time this avenue looks capable of resolving the contributions of the 20 or so possible resonant participants (see Table 2.2), and removing the uncertainty surrounding the existence of the "missing" $\mathrm{D}_{13}(1895)$.

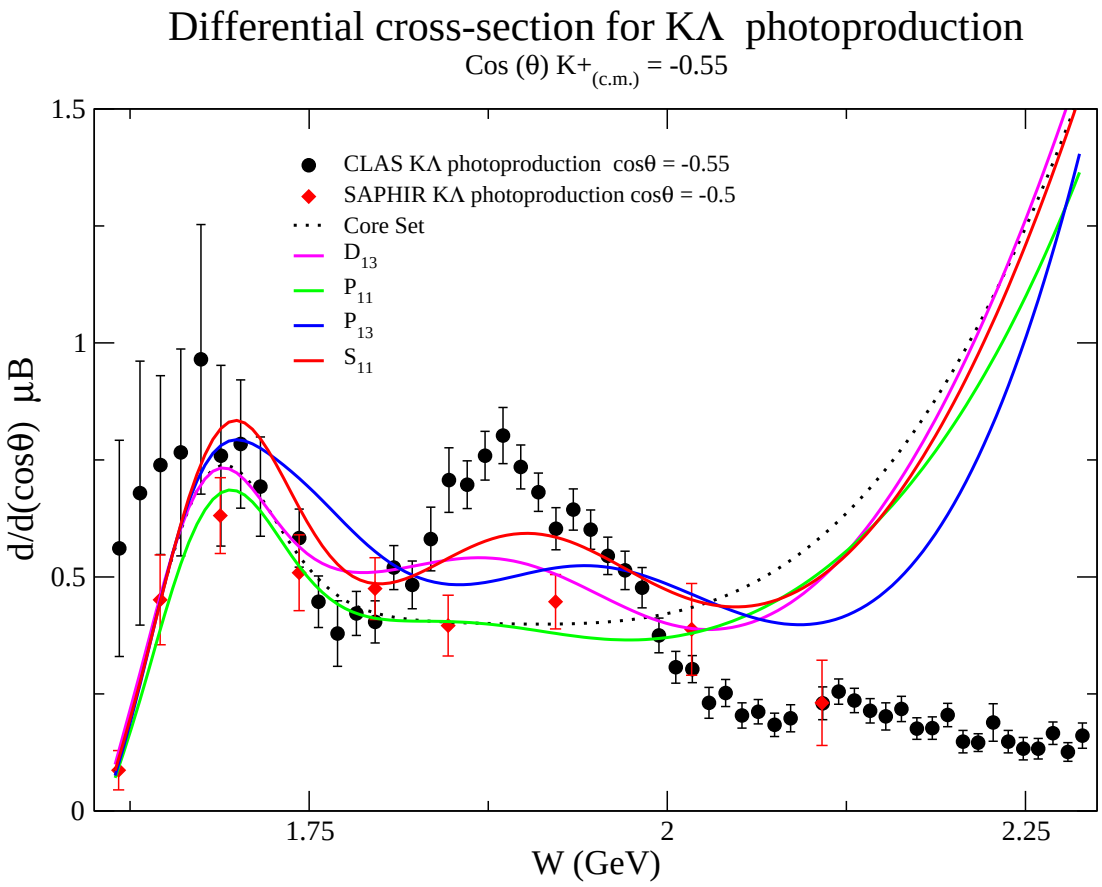

Figure 2.4: *The differential cross-section of* $p(\vec{\gamma},K^+)\Lambda^0$ *at an angle of* cos $\theta_{K^+_{C.M.}}$ = -0.5 *measured by McNabb et al. [34], compared with the equivalent measurement from SAPHIR [27].*
The bump at $W \simeq 1.9$ *GeV confirms the existence of structure just above the production threshold for this reaction, agreeing with the solid line fit in Fig 2.3. The theoretical curves shown here [31] and the sets of resonances used to generate them are described later in Fig 7.1 (and in Table 2.3). They rise dramatically above the data at higher W due to the effect of the background contributions (See Fig 2.6) to the propagator used to calculate the strength of* $K\Lambda$ *photoproduction. This propagator and accompanying formalism are described later in Section 2.4.4.*

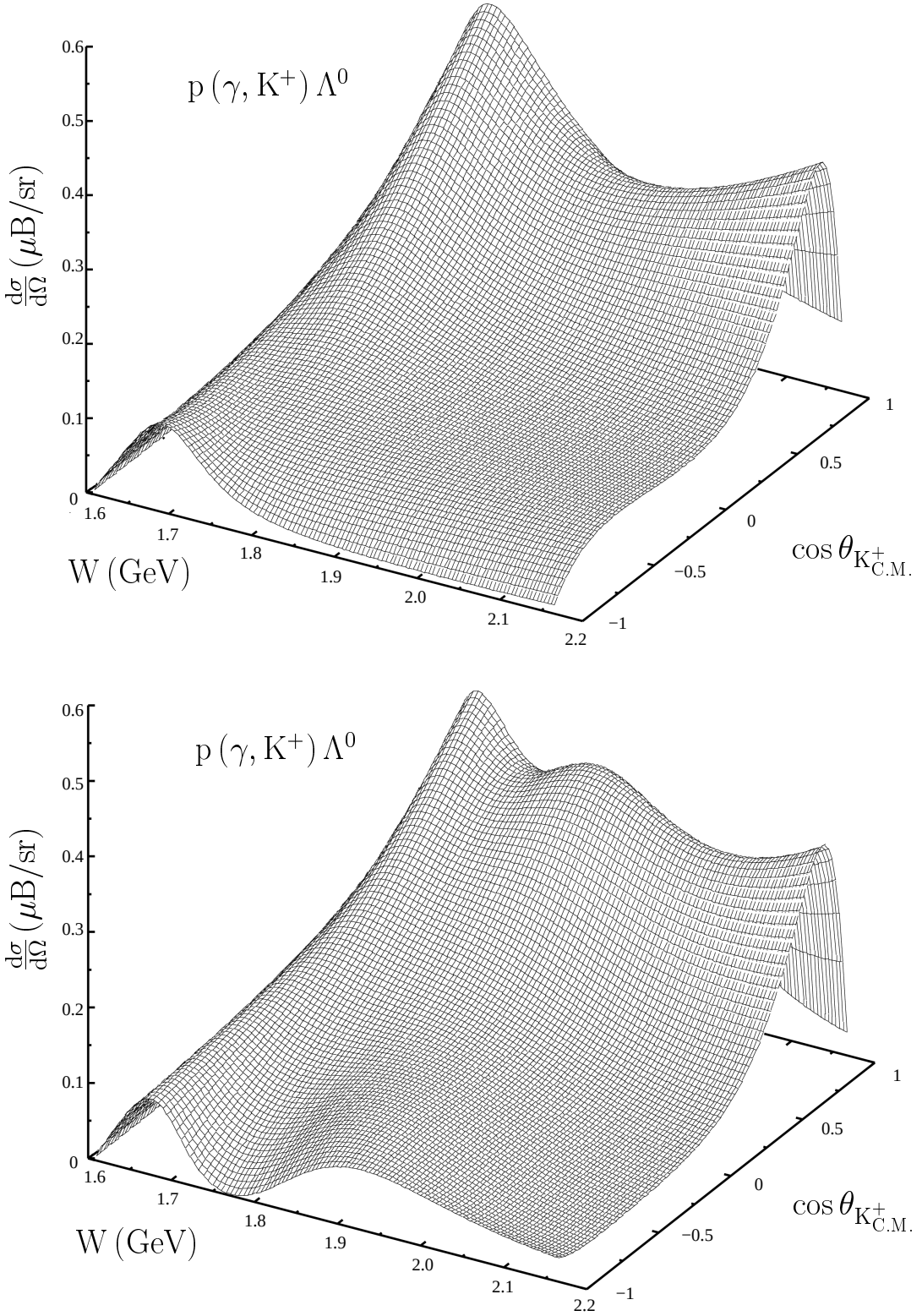

Figure 2.5: *The dependence of the quark model calculation of Mart et al. [11] on the inclusion of the* $D_{13}(1895)$ *resonance.*

Work by Janssen et al. [31, 36] incorporates the latest data on the $\gamma p \rightarrow K\Lambda$ cross-section with recent measurements of the photon asymmetry to create a well-constrained set of parameters for the couplings of possible candidate resonances. Using a new minimisation procedure developed by Ireland (see Section 2.7.1), the number of possible solutions generated by each of the candidate resonances is constrained, and each further measurement of polarisation observables will constrain the coupling parameters even more. The aim of this thesis, and surely that of other experiments in this field, is to improve the knowledge of the polarisation observables to reach the stage where the method developed by Janssen has a clear favourite for the candidate resonance which is producing the structure in the differential cross-sections shown in Figs 2.3 and 2.4.

In the next Section, the theoretical basis and formalism of the $p(\overrightarrow{\gamma}, K^+)\Lambda^0$ reaction is explored to give a deeper understanding of what the basic concepts and variables are that form the theoretical calculations. The latest predictions and how they compare with recent experiments also be examined, concentrating on the isobar model predictions for the polarisation observables, and most importantly the photon asymmetry.

2.4 Kaon photoproduction

2.4.1 Mandelstam variables

The Mandelstam variables [37] are a commonly used set of invariant relations derived from the four-momentum vectors that comprise the initial and final state of an interaction. In the case where $1 + 2 \rightarrow 3 + 4$ denotes two particles interacting, then the Mandelstam variables are derived as follows.

$$s = (1^\mu + 2^\mu)^2, \; t = (3^\mu - 1^\mu), \; u = (4^\mu - 1^\mu) \tag{2.1}$$

where x^μ denotes a vector containing three momentum components and one energy component, $x^\mu = (p_x\,,\, p_y\,,\, p_z\,,\, E)$.

When considering the reaction $\overrightarrow{\gamma} + p \rightarrow K^+ + \Lambda^0$, eqn 2.1 then becomes

$$s = (\overrightarrow{\gamma}^\mu + p^\mu), \; t = (K^{+\,\mu} - \overrightarrow{\gamma}^\mu), \; u = (\Lambda^{0\,\mu} - \overrightarrow{\gamma}^\mu) \tag{2.2}$$

2.4.2 Tree-level diagrams

The best way to analyse the contributions to a reaction channel is to consider the relevant Feynman diagrams which could take part. For the purpose of this thesis, and

also in recent literature [38, 39], only the first order Feynman diagrams are taken to be relevant, and these lower order diagrams are known as the tree-level diagrams as shown in Fig 2.6. Although a full coupled-channel analysis is necessary to disentangle the final state interactions between outgoing particles when higher order diagrams are included, the contribution to the differential cross-section is estimated to be less than 20% [29].

As mentioned in Section 2.4.1, invariant properties of a reaction are extremely useful for determining the reaction type, and we can distinguish between the different possibilities for particle exchange by classifying them as **s-channel**, **t-channel**, or **u-channel** reactions. As Fig 2.6 demonstrates, s,t and u channel exchange can be thought of as the exchange of a particle in a certain physical situation. For example, t-channel exchange is shown in Fig 2.6 as a transverse exchange. This reflects the more rigorous definition as the exchange of energy between the energetic incoming particle and the energetic outgoing particle of eqn 2.2 taking place in the centre of mass Lorentz frame. For the $K\Lambda$ reaction the **s, u** and **t-channel** also exchange excited states, particularly N^* resonances which are exchanged in the **s-channel.** The theoretical description of resonance production is continued in Section 2.4.4.

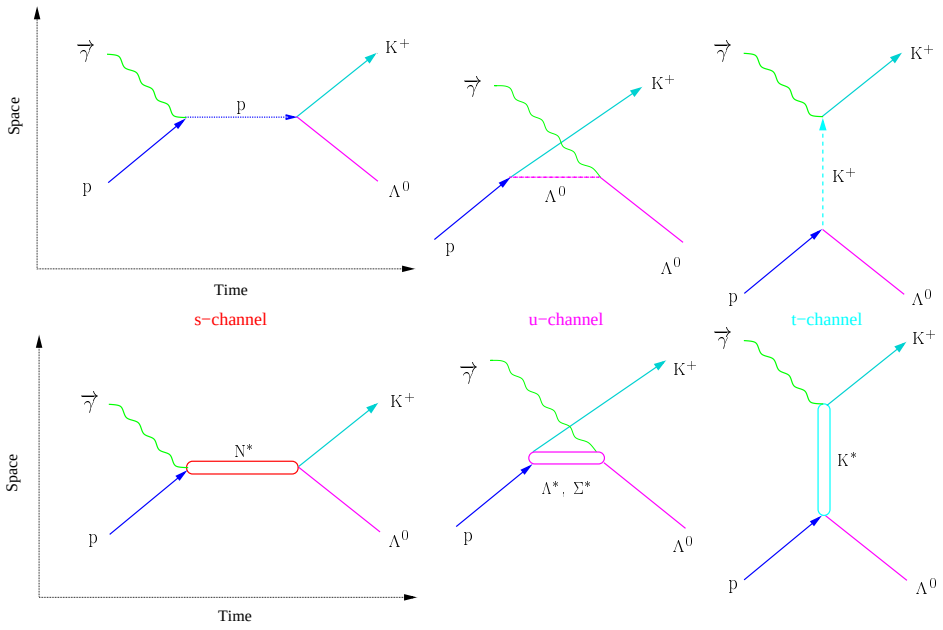

Figure 2.6: *Tree-level Feynman diagrams for $K\Lambda$ photoproduction. On the top row the Born terms describe the straightforward exchange of one of the three massive particles involved in the reaction. On the bottom row, the contributions from the N^* resonances are shown in the s-channel, and the exchange of an excited Λ^*/Σ^*, or a K^* is shown in the u and t-channel respectively.*

2.4.3 Isobar Model

In this phenomenological method, the basis of the Isobar Model is to treat each leading order Feynman diagram as a contributor to the overall reaction, and then the coupling strength of the contribution is determined either by obtaining a best possible fit to the cross-section, or investigating the polarisation observables.

The important components are identified as the terms which define an individual process and the respective coupling constants of those terms. The coupling constants determine how strongly an individual process may couple to the $\mathrm{K}\Lambda$ decay channel. Typically one would have an expression which is included in the invariant Feynman amplitude $\mathcal{M}_{fi}$, and the effect of this term will be modified by the coupling constant $g_{K\Lambda N}$, where N is a nucleon containing up and down quarks only. The relevant Feynman diagram is shown in Fig 2.7. The calculation of these coupling constants is made either using the constituent quark or diquark model as described in Section 2.2.

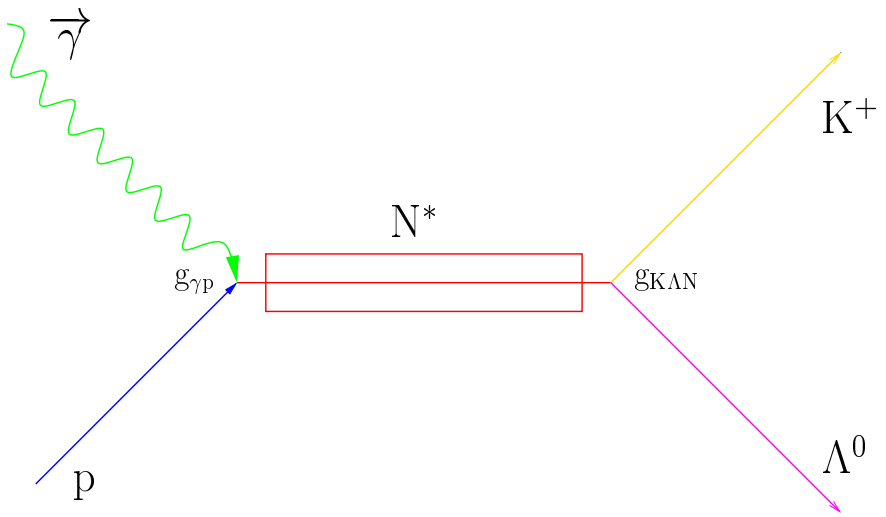

Figure 2.7: *The Feynman diagram for the* $p(\vec{\gamma}, K^+)\Lambda^0$ *reaction.*

For each possible N^* contribution, a separate $g_{K\Lambda N}$ constant is added to the overall expression. For the exchange of a spin$-\frac{1}{2}$ N^* resonance at the $\mathrm{K}\Lambda$ vertex, which is the only type of resonance usually considered for $\mathrm{K}\Lambda$ photoproduction due to isospin selection rules, the effective Lagrangian [40, 41] is expressed as follows.

$$\mathcal{L}_{\mathcal{KBR}} = -\mathrm{ig_{KBR}K^{\dagger}\overline{B}\Gamma R} + \text{ hermitian conjugate} \tag{2.3}$$

Where K represents the effective field of the kaon, B is the baryon field and R is the spin $-\frac{1}{2}$ resonance field. Γ represents the gamma-matrix γ^5 [42].

From this an important property is derived, the resonance parameter $\mathrm{G_R}$.

$$\mathrm{G_R} = \frac{\mathrm{g_{KBR}}}{\sqrt{4\pi}}\mathrm{K_{BR}} \tag{2.4}$$

Since the isobar model is based on treating the interacting particles as effective fields, the masses of the particles and the coupling constants are not directly calculable. One approach to building a consistent isobar model describing the $\mathrm{p}\,(\overrightarrow{\gamma}, \mathrm{K^+})\,\Lambda^0$ reaction is to treat these various $\mathrm{G_R}$ as free parameters to be found by performing a global fit to the data, including cross-section information and the available polarisation observable data set.

The theoretical predictions are sensitive to the coupling constants, so it is convenient to define a χ^2 in terms of the variations between theory and experiment. For N data points

$$\chi^2 = \frac{1}{\mathrm{N}}\sum_{\mathrm{i}}^{\mathrm{N}} \frac{\left[\mathrm{X_i} - \mathrm{Y_i}\,(\mathrm{a_1}, ...\mathrm{a_n})\right]^2}{\sigma^2_{\mathrm{X_i}}} \tag{2.5}$$

where X_i are the observables that are measured and $\sigma^2_{X_i}$ are the corresponding standard deviations. $Y_i\,(a_1, ...a_n)$ are the corresponding theoretical predictions for those observables and included in the parameters a_x are the resonant parameters described above.

The fundamental approach taken to optimise the χ^2 value is to alter the number and type of resonances participating in the isobar model while using the latest experimental data which helps to constrain these free resonant parameters. The basic set of ingredients that has been tried and tested by a number of groups [12, 25, 31, 36, 38, 43] is to include the exchange of Born terms as shown in Fig 2.6, and add to that a set of core resonances [11, 25]. The core set used by Janssen et al. [36] includes the $\mathrm{S_{13}}(1650)$, $\mathrm{P_{11}}(1710)$ and $\mathrm{P_{13}}(1720)$. Recent calculations have indicated a large number of candidate $\mathrm{N^*}$ states that may couple to a strange decay channel, and some of the more well-known states are shown in Table 2.2. It has been observed that the structure seen in the SAPHIR and CLAS data is not only explainable by the inclusion of the $\mathrm{D_{13}}$ state, but also a $\mathrm{P_{13}}(1950)$ state. However, the theoretical prediction of the polarisation observables differs markedly as shown in Fig 2.11, which makes the measurement of polarisation observables an essential component of further progress with the understanding of the isobar model.

The set of resonances used by Janssen et al. [31] to construct an isobar model is shown in Table 2.3. The $\mathrm{N^*}$ states with mass around $1900\,\mathrm{MeV/c^2}$ are all considered

Resonant State (Mass MeV/c^2)	$L_{\{2I\},\{2J\}}$	PDG Star Rating
N(1440)	P_{11}	****
N(1520)	D_{13}	****
N(1535)	S_{11}	****
N(1650)	S_{11}	****
N(1675)	D_{15}	****
N(1680)	F_{15}	****
N(1700)	D_{13}	***
N(1710)	P_{11}	***
N(1720)	P_{13}	****
N(1895)	D_{13}	?
N(1895)	P_{13}	?
N(1900)	P_{13}	**

Table 2.2: The N^* resonances which have been predicted to couple to the p($\vec{\gamma}$,K^+)Λ^0 decay channel. The PDG rating refers to the Particle Data Group publication [24].

as viable explanations for the bump in the KΛ total cross-section [see Fig 2.3], and the different coupling constants for these resonances to the $g_{K\Lambda N}$ vertex give different predictions for the polarisation observables described in more detail in Table 2.4.

Resonant Term	$L_{\{2I\},\{2J\}}$	PDG Star Rating
N(1650)	S_{11}	****
N(1710)	P_{11}	***
N(1720)	P_{13}	****
N(1895)	D_{13}	?
N(1945)	S_{11}	?
N(1950)	P_{13}	?
N(1975)	P_{11}	?

Table 2.3: Janssen's set of contributing resonances.

2.4.4 Formalism

The most common way of describing the photoproduction of the KΛ system is to consider a kaon photoproduction operator. This operator should take account of the fact that the kaon is produced from the excited nucleon and knowledge of the kaon state allows the prediction of the Λ^0 system, and with that the resonant state which produced them both.

The operator is defined by a Scattering Matrix or $\mathcal{S}$-Matrix, which describes the distribution of flux through open reaction channels [42]. This is of the form [38]

$$\mathcal{S}_{fi} = \frac{1}{(2\pi)^2}\left[\frac{\mathrm{M_p M_\Lambda}}{4\mathrm{E_\Lambda E_K E_p E_\gamma}}\right]^{\frac{1}{2}} \mathcal{M}_{fi} \times \delta^{(4)}(\mathrm{p_p} + \mathrm{p_\gamma} - \mathrm{p_K} - \mathrm{p_\Lambda}) \tag{2.6}$$

The invariant Feynman amplitude $\mathcal{M}_{fi}$ governs this reaction, and is strongly correlated to the photon polarisation, the target nucleon, and the recoiling hyperon(Λ, Σ). Here, δ represents a delta function of the difference in energy of the reaction between ingoing and outgoing particles. The mass and energy of the participating particles are given by $\mathrm{M_{p/K/\gamma/\Lambda}}$ and $\mathrm{E_{p/K/\gamma/\Lambda}}$. A useful way for $\mathcal{M}_{fi}$ to be expressed is in terms of the Chew-Goldberger-Low-Nambu (CGLN) [44] amplitudes .

$$\mathcal{M}_{fi} = \left[\frac{\mathrm{E_\Lambda + M_\Lambda}}{2\mathrm{M_\Lambda}}\right]^{\frac{1}{2}} \left[\frac{\mathrm{E_p + M_p}}{2\mathrm{M_p}}\right]^{\frac{1}{2}} \langle \chi(\Lambda) | \mathcal{F} | \chi(\mathrm{p}) \rangle \tag{2.7}$$

where

$$\mathcal{F} = \sigma \cdot \widehat{\varepsilon}\mathcal{F}_1 + \mathrm{i}(\sigma \cdot \widehat{\mathrm{p}}_\mathrm{K})(\sigma \cdot \widehat{\mathrm{p}}_\gamma \times \widehat{\varepsilon})\mathcal{F}_2 + (\sigma \cdot \widehat{\mathrm{p}}_\gamma)(\widehat{\mathrm{p}}_\mathrm{K} \cdot \widehat{\varepsilon})\mathcal{F}_3 + (\sigma \cdot \widehat{\mathrm{p}}_\mathrm{K})(\widehat{\mathrm{p}}_\mathrm{K} \cdot \widehat{\varepsilon})\mathcal{F}_4 \tag{2.8}$$

In the above notation $(\chi\,(\Lambda))$ and $(\chi\,(\mathrm{p}))$ each denote a two-component spinor representation of the standard Lorentz invariant matrix element, as described in Ref. [43]. Here σ represents the standard Pauli matrices, $\widehat{\mathrm{p}}_\gamma$ is the incoming photon momentum in the centre-of-mass frame, $\widehat{\mathrm{p}}_\mathrm{K}$ is the outgoing kaon momentum in the centre-of-mass frame and $\widehat{\varepsilon}$ is the photon polarisation vector. The F terms represent the electromagnetic multipoles [41] of the Feynman amplitude shown in eqn 2.8.

As shown by Adelseck [38], we can define transversity amplitudes in terms of these CGLN amplitudes where θ is the centre-of-mass angle between the outgoing kaon and the incoming photon.

$$\mathrm{b_1} = -\frac{\mathrm{i}}{\sqrt{2}}(\mathcal{F}_1 - \mathcal{F}_2 \mathrm{e}^{-\mathrm{i}\theta})\mathrm{e}^{\mathrm{i}\theta/2} \tag{2.9}$$

$$\mathrm{b_2} = \frac{\mathrm{i}}{\sqrt{2}}(\mathcal{F}_1 - \mathcal{F}_2 \mathrm{e}^{\mathrm{i}\theta})\mathrm{e}^{-\mathrm{i}\theta/2} \tag{2.10}$$

$$\mathrm{b_3} = -\mathrm{b_1} - \frac{\sin\theta}{\sqrt{2}}(\mathcal{F}_3 + \mathcal{F}_4 \mathrm{e}^{-\mathrm{i}\theta})\mathrm{e}^{\mathrm{i}\theta/2} \tag{2.11}$$

$$\mathrm{b_4} = -\mathrm{b_2} - \frac{\sin\theta}{\sqrt{2}}(\mathcal{F}_3 + \mathcal{F}_4 \mathrm{e}^{\mathrm{i}\theta})\mathrm{e}^{-\mathrm{i}\theta/2} \tag{2.12}$$

Adelseck et al. have shown that from these four amplitudes it is possible to create sixteen expressions, termed polarisation observables and defined in Section 2.5, which affect the reaction amplitude shown in eqn (2.6).

2.5 Polarisation observables

These observables completely determine the amplitude of the polarised contribution to the differential cross-section. However, since these observables determine the precise polarisation effects in every part of the $\mathrm{K}\Lambda$ reaction, a special experimental setup is required to measure all of them.

In particular a polarised photon beam is needed, along with a polarised target as well as the ability to detect the final polarisation state of the recoiling baryon, the Λ^0 in this case. If such an experiment is carried out, the modification of the differential cross-section can be compared with the following derivation [45].

We have the formal derivation of the cross-section as

$$\frac{\mathrm{d}\sigma}{\mathrm{d}\Omega}_{\mathrm{K}^+_{\mathrm{C.M.}}} = \frac{1}{64\pi^2}\frac{|\overrightarrow{p}_{\mathrm{K}}|}{\omega}\frac{1}{\mathrm{W}^2}\left|\mathcal{M}_{fi}\right|^2 \tag{2.13}$$

Where $\overrightarrow{p}_{\mathrm{K}}$ and ω correspond to the three-momentum of the kaon and the photon respectively in the centre-of-mass frame, W $(=\sqrt{\mathrm{s}})$ is the invariant centre-of-mass energy and $\mathcal{M}_{fi}$ is the invariant amplitude described by Adelseck et al. From this prescription, Adelseck [38] and more generally Knochlein, Drechsel and Tiator [45] have calculated that the contribution to the measured differential cross-section from the use of a linearly polarised photon beam is of the form

$$\begin{aligned}\frac{\mathrm{d}\sigma}{\mathrm{d}\Omega}_{\mathrm{pol}} &= \frac{\mathrm{d}\sigma}{\mathrm{d}\Omega}_{0}\{1 - \mathrm{P}_\gamma\Sigma\cos 2\phi \\ &+ \mathrm{P}_{\mathrm{x}'}(-\mathrm{P}_\gamma\mathrm{O}_{\mathrm{x}'}\sin 2\phi - \mathrm{P}_\odot\mathrm{C}_{\mathrm{x}'}) \\ &- \mathrm{P}_{\mathrm{y}'}(-\mathrm{P}_\Lambda + \mathrm{P}_\gamma\mathrm{T}\cos 2\phi) \\ &- \mathrm{P}_{\mathrm{z}'}(\mathrm{P}_\gamma\mathrm{O}_{\mathrm{z}'}\sin 2\phi + \mathrm{P}_\odot\mathrm{C}_{\mathrm{z}'})\}\end{aligned} \tag{2.14}$$

Where $\frac{\mathrm{d}\sigma}{\mathrm{d}\Omega}_0$ is the unpolarised differential cross-section, P_γ is the degree of linear polarisation of the incoming photon, $\left(\mathrm{P}_{\mathrm{x}'}, \mathrm{P}_{\mathrm{y}'}, \mathrm{P}_{\mathrm{z}'}\right)$ are the polarisation vector components of the recoiling nucleon, P_Λ is the Λ polarisation asymmetry, T is the target polarisation, $\mathrm{P}_\odot$ is the degree of right-handed circular polarisation of the photon beam, and $(\mathrm{C}_{\mathrm{x}'}, \mathrm{C}_{\mathrm{y}'}, \mathrm{O}_{\mathrm{x}'}, \mathrm{O}_{\mathrm{z}'})$ are double polarisation observables calculated by comparing

the recoil polarisation with the beam polarisation. These variables are all defined with ϕ as the azimuthal angle in the $\mathrm{K}\Lambda$ centre of mass. These observables and their derivations from the transversity amplitudes [46] are shown in Table 2.4.

Table 2.4: The observables contributing to $\frac{d\sigma}{d\Omega}$ and how they derive from the transversity amplitudes(Eqns[2.9 to 2.12]). (b_n^* denotes the respective complex conjugate).

Observable	Polarisation	Transversity Amplitude Description
$\frac{\mathrm{d}\sigma}{\mathrm{d}\Omega}_0$	linear	$= \lvert\mathrm{b}_1\rvert^2 + \lvert\mathrm{b}_2\rvert^2 + \lvert\mathrm{b}_3\rvert^2 + \lvert\mathrm{b}_4\rvert^2$
$\left(\frac{\mathrm{d}\sigma}{\mathrm{d}\Omega}_0\right).\mathrm{P}_\Lambda$ (recoil polarisation)	linear	$= \lvert\mathrm{b}_1\rvert^2 - \lvert\mathrm{b}_2\rvert^2 + \lvert\mathrm{b}_3\rvert^2 - \lvert\mathrm{b}_4\rvert^2$
$\left(\frac{\mathrm{d}\sigma}{\mathrm{d}\Omega}_0\right).\Sigma$ (photon asymmetry)	linear	$= \lvert\mathrm{b}_1\rvert^2 + \lvert\mathrm{b}_2\rvert^2 - \lvert\mathrm{b}_3\rvert^2 - \lvert\mathrm{b}_4\rvert^2$
$\left(\frac{\mathrm{d}\sigma}{\mathrm{d}\Omega}_0\right).\mathrm{T}$ (target polarisation)	linear	$= \lvert\mathrm{b}_1\rvert^2 - \lvert\mathrm{b}_2\rvert^2 - \lvert\mathrm{b}_3\rvert^2 + \lvert\mathrm{b}_4\rvert^2$
$\left(\frac{\mathrm{d}\sigma}{\mathrm{d}\Omega}_0\right).\mathrm{C}_{x'}$ (beam-recoil)	circular	$= -2\Im(\mathrm{b}_1\mathrm{b}_4^* - \mathrm{b}_2\mathrm{b}_3^*)$
$\left(\frac{\mathrm{d}\sigma}{\mathrm{d}\Omega}_0\right).\mathrm{C}_{y'}$ (beam-recoil)	circular	$= 2\Re(\mathrm{b}_1\mathrm{b}_4^* + \mathrm{b}_2\mathrm{b}_3^*)$
$\left(\frac{\mathrm{d}\sigma}{\mathrm{d}\Omega}_0\right).\mathrm{O}_{x'}$ (beam-recoil)	linear	$= 2\Re(\mathrm{b}_1\mathrm{b}_4^* - \mathrm{b}_2\mathrm{b}_3^*)$
$\left(\frac{\mathrm{d}\sigma}{\mathrm{d}\Omega}_0\right).\mathrm{O}_{z'}$ (beam-recoil)	linear	$= 2\Im(\mathrm{b}_1\mathrm{b}_4^* + \mathrm{b}_2\mathrm{b}_3^*)$

For the analysis presented in Chapter 6, the observable that is explicitly measured is the photon asymmetry Σ. This is defined experimentally by Adelseck and many others [43, 45, 46] as the ratio of the measured cross-section parallel and perpendicular to the plane of the electric vector of the polarised photon beam. The angles used to define the direction of these planes are shown in Fig 2.8.

$$\Sigma = \frac{1}{\mathrm{P}_\gamma}\left(\frac{\frac{\mathrm{d}\sigma}{\mathrm{d}\Omega}_{||} - \frac{\mathrm{d}\sigma}{\mathrm{d}\Omega}_{\perp}}{\frac{\mathrm{d}\sigma}{\mathrm{d}\Omega}_{||} + \frac{\mathrm{d}\sigma}{\mathrm{d}\Omega}_{\perp}}\right) \tag{2.15}$$

The other polarisation observables that can be measured using a linearly polarised photon beam are given by the same kind of relation with respect to a different quantisation axis.

The recoiling Λ polarisation is given by

$$\mathrm{P}_\Lambda = \left(\frac{\frac{\mathrm{d}\sigma}{\mathrm{d}\Omega}_{(+)} - \frac{\mathrm{d}\sigma}{\mathrm{d}\Omega}_{(-)}}{\frac{\mathrm{d}\sigma}{\mathrm{d}\Omega}_{(+)} + \frac{\mathrm{d}\sigma}{\mathrm{d}\Omega}_{(-)}}\right) \tag{2.16}$$

where the $(+/-)$ sign indicates whether the measured hadronic cross-section is parallel(anti-parallel) to the relevant quantisation axis, which in this case is the direction of the Λ^0 spin in the centre-of-mass frame (see Fig 2.9). The target polarisation T is given by a similar expression to eqn 2.16 but is not given here since the G8a target

is unpolarised hence this variable will not be independently accessible. P_Λ is measurable in the G8a experimental set-up since CLAS is well suited to measure the angular distribution of hadronic decays, but determining the target polarisation observable and hence accessing the double-polarisation observables as shown in Table 2.4 is planned for a future experiment in Hall B [32, 33].

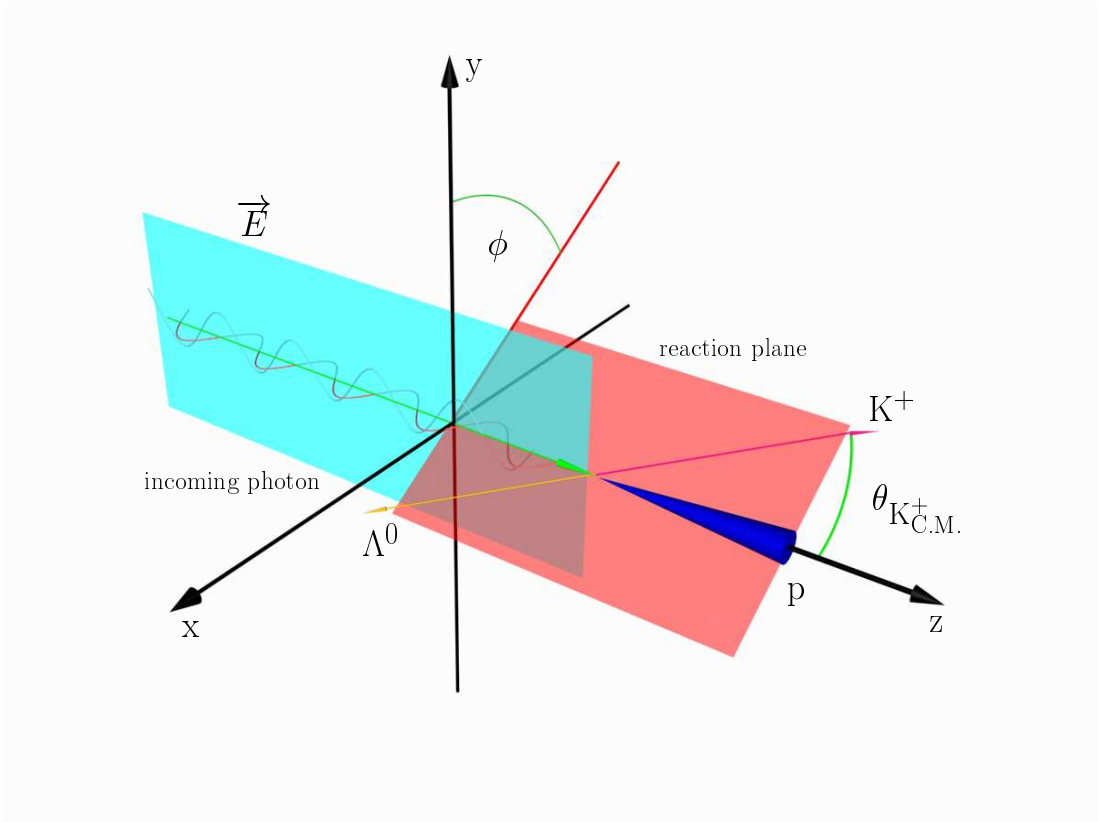

Figure 2.8: *The geometry of the $K\Lambda$ reaction plane and the angles that are used to determine the photon asymmetry. The angle ϕ is defined as the angle between the reaction plane and the electric vector plane of the incident photon. The angle $\theta_{K^+_{C.M}}$ is defined as the angle between the direction of the K^+ in the centre-of-mass frame and the* **z***-axis.*

2.6 Measuring the photon asymmetry

The photon asymmetry is defined according to eqn 2.15. From this expression the variables that are accessible in the G8a experimental setup are the degree of linear polarisation P_γ, and the actual direction of the electric vector of the polarised photon which defines the quantisation axis for parallel and perpendicular yields.

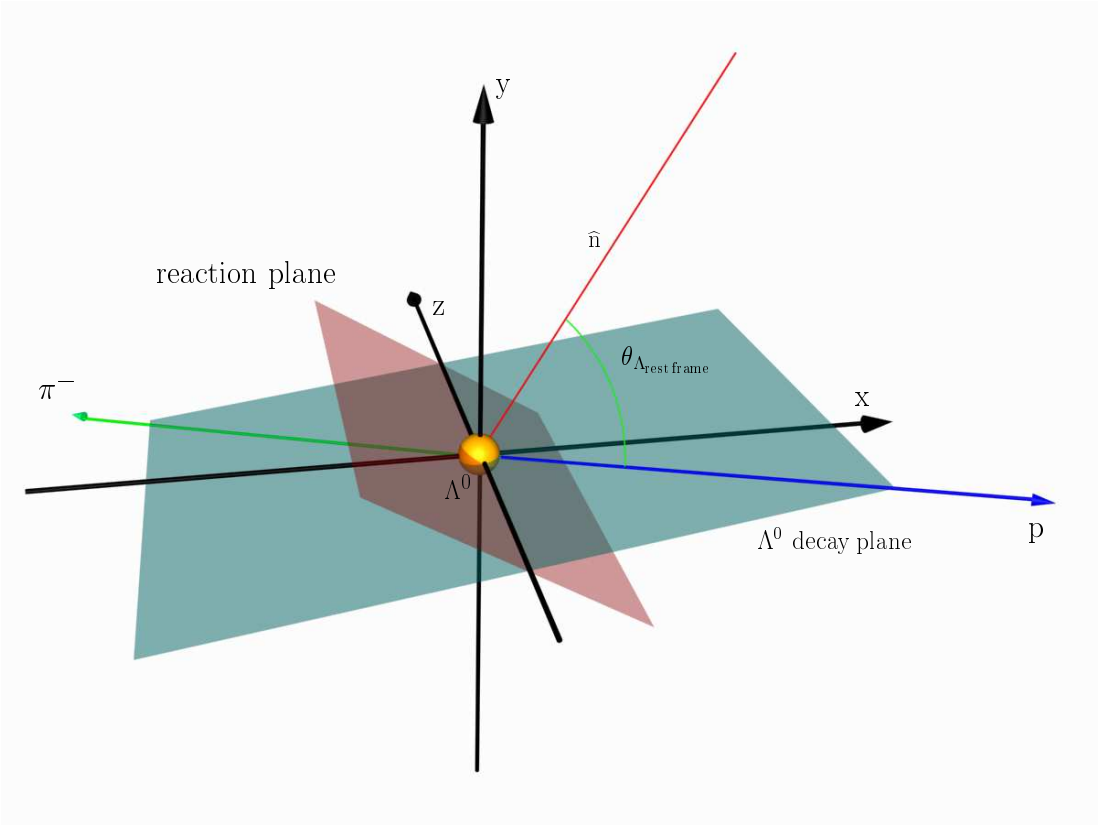

Figure 2.9: *The geometry of the lambda rest frame and the angle $\theta_{\Lambda_{R.F.}}$, which is used to calculate the Λ recoil polarisation [34].*
$\theta_{\Lambda_{R.F.}}$ is defined as the angle between the plane defined by the direction of the proton in the rest frame and the normal $\hat{n}$ to the reaction plane as defined in Fig. 2.8.

The cross-section is not directly measurable since there was no way to accurately calculate the total photon flux due to hardware problems. However, from Table 2.4 the expression for the photon asymmetry derived from the transversity amplitudes is related to the equivalent expression for the total cross-section. In fact since the rest of the polarisation observables are not accessible in this experiment the form of Eqn 2.14 can be reduced to

$$\frac{\mathrm{d}\sigma}{\mathrm{d}\Omega_{\,\mathrm{pol}}} = \frac{\mathrm{d}\sigma}{\mathrm{d}\Omega_{\,0}} \left\{1 - \mathrm{P}_{\gamma}\Sigma\cos 2\phi\right\} \tag{2.17}$$

and from this the normalisation factors cancel out on either side of the equation.

It follows then that it is possible to use unpolarised data from an amorphous radiator to produce an un-normalised data set containing the acceptance and angular information from CLAS and compare this to polarised data. If the data is taken with the same angular bin width it is feasible to divide the polarised data set by the unpolarised data set to remove the systematic effects of acceptance variation within CLAS. If this resulting data set is then scaled appropriately to an average value of 1, Eqn 2.17 is then satisfied and provided the degree of linear polarisation of the photon beam is known, the photon asymmetry Σ is directly accessible.

In Fig 2.10 the expected angular dependence of ϕ produced using a polarised photon beam is shown. The azimuthal angle ϕ is defined in Fig 2.8, and the expected data set has been normalised to a baseline value of 1, while removing the expected systematic variations in the acceptance of CLAS .

This procedure is assumed to work under the assumption that the systematic variations in CLAS change very slowly over the duration of the experiment. This is in fact a reasonable assumption, as will be discussed in Section 6.3.

2.7 Recent measurement of Σ

The LEPS [47] collaboration working at the SPring-8 [14] facility in Japan have recently made a measurement of the photon asymmetry from the $\mathrm{p}\,(\overrightarrow{\gamma},\mathrm{K}^{+})\,\Lambda^{0}$ reaction [48]. Their experimental set-up was based on laser produced Compton backscattering $\overrightarrow{\gamma}$ production. While the experimental measurement was restricted in the angular coverage of $\theta_{\mathrm{K}^{+}_{\mathrm{C.M.}}}$ an interesting comparison with theory was still possible, and has been published recently [31]. Fig 2.11 shows the results from SPring-8 compared with the isobar model calculations by Janssen et al., demonstrating a good agreement with theory between $0.5 < \cos\,\theta_{\mathrm{K}^{+}_{\mathrm{C.M.}}} < 1$.

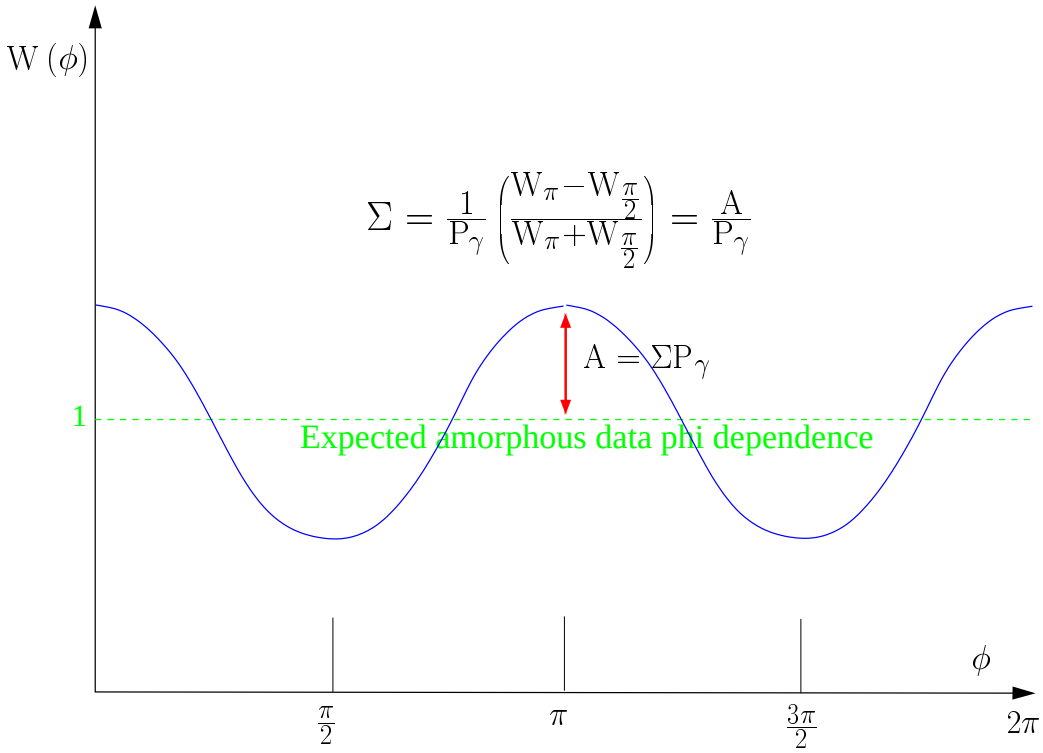

Figure 2.10: *The expected form of the photon asymmetry when the data has been normalised.* $W(\phi)$ *represents the particle yield at a particular azimuthal angle in CLAS. The cosine distribution of the polarised data set (shown in blue) has no phase offset if the electric vector of the incident polarised beam is aligned with the y-axis in the CLAS coordinate system (See Fig 2.8).* P_γ *is the degree of linear polarisation of the photon beam.*

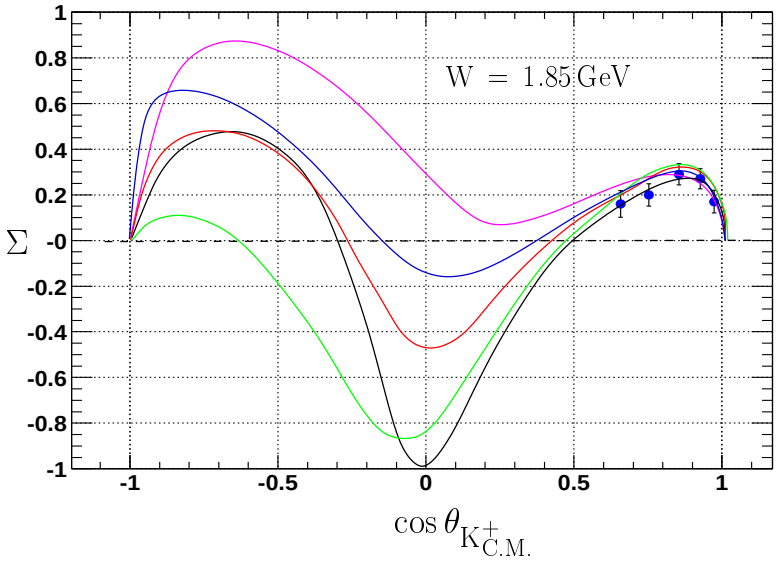

Figure 2.11: *SPring-8 results for the measurement of* Σ *in the p(*$\vec{\gamma}$*,*K^+*)*Λ^0 *reaction at a photon energy of 1.85 GeV. The theoretical curves have been generated from a recent calculation by Janssen et al. [36]. The recipe of resonant states used in this calculation is shown in Table 2.3 and the* D_{13} *resonance is represented by the purple line,* P_{11} *is green,* P_{13} *is blue, and* S_{11} *is red.*

The latest calculations of Janssen et al. [31] do not represent an unique solution for the properties of the polarisation observables of the $\mathrm{K}\Lambda$ reaction. In fact, recent advancements in the use of iterative techniques and numerical solutions of equations by computer point to a new approach for resolving the variety of resonant states that may couple strongly to the $\mathrm{K}\Lambda$ decay channel.

2.7.1 Genetic algorithms

A pioneering approach by Ireland [49] uses a numerical method based on evolutionary principles, known as genetic algorithms. Genetic algorithms mutate and evolve to find the "fittest" solution to a problem, for example finding the most likely coupling constant parameter of a particular resonance. The combination of polarisation observables, and resonant states with measured coupling constants to the $\mathrm{K}\Lambda$ decay channel, defines a parameter phase space. This iterative procedure has been used by Ireland et al. [31] to loop through the available parameter space of the $\mathrm{K}\Lambda$ reaction, testing different variations of coupling constant parameter for each resonance, and as the iteration progresses, the solutions evolve towards a set of likely values for the resonance cou-

pling strength. These variations in coupling constant value tend to lead to significant differences in the polarisation observables which then indicate that the experimental measurement of polarisation observables is sensitive to the actual quantum numbers of the resonant state being investigated.

More importantly, new data serves to restrict the accessible phase space still further which allows a convergent progress towards the correct answer. As shown in Fig 2.11 the data from SPring-8 already constrains the phase-space allowed for the prediction of Σ in the forward polar angles, and this has a direct effect on the range of values allowed for the other polarisation observables predicted by Janssen et al.

2.8 Current Work

This thesis presents a measurement of the photon asymmetry over an photon energy range of $1.6\,\mathrm{GeV}$ to $2.0\,\mathrm{GeV}$. The polar angle $\theta_{\mathrm{K}^+_{\mathrm{C.M.}}}$ coverage of this measurement is from $20^0 < \theta_{\mathrm{K}^+_{\mathrm{C.M.}}} < 120^0$, with the azimuthal coverage only limited by the areas of no acceptance in CLAS where the magnetic coils are located. The main issue to be addressed in the analysis of the data set is the sensitivity of the photon asymmetry to the presence of different N^* resonances in the isobar model calculations carried about by Janssen et al. The analysis presented in Chapter 6 of this thesis presents a measurement of the photon asymmetry at intermediate angles, which extends the measurement made by the LEPS collaboration and allow a better discrimination between the model predictions shown in Fig 2.11.

Chapter 3

Experiment

3.1 Facility

The g8a experiment which forms the basis of this thesis was performed in the summer of 2001 using the Thomas Jefferson National Accelerator Facility [13, 50], also known as the Continuous Electron Beam Accelerator Facility or CEBAF. This accelerator facility uses the racetrack configuration, shown in Fig 3.1, to produce a high quality continuous wave electron beam with energies of up to 6 GeV.

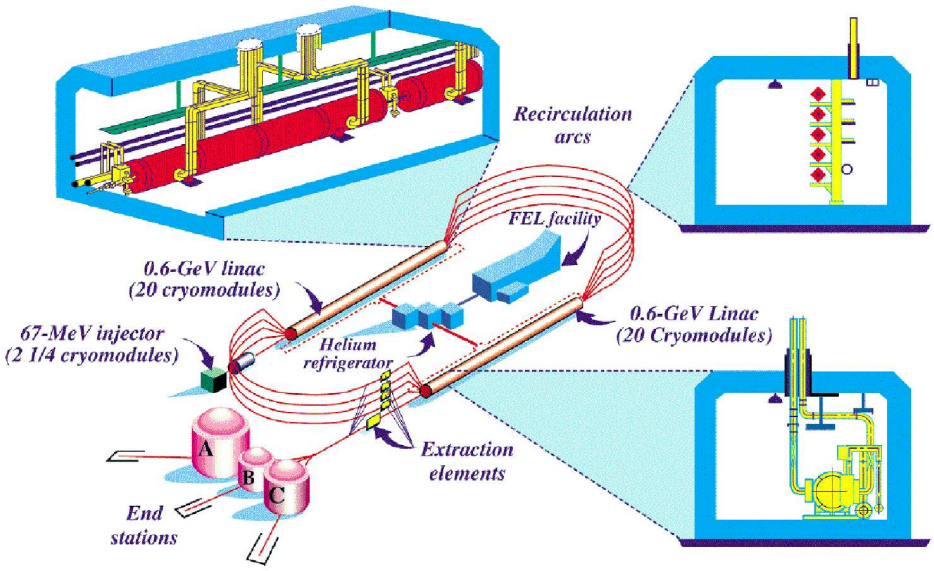

Figure 3.1: *CEBAF: The two main linacs provide an acceleration of 0.6* GeV *each to an electron for a maximum of five passes.*

Jefferson Lab is groundbreaking in its use of super-conducting technology to achieve these high beam energies. The accelerator consists of two linear accelerators which use special cryomodules made of niobium to provide the electric and magnetic fields necessary to accelerate electrons to 99.9% of the speed of light.

A cryomodule consists of eight niobium cavities, and each cavity has a radio frequency (RF) of 1.5 GHz. In effect the electromagnetic field inside the cavity is being cycled at a rate of around 1.5 billion times per second by a microwave device called a klystron. Each linear accelerator contains 160 cavities, which equates to 20 cryomodules.

The two linacs are joined by two arcs which use strong magnetic fields to redirect the beam and keep it focused. Typically the beam will pass through the racetrack up to 5 times before it has acquired enough energy to be used in one of the Experimental Halls. The journey of an electron normally starts by a process of thermionic emission in the the injector part of the accelerator site. This process produces electrons with an initial energy of 100 keV and then two and a quarter cryomodule units accelerate the beam further before it enters the racetrack with an energy of around 67 MeV.

As the electron passes into the first linac it is kicked along by oscillating electromagnetic fields in the niobium cryomodules which achieve extremely high intensities by virtue of the extremely low temperatures they are operated at. Liquid helium keeps these modules cool and the super-conducting characteristics allow CEBAF to achieve the aforementioned 6 GeV maximum beam energy.

The three experimental halls are named A, B and C, and aim to cover a broad range of physics programs. With each hall containing instruments tailored toward different studies, beam energies and currents are required to vary independently for each hall to allow simultaneous measurements. This is achieved by using three independent lasers which hit the photo-cathode in the injector effectively creating three different beams, each with an RF frequency of 499 MHz, and that may vary in terms of polarisation and charge. These intertwined beams are separated by an RF separator system [51] after the final pass through the accelerator[1].

The simultaneous demands of each Hall require the beam buckets to be physically diverted from the main beam-line and this is achieved by operating a group of RF separator cavities which are synchronised with the RF frequency of the components of the beam at 499 MHz each. The separator kicks out one pulse from a group of three which constitute the overall 1497 MHz beam, then diverting it into a specific hall. This

[1] A useful terminology introduced here to refer to these distinct packets of electrons is the 'beam bucket'. This will be mentioned again in Chapter (3).

means that each hall receives one-third of the total beam frequency, which corresponds to a bunch of electrons arriving in each Hall every 2 nanoseconds. The G8a experiment was carried out in Hall B, which houses the CLAS detector (CEBAF Large Acceptance Spectrometer [52]), the Photon Tagger and the Coherent Bremsstrahlung Facility [53]. In combination these facilities provide the unique opportunity to carry out linearly polarised photon experiments with several charged particles in the final state.

3.2 Coherent Bremsstrahlung facility

G8a was a new experimental development at Jefferson Lab because this was the first run to use linearly polarised photons incident on a target. In order to produce polarised photons from an electron beam certain techniques which were pioneered during the DAPHNE [54] experiment at the Mainz accelerator facility [55] were used. These techniques involved the use of a diamond crystal, which if oriented correctly, can produce linearly polarised photons via coherent bremsstrahlung.

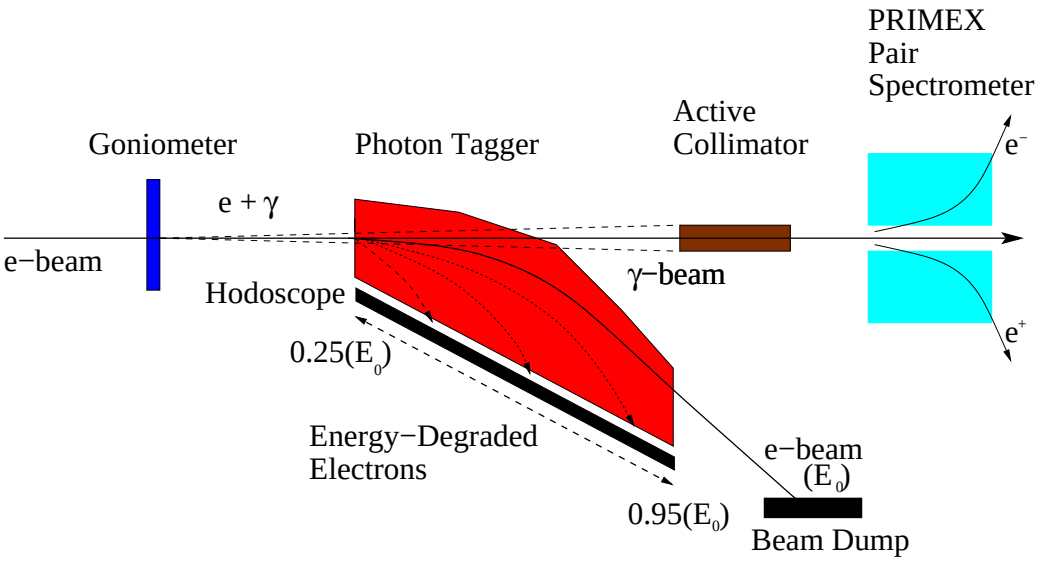

Figure 3.2: *Layout of beamline and the Coherent Bremsstrahlung Facility. The electron beam is steered away from CLAS by the Photon Tagger, and electrons which do not lose energy passing through the radiator in the goniometer have their original energy E_0. These electrons are then bent into the beam dump as shown. The PRIMEX pair spectrometer was present on the beam line during G8a but was not used.*

3.2.1 Process

The process of coherent bremsstrahlung production was used in the G8a experiment to produce a beam of linearly polarised photons. The initial consideration must be how the crystal actually produces a beam of coherent linearly polarised photons [56]. If an electron passes close by an atomic nucleus, it emits radiation as it decelerates through the accompanying electromagnetic field. This radiation is known as bremsstrahlung or "breaking radiation" and is the usual technique used to produce X-rays. If an electron beam hits a material where the molecular structure is not crystalline[2], the bremsstrahlung energy spectrum has a smooth shape which falls off monotonically with increasing photon energy, as shown in Fig 3.3.

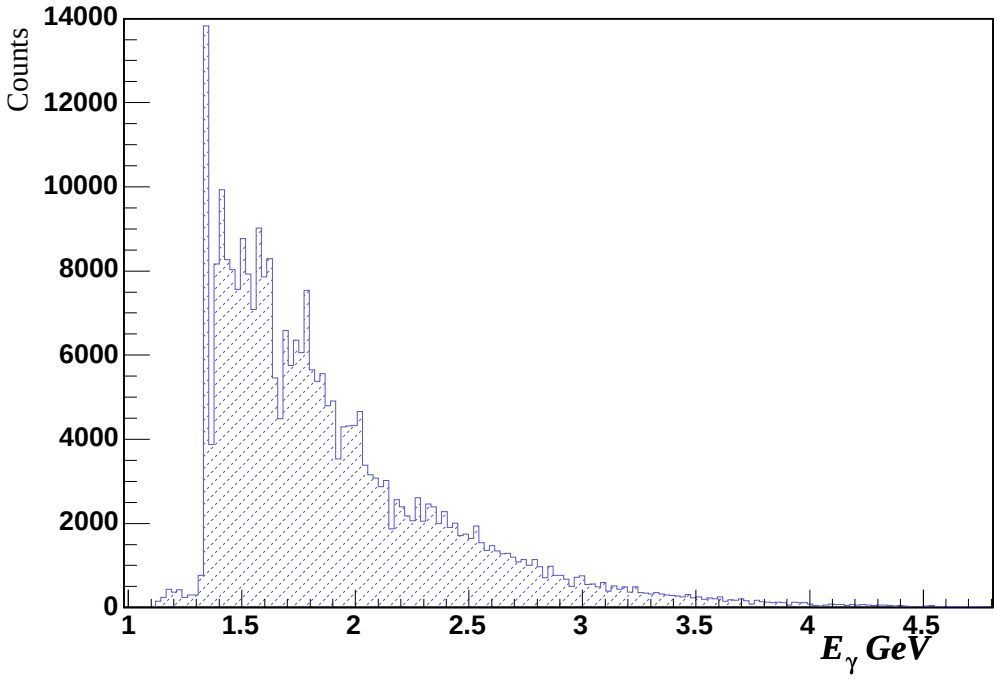

Figure 3.3: *The typical bremsstrahlung energy spectrum produced by an amorphous material such as carbon. The random fluctuations here are due to varying counter efficiencies.*

If the electron beam hits a crystalline structure, the regular order in the placement of electrons in the crystal tends to enhance the intensity of the photons produced at specific energies. This process is similar to Bragg Scattering in principle. At the top of Fig 3.4, a simulated coherent bremsstrahlung spectrum is plotted against energy,

[2]Most types of metal would be a good example.

produced by the **anb** code [57].

Usually a diamond crystal is used, due to its high Debye temperature and relatively small lattice parameter [58]. The highly ordered sets of crystal planes which are present in the diamond have to be carefully oriented with respect to the incident electron beam to achieve the desired effect of producing polarised photons. Fig 3.2 shows the experimental setup used in Hall B, where the beam entering the hall reaches a device called a goniometer, then passes to the photon tagger and on through the PRIMEX pair spectrometer towards the main detector in Hall B. This is discussed more fully in Section 3.5.

3.2.2 The Diamond Radiator

The quality of the linearly polarised photon beam is controlled to a large extent by the type and quality of the radiator used to produce it and as mentioned in Section 3.2.1 above, diamond is a favourable choice. Any defects in the crystal adversely affect the production process, and the background process of bremsstrahlung production from randomly oriented nuclei becomes more significant.

As shown in Fig 3.3 a typical incoherent bremsstrahlung spectrum varies monotonically with energy. The coherent contribution from the crystal planes in a diamond radiator appears as a set of peaks sitting on top of the incoherent background. Fig 3.4 shows a simulation of the total photon spectrum from diamond, consisting of an incoherent background spectrum as well as the coherent contribution. The simulated spectrum is generated by the **anb** code [57] which takes into account the effects of the electron beam divergence, crystal thickness and crystal plane orientation.

The properties of the diamond radiator need to be assessed using a number of tests. Firstly, linearly polarised visible light is shone through the crystal using a polarising lens. Another polarising lens is rotated 90^0 with respect to the first lens, which then allows areas of crystal anomalies such as stress and strain defects to be seen clearly. Fig 3.5 (left) shows the resulting photograph, and the crystal is near-perfect with some surface dust and growth horizons being the only visible features.

The next technique used to test the quality of the crystal is X-ray topography [59]. Here the crystal is placed in an X-ray beam at the Bragg angle for a particular set of planes. A perfect crystal shows minimal features in the photographic plate used to analyse the diffracted X-rays, while lattice defects change the image intensity.

Finally, the rocking curve [60] of the diamond is analysed. This is a plot of the intensity of diffracted X-rays versus crystal angle, which is a measure of how well the

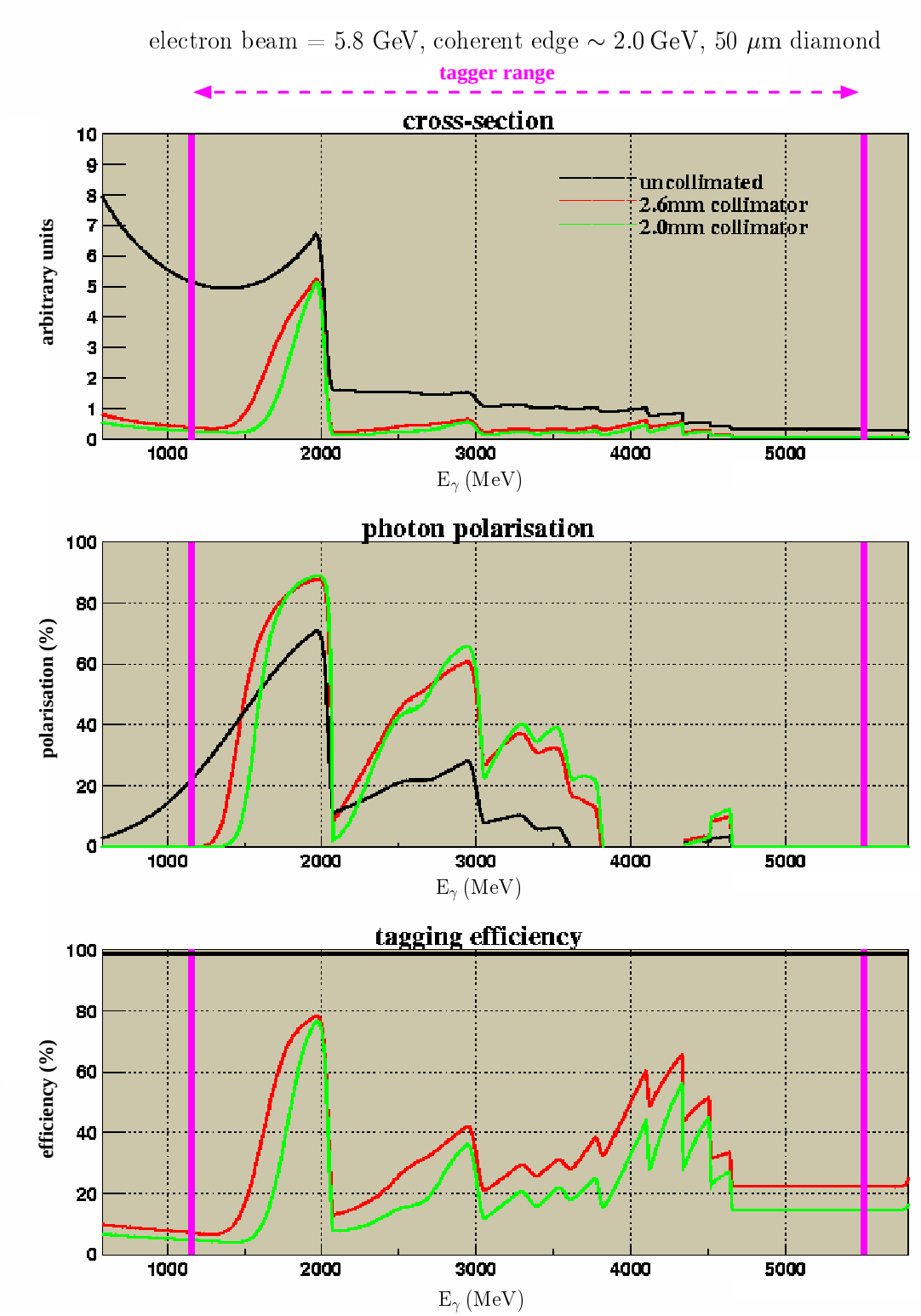

Figure 3.4: *A typical coherent bremsstrahlung spectrum from simulated data produced by the* **anb** *code.*
Top: *Cross-Section versus photon energy.* **Middle:** *Percentage linear polarisation versus photon energy.* **Bottom:** *Tagging Efficiency versus photon energy. The black line is an uncollimated simulation, the red is for a collimator aperture of* 2.6 mm *, and the green is for an aperture of* 2.0 mm.

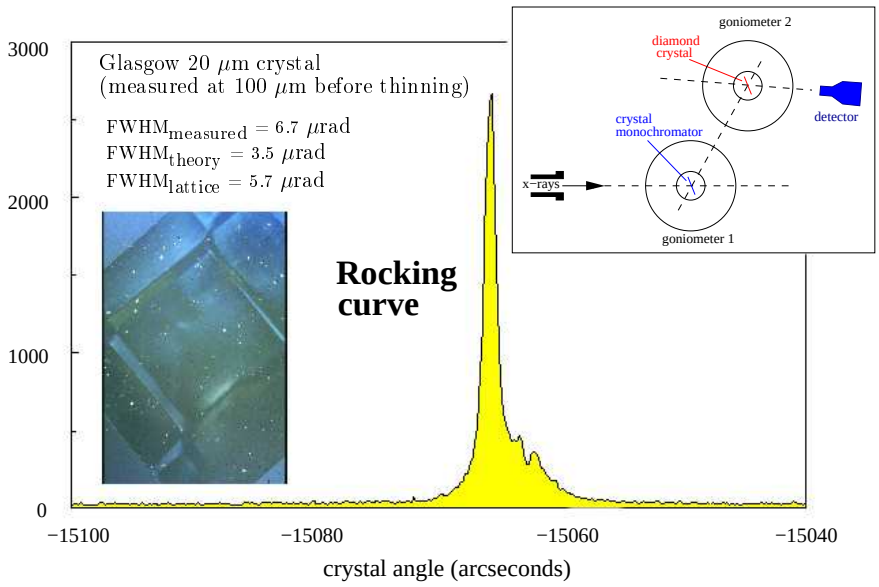

Figure 3.5: *The properties of a 20 μm diamond crystal.* **Left** *shows a photographic image of polarised light passing through the crystal.* **Top Right** *shows the experimental setup for performing an X-ray rocking curve measurement.* **Main picture** *shows a typical rocking curve, plotting crystal rotation angle against X-ray intensity.*

crystal planes within the lattice are oriented. If the width of the curve is narrow, the crystal has a highly regular lattice which is an important requirement for producing linearly polarised photons.

For the G8a experiment, deciding how thick the crystal radiator should be depends on two main factors. Firstly the multiple scattering angle of electrons passing through a crystal depends on the thickness of the crystal and the electron beam energy. The bremsstrahlung characteristic angle also varies with the energy of the incident electrons. If these two angles match then conditions are optimum for highest polarisation and photon flux [56]. The beam energy used in the G8 experiment is ~6 GeV, which translates into the required crystal thickness of $20\,\mu$m.

During run conditions the $20\,\mu$m diamond produced poor quality data, with dramatic variations in polarisation. The suspected cause was an instability in the mounting of the crystal to the goniometer target ladder, so during the experiment a $50\,\mu$m diamond had to be used instead. This crystal produced a much more stable photon beam, with the main disadvantage being a slightly reduced degree of linear polarisation (See Section 3.2.3) of the photons.

As shown in Fig 3.9 a number of other targets were used in the goniometer. A $50\,\mu$m thick carbon radiator was used to produce incoherent bremsstrahlung photons.

This radiator is an called an amorphous radiator since the random arrangement of the atoms in the carbon means that there is no regular crystal lattice to produce coherent bremsstrahlung, hence the photon beam produced has no overall polarisation. A zinc sulphide screen, $20\ \mu\mathrm{m}$ thick, was used as a scintillating screen to locate the position of the electron beam when preparing to start taking data during the experiment.

3.2.3 Polarised Photons

Throughout this work, the degree of linear polarisation of a photon beam is defined as P_γ. This is defined as a percentage, since a linearly polarised beam is never 100% polarised. An individual photon can be characterised in a binary fashion as either one of two polarisation states, polarised with respect to a particular plane or not polarised. The photon can be said to be plane-polarised (or linearly polarised) when the direction of its electric field vector lies in the plane.

A photon beam produced by incoherent bremsstrahlung (eg: by passing an electron beam through copper foil) will consist of a flux of photons, the electric vectors of which have a random orientation. By this definition, such a beam will have an average polarisation of 0%, not taking account of any statistical fluctuations which may occur. If the photon beam is produced by coherent bremsstrahlung (eg: the electron beam passing through a diamond), then the condition analogous to Bragg Scattering as referred to in Section 3.2.1 will be met and the electrons will interact with the diamond to produce plane-polarised photons. The plane of polarisation is determined by the diamond internal crystal-lattice geometry.

However, since this is not an idealised situation, the electron beam has a finite width, as does the diamond crystal, so even from simple geometry considerations and beam alignment issues, the beam will interact with the diamond occasionally when the conditions for coherent bremsstrahlung are not met. Under these realistic circumstances, for all the possible orientations of the electric vector of each individual photon, a majority of photons are expected to be polarised with respect to the diamond crystal lattice, with a minority oriented randomly.

This leads to a description of the polarised photon spectrum as having an incoherent part and a coherent part. The degree of linear polarisation at a measured photon energy is then simply the ratio of coherent polarised photons and incoherent unpolarised photons. Although the process of disentangling these contributions can be complex, since the edge of the coherent peak in the photon energy spectrum is sharp, the degree of linear polarisation in the vicinity of the peak is well-defined (Shown in Fig 3.6). The

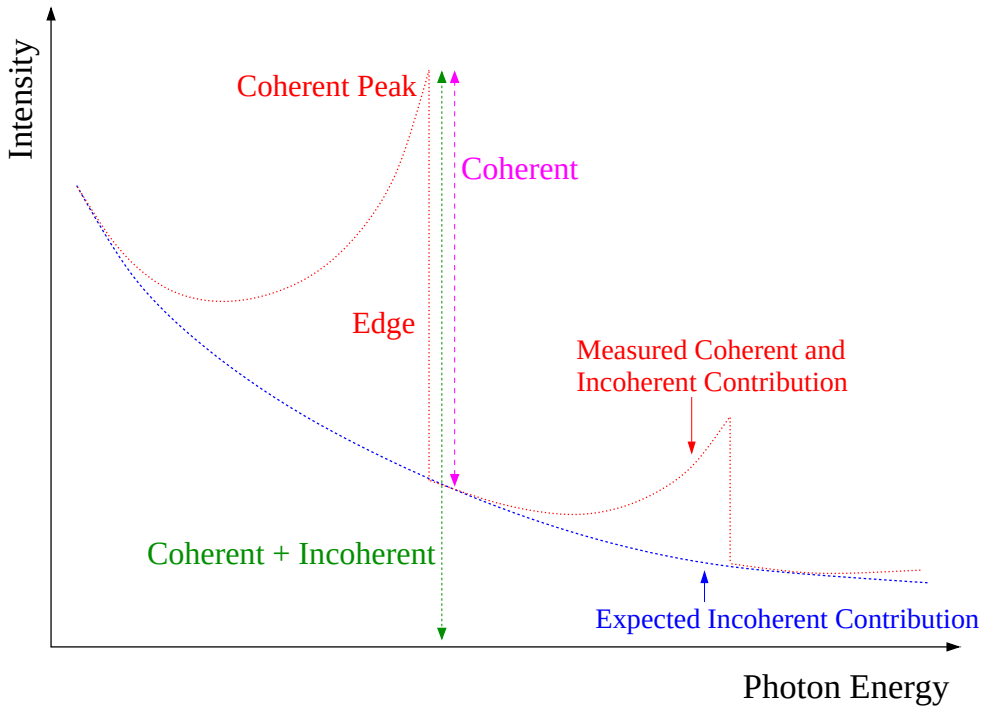

Figure 3.6: *The method of measuring the degree of linear polarisation at the coherent peak edge.*

degree of linear polarisation is given by the ratio:

$$\frac{\mathrm{I_{COH}}}{\mathrm{I_{COH}} + \mathrm{I_{INCOH}}} \tag{3.1}$$

which is equivalent to the ratio of the height of the coherent peak relative to the incoherent background, divided by the absolute height of the peak including the background at the coherent edge as illustrated in Fig 3.6. Here $\mathrm{I_{COH}}$ is the intensity of the coherent part of the photon energy spectrum and $\mathrm{I_{INCOH}}$ is the incoherent intensity. Measuring the degree of polarisation at other energies in the photon energy spectrum requires a detailed simulation of the coherent and incoherent photon energy distributions, which for the G8a experiment was provided by the **anb** code [57].

3.2.4 The Goniometer

The orientation of the diamond crystal was controlled by a goniometer [61]. This device is shown in Fig 3.7 and possesses 3 axes of rotation, shown in Fig 3.8 and corresponding electrical motors which allow the crystal to be moved to the desired position for production of linearly polarised photons of a certain fraction of the electron

beam energy.

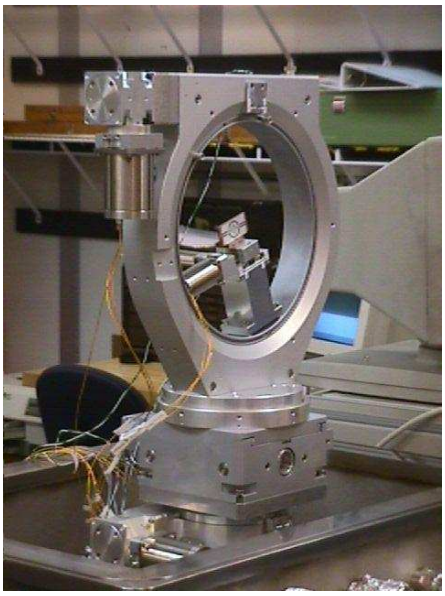

Figure 3.7: *The George Washington University goniometer* [61] *used in the G8a experiment. The target ladder is visible in the centre.*

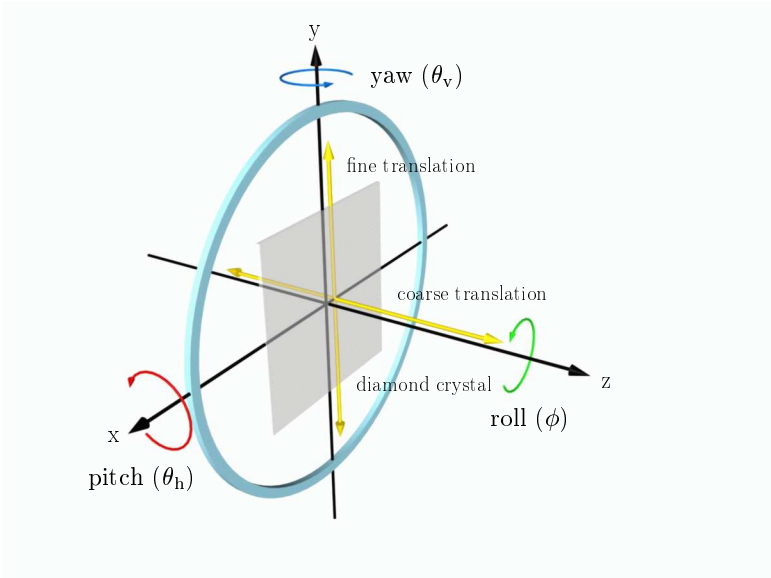

Figure 3.8: *A schematic diagram of the degrees of freedom of the GWU goniometer.*

The goniometer sits about 10m upstream (closer to where the beam enters Hall B) from the next piece of apparatus on the beamline , which is the Photon Tagger. This device is vital for the production and measurement of linearly polarised photons.

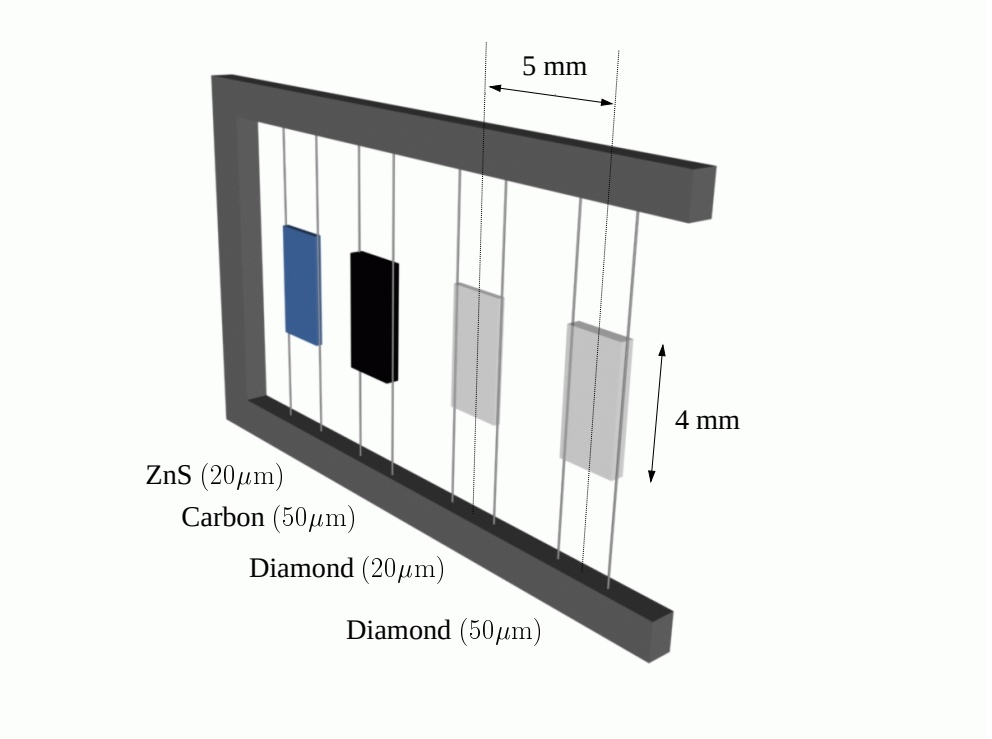

Figure 3.9: *Target Ladder Representation. The thickness of each radiator is shown.*

3.3 Photon Tagger

After the electron loses energy by interacting with the diamond crystal, it passes through the magnetic field of the Photon Tagger, then on to the Tagger beam dump. The Photon Tagger [62] works by making a coincidence measurement between the energy-degraded electrons it can measure the energy and time of, and the triggered event in CLAS. By using the event time from CLAS, the Photon Tagger "tags" an electron closely matching that event time and records the energy of the deflected electron to allow the reconstruction of the photon energy and time. Fig 3.10 shows the overall position of the tagger inside the experimental hall.

Fig 3.11 shows a perspective of the vertically-mounted Photon Tagger, which consists of a yoke magnet assembly along with a detector system which is located on the focal plane of the magnet as shown in Fig 3.2. A vacuum window separates this detector plane from the beamline . Spaced at discrete intervals along this plane are 384 4mm thick scintillators, below which lie 61 2cm thick pieces of scintillator. They are arranged so that any electron passing through one of the 61 scintillator strips must also have interacted with a certain group of the 384 counters. The 61 larger scintil-

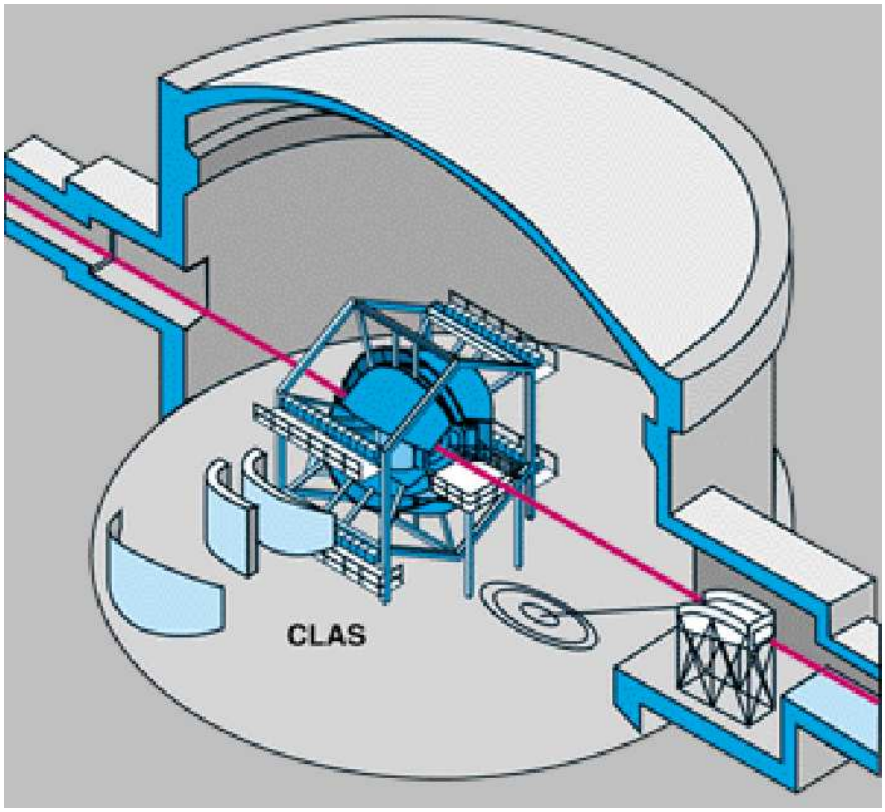

Figure 3.10: *Hall B: The electron beam enters from the right, having struck the diamond crystal and produced a polarised photon beam. The electron beam is then bent through the tagger into the tagger beam dump while the photons continue on into the CLAS detector and cause a physical interaction.*

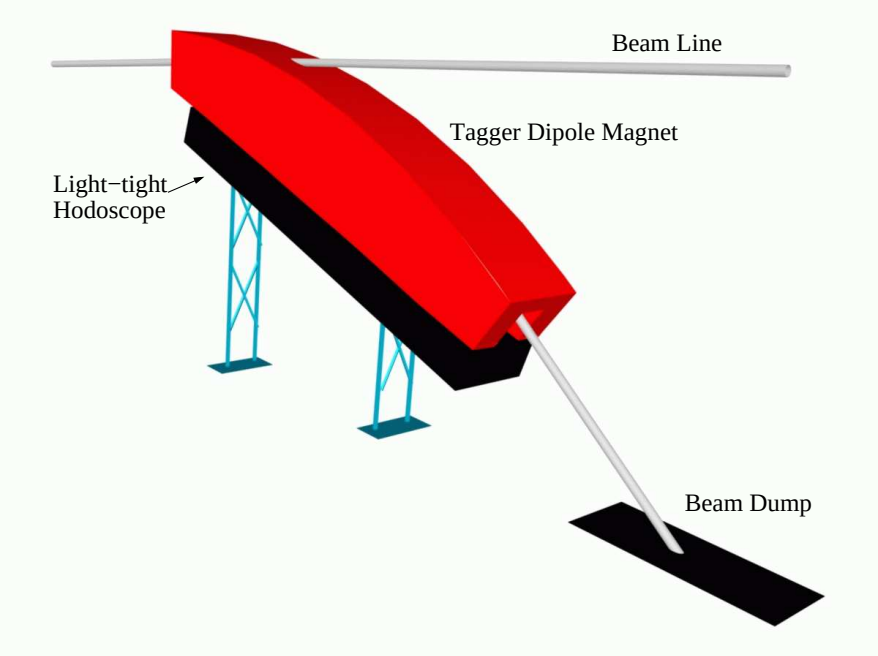

Figure 3.11: *Hall B Photon Tagger.*

lators are called T-Counters because they have good timing resolution, and the 384 smaller counters are known as E-Counters because their smaller size and greater number gives greater energy resolution, although they have inferior timing resolution. The T-Counters have a maximum resolution of 50 picoseconds while the E-Counter resolution is typically 10 times worse at around 500 ps maximum.

The geometry of the scintillator arrangement inside the Tagger Hodoscope makes use of overlaying the detectors to create extra energy and time bins, as shown in Fig 3.12. In the case of the E-Counters this “venetian blind” geometry results in 767 reconstructable energy bins, and for the T-Counters there are 121 final timing bins. These overlaps also provide a way of cutting out background that does not come from the same direction as the deflected electrons bent in the tagger magnetic field.

Both of these layers of the detector plane are connected to Photo-Multiplier Tubes (PMTs). For the T-Counters, PMTs are attached at both ends of the scintillator bar, and for the E-Counters, a light guide connects to an optical fibre which passes light down to a single PMT situated below the hodoscope. The T-Counters are connected to a LeCroy FastBus 1876 Time-Digital-Converter module with a timing resolution of 50 ps per channel, while the E-Counter signal passes to a LeCroy 1877 TDC module, which although having a lower resolution has the advantage of being able to record multiple hits in a given time window. This makes calculations of the total photon flux

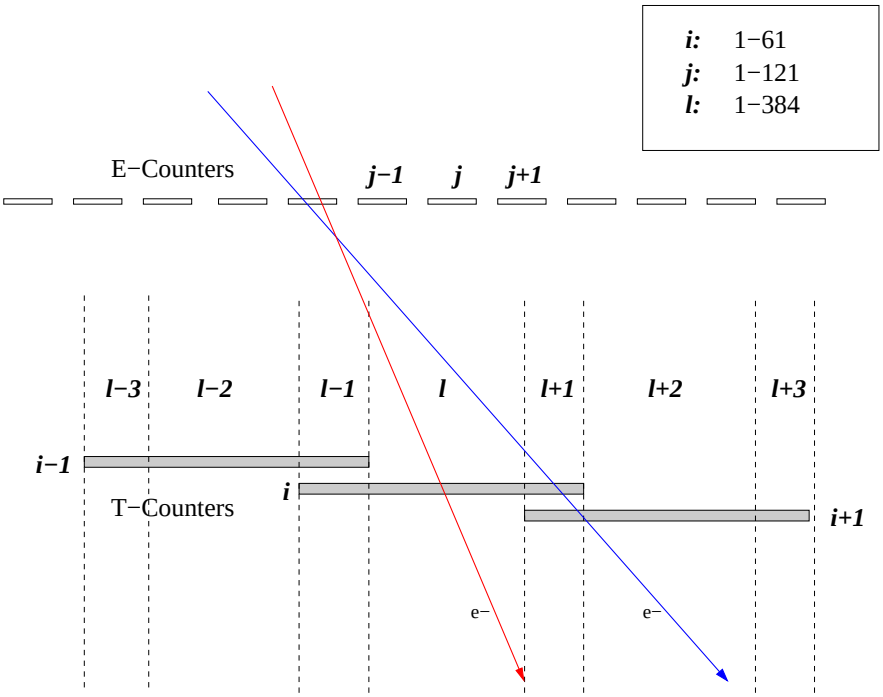

Figure 3.12: *The T-Counter to E-Counter Overlap and how this is used to distinguish events in the tagger. The overlap between the T-Counters provides extra information on the trajectory of the incoming electron and, including a coincidence with the E-Counters above, is used to reduce background noise in the Tagger.*

much easier in principle.

The tagger is designed so that the tagger magnet creates a magnetic field sufficient to deflect electrons with the beam energy into the tagger beam dump. Any electrons that have interacted with the crystal to produce a photon will be energy-degraded and will follow a more sharply curved trajectory in the tagger's magnetic field. The detector elements situated on the focal plane of the tagger magnet can detect energy-degraded electrons from 20% to 95% of the original incident electron energy.

Signals from the E-Counter TDCs pass into a multiplexed discriminator module known as an Amplifier-Discriminator-Multiplexer Logic module. This board multiplexes 4 E-Counters together and can be used to adjust the gain of this group as well as the discriminator levels for the E-Counter TDCs.

The output of each Tagger TDC module forms part of the CLAS trigger system and by passing the signals through quad Fan-In/Fan-Outs they are grouped together in blocks of 4, then ORed in a logic unit referred to as the Master OR. This OR can count at rates up to 10 MHz and should be representative of the photon flux into the CLAS detector.

The electrons either stop in the tagger beam dump or interact in the tagger hodoscope, while the related photons travel down the beam line toward the target.

3.4 Beamline monitoring devices

Because of the importance of the positioning of the electron beam on the diamond crystal, the G8a experiment had to carefully monitor the beam position to be sure of maintaining a good quality photon beam. As the electron beam pulse travels down the beam pipe from the switcher to the experimental Hall, it is necessary to make measurements of the spatial distribution of the beam pulse in order to verify that the beam is being correctly focused by the beam line magnets and is of a high enough quality to be used for the experiment. There are several beamline monitors that allow such measurements to be made, and they are located in several different positions.

3.4.1 Beam Position Monitors

The Beam Position Monitors are the most often used and are sited in three different locations. 2C21A is just upstream of the goniometer, 2C24A is just upstream of the tagger and 2H01A is downstream of the tagger but is not used in photon experiments [63]. These BPMs record the position of the electron beam by measuring the induced

current in wires adjacent to the beam. This induced current varies with the position of the beam. In Fig 3.13 the relative positions of the BPMs compared with the tagger and the goniometer can be seen.

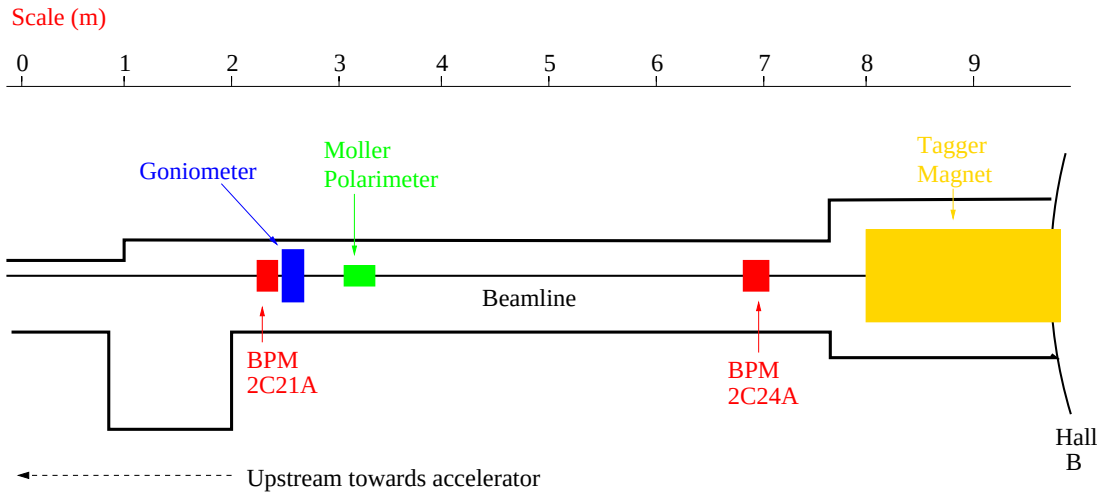

Figure 3.13: *Hall B beamline, BPM position and other beam line devices.*

3.4.2 The Active Collimator

Another device that G8a used for monitoring the beam quality was the Active Collimator [64] which was active in the sense that it possessed 4 PMTs embedded inside it which could measure the photon flux and also the position of the beam when properly calibrated. Fig 3.14 shows the external appearance of the device.

The collimator consisted of a hollow tube containing tungsten and nickel diskettes $15\,\mathrm{mm}$ thick and $50\,\mathrm{mm}$ wide with a $2\,\mathrm{mm}$ hole drilled through their centres. The principal reason for collimation of the polarised beam was because it increases the effective polarisation of the beam by increasing the coherent relative to the incoherent component of the bremsstrahlung passing through the collimator.

The first three diskettes are made of tungsten alloy, and the rest are made of nickel, the reason for this being the need to attenuate the photon beam and reabsorb any secondary radiation while keeping the collimator at a manageable length. The choice of a $2\,\mathrm{mm}$ diameter hole is related to the electron beam energy, and the distance from the goniometer to the collimator. Ideally the collimator should only allow photons within half a characteristic angle θ_γ [3] to pass through. For G8a the goniometer-collimator

[3] $\theta_\gamma = \frac{\mathrm{mc}^2}{\mathrm{E}_0}$, where m is the mass of the electron and E_0 is the beam energy.

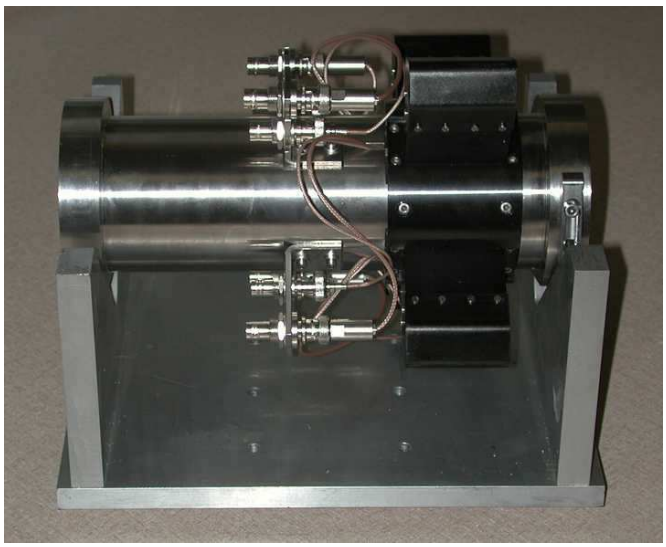

Figure 3.14: *The Active Collimator from UTEP-Orsay* [64].

distance is $22.9\,\mathrm{m}$, and with the electron beam energy of $5.7\,\mathrm{GeV}$ and diamond thickness of $20\,\mu\mathrm{m}$, the appropriate width of the collimator aperture is $2\,\mathrm{mm}$. The effect of variation in these parameters can be seen in Fig 3.4. The active part of the collimator consists of 4 small pieces of scintillator radially mounted between the first and second diskettes, with corresponding light-guides and PMTs, shown in Fig 3.15.

Collimating the polarised photon beam has the beneficial effect of increasing the coherent to incoherent bremsstrahlung ratio passing into the CLAS detector, while reducing unwanted noise and incoherent background that would be present at larger polar angles. Fig 3.4 shows the effect on simulated data produced by the **anb** code [57]. A similar effect is seen in Fig 3.16, which displays real data taken during the G8a run. Shown at the top is the uncollimated tagger spectrum obtained by dividing the spectrum obtaining during a diamond radiator run with the spectrum measured under the same conditions from an amorphous carbon radiator run. This method is explained more fully in Chapter 6. At the bottom, the comparison of collimated spectra is shown. Both data sets are compared with the **anb** code predictions and the agreement is very good. The maximum polarisation of the coherent peak, created by scattering from either the $[0, 2, 2]$ or the $[0, 2, \overline{2}]$ crystal planes, is increased using the collimator reaching a maximum value of 84%.

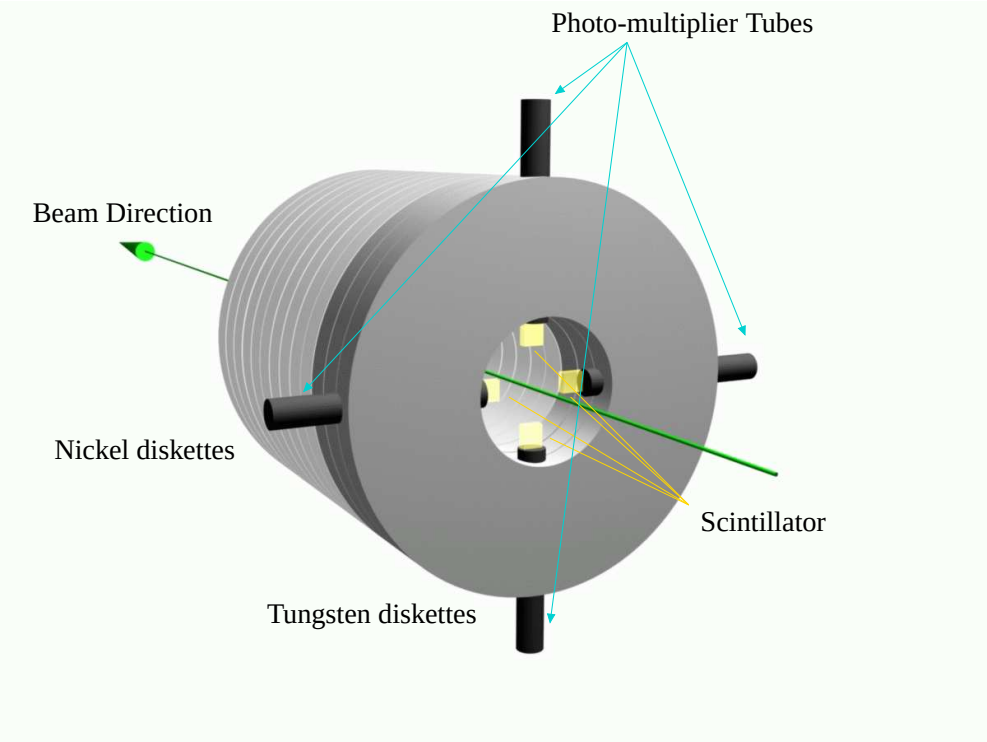

Figure 3.15: *A conceptual representation of the layout of the Photo-Multiplier Tubes in the Active Collimator.*

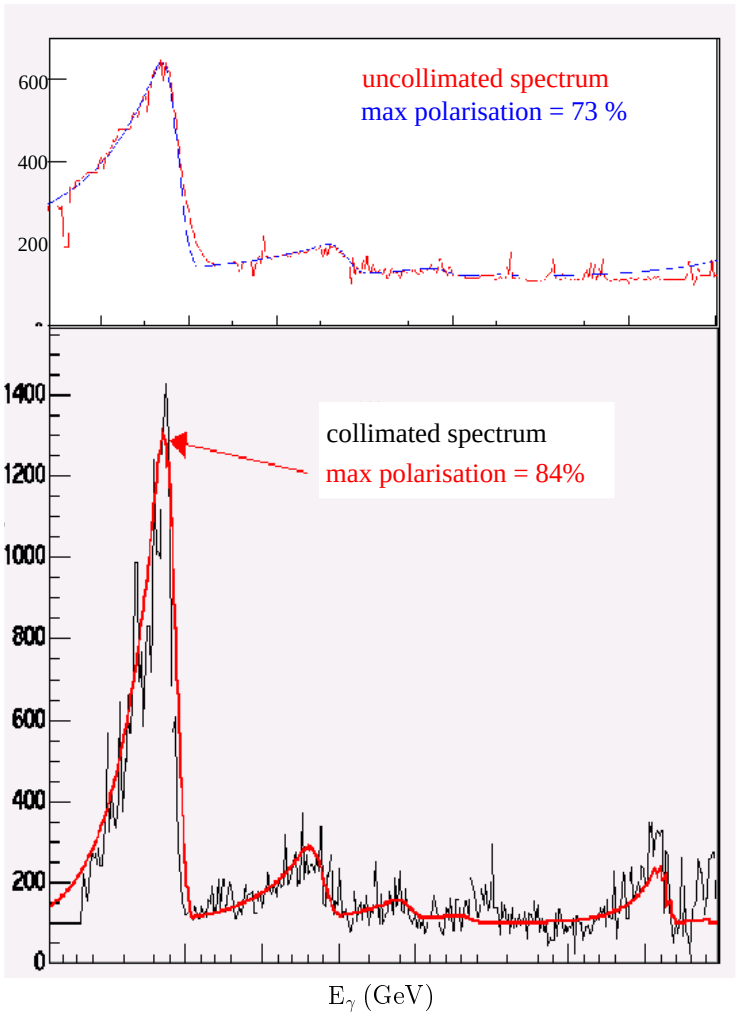

Figure 3.16: *The effect of the collimator on the tagged photon energy spectrum after normalisation. Top: Uncollimated tagger data compared with the* **anb** *simulation. Bottom: G8a collimated tagger data compared with the* **anb** *simulation including the calculated effect of the collimator.*

3.5 CEBAF Large Acceptance Spectrometer

3.5.1 Introduction

Beyond the collimator lies the CLAS detector [52], occupying the centre of Hall B. This detector is actually an assembly of several different types of detector systems, giving a variety of information on the charge, momentum, mass and velocity of any particle that is to be studied. The detector is called Large Acceptance because it covers well over 2.5 π in solid angle, ranging from 8 degrees to 140 degrees in polar angle and 0 to 360 degrees in azimuth, with certain regions having no acceptance due to the presence of the magnetic field coils. The coils are superconducting, and are configured to produce a toroidal magnetic field around the beam line passing through the centre of CLAS. The configuration of the coils is shown in Fig 3.17.

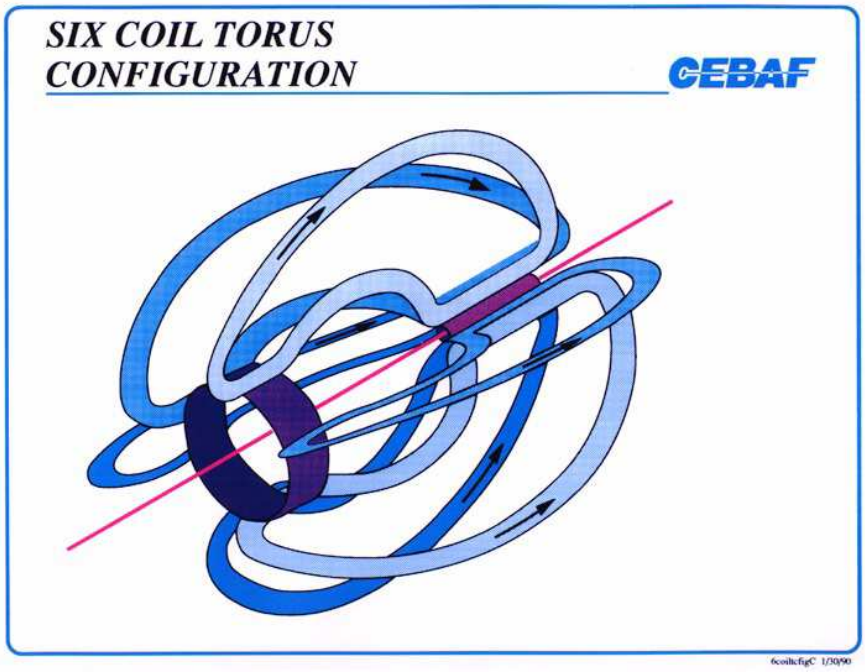

Figure 3.17: *The magnetic coils of CLAS.*

Fig 3.18 shows a cross-section of the CLAS detector, and the layered internal construction is evident. The three drift chamber regions give high position resolution and combined with the Time-of-Flight scintillators on the outermost layer, provide the basis for identifying particles produced in the target. A cut-away of the detector reveals even more of the layer structure, and in Fig 3.19 the extent of this structure can be clearly seen.

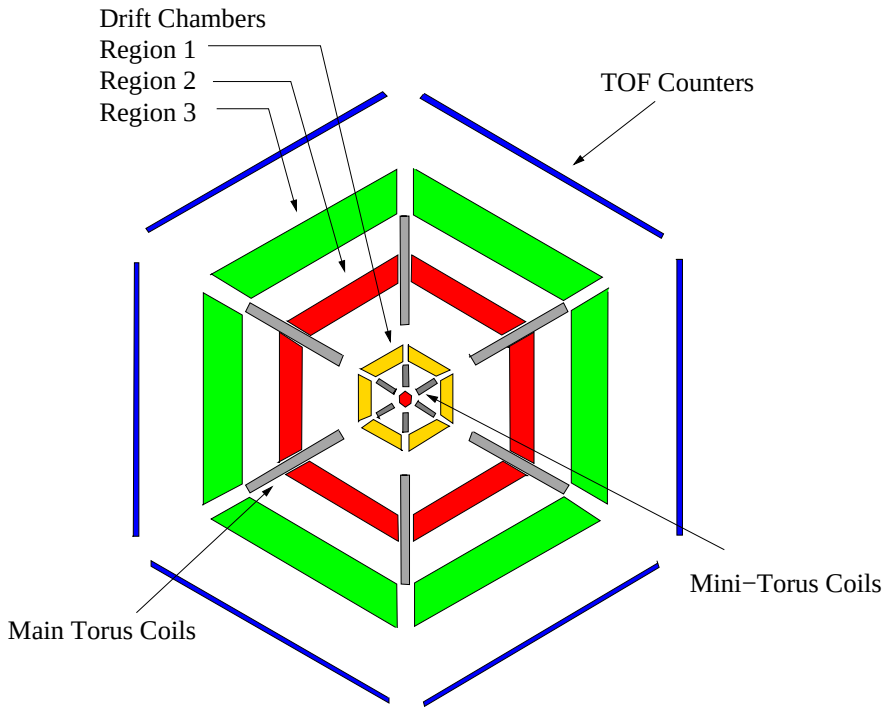

Figure 3.18: *Cross-section of the CLAS detector, showing the position and definition of the six drift chamber regions.*

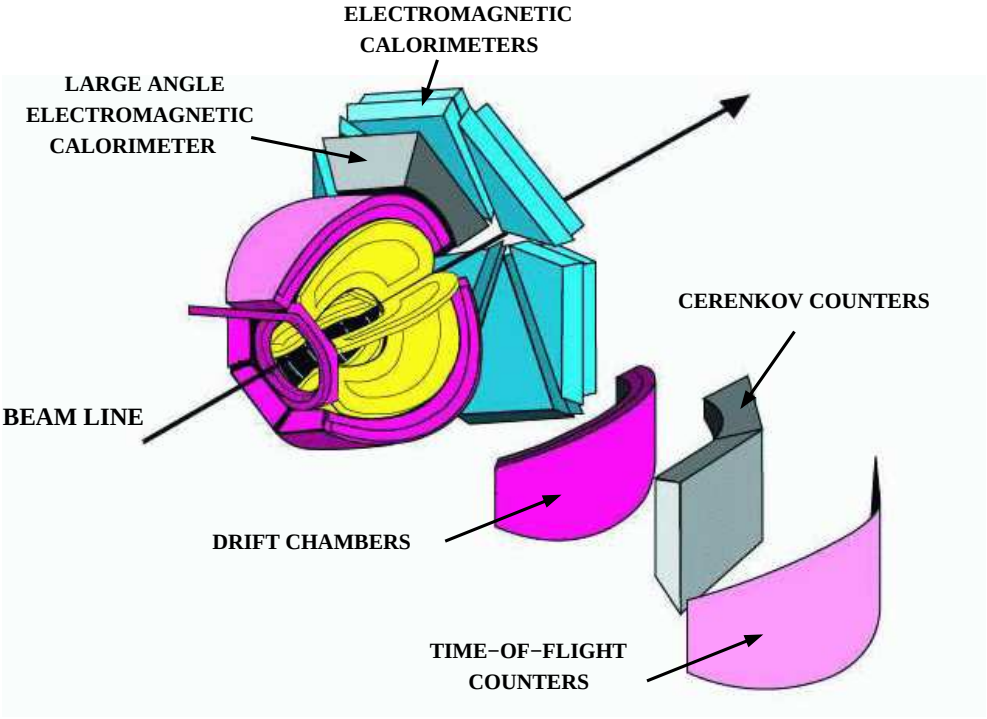

Figure 3.19: *An overall schematic of the components of CLAS.*

3.5.2 The G8a target

The G8a run used a liquid hydrogen target [65] consisting of a Mylar cylinder 18 cm long with a ~2 cm window at the end positioned centrally inside CLAS. The target is cryogenically cooled to ~10K and is mounted upstream of the centre of CLAS so that it is independent of any of the internal structure of the detector. Fig 3.20 shows the Mylar cylinder and connecting structure.

Figure 3.20: *The G8a liquid hydrogen target cell, made of Mylar.*

Upon interacting with the target, some physical process is expected to take place during which the incoming photon transfers its energy and polarisation to the target nucleus. Baryons and mesons produced from this energy transfer should be closely correlated in time with the photon detected by the tagger, and this helps us determine the total energy of the reaction, but CLAS needs to identify the particles produced by detecting their velocity, mass, momentum and charge. In order to obtain these quantities, the initial value of interest must be the start time of the process to be observed.

3.5.3 Start Counter

In photon runs, because there are no electrons from the beam interacting in the detector, there is very little background. It makes sense to try to time the start of an interaction directly using a scintillator to detect charged particles. In CLAS, the Start Counter [66] performs this task and consists of six pieces of scintillator wrapped closely around the target cell.

Fig 3.21 shows how the Start Counter fits around the target. However, an important detail of the Start Counter construction is that the six pieces of scintillator are joined together in a coupled paddle design that connects together to give effectively three sectors of scintillator in the forward direction, as shown in Fig 3.22.

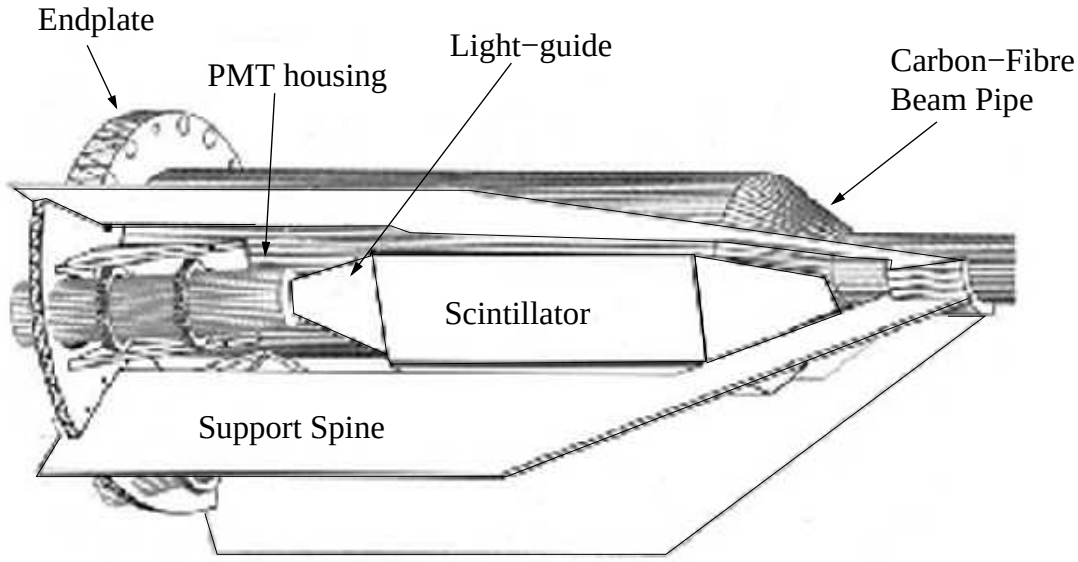

Figure 3.21: *The CLAS Start Counter. Apart from the forward direction the Start Counter's angular coverage is exactly the same as the Time-of-Flight system.*

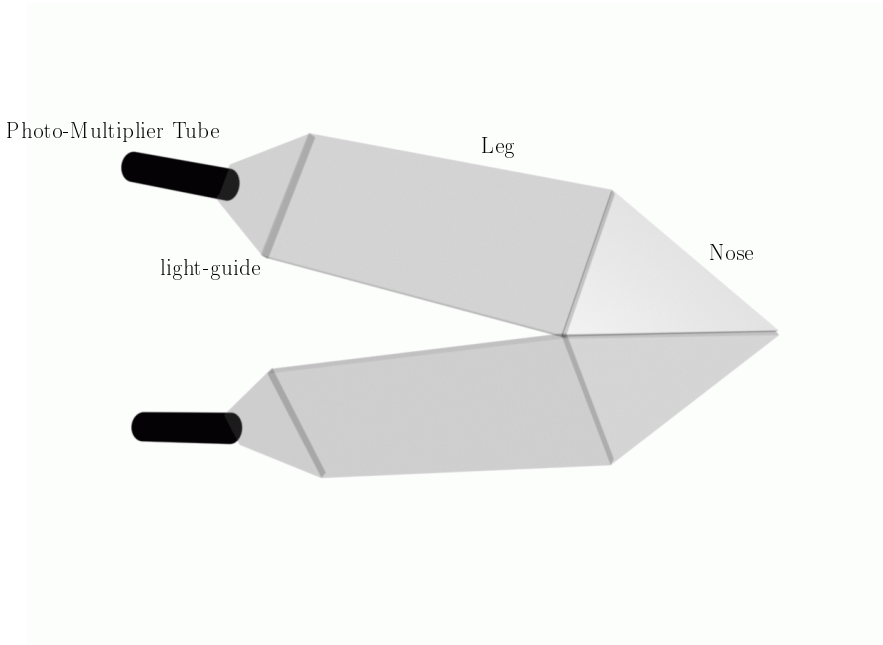

Figure 3.22: *The construction and dimensions of a start counter paddle.*

The scintillators are connected to 6 PMTs mounted in the backward direction: i.e. greater than 140 degrees in polar angle. This means that they do not create any background or suffer radiation damage. These PMTs are in turn connected to ADCs and 1876 LeCroy FastBus TDCs. The TDC signal forms an important part of the hardware trigger that CLAS uses to identify real physical events. In particular, in the forward direction, the mean time from the 2 pieces of scintillator gives a well-defined start time for a final state particle, which makes identifying the correct RF beam bucket associated with the event much simpler.

3.5.4 Drift Chambers

The Drift Chambers [67] of CLAS are arranged around the target between the superconducting magnetic coils, and have multiple layers which give the system a good position resolution. The overall structure of the drift chambers has three distinct regions. Each region is naturally divided into six by the magnetic field coils, resulting in 18 drift chamber wedges overall. The three regions are positioned at increasing distance from the target. Region 2 is located where the magnetic field is strongest. The strong magnetic field region has the best momentum resolution and so particles are identified partly on the basis of how much their track is deflected as they pass through Region 2.

Each region covers a 60^0 azimuthal range and is constructed to make the wire plane approximately parallel to the plane of the magnetic field. Fig 3.23 shows the shape of one of the drift chamber regions, with the curved construction evident.

There is more detail inside each region. The construction consists of two superlayers which have six wire layers each. The wire layers are offset with respect to each other as shown in Fig 3.24. The offset is half of the spacing from wire to the next. This results in a staggered arrangement and, with a recurring pattern of two field wires and one sense wire, resembles a hexagonal grouping, shown in Fig 3.24, which increases in diameter depending on distance from the target. So for region 1 the cell size is 0.7 cm, 1.5 cm in region 2 and 2.0 cm in region 3.

The two super-layers in each region are arranged at different angles to each other to provide the tracking information. The first “axial” super-layer is arranged axially along the magnetic field so that the direction of the wires is in the plane of the magnetic field but at 90^0 to it.

The second “stereo” super-layer is arranged with an offset of 6^0 in the same plane as the axial super-layer, which gives azimuthal information about the trajectory of a

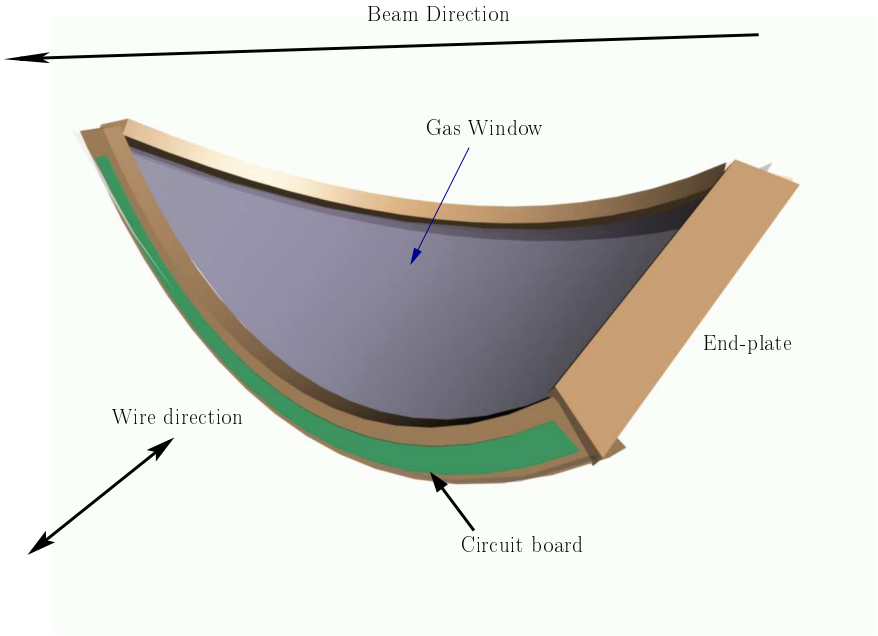

Figure 3.23: *A typical drift chamber segment and its components.*

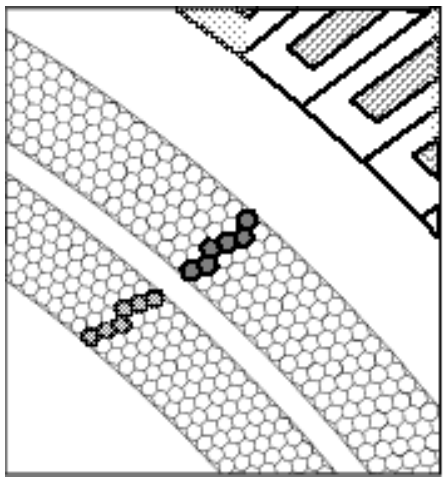

Figure 3.24: *The hexagonal arrangement of field and sense wires can be clearly seen here, and the increasing size of the cells with radius. A hit can be seen above, triggering the cells in a distinct pattern.*

charged particle.

The drift chambers contain a mixture of 88% Argon and 12% Carbon Dioxide. An automated regulation system cycles this gas through each chamber to maintain a constant pressure which is independent of atmospheric pressure and temperature changes.

Every sense wire is kept at a positive voltage, while the field wires are kept at a negative voltage of half the value for that of the sense wires. Guard wires are situated along the perimeter of each super-layer and are kept at a high voltage to balance out the effects of earthed components nearby and create an approximation of an infinite grid electric field. Each sense wire reads out through a pre-amplifier and then to a post-amplifier and discriminator crate which produces a digital logic pulse. The output from the post-amplifier and Discriminator board (ADB) then passes to a multi-hit common stop TDC crate.

The layer efficiency of the Drift Chambers is greater than 98%, and hence the probability of all the layers recording a good hit when a charged particle passes through is very high. With a total of more than 35,000 sense wires in the Drift Chamber system, this represents a large part of the overall technological complexity of CLAS.

3.5.5 Time-of-Flight Scintillators

The Time-of Flight system [68] in CLAS matches the coverage in polar and azimuthal angle of the six drift chamber regions as well as the coverage of the Start Counter.

Figure 3.25: *Photo of the outside of CLAS. The Drift Chambers are still in position here but the Time of Flight paddles can be seen to the left of the main detector. Note the direction of the bars.*

Overall, the system consists of 324 paddles: i.e. 54 per sector. Since the last 12 in the backward direction are coupled together this gives a practical total of 48 per sector. The paddles vary in size, are mounted perpendicular to the axis of CLAS, and increase in length with the width of each sector. Fig 3.25 shows the CLAS detector being disassembled, and the Time-of-Flight assembly can be seen separated from the Drift Chambers.

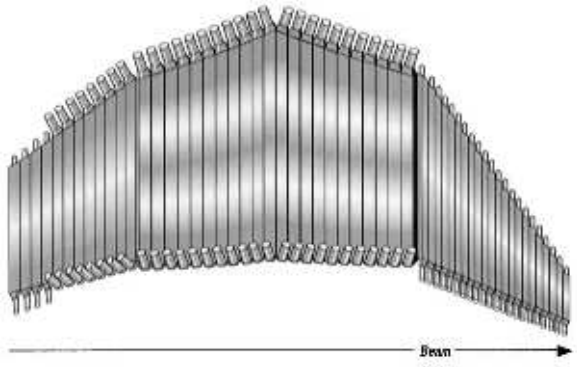

Figure 3.26: *Standard view of a single sector Time-Of-Flight system.*

Every paddle in the Time-of Flight system has a thickness of 5.08 cm, and has a width corresponding to a 1.5^0 scattering angle, which for polar angles less than 45^0 translates to a width of 15 cm, and at larger polar angles to a width of 22 cm. The scintillator material is Bicron BC-408, and the forward angle paddles range from 32 to 376 cm in length, while at larger polar angles the range is from 371 to 445 cm.

The typical Time-Of-Flight sector has 4 separate panels to cover the desired polar angle coverage.

The paddles have a PMT attached to both ends and the outputs are fed to a Fan In/Fan Out and then on to both ADC and TDC boards. The output from the TDC board is an important part of the Level 1 trigger, and in conjunction with the start time information from the Start Counter, is essential for calculating the $\beta\,(=\frac{v}{c})$ of charged particles. Therefore the Time-of-Flight System is an integral part of particle identification.

3.5.6 Cerenkov Detector

The Cerenkov Counter [69] is a forward-angle $(\theta < 45)$ device aimed at separating pions from electrons and also triggering on electrons. It exploits the fact that the torus coils mask the light collection cones and PMTs in an area of low particle acceptance.

However, for the rest of the sector, coverage is mainly by mirrored chambers filled with a low-refractive index gas, which are designed to focus the Cerenkov radiation onto the light-collection cone.

The main design goals for the Cerenkov Counter are to maximise the angular coverage while keeping to a minimum the amount of material used, because this could interfere with the energy resolution of both the Time-Of-Flight system and the Electromagnetic Calorimeter. The Light Collection module on each end of the mirrored chambers consists of a light-collecting (Winston) cone and an adjoining PMT.

The overall design consists of twelve sub-sectors, two around each symmetry plane bisecting each sector. Each sector is split into 18 regions in polar angle resulting in a total of 216 light-collecting modules. Fig 3.27 shows two of the sub-sectors joined together.

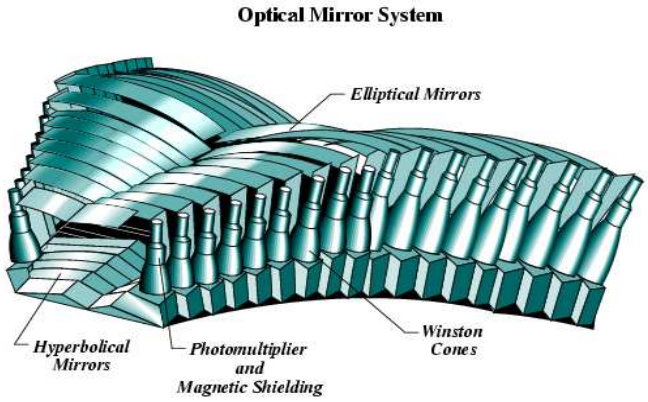

Figure 3.27: *The Cerenkov Counter design maximises angular coverage in the forward-angles but minimises compromising the energy resolution of CLAS by utilising a highly efficient design.*

The gas used is perfluorobutane (C_4F_{10}), giving an index of refraction of 1.00153 resulting in a pion-momentum threshold of $2.5\,\mathrm{GeV/c}$.

3.5.7 Electromagnetic Calorimeter

The Electromagnetic Calorimeter [70] also covers the forward polar angle range $(\theta < 45^0)$, and while it can detect charged particles like electrons above 0.5 GeV, its primary use is the detection of neutral particles such as photons and neutrons, which is essential for reconstructing neutral decays. The detector is a scintillator-lead sandwich, as shown in Fig 3.28, with a total of 39 layers in each sector. Having a sandwich arrangement of layers is ideal for detecting any particle since it will interact in the lead and create

a shower which is detected by the scintillator layers. This can then be used to identify the particle on the basis of the position and magnitude of the shower.

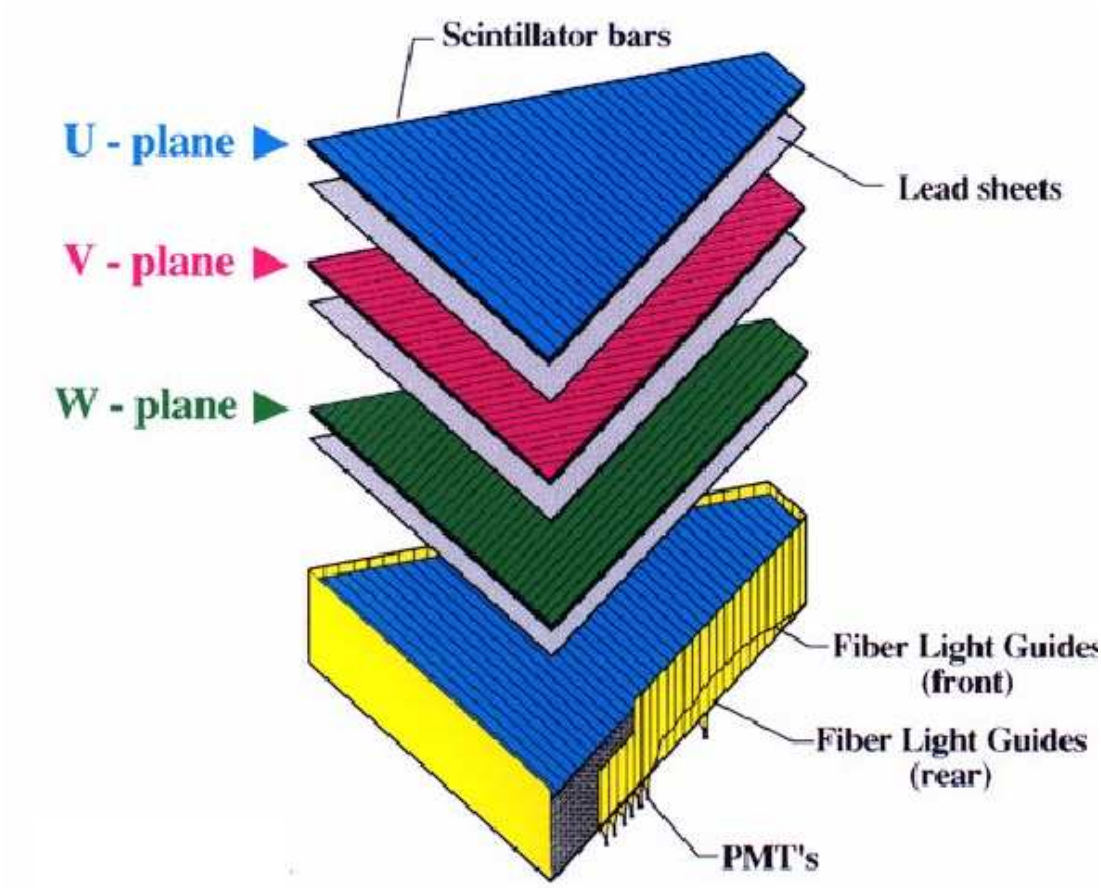

Figure 3.28: *Diagram showing the composition of the Electromagnetic calorimeter.*

In such a layer, the scintillator is 10 mm thick and the associated lead is 2.2 mm thick. The overall shape of a layer for each sector is approximately an equilateral triangle. This essentially determines the readout method, and indeed the positional information relies on each scintillator layer consisting of 36 strips parallel to one of the triangle sides being read out from one side of the triangle. Going down each successive layer, the orientation of the strips changes by 120^0, and this gives the position of the hit by determining if there was a coincidence between strips of different layers. The sets of three recurring planes of the sandwich are labelled u, v and w. Fig 3.29 shows a reconstructed hit in the Electromagnetic Calorimeter, with the position of the hit determined from the information from the u,v and w layers.

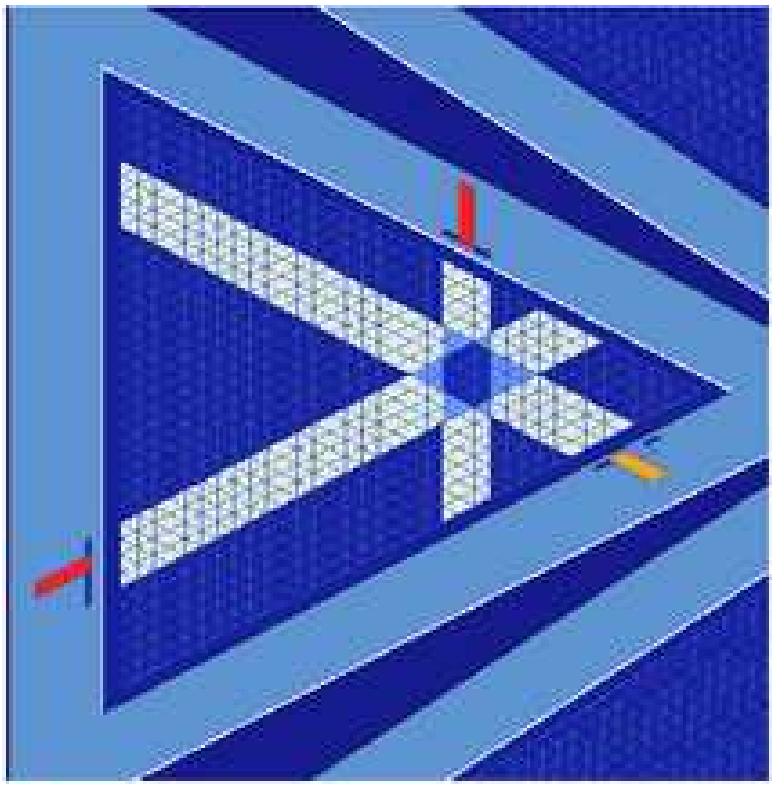

Figure 3.29: *A hit in the EC - different layers with different position information give the intersection point of the hit.*

The layers are grouped into an inner layer of 5 and an outer layer of 8 to give the possibility of measuring the shower created by an electron or hadron travelling out from the target, and therefore being able to distinguish between these two types of event.

In total, for the 6 sectors with 2 layer groups containing 36 strips, 1296 PMTs are required to instrument the Electromagnetic Calorimeter.

3.5.8 Large Angle Calorimeter

The construction of the two modules comprising the Large Angle Calorimeter(LAC) [71] is very similar to that of the Electromagnetic Calorimeter, but the aim of this detector is somewhat different. With an azimuthal coverage of only 120^0, but from 45^0 to 75^0 in polar angle, the LAC aims to detect scattered electrons, as well as neutrals from processes involving radiative decay. For example the decay of η and π^0 mesons will produce photons at such backward scattering angles. The LAC is designed to detect such events in CLAS.

Each LAC module consists of 33 layers, except this time they are in the overall form of a square, see Fig 3.30. This gives the same type of positional information as the forward calorimeter except each layer is rotated 90^0 successively. The inner and outer longitudinal layers have 17 and 16 layers respectively. A 0.2 mm thick Teflon layer sits under a lead layer of thickness 0.2 cm to minimise optical coupling. The scintillator is NE110A with a thickness of 1.5cm and a width of 10 cm.

The overall dimension of an LAC module is roughly 400 cm by 240 cm and each cell, defined as the longitudinal overlap of scintillators from different layers, is 10 x 10 cm^2, giving a matrix of 40 x 24 cells in each module.

3.6 Downstream Devices

Another few meters downstream of CLAS, just in front of the Hall B beam-dump, three devices are sited to monitor the quality and magnitude of the photon beam that has passed through CLAS. Fig 3.31 depicts the positions of each of these three devices.

The furthest downstream of these is the Total Absorption Shower Counter(TASC), which is a large lead glass detector with an efficiency of almost 100%. However, due to a count-rate pile-up problem the TASC cannot be operated at beam currents above 100 pA, which makes operation under normal conditions impossible. The middle device is the Pair Counter which acts as a backup for monitoring beam intensity. It consists

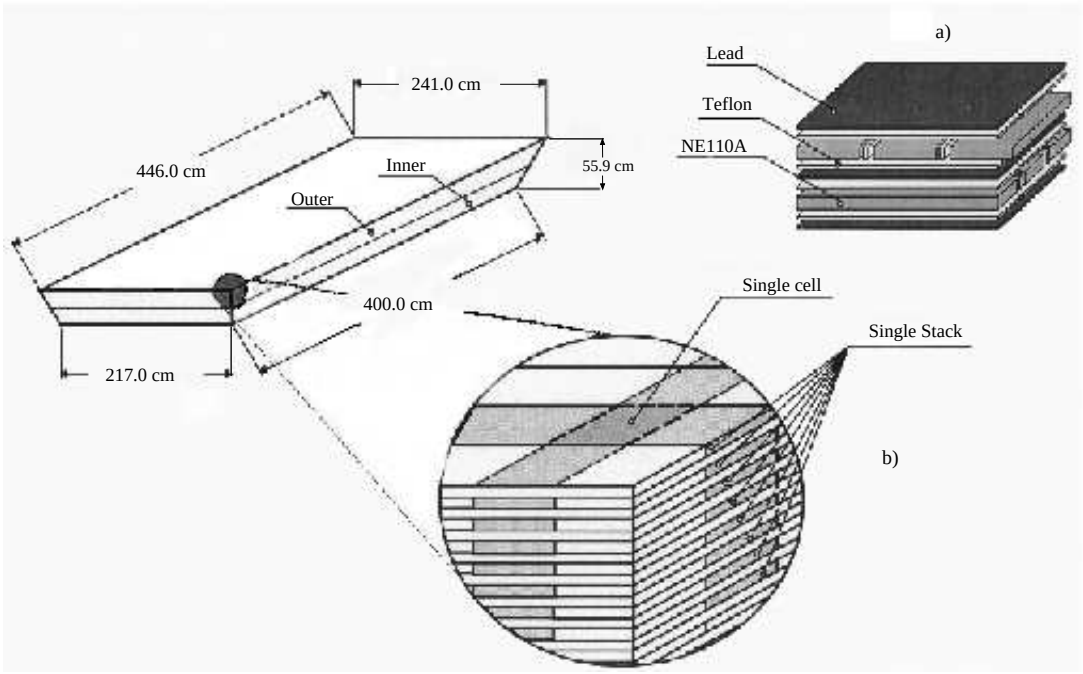

Figure 3.30: *The composition of a Large Angle Calorimeter module. Shown in (a) is the structure of the calorimeter layers and (b) shows the shape of the stack and the cells that are read out together.*

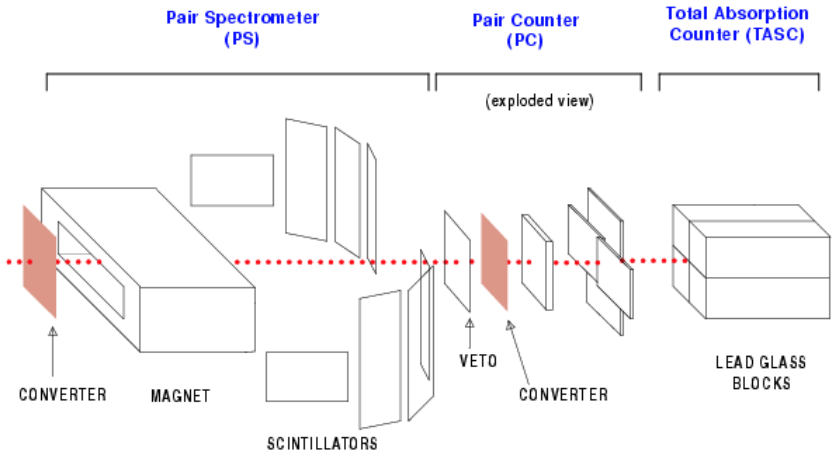

Figure 3.31: *A close-up of the positioning of the downstream devices.*

of a charged particle veto to eliminate background from CLAS, a thin converter for electron pair-production and a group of four scintillators positioned around and behind a central scintillator spanning the beamline.

The furthest upstream device is the Pair Spectrometer which has a much lower absolute efficiency. It is almost linear in response to the photon flux and can be operated at much higher beam currents than the TASC. If calibrated properly against the TASC the pair spectrometer can be useful in measuring the photon flux during normal running conditions. Unfortunately the placement of this pair spectrometer device has some serious disadvantages. For example, the extra pair production inside CLAS and from the material between CLAS and the pair spectrometer causes extremely high rates and makes the system unstable. The photons which cause this extra pair production have to be subtracted from the total flux, which is a sizeable correction.

There is also a photon profile monitor which gives some measure of the photon beam position. The profile monitor, the BPMs and the Active Collimator all help to ensure that the beam is of good quality and stability during a run.

3.7 Trigger System

3.7.1 Introduction

The signals generated when a charged or neutral particle is detected in CLAS must be read out in such a way that it should be possible to determine if the event is real and not an accident.

This is accomplished by using a specific trigger configuration, and the trigger may be configured in different ways to suit different conditions for different experiments. For example, for a photon run it is extremely important to use the Start Counter time as part of a Logical OR in the trigger configuration, along with the Master OR from the Tagger.

In general, a trigger is a signal that passes through any timing gates and satisfies coincidence conditions such as a start time within a given time window and, more importantly, it informs the data acquisition system that real information is ready to be read out. CLAS utilises a two-level trigger scheme that allows events to be accepted or rejected in a manner which keeps the dead-time of the detector as low as possible.

In the event that some process causes any of the outer detectors like the Time-Of-Flight or Electromagnetic Calorimeter to fire, an acceptable first-level trigger is formed. This trigger is used

a) to gate the relevant hardware electronics by sending a common start to all the relevant TDCs.

b) by including some delay, to generate the common stop signal for the Drift Chamber TDCs.

The Drift Chamber can come into play for a second-level trigger by using rough position information from each super-layer, defined by a charged particle passing through a given cell. Each cell is defined using the same method as the Hit-Based Tracking method discussed in Section 4.9. This Level 2 trigger then either allows or rejects hits on the basis of finding an acceptable track in the Drift Chamber, and rejects an event by sending all TDCs a fast clear signal which erases all information of the stored event. Thus, CLAS usually operates with 2 different classes of trigger, the first trigger being a Logical trigger requiring specific conditions to met for hits in various detectors depending on the experiment being run.

3.7.2 Level 1

The Level 1 trigger [72] was designed to have negligible dead-time and makes use of all timing or position information promptly available from the numerous TDCs in CLAS, to decide if an event was physically interesting. At this level, the trigger utilises information from the Time-Of-Flight system, Cerenkov detector and the Electromagnetic Calorimeter.

Essentially the trigger consists of a three-stage memory look-up which takes signals from the relevant detector surfaces in each sector, as shown in Fig 3.32. The first two look-up tables compress this data, which consists of position and time information, then reduces 62 bits of trigger data to four groups of three bits, or four trigger words for each sector.

The third stage involves taking one of these trigger words from each sector and making geometrical matches to take account of multi-pronged events. For example, the case in which a π^- is detected in one sector the trigger can look up events in which a proton is detected in the opposite sector and then conclude that this is a good event. The three stages [73] take ~90 ns of processing time to complete, then the trigger is passed on to the Trigger Supervisor which is a module which issues the common stop signals and others required for the physical information to be read out by the electronics.

The Level 1 trigger can be configured for the number of charged particles desired for each event that the experiment should consider real. For G8a this condition was

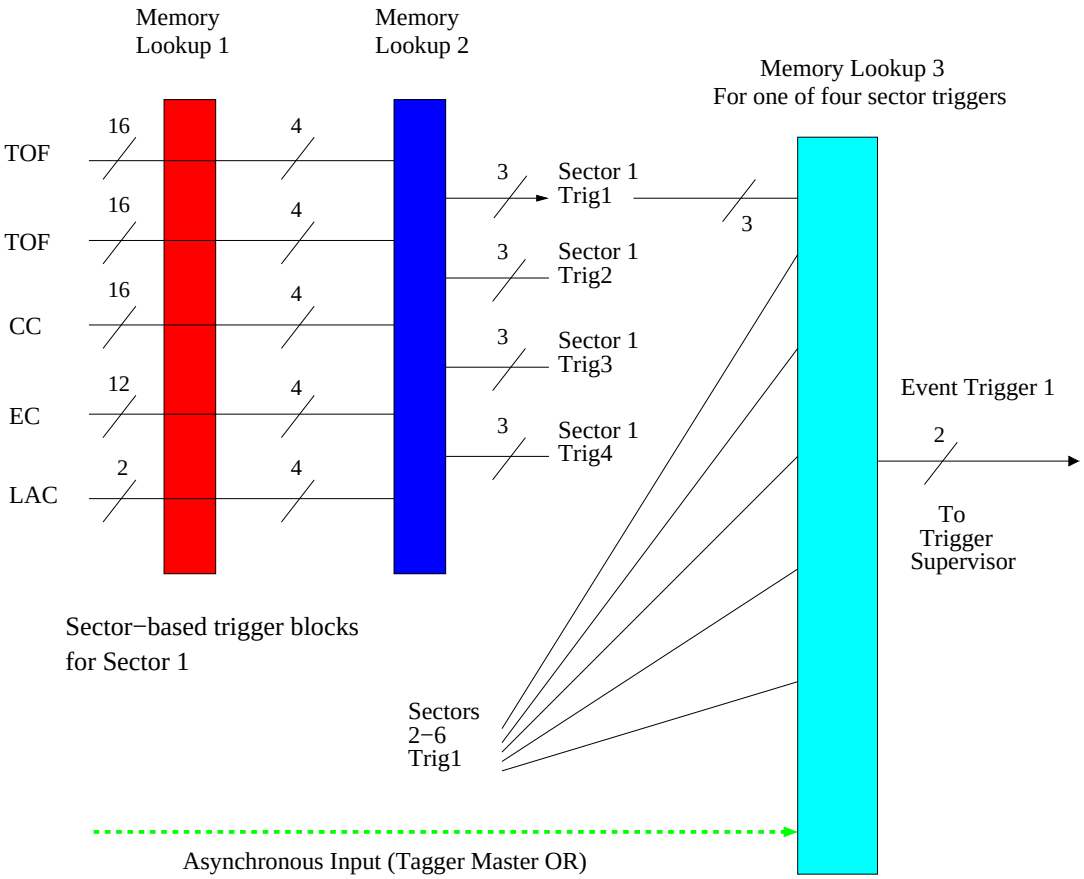

Figure 3.32: *The three-stage memory look-up for the Level 1 trigger. The information from the Time-of-Flight detector is vital for the G8a Level 1 trigger, and the Start Counter signal is included at the expense of one of the other detector systems to meet the requirements of a photon experiment.*

set at one charged particle per trigger, which greatly increased the trigger rate, and therefore the random background in the experiment. However, this condition also broadens the range of different channels that can be analysed in the data.

Fig 3.33 shows the principle behind the level one trigger configuration used for G8a. This consisted of a Logical OR between the Master OR, Start Counter and the Time-Of-Flight system. The coincidence can only occur within a certain hardware timing window that varies with detector. In the G8a experiment the Master OR had a hardware timing gate of 10 ns, with the Start Counter having a slightly wider gate of 15 ns, and the Time-Of-Flight the largest gate of 120 ns.

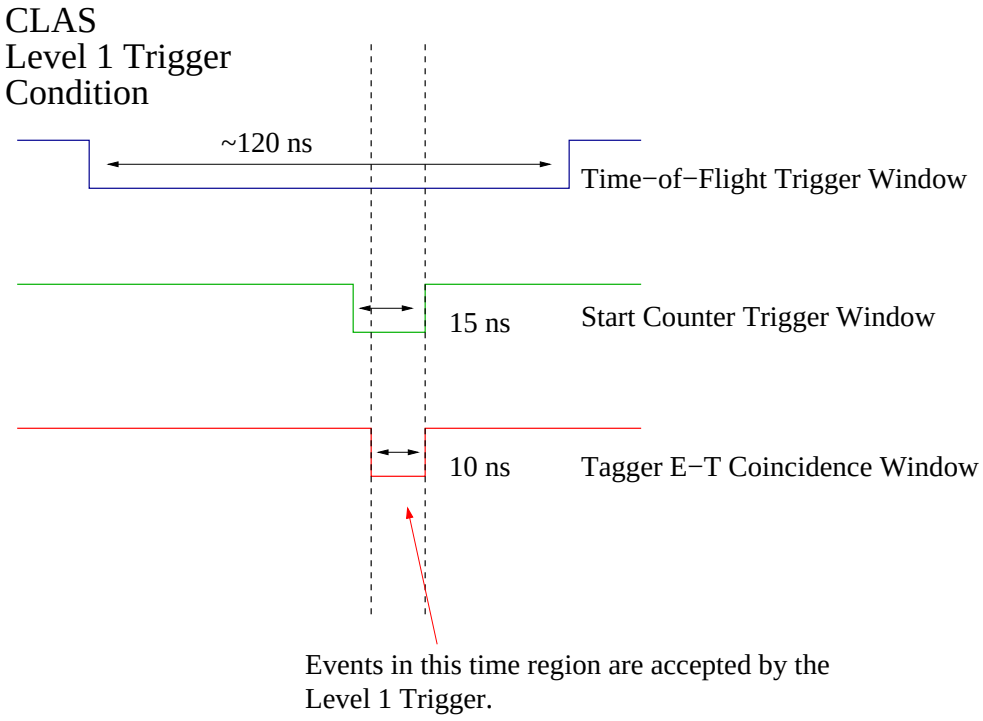

Figure 3.33: *The overlap in time between the three components of the level one trigger for G8a. This figure demonstrates the conditions under which the Level 1 Trigger will fire. There must be a pulse from the Tagger Master OR, the Start Counter, as well as the signals from the Time-of-Flight systems (See Fig 3.32) in order for the event to be read out. The responsibility of accurately detecting a physical event within the Level 1 Trigger Window then falls to the Photon Tagger.*

3.7.3 Level 2

As mentioned before, the Level 2 trigger [73] makes use of the Drift Chambers to obtain tracking information, and the whole trigger system is designed to give fast in-

formation on the occurrence of an interesting physics event. However, the Level 1 trigger can be set from a cosmic ray event, and in this case no track would be present in the Drift Chambers, so the Level 2 trigger sends a fast clear signal to all TDCs if no tracks are found.

The Level 2 trigger can do much more than this, since it can actually make a real-time comparison between the geometrical or sector information from Level 1 and then pass or fail the signal depending on the physics requirements of the experiment. However, the processing time of $\sim 4\mu s$ contributes directly to the dead-time of the detector since no new triggers can be accepted until either all information is fast-cleared, or digitised and read out.

The position information is obtained from five super-layers, not including the Region 1 stereo layer, and a segment finder board automatically compares track segments with 9 templates designed to catch all possible tracks passing through a super layer at up to 60^0. If three good track segments are found out of five, then the track is considered good and the Level 2 pass signal can be either the Logical OR from all six sectors or alternatively, a more direct comparison with the Level 1 geometric information.

3.7.4 Trigger Supervisor

This extremely important custom-built module takes the outputs from Level 1 and Level 2 and issues fast-clear signals, common start signals and common stops signals to all TDCs, as well as gates and resets for all the detector electronics. The Trigger Supervisor [73] can be programmed to use Level 1 trigger information only, which is a CLASS 1 configuration, or else Level 1 and Level 2 which constitutes CLASS 2.

For CLASS 1 the Trigger Supervisor will generate the time gates for all detector electronics, wait until all the crates have finished digitising their information and then place the event on a readout queue for the Data Acquisition System.

In CLASS 2 the same happens but the Trigger Supervisor will wait until the Level 2 processing is finished, and if the Level 2 has failed, then a fast-clear will be issued to all front-end detector electronics to reset them. This takes around $1\mu s$, and if Level 2 passes, the event will be placed on the read-out queue in the same way as CLASS 1.

3.7.5 Data Acquisition

After the Trigger supervisor gives the all-clear, the process of data acquisition [74] begins and the information in the relevant TDCs is digitised and sent to 24 VME[4] Read-Out Controllers. Each ROC relates to a different detector or subsystem, and for each digitised value received, is tabulated and given an identification number specifying the position or number of the active part of the detector .These event fragments are then sent to the online acquisition computer which performs three major operations on the data.

Firstly the Event Builder rebuilds event fragments into large data banks and labels are attached to specify the detector type. A complete event also has a header bank attached which details the event type, run number, event number and trigger bits that fired when the event was created. Next the Event Transport loads the complete event into shared computer memory and makes the event information available for online analysis programs and raw data monitoring programs. Finally the Event Recorder takes these events out of the Event Transport and writes the data straight to storage media. Six RAID disks receive the data and then transfer the files to a remote tape silo ready for offline analysis. Fig 3.34 shows this complete system and how it is networked together. The maximum event rate in CLAS at this moment is roughly 4 KHz, which equates to 10 megabytes per second. This is not limited by the hardware but by the file transfer speeds in the Linux filesystem and the speed of writing the data to storage tapes.

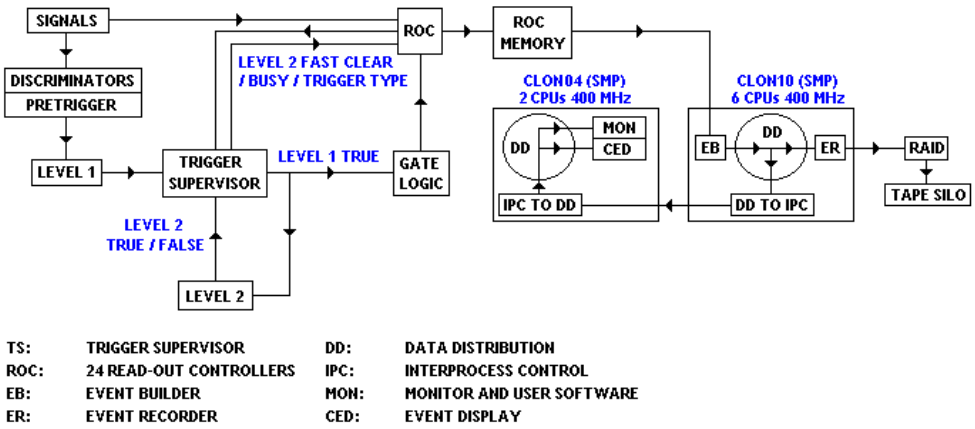

Figure 3.34: *A flow diagram showing the CLAS Data Acquisition System.*

[4]V.M.E. , the VERSAbus Module Eurocard format, a computer hardware architecture first released in 1981.

Chapter 4

Calibration Software and Data Reconstruction

4.1 Introduction

After taking data during an experiment, it is important to interpret the raw numbers correctly. This is also the area where misinterpretation of the data can waste valuable experimental information. Hence every effort must be made to ensure that the information returned from each detector system has sensible timing information, position information and energy or momentum values.

As a first step it is vital to take account of detectors that are not working properly, and this generally means making use of a software 'flag' that makes the status of faulty detectors known to the calibration and reconstruction software.

Reconstructing the timing of an event is the next important step, and it is desirable to have a reference time against which all the other detectors can be checked. In Fig 4.1, the idea of having a calibration cycle based on a reference time is shown. Using a universal timing reference means that a multi-component detector can be calibrated to an external trigger more easily, with the end result being internal agreement after synchronisation with the reference time.

A misidentification that can happen in this procedure occurs when a detector returns a time which, although appearing like a real trigger, does not actually come from one of the RF buckets generated by the accelerator.

In order to avoid such difficulties, a common time must be adopted to define a real physical event, and in the case of Hall B, the RF frequency of the beam is used. Naturally such an event would have to appear inside one of the RF beam buckets that

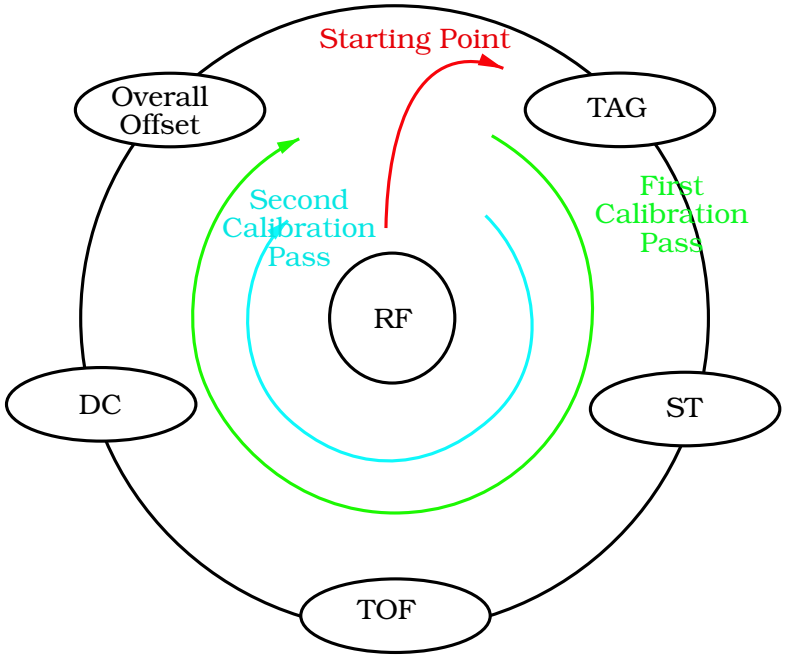

Figure 4.1: *The calibration procedure for CLAS in the case of a photon experiment. Note how the RF time is central to the calibration process as discussed later.*

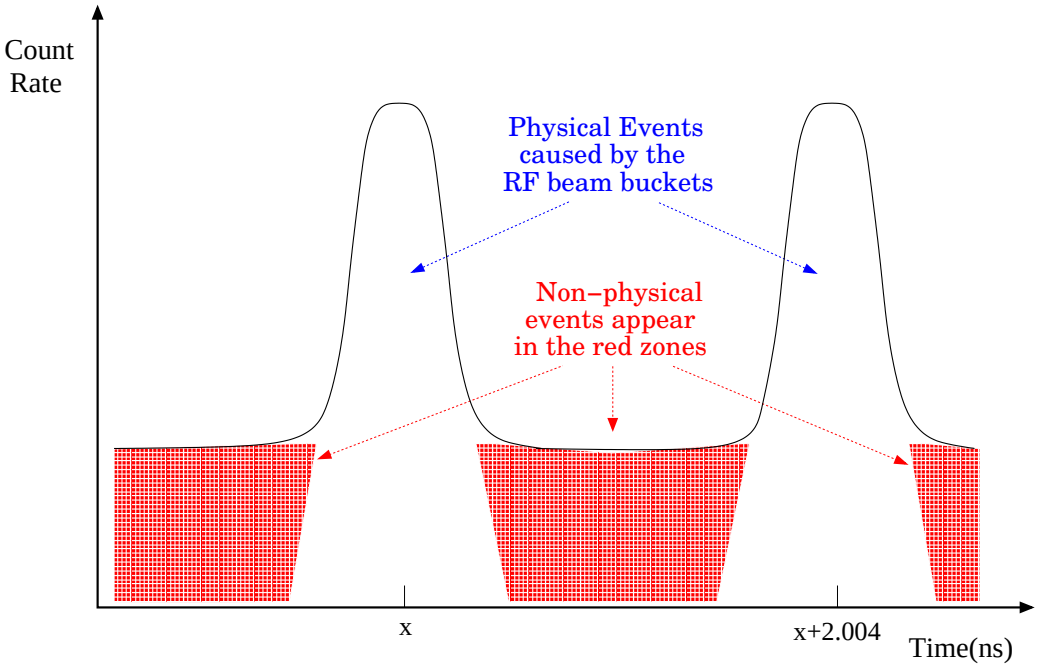

Figure 4.2: *The RF time can be used to determine whether an event is real or background. For all of the subsystems of CLAS, some method is adopted to take care of the situation where a nonphysical event creates a realistic looking trigger. These events should be rejected if possible.*

arrive in Hall B every 2.004 ns [50], so this is a strict criterion applicable to all the detectors, namely that if they detect an event not associated with a beam bucket, it should be rejected as noise. This point is illustrated in Fig 4.2.

More importantly, if the detector system in question does not show the 2ns RF structure from the accelerator, then it is unlikely to be well calibrated internally. By internal calibration, it is meant that all the components of a detector agree on the same time for a physical event.

For example, in the Time-Of-Flight system, each paddle should see the 2ns structure, but if the paddles are not correlated correctly with each other then the detector as whole will not see the structure, and thus be unable to determine if an event occurred inside an RF bucket or not.

This is similar to the Photon Tagger. Fig. 4.3 is a plot of each tagger T-Counter's reconstruction of the difference between the RF time and the hit time in that T-Counter. This plot clearly shows the discrepancies between each element of the Tagger, and when looking at the reconstructed time from the tagger as a whole, the detector will be unable to resolve which beam bucket caused an event in CLAS.

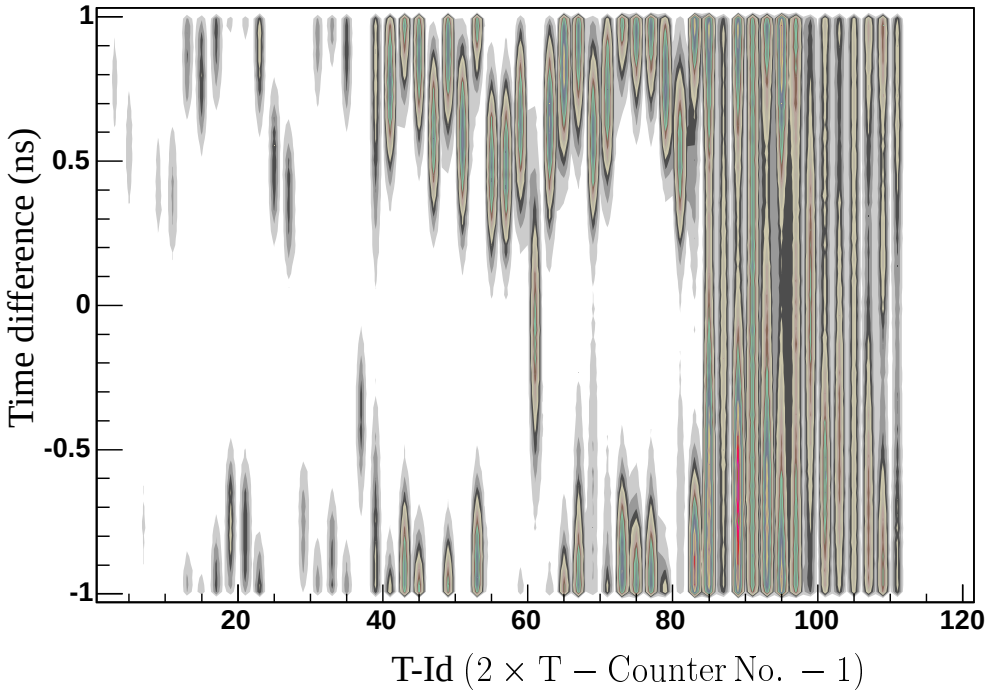

Figure 4.3: *Tagger T-Counter TDC time - RF TDC time for the whole range of tagger T-Counters. The effect of bad calibration is to shift the time for each T-Counter away from zero.*

The master clock against which every event in the detector must be measured is the RF frequency of the beam buckets, which is used for the first stage of calibrating all the detectors and ensures that they agree in time.

4.2 Hardware and Software

Some of the principles behind the collection and manipulation of the data are introduced next. The establishment of the way the electronic hardware records and stores time information is vital for defining these principles since practically all of the detectors in Hall B are read out through technically similar TDCs or ADCs. For calibration purposes the TDCs are particularly important because of the vital timing and position information they provide.

4.2.1 TDCs

A TDC converts physical time into a digital signal by using a fast electronic switch. In the case of a LeCroy 1875A TDC, a quartz piezo-electric crystal is used to give an extremely fast clock speed. The digital range of the TDC may cover over 2000 channels and each channel is the equivalent of 50 ps or more depending on the type of TDC.

When a TDC is given a start signal it counts against its internal clock and accumulates charge in each channel until the arrival of the stop signal. In this manner the time between start and stop signals is digitised and stored. From the software point of view the stored channel number needs to be converted into a real physical time, and this is done by knowing what each channel corresponds to in terms of time. For a more accurate conversion, attention has to be paid to the fact that a TDC does not always have a linear conversion from time to channel number, which must be taken into account when converting a TDC channel number back to time.

This means that for every TDC in Hall B, to convert channel number to physical time, the channel number where a peak of interest occurs must be known, as must be the calibration of that TDC. The equation for calculating time from a TDC is given in eqn 4.1.

$$\mathrm{T_{phys}} = \mathrm{C_1} + \tau \mathrm{C_2} + \tau^2 \mathrm{C_3} \tag{4.1}$$

Therefore for any given TDC three offsets must be determined to reconstruct the physical time $\mathrm{T_{phys}}$ from the TDC Channel number τ. $\mathrm{C_1}$ represents the base peak

position, C_2 is equivalent to the slope of the TDC and C_3 represents the general trend of the slope, which depends on the range of the TDC.

4.2.2 Calibration Database

The calibration procedure requires storing these TDC offsets so that whenever a software package is required to reconstruct the physical time from a given TDC, the offsets should be readily accessible.

In the past in Hall B, offset **maps** were used, which were effectively text files containing offsets relative to a specific detector system. They were stored in a certain place and all reconstruction software knew where to look for the appropriate map.

For G8a a new system using MYSQL [75] - a database language - was used. Known as CALDB this was a database running on a separate server which indexed all the constants required for all detector systems. Conveniently, the offsets could be stored in a central place for different run periods, which meant that users could access and change constants without affecting other user groups or overwriting essential offsets by mistake. Every constant obtained through the process of calibrating G8a data was stored in a private index completely specific for the experiment.

4.2.3 BOS Input/Output

The data read out from CLAS is transferred, at the point where the information from each detector system that fired for a given Level 1 trigger is collated into an event, into a FORTRAN 77 dynamic memory allocation structure structure known as BOS [76, 77]. This acronym stands for Bank Operating System [76] and every detector has a BOS data bank containing the raw TDC or ADC channel numbers that fired for each event. The key to any calibration or data analysis software is using either FORTRAN or C-wrapped FORTRAN function calls to access data from the relevant BOS bank. An example of a typical BOS bank and the accompanying data fields is the TAGR (Tagger Reconstructed) BOS bank shown in Table 4.1.

4.2.4 Cooked data

During data reconstruction, raw BOS banks are converted into cooked BOS banks by the process of converting TDC channel information to time, and also doing Drift chamber tracking and other analyses that will be mentioned later. After an experiment has finished running, the raw unprocessed data is first calibrated, then when adequate

Table 4.1: The reconstructed Tagger bank, TAGR.

Bank Entry	Min. Value	Max. Value	details
ERG	0	10	Energy of the photon in GeV
TTAG	-20	200	Reconstructed photon time
TPHO	-20	200	Reconstructed photon after RF corr.
STAT	0	4096	Status Flag
T_id	1	121	T-Counter Id
E_id	1	767	E-Counter Id

constants have been obtained, the data is cooked [78]. Fig 4.4 shows this process as a flow chart, and apart for any iterations for refining the calibration constants, the data reconstruction flows sequentially in this way. This is computationally intensive and can frequently take over 3 months to complete on the Jefferson Lab farm computer system.

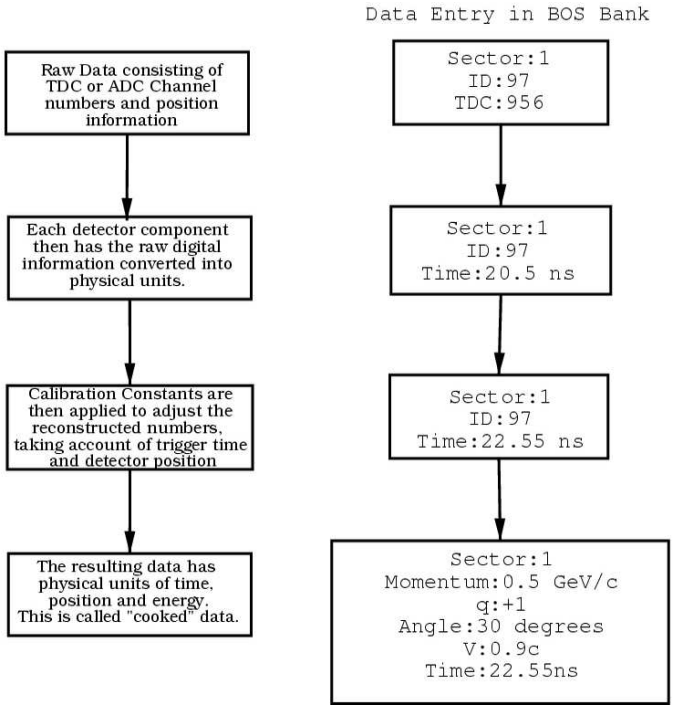

Figure 4.4: *Flow chart showing the processes involved in going from raw to cooked data. Shown on the left hand side is the process being followed by the reconstruction software, and on the right the corresponding entries in a typical BOS bank are shown.*

In the final cooked files the BOS format is used and the raw and cooked banks are both present, and analysis programs are able to access physical time, momentum and

other physics information directly.

4.3 Beam RF frequency calibration

To have an accurate measure of the RF pulse of the electron beam as it arrives in Hall B, a PMT is situated close to the beam, passing to a TDC module the timing information. The signal from this TDC is pre-scaled by 40 and then chopped into two. The two different ranges are designed to give a trustworthy average but in practice it makes no difference to use one or other, or even a combination of both. The pre-scale gives a signal with a period of 80 ns which allows an accurate determination of the RF time. A software package builds a BOS bank called CL01 which contains the RF information. Only one RF TDC time is reconstructed, so a plot of the time distribution is a single gaussian peak positioned relative to the trigger. However, it is very useful to work out the phase shift between different detector components, and since detector components are normally synchronised to some trigger time, a typical detector offset from a real physical event time is of the form.

$$\mathrm{T_{phys}} = \mathrm{T_{tdc}} + \mathrm{RF_{Phase-shift}} + \mathrm{k} \star 2.004 \tag{4.2}$$

Here $\mathrm{T_{phys}}$ is the physical time of the events recorded by the detector, and $\mathrm{T_{tdc}}$ is the converted time recorded by the detector TDC. The constant k is an integer number of RF beam buckets that the given detector component may be offset from a trigger time after the RF phase correction is made to bring the RF TDC time to zero.

The typical signal from RF1 can be fitted and compared with other detector components, in particular the photon tagger (there is a 2 ns structure in the photon beam since it is produced directly from the electron beam). However, the times given for a beam bucket by the Tagger and the Beam RF TDC must be synchronised for the rest of the calibration to proceed.

In calibrating the RF TDC, a Gaussian is fitted to the TDC peak, as shown in Fig 4.5. The measurement of the mean position of the peak creates a constant to be taken account of in the RF TDC time reconstruction in order to shift the peak of the distribution to zero. This then sets the Hall B RF time to zero, and the next stage is to compare this time with the detector that measures the time of the photons that cause the measured reaction, i.e. the photon tagger. In that comparison the actual RF frequency of the electron beam and the related frequency of the photon beam are matched by the addition of an offset. Then the photon time given by the tagger can be used as the

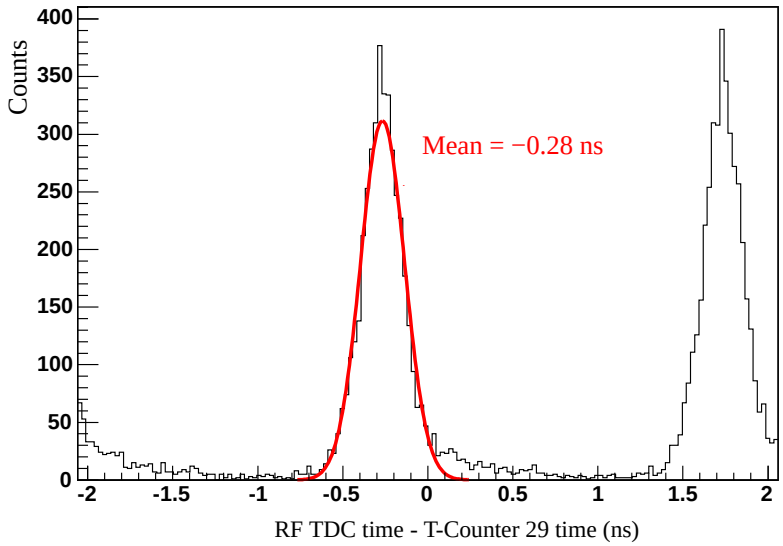

Figure 4.5: *The output from the RF1 TDC compared with a single Tagger T-Counter TDC time shows the 2ns RF structure of the beam.*

reference for the other detectors which have to be calibrated.

4.4 The Start Counter

4.4.1 Concept

The calibration of the Start Counter is straightforward in principle because all that is needed is for a start time to be synchronous for the three different paddles of the detector. In Section 3.5.3 it is mentioned that the six legs of scintillator are joined into pairs to give an overall surface of $\sim 120^0$ azimuthal coverage for each sector pair in the forward direction. This implies that the TDC timing information must also be considered in pairs. A single hit should give a constant mean time between the two TDCs, regardless of where the hit took place in the scintillator. This fact can be used to calibrate the three pairs.

Fig 4.6 shows the typical timing information used to calibrate a Start Counter pair. On the vertical axis the difference of the times from each TDC divided by 2 is shown, versus the mean on the horizontal axis.

By consideration of the properties that different hits will have, the lines that appear as diagonals in the above plot can be interpreted as hits where one PMT fired and the

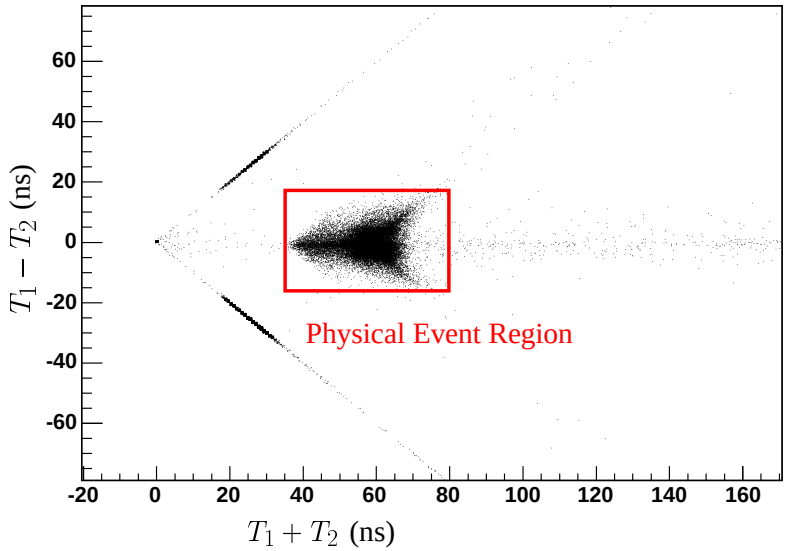

Figure 4.6: *The calibration of a Start Counter Paddle. The difference in time is plotted versus the time sum of both TDCs, and the physical events considered as real hits in CLAS are shown inside the red box above. Below, a side-on view is taken which allows a clearer view of the position of the centre of the event distribution. This is the view used to align the distribution, and the alignment is checked by fitting this peak to zero and making small adjustments to the relevant constants.*

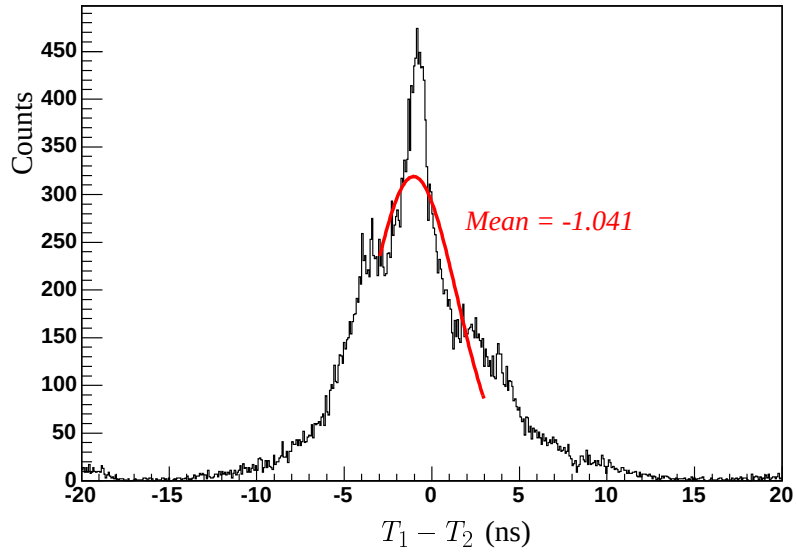

other did not. Such events are considered as nonphysical for the purpose of calibration, and real hits are considered where the difference remains close to zero. If the general shape of the distribution resembles that above, but the strong horizontal line is offset from zero, a constant is applied in the software that corrects an individual TDC to bring the central line back to zero. When this is achieved the pair is considered to be internally calibrated.

But what about the other two pairs? After calibrating the other pairs in the same way, it is necessary to compare the three pairs with any given external time that has a statistical width of < 1 ns. If the tagger is sufficiently well calibrated then the whole detector can be used. However for G8a a single T-Counter TDC sufficed to provide an external reference for aligning the three pairs.

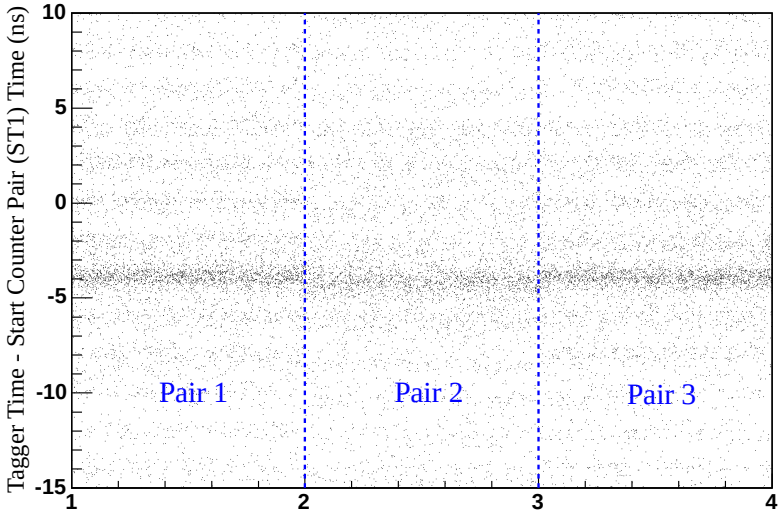

Figure 4.7: *A plot of Tagger time minus ST1 mean time for all pairs.*

Fig 4.7 shows on the vertical scale the pair mean time - the selected tagger TDC time, and on the horizontal axis the three pairs of the Start Counter are shown. Clearly the Start Counter detector components can be considered well-aligned if they agree on the same time for the tagger TDC to fire to within 1 ns of the width of the tagger TDC peak. Another view of the histogram shown in Fig 4.8 confirms the satisfactory alignment of the three start counter pairs.

If the Start Counter pairs agree on the time, then times reconstructed from the Start Counter can be used in the calibration of other detector systems as the reference point for the timing of a physical event, where a physical event is defined as an event within

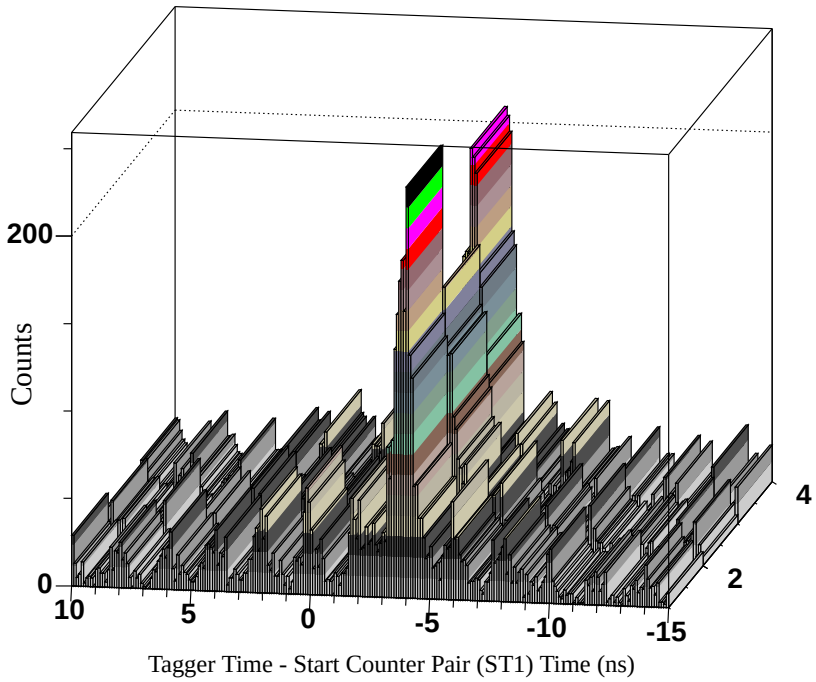

Figure 4.8: *Profile of Fig 4.7 showing the width of the Start Counter distribution that corresponds to a single Tagger TDC.*

a beam bucket that fired the Level 1 trigger.

4.4.2 Software

The software used was developed in co-operation between the author and two other colleagues, Chris Gordon and Juan Carlos Sanabria. Based on the concepts outlined above, the goal was to create some software which had the capability to read the Start Counter pair time from the appropriate BOS bank - ST1 - and compare with the Tagger time read from TAGR. By using the CLAS software framework, a program named **st_dt [79]** was written which compares the two halves of each Start Counter pair and calculates and displays the values required to evaluate the appropriate constants to be added for each individual TDC. The overall alignment of the Start Counter can also be plotted with respect to any tagger TDC or all of them. This package proved very effective in allowing changes to made to the Start Counter constants with one pass of the program over cooked data. The author was personally responsible for making improvements to the software which allow for partial re-cooking of banks to allow the user to run on raw data as well, which makes calibration immediately after an experimental run has finished more straightforward.

This modified version of **st_dt** was extremely useful in adjusting the Start Counter timing constants to allow for the fact that there was a hardware problem, specifically a low gain on one of the PMT tubes in Pair 2. This was done by rebuilding the TBID BOS bank and checking the difference in event vertex time measured by the TOF and the Start Counter. The Start Counter timing constants, described in Section 4.4.3, were then adjusted to bring this difference as close as possible to zero. The author also modified some FORTRAN routines which build the ST1 event time, in this case a limit was needed which would not allow out-of-time events to creep into the reconstructed STR bank. This was the cause of major difficulties early on in the process of calibration.

4.4.3 Process

The process of calibrating the Start Counter initially focuses on internal timing alignment. The program **st_dt [79]** plots the time difference from a start counter TDC pair versus the mean time. For a real single particle event the measured time difference should always be constant, so the straight line shown in Fig 4.6 is the first measure of calibration in this process. Depending on the individual gain of the TDCs, this straight line can have a range of offsets from the x-axis, but for convenience the pair is considered calibrated when this line is centred on the x-axis, with a time difference of zero.

This requires adjusting one of the six constants that reconstruct the TDC time.

So **st_dt** primarily deals with three pairs of the six Δt TDC constants, where each pair corresponds to the start counter design of six scintillators joined into three pairs. Upon suitable adjustment of these three pairs of constants, each pair is considered to be internally consistent. However, due to the fact that the individual performance of each TDC may vary considerably, this does not guarantee that each pair of the start counter would return the same time for a given physical event.

The next step in the **st_dt** program is to display all three pairs on a single histogram, using the time from a single T-Counter in the tagger as a reference.

Combining the three pairs like this (shown in Fig 4.7) with reference to an external time reveals how well the start counter pairs are calibrated, and if a pair has a significant offset from the desired straight line then the two TDC constants relating to that pair are modified. Then step 1 is repeated to ensure the straight line for the time difference between the two pairs is still at zero. Selecting different individual constants for each start counter TDC does not necessarily affect the mean time alignment of a pair, since having the reconstructed time difference at zero only measures the relative times, and therefore the relative values of the constants required to reconstruct each TDC, not their absolute values.

If the comparison of the event time in the three pairs in **st_dt** shows a straight line, and the profile of this peak in the y-axis has a width of $\sim 1\,ns$ then the start counter is considered to be well aligned internally.

In the process of running **st_dt**, the user notes the values of the six TDC constants, and enters these values into the private run index of the Calibration Database for the experiment being calibrated. **st_dt** then reprocesses the relevant Start Counter BOS banks to enable a direct comparison to be made with the previous values stored in the Calibration Database. The user can then quickly calibrate the Start Counter for a number of data files using this procedure.

The Start Counter signal can then be used in the calibration of the Photon Tagger and the Time-Of-Flight system.

4.5 Coherent Bremsstrahlung

4.5.1 Process

Producing coherent bremsstrahlung relies on being able to orientate the radiator to bring specific crystal planes into alignment with the beam. A high quality polarised

photon beam requires the set of planes parallel to the electron beam to be aligned within 1 mrad. This alignment is achieved by establishing the physical crystal position relative to the beam, then carrying out a set of calibration scans which determine where the crystal planes are oriented. These scans can then be used to determine the relation ship between crystal angle and the photon energy of the main coherent bremsstrahlung peak in the photon tagger spectrum. A more in-depth description of the method used to align the diamond crystal can be found in Appendix A.

4.5.2 Calibrating the Coherent photon spectrum.

The final stage of the calibration is to use a method defined by Lohmann [80] to measure the dependence of the position of the coherent maximum, or coherent bremsstrahlung peak, with either θ_{v} or θ_{h} as defined in Fig 2.7. This is done by doing a scan of photon energy against both θ_{v} and θ_{h} in order to provide two orthogonal planes of polarised photons, which is desirable for the later stages of analysis (see Section 6.5). The result is a table of goniometer angle and coherent peak energy. At the top of Fig 4.9 an example of such a scan produced from the G8a run shows that the crystal axis orientation is off by 2 mrad, however such a plot can still be used to calculate the required goniometer angle parameters to produce a given coherent bremsstrahlung peak energy measurable in the photon tagger. With such a table, compensation can be made for situations like variation in beam position and changing the plane of polarisation for experimental purposes. At the bottom of Fig 4.9 the tagger energy spectrum is plotted for a particular crystal angle that has been calculated to give a peak energy of approximately $2\,\mathrm{GeV}$.

4.6 The Photon Tagger

4.6.1 Concept

For the G8a experiment a single T-Counter TDC from the Photon Tagger was used to calibrate the Start Counter, but for the next stage of calibration the Start Counter must then be used to complete the calibration of the Photon Tagger.

This is because each component of the tagger can be easily matched to an RF beam bucket since the electrons arriving in the hodoscope will still retain that time structure. However it is much harder to be certain that the tagger element under consideration is attuned to the time of the physical event that occurred in CLAS, especially if the level of background in the tagger is high, as it was during G8a. High levels of background

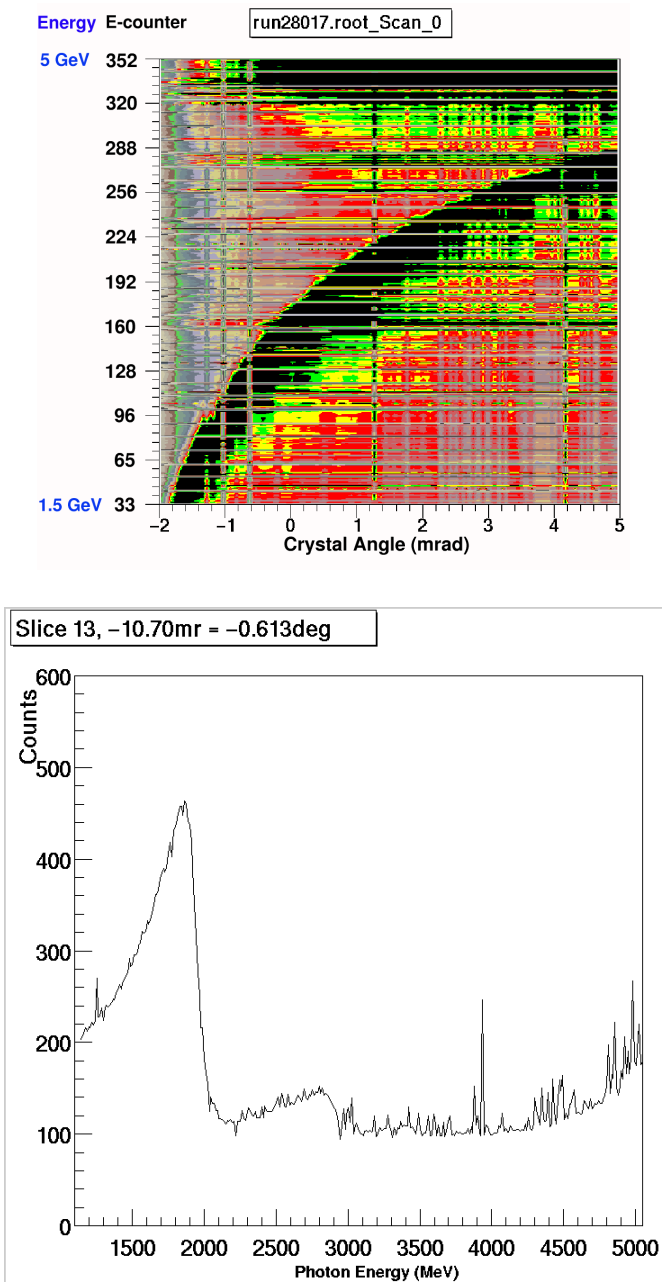

Figure 4.9: *Plotting the Photon Energy Spectrum of the tagger against the crystal angle (θ_v or θ_h) of the goniometer. The coherent bremsstrahlung peak energy shows here as a dark curved band running approximately diagonally across the top plot. The bottom plot shows a slice taken vertically through the top plot for a particular crystal angle corresponding to the peak energy being at ~ 2 GeV.*

can obscure the true event timing in the tagger. In Fig 4.10 the Tagger TPHO time (described in Table 4.1) for all the 121 T-Counter bins in the tagger is plotted and the projection into 2 dimensions shows the variation in timing of each tagger element.

It now becomes necessary to use another measure for timing a physics event to give the reference for each T-Counter and E-Counter, and this is provided by the Start Counter. This implies that the calibration of the tagger is a two-stage process [81], and the method followed for G8a was to synchronise each T-Counter TDC to the RF1 time by making a fit and then calculating the offset required to bring the time, measured at the peak of the Gaussian distribution, to zero. This process uses a similar approach to that shown in eqn 4.2 and Fig 4.5. With this offset added, then each T-Counter TDC can be moved by beam-bucket integers until it matches the time measured by the Start Counter, with a suitable offset for each TDC added to take account of the extra distance between the Start Counter and the Tagger as well as cable delay.

4.6.2 Software

G8a is heavily indebted to Ji Li from the G6c run group, who used the concepts from CLAS-NOTE 1999-04 to create a new C++ program called **photonTcal [82]** which automated the procedure of calibrating the slope of each TDC, finding the left-right balance between the TDCs attached to each end of the given T-Counter, fitting each TDC peak and finding the RF correction needed, then finally comparing each T-Counter Channel with the Start Counter mean time.

The program **photonTcal** uses several FORTRAN data processing routines to allow the cooking of the Photon Tagger BOS banks, allowing the user to check the validity of the automated fitting procedure which calculates the necessary TDC constants for each T-Counter.

The author was involved in using **photonTcal** to evaluate the quality of experimental runs and deciding which runs should be used to calibrate the overall system for a period of subsequent runs. This work also involved making manual adjustments to the Photon Tagger timing constants to allow the best possible calibration despite the hardware problems which are documented in Section 7.2.

In a complete calibration pass **photonTcal** runs on approximately 300,000 events and the process consists of 4 steps shown in Table 4.2.

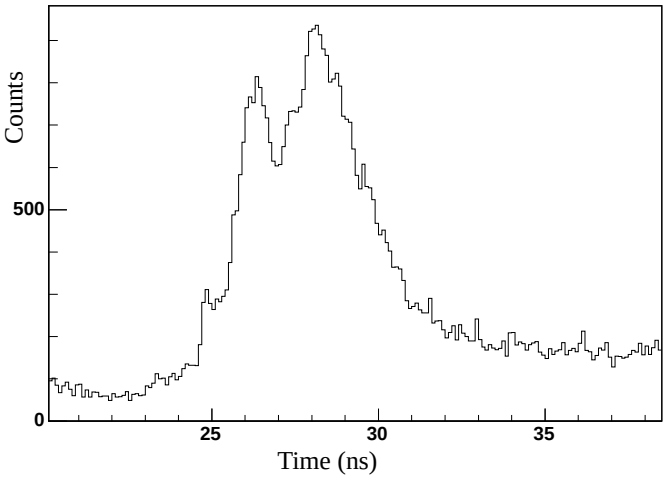

Figure 4.10: *Tagger Tpho time, showing the spreading out of the real peak. Below a 3-dimensional representation of the Tagger's timing behaviour can be seen. From this it is clear that there is a problem with the individual timing of the T-Counters in the Tagger since for the range T-Id > 80 the timing peaks are very broad.*

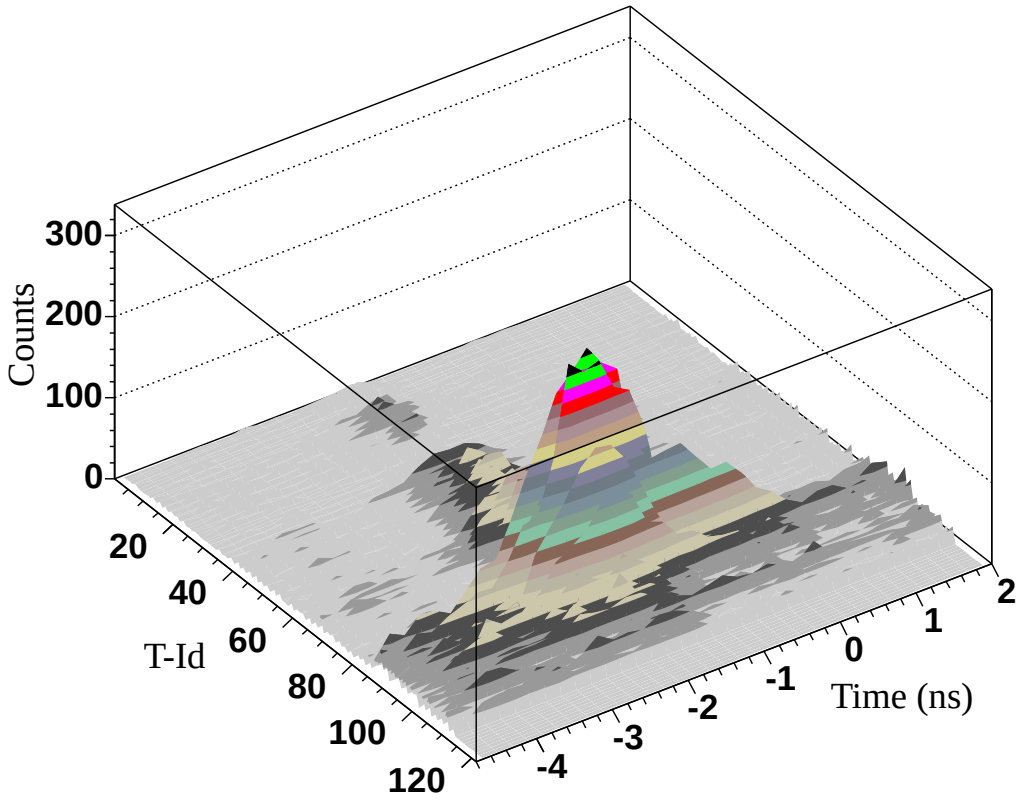

Step	Process
1	Calibrate RF time
2	Calibrate TDC Peak Position
3	Find L/R slope balance for each T-Counter
4	Calculate C_i RF adjustment for each T-bin
5	Calculate each C_i offset from reference detector

Table 4.2: Tagger calibration procedure

4.6.3 Process

For the first part of the calibration process, **photonTcal** created the reconstructed Tagger bank - TAGR - with constants from a previous run. In the TAGR bank each T-Counter is split into two - owing to the geometrical overlap in the design of the hodoscope, giving 121 Tagger Ids or T-bins to be calibrated (See Fig 3.12). A look-up table is used to make a geometry-based match between the hits in the E-Counters and T-Counters, taking into account that often a single hit in a T-Counter will match several hits in separate E-Counters.

Calibration of the E-Counters is done in a very similar way to the T-Counters, a geometrical overlap creating 767 distinct E-bins, which then have their base peak position calculated and subtracted from the raw TDC channel number. The E-Counters run in common-stop mode but they are closely linked to the triggering of the T-Counters, because the T-Counter timing forms part of the Level 1 trigger. A timing coincidence between an E-bin and T-bin is also still required in the software for successful reconstruction of a Tagger event.

This coincidence measurement is based on finding an acceptable trajectory through a group of E-bins and a T-bin for an event in the tagger hodoscope. The hardware is set to accept coincidences within a 20 ns window, and if the T-Counters are calibrated properly and the E-Counter to T-Counter geometric matching works properly, a straight horizontal line will be seen when plotting $(\mathrm{T_{e-counter}} - \mathrm{T_{t-counter}})$ versus the E-Counter E_id Number, as shown in Fig 4.11.

The geometric matching between hits in E-bins and T-bins is performed by a look-up table text file that is read by **photonTcal** and compared with the raw data. Depending on where the T-bin is in the hodoscope, the range of E-bins that would be considered as contributing to an acceptable hit can change, since the direction of the magnetic field changes over the length of the tagger and this results in energy-degraded electrons arriving at a E-Counter/T-Counter location at a different angle relative to the

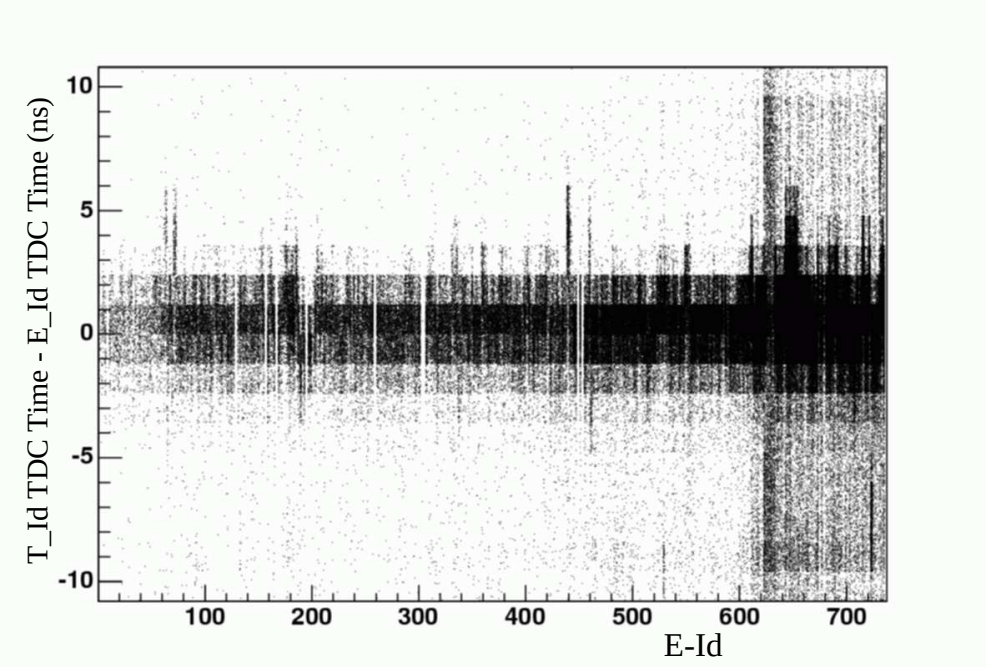

Figure 4.11: *E -Counter compared with T-Counter timing coincidence plot from the Tagger.*

detector plane.

The calibration process continues by comparing the TDC time with the RF1 TDC time. As shown in Fig 4.12 a plot is made of the TDC reconstructed time minus RF1 and then the peak is fitted to give the RF offset for that TDC.

For calibrating the Photon Tagger, one deals with the T-Counters. Each T-Counter has a PMT attached to each end of the scintillator bar, which feeds in to a separate TDC module for each side. The reconstructed time from the T-Counter therefore depends on which PMT registered a hit, and how the TDC time conversion per channel varies between the left and right sides.[1]

The Tagger TDCs run in common-start self-triggered mode, which means that they will start to measure time either when the CLAS level 1 trigger fires, or else they are started by their own trigger based on an electron hit on a T-Counter, which then becomes part of the Level 1 trigger. The TDC peak position calibration constant that is used to reconstruct the TDC time is actually the mean position since either the left or right TDC can register the earliest time for a given T-Counter, which then becomes its trigger. This means that the overall time for the T-Counter tends to be skewed slightly, since if the hit occurs first in one side of the T-Counter the opposite side

[1]There are two TDC modules, one for each side, each consisting of 64 TDCs.

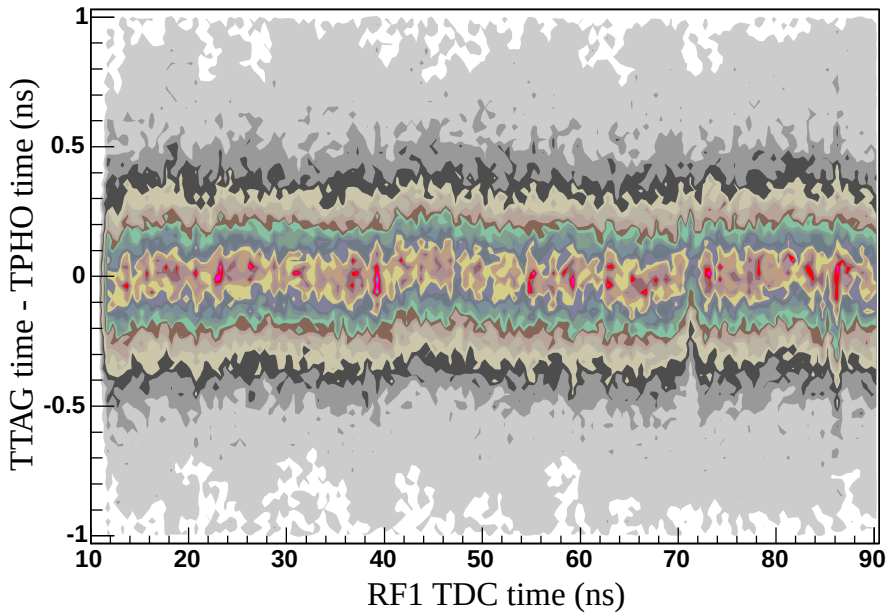

Figure 4.12: *Tagger time* **(TTAG)** *minus RF corrected Tagger time* **(TPHO)** *time for all of the 121 T-bins plotted against the RF1 TDC time on the x-axis.*

TDC has a broader time distribution due to light dispersion in the scintillator. Useful quantities to calibrate the reconstructed time of a T-Counter, by taking into account peak positions and the difference in time distributions from either PMT causing the trigger, are therefore the absolute peak positions for the **i**-th T-Counter.

$$< \mathrm{Peak(L_i)} > = < \mathrm{TDC(L_i)} > - < \mathrm{T(L/R)_i} > \tag{4.3}$$

$$< \mathrm{Peak(R_i)} > = < \mathrm{TDC(R_i)} > - < \mathrm{T(R/L)_i} > \tag{4.4}$$

Here the number $< \mathrm{Peak(L_i/R_i)} >$ is the absolute peak position in the right or left TDC connected to a particular T-Counter. This number is considered absolute because the equivalent expression contains both a raw TDC channel number $< \mathrm{TDC(L_i/R_i)} >$for the peak position, as well as a measure of the relative time difference between the left and right TDCs for this particular event. The raw TDC channel number can be seen in Fig 4.13.

The quantity $< \mathrm{T(L/R)_i} >$ relates to the relative time delay between the Left and Right PMTs that connect to the respective TDCs, and this quantity is well established from previous runs, being due to a fixed cable delay and other systematic physical

factors. The peak calibration is done to allow the subtraction of the time taken from the trigger firing until each TDC actually records a time. Doing this subtraction results in a Tagger time of zero compared with the Level 1 trigger time in CLAS. The constants are found by an approximate Gaussian fit performed by a subroutine in **photonTcal** and then written to the Calibration Database.

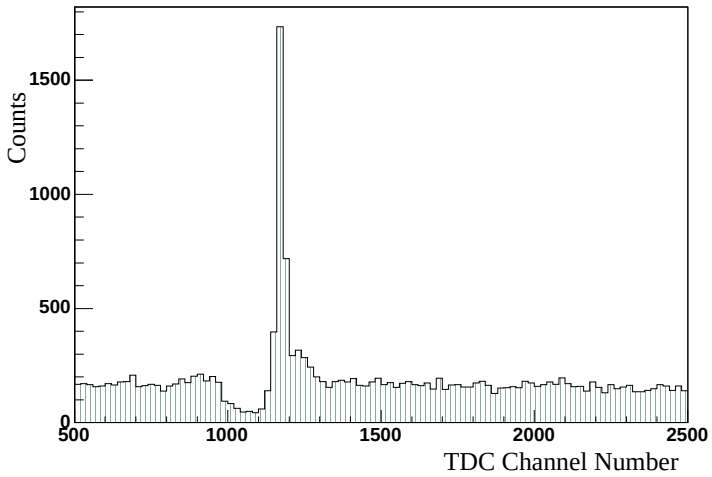

Figure 4.13: *Base peak calibration in* **photonTcal**. *The calibration routine finds the TDC channel number with the most number of events and records this as the peak position. A dip can clearly be seen in the count-rate for this TDC on the left-hand side of the main peak. This is thought to be due to TDC pile-up caused by the very high count-rate seen in the photon tagger during the G8a experiment.*

Calibration of the T-Counter TDC slopes is done to counteract the effect of individual variations in different TDCs from the preset 50 picoseconds per channel time conversion[2]. This means that a comparison between the Left and Right TDCs for each T-Counter should show if one converts time at a different rate than the other.

A suitable comparison is to plot the left/right time difference versus the mean time t_i^{mean} i.e:

$$\frac{t_i^L - t_i^R}{2} \propto \left(\frac{t_i^L + t_i^R}{2} = t_i^{mean} \right) \tag{4.5}$$

As seen in Figure 4.14, when the slope of a particular T-Counter is not acceptable, this plot shows a non-horizontal line departing from zero, whereas a well-calibrated counter should have a straight horizontal line at zero. This particular procedure often

[2]The slope for E-Counters is 500 picoseconds per channel.

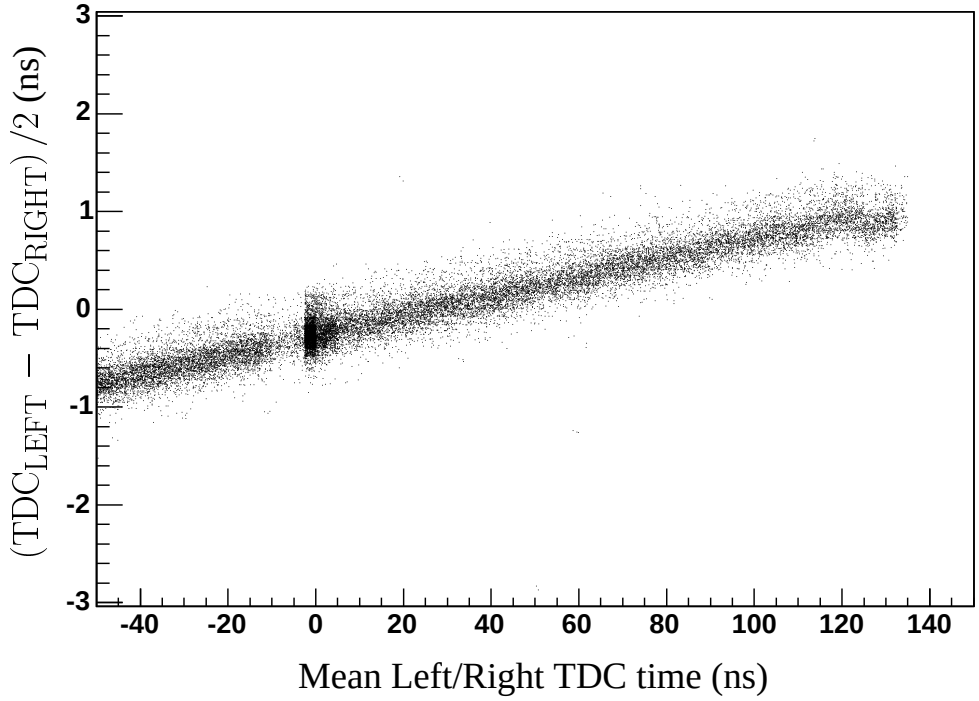

Figure 4.14: *Slope Calibration from* **photonTcal**. *Once all the slopes are calibrated for each T Id, each T-Counter will reconstruct the time of an event properly whether it is read from the Left or Right TDC. Below, the final slopes for all the T Ids are shown for a G8a calibration run.*

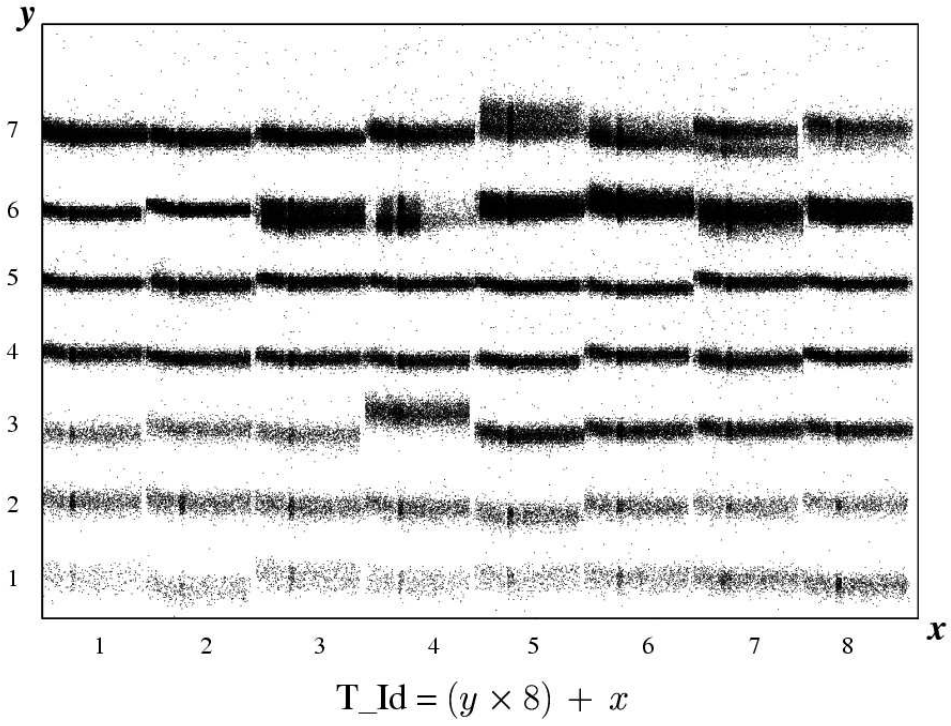

needs to be checked and modified by hand since **photonTcal** was unable to obtain a reliable fit to the data for this procedure.

At this point each T-Counter has the peak position subtracted and the slope from left to right TDC should be balanced. However, the RF signal should now be taken into account.

Using the mean time from each T-Counter and the information from the CL01 BOS bank, **photonTcal** creates a histogram of this mean time minus the RF time, and makes a Gaussian fit to the peak of this distribution. The offset required to bring this peak to zero is entered into the Calibration Database as the C_i^{RF} constant for each T-Counter. This ties in with equation 4.2, taking into account the RF phase offset that each component of a detector may exhibit. Once this step is complete, the RF time from CL01 can be substituted in place of the time recorded by a T-Counter TDC, giving much greater precision to the reconstructed tagger time. Fig 4.15 clearly shows this improvement, particularly when contrasted with the state of the tagger before being calibrated, as shown in Fig 4.3.

Thus, the time displayed in the TAGR bank , ttag from Table 4.1, is now used for each T-Bin, and is also used to calculate the most important quantity obtained from the tagger calibration, tpho.

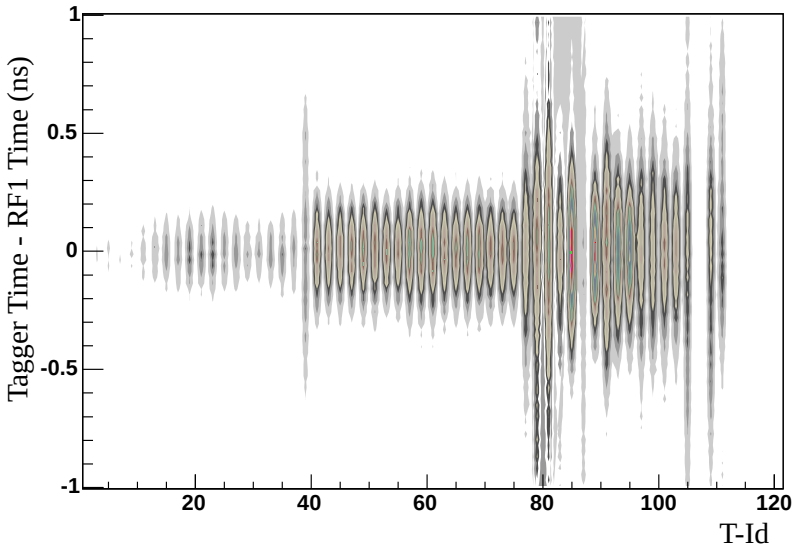

Figure 4.15: *The TPHO time minus RF time is plotted here for each T-Bin.*

To complete the Tagger calibration, each T-Counter needs an additional offset to be added that takes into account an integer number of beam buckets in which the signal

may be offset from the trigger time, depending on delays and experimental conditions. This is the final component of equation 4.2, adding k beam buckets on to each T-Counter to define the final set of constants to be written to the Calibration Database, the $\mathrm{C_i^{REF}}$. The way that **photonTcal** works this out is by using the Start Counter as the reference detector which gives the timing of the event seen in the Tagger.

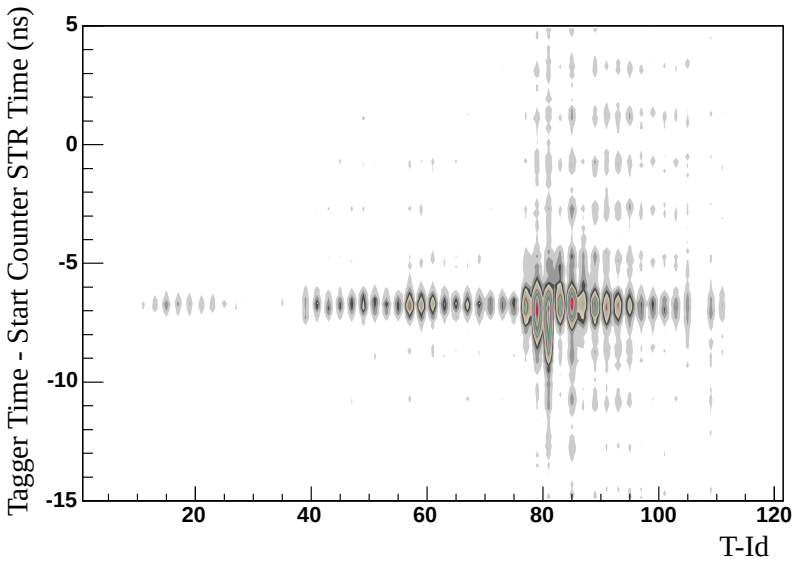

Figure 4.16: *Plot of the calculated C_i^{REF} for each T-Bin. This is the calibrated Tagger (TPHO) time minus the Start Counter (STR) time.*

PhotonTcal uses the mean pair time $\mathrm{T_{ST1}}$ from the Start Counter to create a fit of this relative time by plotting $(\mathrm{t_i^{mean}} - \mathrm{T_{ST1}})$ for each T-Counter,. The Start Counter picks out the real peak from the background that the tagger detects for each T-Counter, and this peak is fitted with a Gaussian and the value of the offset is the $\mathrm{C_i^{REF}}$, which is stored in the Calibration Database. This number takes note of the offset from the reference detector for each T-Bin, and Fig 4.16 clearly shows that after all the calibration steps, a straight line should be seen on a plot of $(\mathrm{t_i^{mean}} - \mathrm{T_{ST1}})$ versus T-Bin. If some elements of the Tagger are out of alignment on this plot, an adjustment of the relevant $\mathrm{C_i^{REF}}$ by an integer of 2.004 should bring the tagger back into alignment[3].

This constant is used to calculate the timing of a hit in each T-Bin on an event-by-event basis, and this is done by creating a number tpho in the TAGR bank, i.e.

$$\mathrm{tpho} = \mathrm{ttag} - \mathrm{C_i^{REF}} \tag{4.6}$$

[3]The frequency of the beam-bucket in Hall B is 2.004 ns so adjustment by an integer number of beam-buckets means an integer number times 2.004.

which is equivalent to :

$$\mathrm{tpho} = \mathrm{t}^{\mathrm{RF}} - \mathrm{k} \times 2.004 \tag{4.7}$$

This number takes into account the way in which a T-Bin may not have the same electronic delays as one of its neighbours, and once the RF correction has been applied, it should be displaced in time by an integer number of beam-buckets in time from the real event which caused the trigger.

4.7 The Time-Of-Flight System

4.7.1 Concept

The Time-Of-Flight calibration [83] is again linked to the idea of a physical reference event time first mentioned in Fig 4.1, with respect to which all the components of the system should agree. For this case it is a prerequisite to identify which charged particle causes the signal in the TOF TDCs, and this is done by looking at the energy deposition in a TOF scintillator bar. In accordance with the Bethe-Bloch equation [84], the amount of energy deposited by a charged particle in a given material is related to its mass and charge, so if the Energy Deposition per unit thickness is plotted as a function of momentum it is possible to disentangle pions from protons.

Plotting the $\mathrm{dE/dx}$ of charged particles versus their momentum shows a curve that approximates a Landau distribution. More importantly, the distribution of the pions is peaked at a lower momentum, and a significant number of pions lie beneath the Landau peak of the proton distribution, which makes it possible to make a loose cut to roughly identify pions for the purpose of calibration, as shown in Fig 4.19. A reconstructed vertex time is used for each candidate. The vertex time is the detected time minus the time taken for the particle to propagate to the outer region of CLAS.

This identification allows the use of a graphical cut to separate the pions from protons for each scintillator bar in the Time-Of-Flight System and a comparison of the pion vertex time with the tagger time from the TAGR bank. Again, a physical event should have correspondence with the RF structure and this is seen when plotting Tagger time minus pion vertex time for any TOF TDC, and any offset between the physical event peak picked out by the tagger and the time of the event recorded by the scintillator TDC is calculated by fitting the main peak of this distribution.

Ideally,

$$(\mathrm{TAGR}_{\mathrm{tpho}} - \mathrm{TOF}_{\mathrm{vtime}}) \simeq 0 \tag{4.8}$$

where once again $\mathrm{TAGR}_{\mathrm{tpho}}$ is the calibrated photon time calculated by the tagger, and $\mathrm{TOF}_{\mathrm{vtime}}$ is the pion vertex time obtained from the time distribution of pion events selected in Fig 4.19.

A large part of the calibration procedure in the Time-Of-Flight system is to ensure that the TDCs and ADCs at each end of one of the scintillator bars can determine the correct pulse-height, and the correct time for a particle that arrives in the centre of a bar. If these quantities are correctly calibrated then the system can be trusted to measure the time, position and energy of any charged particle passing out from the centre of CLAS correctly.

In principle each TDC must also be calibrated for slope, drift, and time-walk as well but this requires special calibration data generated by use of a pulsed laser. This data was not taken during G8a, and the offsets from the previous run were used, on the reasonable assumption that the experimental conditions would not have changed much in the space of a few weeks. The overall process is detailed in Table 4.3.

4.7.2 Software

There are four programs under the sc_calib package in the CLAS software that perform calibration of the TOF from raw or cooked data for photon running. These are all written mainly in **C**, using **PAW** libraries to create **hbook** output files. **PAW** is a analysis software package developed in CERN [85], and the **hbook** output is a file format containing histograms and ntuple file structures. **PAW** also allows the use of macros called **kumacs** which are used to manipulate the **hbook** data. This allows the use of **PAW** to automate the fitting procedures used to calculate gradients and means relevant to the calibration constants.

The first program to be used is **gmean**, which calculates the geometric mean of Minimum Ionising Particles for each scintillator bar. Run on one cooked data file, this program generates constants that are used in the next stage of calibration.

These constants are picked up by **atten_len** which calculates the attenuation lengths of each TOF bar from the geometric mean constants given above. The output from **atten_len** is used to determine ADC gain-balancing constants for each left/right PMT.

To determine the effective velocity of light in each bar, **veff** is used to measure the gradient of the slope determined by the left and right TDC times for events at different locations along each bar.

The program that determines the counter-to-counter offset is called **p2p_delay_ph** and calculates the offset for each TOF counter by looking at the vertex time of selected

events and comparing those times with the Photon Tagger time for the same events.

Here the author was involved in a group effort and specifically performed calibrations for the effective velocity calculation and counter-to-counter offsets. This work was carried out in close contact with the Tagger calibration process.

4.7.3 Process

Calibration process	requirements
Pedestals	Dedicated DAQ configuration
TDC Calibration	Pulser data
Time-Walk correction	Laser data
Left-Right Adjustment	Raw BOS data
Energy Loss	Good L/R constants, cooked data
Attenuation Length	Good L/R constants, cooked data
Effective Velocity $(\mathrm{V_{eff}})$	Good time-based tracking, and same as Eloss
Counter-to-counter delays	As Effective Velocity
RF offset	As Effective Velocity

Table 4.3: Time-Of-Flight calibration procedure

The Pedestal and TDC calibration steps require dedicated data and data acquisition, along with the Time-Walk correction procedure. These steps were performed during the previous experimental run and are usually assumed not to change significantly over the course of a year.

The process of calibration of the Time-Of-Flight systems continues from this point by assuming that the TDCs are in good working order. Then raw data is used to examine how the system is performing.

In calculating the Left-Right Adjustment, the TDCs reading out from either end of a scintillator bar are compared and an offset is calculated from a scatter plot of $\ln\left(\mathrm{A_L}/\mathrm{A_R}\right)$, where $\mathrm{A_L}$and $\mathrm{A_R}$ are the respective heights of the ADC pulses measured from the PMTs at each end of the counter.

The edge of this distribution along the x-axis determines two parameters, $\mathrm{P_L}$and $\mathrm{P_R}$ which allows the offset determining the Left-Right adjustment for each bar to be defined.

$$\Delta \mathrm{t} = \left(\mathrm{P_L} + \mathrm{P_R}\right)/\mathrm{V_{eff}} \tag{4.9}$$

Here Δt is the time difference between the event signal reaching either end of the scintillator, which is plotted on the x-axis in Fig 4.17, and $\mathrm{V_{eff}}$ is the effective

velocity of light in the scintillator bar. This method attempts to ensure that the timing of the TDCs is not relied on to calculate the effective velocity and the other calibration parameters, although the times from each TDC T_L and T_R could in principle be used as well.

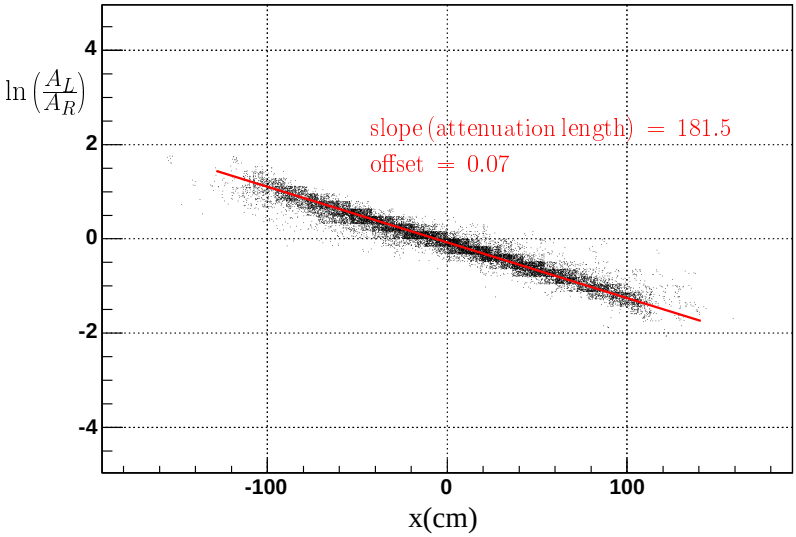

Figure 4.17: *G8a calibration plot of L-R adjustment.*

For each sector in CLAS the Left-Right alignment can be plotted to ensure that the calibration offsets are in agreement with the geometry of each TOF detector region. Fig 4.18 shows all the TOF bars in Sector 1 properly aligned with each other.

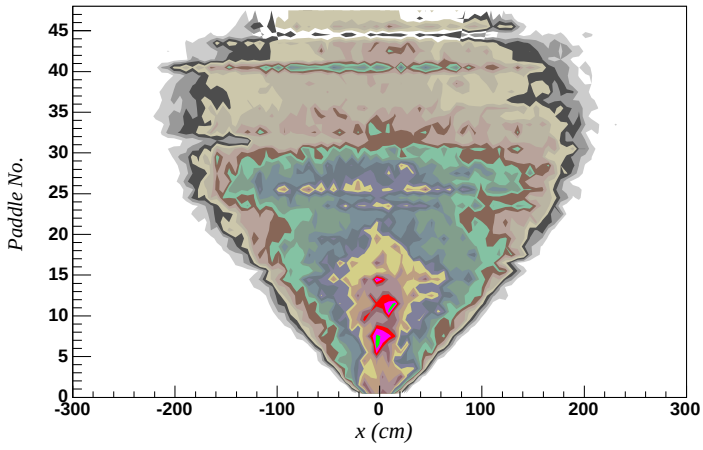

Figure 4.18: *The Left-Right alignment of the Sector 1 TOF system during the G8a run.*

Next, plots of Energy Loss are made to calculate the geometric mean. This means selecting pions from Fig 4.19 and calculating the geometric mean position of the Minimum Ionising Particle pulse height distribution along each scintillator. The pulse height of the ADC output of the left and right PMTs is used to determine the geometric mean of the scintillator. Once each ADC is properly adjusted and the ADC pedestals are taken into account, the pulse height for a MIP passing through the centre of the scintillator should be equivalent to 10 MeV [83].

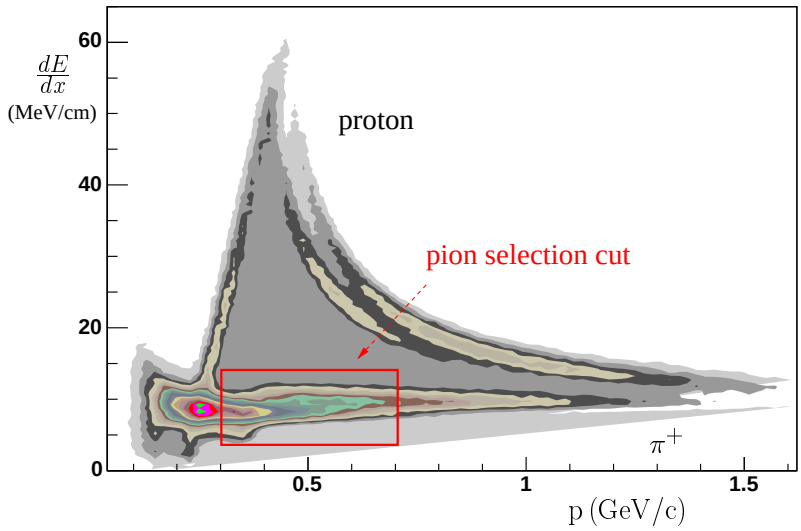

Figure 4.19: *Energy Loss versus momentum for charged particles in the TOF detector system during a G8a calibration run. The graphical cut illustrated is used to select pions for further calibration of the TOF system. The typical cut used to identify pions in the TOF system was to allow 0.3 GeV/c<* **p** *< 0.7 GeV/c, and 4 MeV.*cm^{-1} *< (dE/dx) < 14 MeV.*cm^{-1}.

Calculating the attenuation length follows on from the previous steps. This involves using the geometric mean from the step above and calculating the gradient of a plot of the amount of light arriving at each PMT versus distance along the scintillator.

The penultimate step is to calculate the effective velocity for each TOF bar, $\mathrm{V_{eff}}$. This should range from 1.4×10^8 to 1.9×10^8 ms^{-1} . This is calculated by finding the gradient from a plot of the time difference $\mathrm{T_L} - \mathrm{T_R}$ versus position along the TOF bar, as shown in Fig 4.20.

The last part of the TOF calibrations involves calculating the counter-to-counter delays, and conceptually this is the same type of offset as for the Tagger $\mathrm{C_i s}$. In fact the same type of adjustment is made here, in the sense that each paddle must have an

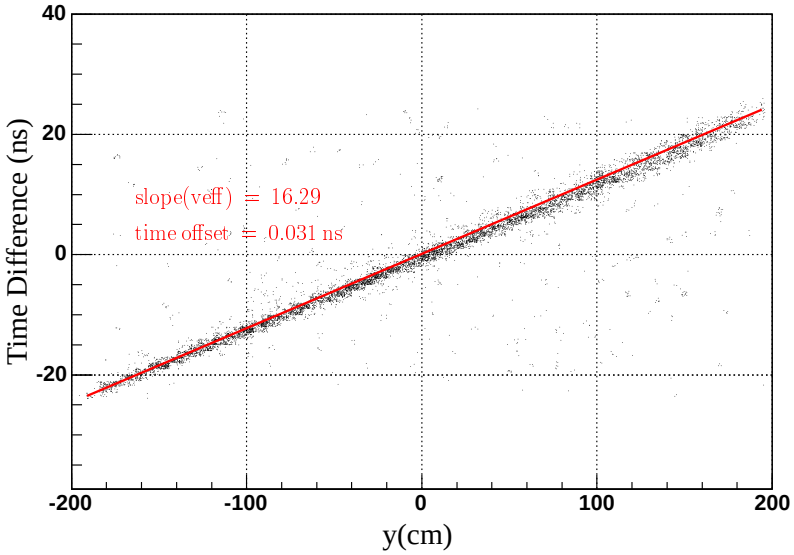

Figure 4.20: *G8a calibration plot of effective velocity. The effective velocity of light in the TOF bar is calculated from a fit to the straight line shown above.*

RF correction to the measured event distribution such that the vertex time for the TOF paddle minus the start counter vertex time equals zero (See eqn 4.8).

A Gaussian fit is applied to the (pion vertex time - tagger time) plot for each of the 288 TOF counters, and an offset is determined from the fit parameters. Fig 4.21 shows a typical calibration plot from the G8a run, and the main Level 1 trigger peak can be seen at an offset of $2\,\mathrm{ns}$.

When each counter has the correct offset applied, the overall Time-Of-Flight signal for physical events should be synchronised such that a plot of the pion vertex time minus the tagger photon time should show clearly a well-defined main peak within one beam bucket. Fig 4.22 shows this main peak centred on zero. This corresponds to real events being detected by the Start Counter, as well as the Photon Tagger and the Time-Of-Flight system.

The next stage, which is not really a part of the Time-Of-Flight calibration, is to adjust the time delay in the software so that the tagger and the Time-Of-Flight system agree on a particle vertex time. This is an overall constant that relates to the time difference between two different detector systems. In effect this means that the final stage of both the Tagger and TOF calibration procedures ensure that the sub-components of the detector yield a consistent time internally. But in order to take into account the dif-

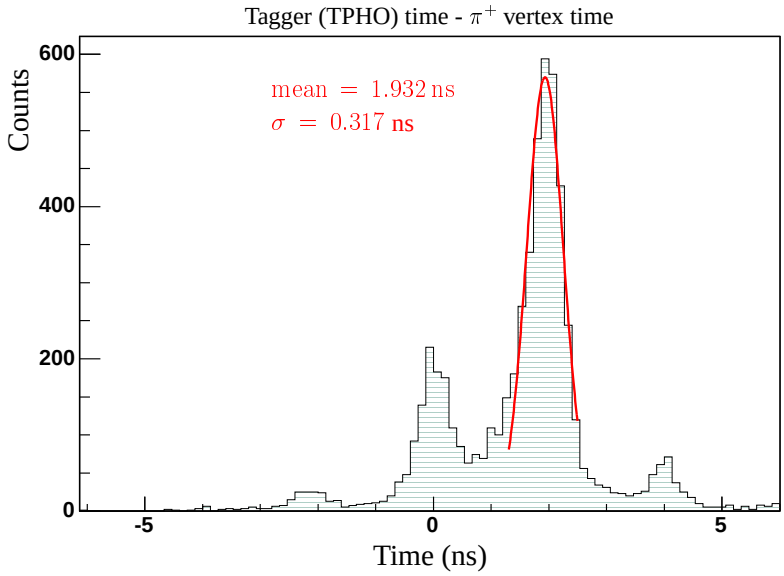

Figure 4.21: *Independent counter pion vertex time minus tagger tpho time.*

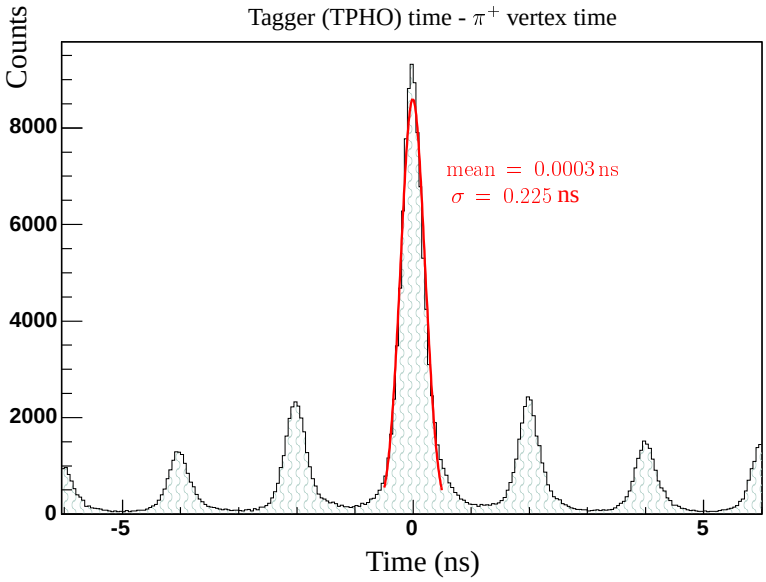

Figure 4.22: *Pion vertex time minus tagger tpho time for the whole TOF system after the calibration has been completed.*

ferent physical positions of the detector systems, as well as substantial cable delays[4], overall constants need to be added generally to every sub-component; for example, to ensure the TOF and the Tagger agree in real time when a physical event occurs in CLAS. In this case the relevant constant is known as **tag2tof**.

4.8 Adjustment of Detector offsets

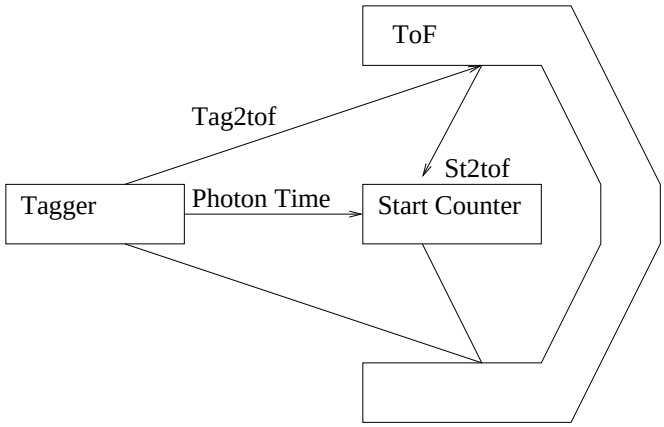

Figure 4.23: *The relationship between the Tagger, Start Counter and Time-Of-Flight. The physical time delay between the detector systems is taken account of by the detector time offsets shown above, which are added or subtracted from the relevant detector time to set the time of a physical event to zero in each system.*

Once each of the three important timing detectors are calibrated internally, adjustment needs to be made to the overall time returned by each detector, so that all the detectors are synchronised when an event occurs in the centre of CLAS. An overview of these offsets and how they relate to each other can be seen in Fig 4.23.

From the point of view of the tagger, an earlier time is recorded in each T-Counter than the time of the interaction at the centre of CLAS, since the electron arrives in the hodoscope at an earlier time than the interaction.

An offset is then required which will create a photon time that is the effective time that a photon would arrive at the target.

This artificial quantity, incorporated into the TAGR “tpho” time, is determined by the specific distance and cable delays for each T-Counter. After treating the tagger

[4]Cable delays are due to the physical time that elapses while an electronic pulse travels down a certain distance of cable. The registered time of an read-out event is likely to be affected by some constant related to this delay.

time in this way, a true synchronisation is achieved and the analysis programs reading a particular event will find the photon time from the Tagger, and the Start Counter will register the same time for the interaction at the target.

A further offset, **st2tof,** takes into account the distance between the Start Counter and the TOF system which then gives agreement between the calculated vertex time from the TOF and the Tagger photon time.

For G8a, this allows simple timing cuts to be used to get rid of accidentals, and the analysis code is thereby reduced in complexity.

Since this process was carried out within the scope of Fig 4.1, the author was involved in continuously updating these constants as each stage of the calibration was performed, to ensure that all the detector systems agreed on the physical event time.

The author was directly responsible for developing a modification of the **st_dt** program, as mentioned earlier in Section 4.4.2, which rebuilt relevant BOS banks to allow the user to view the timing offset between the Start Counter and Time-Of-Flight System. This made modification of the **st2tof** offset much simpler, and also allowed the author to fine-tune the Start Counter Δt constants to ensure that despite low gain in the Start Counter in Sectors 3 and 4 which affected the timing slightly, all six sectors agree on the vertex time between the TOF and the Start Counter. Fig 4.24 shows the agreement in Sector 3 between the Start Counter vertex time and the Time-of-Flight vertex time.

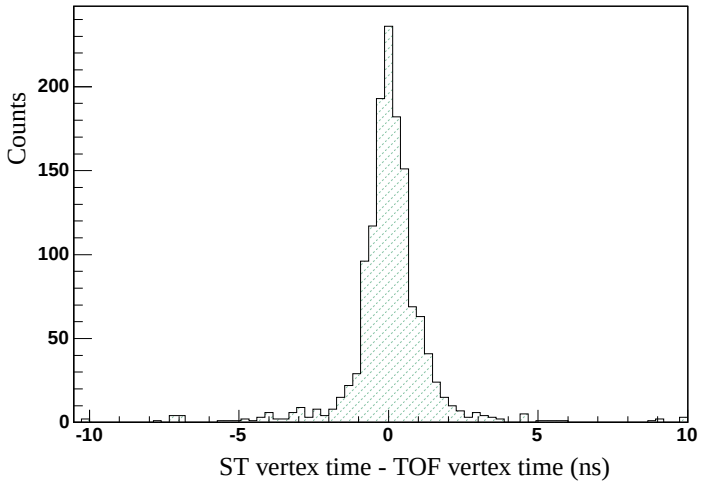

Figure 4.24: *Start Counter Vertex time - TOF vertex time.*

4.9 Drift Chambers

Unlike the other detectors mentioned where it is most important to determine the correct timing, for the Drift Chambers it is necessary to calibrate the TDC output of each sense wire in the Drift Chambers so that reliable position information can be constructed [86]. Accurate position information is vital for creating and fitting tracks in CLAS.

At this stage it is worth mentioning that there are two different types of track reconstruction, Time-Based Tracking (TBT) and Hit-Based Tracking (HBT).

HBT has lower resolution, because it relies on finding a few cells in each superlayer which may correspond to a charged particle passing through the region. If three out of five super-layers register a suitable hit, the track is considered good and the curvature of the track is fitted through each cell that fired.

The resolution of HBT tracking is poor, the resolution of the momentum of a $1\,\mathrm{GeV/c}$ particle being of the order of ~3-5%. However it can be done quickly at a hardware level which allows basic track-matching to become part of the CLAS trigger. Also, since it does not rely on timing information to determine a track, it can be used to provide a first estimate of how well the Drift Chambers are working.

The Time-Based Tracking approach can benefit from the HBT results because random noise that may trigger sense wires in the Drift Chambers can be excluded if it is not detected by the HBT.

Time-Based Tracking takes the TDC signals from the sense wires that fired and tries to reconstruct the drift time of the particle and the distance of closest approach (DOCA).

The quality of the Drift Chamber calibration is determined by the size of the residual, which is defined by the following equation.

$$\mathrm{RESI} = \mathrm{abs}\,(\mathrm{DOCA}) - \mathrm{abs}\,(\mathrm{DIST}) \tag{4.10}$$

Where RESI is the residual, and $DIST$ is the distance from the sense wire to the track as calculated by the drift time (t). The residual needs to be evaluated using a least-squares fit for each wire and and the resulting χ^2 needs to be kept below a predetermined value.

$$\chi^2 = \sum_{\mathrm{i}=1}^{\mathrm{N}} \left(\frac{\overline{\mathrm{DOCA(t)}} - \mathrm{DIST}(\mathrm{t}, \overrightarrow{p}, \overrightarrow{\alpha})}{\mathrm{ERR(t)}} \right)^2 \tag{4.11}$$

Where $\overrightarrow{p_f}$= parameters varied in the fitting procedure, and $\overrightarrow{\alpha}$ represents the angle

parameters applicable to the fit. $\mathrm{ERR(t)}$is the standard deviation of the fit.

When well-calibrated, the TBT approach has momentum resolution of a $1\,\mathrm{GeV/c}$ particle of ~0.5%.

4.10 Electromagnetic Calorimeters

The process of calibrating the Electromagnetic Calorimeter and the Large-Angle Calorimeter [87] depends very much on the quality of the Time-Of-Flight Calibrations. A dependable value for the vertex time of a charged particle needs to be available to calibrate these systems.

In both cases, the Drift Chamber calibrations need to be of sufficient quality to determine the identity of a charged particle, so that a reasonably pure pion signal can be extracted from the data. This is then used to check the timing of each of the individual u-v-w type cells. This generates a large number of individual constants to give the correct reconstructed signal return time of each layer and sector. Once the components of the detector agree in time for a pion signal, the vertex time of the detector should agree with that of the Time-Of-Flight system for a charged particle traveling through CLAS. Fig 4.25 shows a comparison between the resulting vertex times from both calorimeters compared with the TOF pion vertex time.

The procedure is practically identical for the LAC except that there are different numbers of constants relating to the different number of cells.

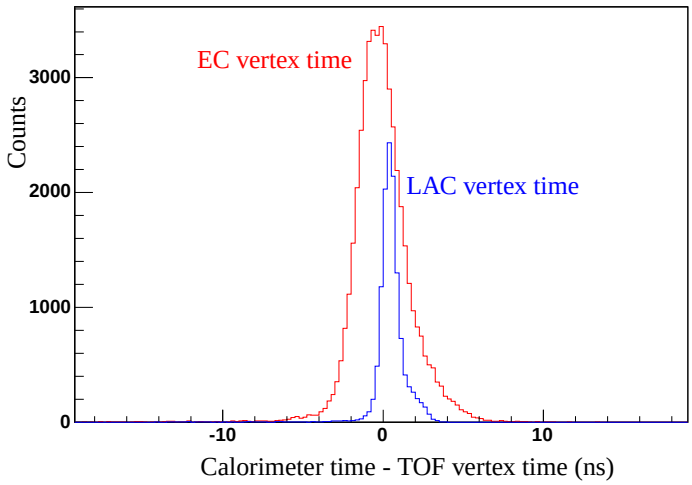

Figure 4.25: *The vertex time for the Electromagnetic Calorimeter (red) and Large Angle Calorimeter (blue) compared with the TOF system.*

4.11 Active Collimator

Initially, one must make sure that the four PMTs which constitute the active part of the Collimator are operating at the correct voltage, and this was checked by using a light pulser and finding the plateau for the gain of each PMT by adjusting the supply voltage. During the experiment however, because each PMT will have different characteristics it is necessary to compare the signals from each of the four PMTs with the signals received from the BPMs.

In effect the Collimator is calibrated on its centre position by checking the output from each PMT when the BPMs report the beam passing through with minimum deviation from the centre of the beamline. Fig 4.26 shows the relationship between the output of the Collimator PMTs and the BPMs, and Fig 4.27 shows the calibration plots [88] used during G8a which measured the six possible asymmetries between the output of the PMTs and calibrated their slopes using the BPM beam position measurement.

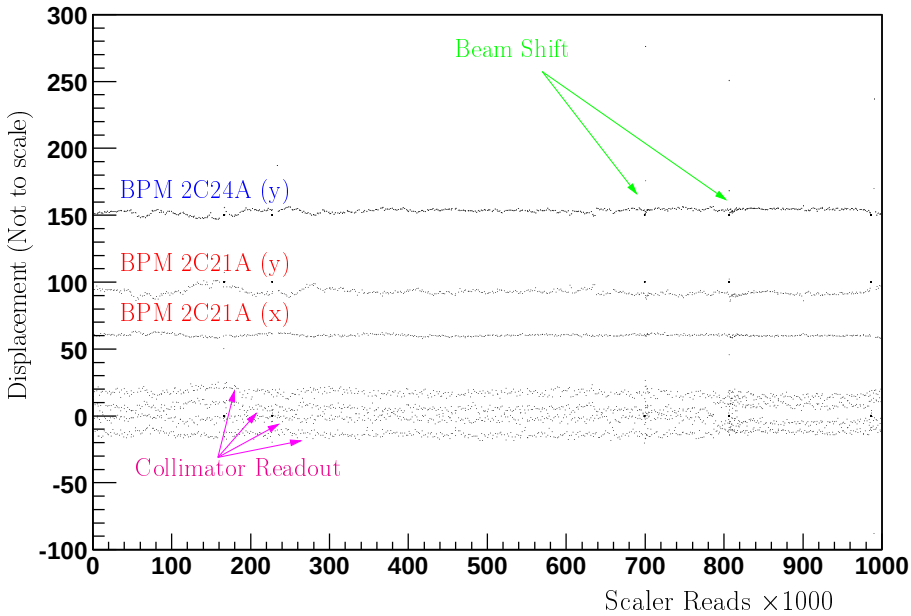

Figure 4.26: *Typical output of the PMTs of the Active Collimator compared with the output from the BPMs.The BPM and Collimator information is read out every 2 seconds, and the number of these read-out events is indicated on the x-axis. A shift in beam position is also seen by all three instruments.*

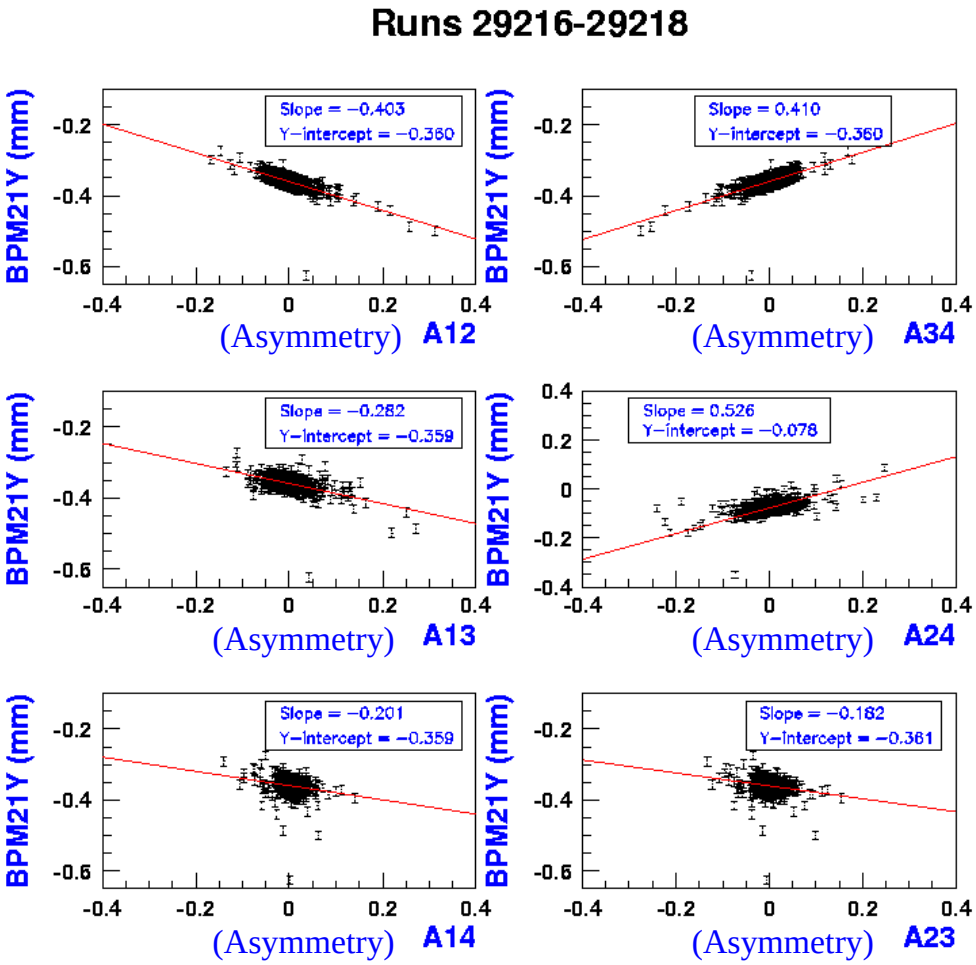

Figure 4.27: *The calibration of the various asymmetries obtainable by comparing the six different combinations of the PMT outputs. These slopes are calibrated using the BPM monitors and result in a maximum resolution of the photon beam position of* $\sim 20\mu$*m. On the y-axis of each plot is shown the BPM position measurement, and the degree of correlation between the BPM position and the measured asymmetry between the different combinations of PMT output shown on the x-axis is used here to determine the position resolution of the collimator.*

Chapter 5

Particle Identification

5.1 Introduction

To perform the intended analysis for this thesis, first one must be able to identify the reaction in question, and in Nuclear Physics this often means detecting decay particles directly. The $\overrightarrow{\gamma} + \mathrm{p} \rightarrow \mathrm{K}^+ + \Lambda^0$ reaction obeys this principle, since a short-lived N^* resonance is involved in the reaction which decays via the strong force. The Λ^0 and $\mathrm{K}^+$are produced from this strong interaction and in the case of the K^+, CLAS can detect this particle directly. The Kaon produces a positive charged track in CLAS that is very similar to that of a pion but can be resolved from a π^+at energies of up to 2 GeV [89]. However, the Λ^0 decays weakly before interacting inside CLAS and therefore the decay particles are detected. Normally the Λ^0 decays into a proton and a π^-, which is an easily identifiable signal in CLAS, so the overall reaction of interest is defined by three charged tracks in CLAS which should be exclusive[1].

General problems arising when identifying particles in CLAS obviously centre upon the issue of timing, since in order to determine particle quantities in a photon experiment it is necessary to have the time and energy of the photon which caused the event.

This information is then compared with valid trigger times given by the Start Counter, then matched with suitable hits in the Drift chambers and TOF.

The Drift Chambers give track curvature information, which gives momentum and charge when combined with Time-Of-Flight information.

As discussed below, defining a good quality particle or event in CLAS requires a number of correlations between the relevant BOS banks to be established.

[1]Exclusive is taken to mean that no other energy should be deposited in the CLAS detector systems when these three tracks are seen.

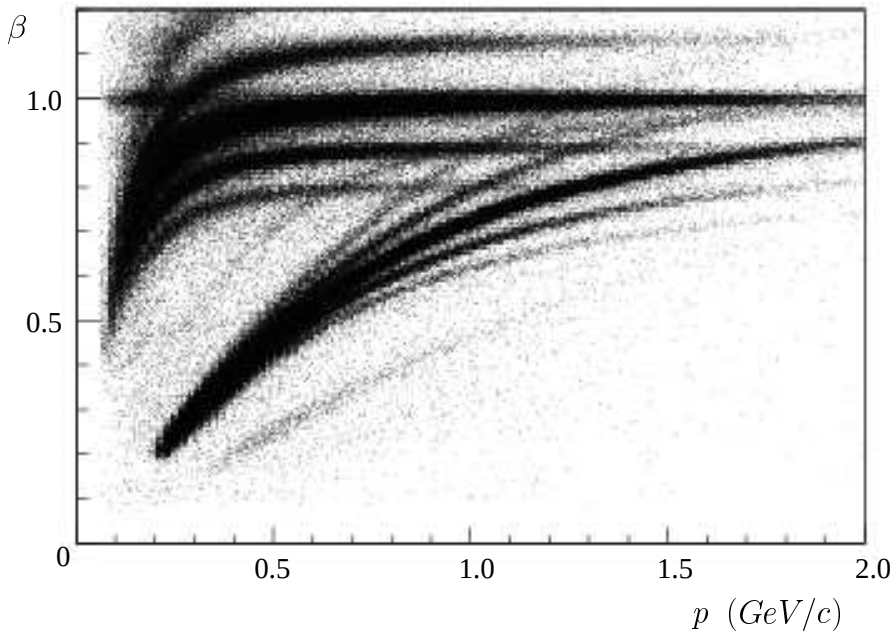

Figure 5.1: *Plot of β versus momentum without any timing restrictions in place.*

The data can look very different depending on whether or not one demands these correlations to be present.

Plotting the Time-Of-Flight β value[2] against momentum as seen in Fig 5.1 is a useful way of seeing how well the detector resolves different particles, and it can also be useful to see if the criteria used for determining good events works correctly without throwing away data unnecessarily. Here the criteria are very relaxed, simply showing all particles that are detected in CLAS for a given run. It is very difficult to distinguish particles in Fig 5.1, since for each band of particles there are at least 2 sets of particles that are definitely associated with the wrong beam bucket on either side of the regions where particles would be considered well-identified. In this case the problem is unresolvable by adjusting the requirements of timing correlations in the data, since the Photon Tagger had a large real event peak spanning 10 nanoseconds or 5 beam buckets.

The main limiting factor in identifying particles, assuming the detectors are all well-calibrated, is the intrinsic resolution of the detectors. Therefore the individual resolution of each TDC and the strength and curvature of the toroidal magnetic field limit the maximum resolution expected.

Another important point is that the stronger the magnetic field, the more vital that

[2] $\beta = \frac{v}{c}$, where v is the measured speed of the particle and c is the speed of light.

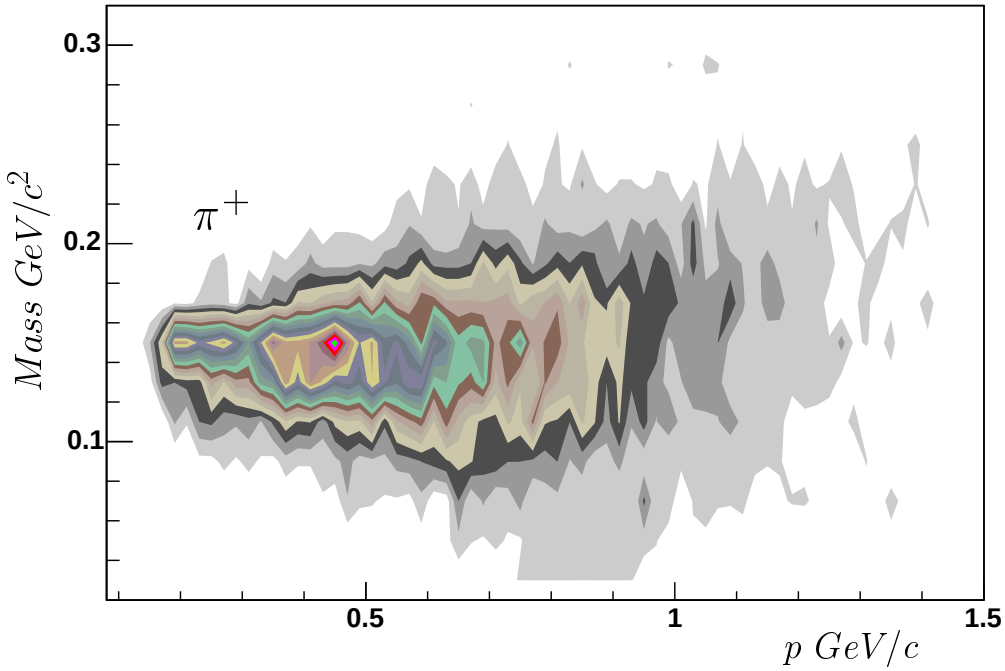

Figure 5.2: *Plot of Mass versus Momentum.*

precise knowledge of the position and magnitude of this field is obtained for particle reconstruction, since any errors here propagate directly to the final estimation of the particle position and momentum.

Fig 5.2 shows how, when particles have higher momentum, their resolution in CLAS worsens. This effect is due to the fixed uncertainty in time conversion from the TOF TDCs, the unknown but fairly small effect of imprecise knowledge of the geometry of CLAS (See Section 5.5.2), and the shortening time-of-flight with increasing particle momentum. From this, the roughly fixed error in timing contributes an ever larger uncertainty to the knowledge of particle momentum as the momentum increases. Hence every particle has an intrinsic uncertainty in its reconstructed mass, coming from these limitations and uncertainties in the system.

5.1.1 Particle quantities

In identifying a particle it is important to establish certain quantities to allow physics analysis of reactions in CLAS. The useful quantities include $\beta(=\frac{\mathrm{v}}{\mathrm{c}})$, which is calculated from the time-of flight and distance from the reaction vertex to the TOF paddle

where the particle exits CLAS.

$$\beta = \frac{1}{c}\left(\frac{D_{TOF} - D_{ST}}{t_{TOF} - t_{ST}}\right) \tag{5.1}$$

Where c is the speed of light, D_{TOF} is the distance to the TOF scintillator from the center of CLAS, D_{ST} is the distance to the Start Counter from the center of CLAS, t_{TOF} is the event time in the TOF system and t_{ST} is the trigger time as determined by the Start Counter.

The charge of a particle is determined from the curvature of the track in the Drift Chambers. Since the Toroidal magnetic field has a controllable polarity, experiments can be configured to bend positively-charged particles toward or away from the beam-line, and for G8a, the polarity was set to bend positively charged particles outward. The quantity of charge can then be determined from the sign of a polynomial fit to the particle track through the Drift Chambers.

The momentum of the particle is dependent on the value of β but the trajectory of the particle can be determined from direction cosines (p_x, p_y, p_z), which give the angle of the track with respect to the $x - y - z$ co-ordinate system in CLAS. The momentum is then reconstructed using the β-value established from eqn 5.1.

$$p = \sqrt{(p_x^2 + p_y^2 + p_z^2)} \tag{5.2}$$

Upon determining the momentum of the particle, the mass can be calculated from the total momentum and the value of β.

$$m = \frac{p}{\gamma\beta c} \tag{5.3}$$

Where γ is the relativistic quantity

$$\gamma = \frac{1}{\sqrt{(1 - \frac{v^2}{c^2})}} \tag{5.4}$$

5.2 PART Identification Scheme

One possible scheme of using detector information to reconstruct events in CLAS is the PART method, so-called because it creates a BOS bank called PART in the cooked data. This PART bank contains structures which store relevant physics properties of identified particles, such as energy, charge and momentum components. The tracking

in CLAS gives the latter two components of the reconstruction, but timing information from the Tagger and Time-Of-Flight is needed to calculate an accurate β-value, which means that the PART method must consult the TAGR bank to find a photon which matches the trigger time recorded by the Start Counter and the vertex time recorded by the Time-Of-Flight.

In creating a particle identification scheme based on the PART bank, a typical software routine sorts through arrays of data, assuming that events are correlated when they occur within a timing restriction, as in equation 5.5.

$$\left|\mathrm{T_{TPHO}} - (\mathrm{T_{ST_{V-TIME}}} + \mathrm{T_{PROP}})\right| \leq 1\mathrm{ns} \tag{5.5}$$

Where $\mathrm{T_{TPHO}}$ is the Tagger TPHO time, $\mathrm{T_{ST_{V-TIME}}}$ is the Start Counter vertex time for the same event, and $\mathrm{T_{PROP}}$ is the propagation time calculated from the difference between the measured vertex position and the center of the target. Given that the Tagger is calibrated so that each element agrees on a given trigger time from the Start Counter, and the fact that the real triggers will occur at a set time from the Common Start signal which starts all the TDCs on the process of measuring event time, the Tagger should always provide the same time for a sensible trigger in CLAS. The PART method makes a cut around this particular TPHO time for all events, allowing for a certain statistical width $(\sim 1\mathrm{ns})$ due to the TDC resolution and the fact that the T-Counters have Left and Right TDCs, either of which can cause the Tagger Master OR trigger (see Section 3.7). This trigger effect gives a certain width to the T-Counter time-distribution due to transverse light dispersion along the scintillator. When this kind of condition has been satisfied, a typical identification scheme classes the event as having a reasonable time with respect to all the relevant detectors.

The actual creation of the PART bank does not deal with this aspect of particle identification directly, in fact all the PART bank really contains is a basic sorting of the data into groups based on mass reconstructed from the event start time and the Time-of-Flight. This is not necessarily the best way to distinguish a pion from a proton however, and the obvious limitations of using a straightforward mass cut are that there is no means of being certain that what falls into the mass cut of a pion is not in fact a heavier more energetic particle with the same Time-of-Flight. However, if a software routine to compare the event time stored in the PART bank with the Photon Tagger TPHO time is used, the PART bank becomes the basis of a reasonable method of particle identification.

If the masses of all the particles deemed to have a reasonable time are plotted, certain peaks are observed which correspond with the masses of the detectable particles.

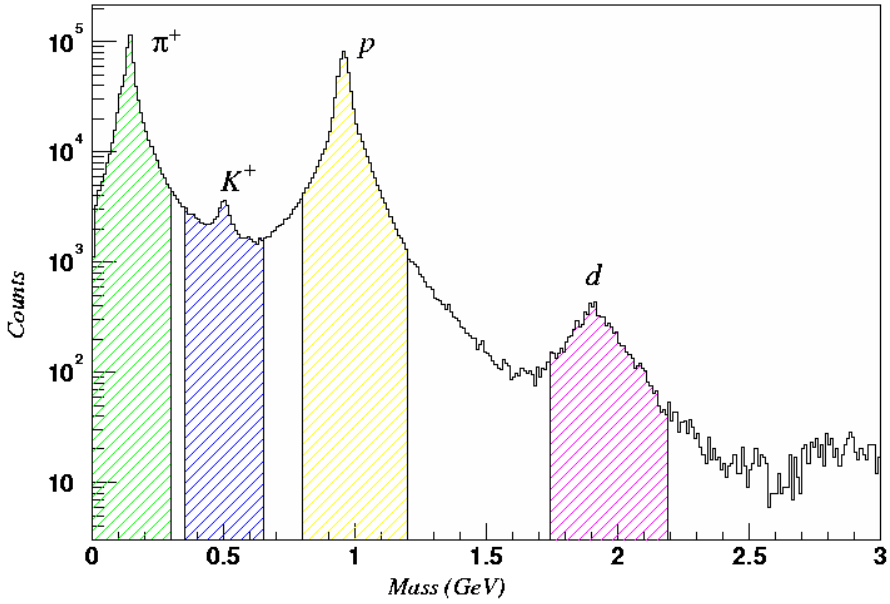

Figure 5.3: *The missing mass particle classification used in the PART bank.*

For instance, in Fig 5.3, a clear peak at 140 MeV marks the π^+, and peaks at 490 MeV and 940 MeV identify the presence of kaons and protons respectively. From this stage the identification is made on the basis of a mass range which is assigned to that particle. For instance a π^+ is identified if a particle has mass between 0 and 300 MeV.

The amount of background under each of these peaks, which should not overlap at energies of up to 2 GeV, depends very much on the timing cut which is used to establish the β-value for each particle. Although this effect is also dependent on the count-rate in the Tagger, it is the case that for a wider timing cut more random coincidences are included in the data which can match with tracks in CLAS that may have come from a cosmic ray or a secondary reaction and therefore should not be regarded as useful particles to perform analysis on. So, successful implementation of particle identification based on the PART bank relies on cutting as tightly as possible on the range of allowed photon times from the tagger to ensure low background in the mass plot.

5.3 GPID Identification Scheme

The PART method is highly successful in the situation where the tagger count-rate is low and the random background is kept to a minimum. However there are situations where the background that is included in the mass cut for identifying a particle can be very large. Specifically for G8a, the tagger did not have a well-defined normal trigger time due to hardware problems, and this compromised the main strength of the PART method.

The alternative method [90] follows a different approach. Named GPID from the concept γPID primarily aimed at photon experiments in CLAS. How this scheme differs from particle identification based on PART lies mostly in the amount of significance which is attached to finding the photon time, shown in Fig 5.4, which identifies the correct amount of energy causing the reaction in CLAS. Where a method based on the PART bank places prime importance on finding the tpho time for an interaction and substitutes tpho for $\mathrm{t_{ST}}$ in equation 5.1, GPID uses eqn 5.1 in its original form and makes sure that the reaction identified in CLAS is sensible before checking the tpho times in the TAGR bank to establish the incident energy of the reaction.

GPID is also more sophisticated in its approach to calculating the β quantity for each particle. By treating each particle track as being of good quality, GPID assumes that the β value approaches an accurate value, then tests the identity of the track by substituting the accepted mass of each particle that the scheme tries to identify. In doing this, GPID calculates what β should be for the case of a π^+, $\mathrm{K}^+$and so on, until the closest match for the measured β of the track is found. Relying on the assumption that the tracking is always of good quality in CLAS, GPID then changes the β value of the track and stores this as the measured β. In this way the particle mass and momentum can be established solely on the basis of the tracks in CLAS, and when combined with the photon time measured from the Tagger, real physical events are more easily identified.

The GPID method dramatically cleans plots of β vs. p as seen in Fig 5.5, since the β value is directly modified. Using a β versus momentum plot then allows for much increased resolution in identifying kaons right up to the energies where they become indistinguishable from pions.

Fig 5.6 shows the effect of this approach on the measured Time-of-Flight mass for charged particles, compared with the original TOF mass calculated from the entries in the PART bank. Here it can be seen than the number of kaons is significantly reduced. However Fig 5.6 also shows that the extra particles thrown away were probably mis-

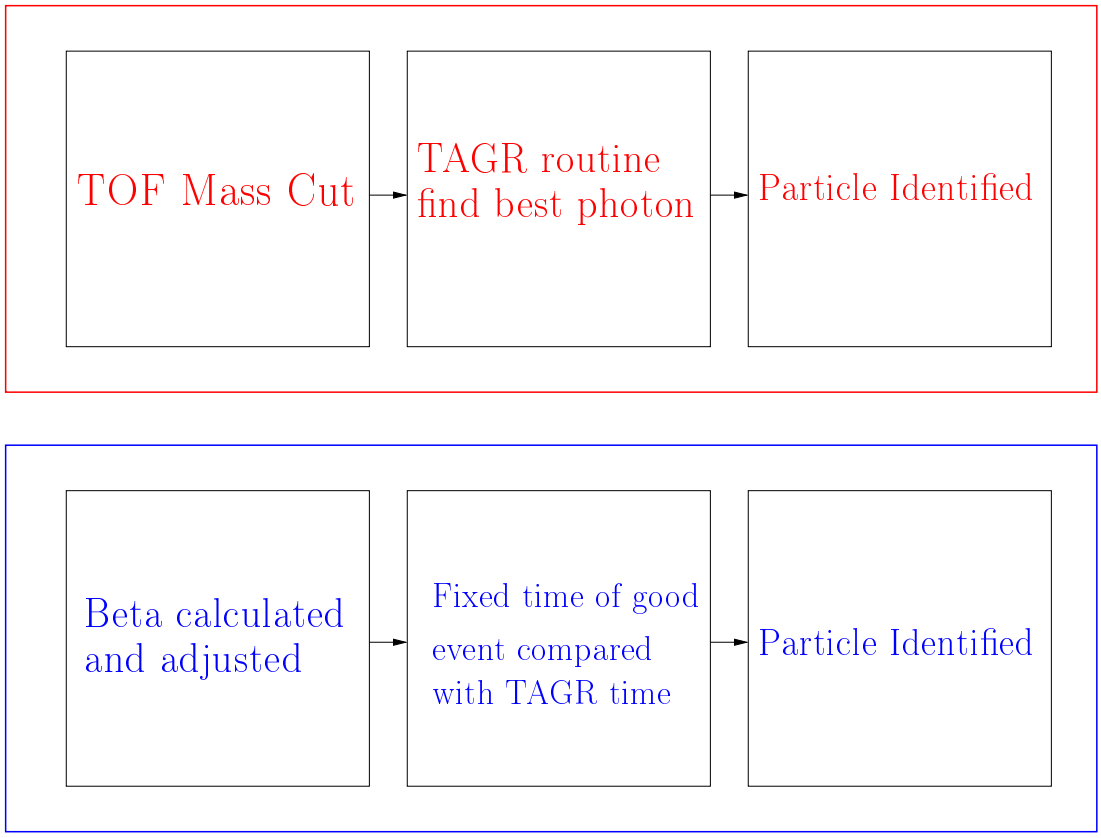

Figure 5.4: *The difference in process when identifying particles using the PART bank(red) or the GPID method(blue).*

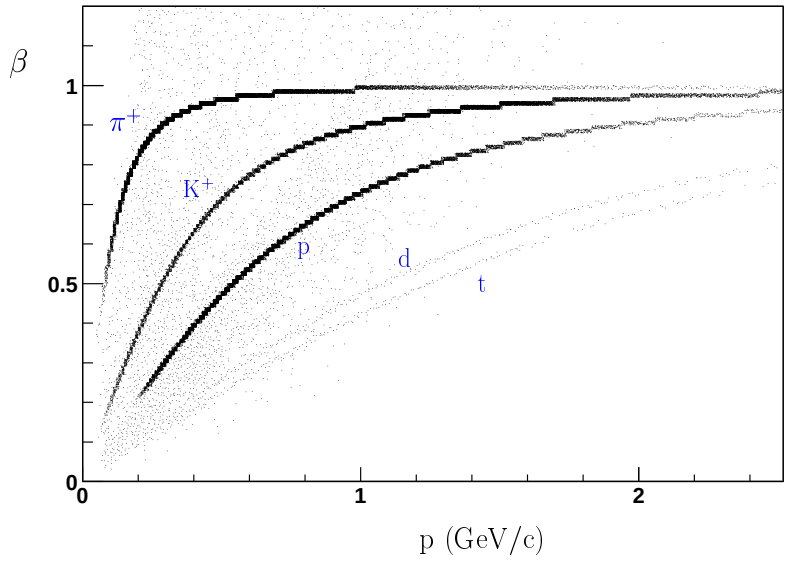

Figure 5.5: β *vs. momentum GPID plot. The plot shows a clear band defining each particle, including protons, pions, kaons, deuterons and tritons. The two latter particles are definitely not visible in Fig 5.1. The background seen between the clear bands will be discussed in Section. 5.6.*

identified pions. This contamination of the PART bank definition is possible because the timing of the event is crucial, and if it is not possible to decide a particle's mass based on a well-defined event time from the Tagger, then it is entirely feasible that a pion may be mis-identified as a kaon because the event time is not distinguishable in the Tagger. In this situation the Tagger may have multiple times recorded for photons possibly attributable to the physical event, and if the Tagger time is not stable and reliable it is not possible to untangle the timing information required.

5.4 Identifying $\overrightarrow{\gamma} + \mathrm{p} \rightarrow \mathrm{K}^+ + \Lambda^0$

For the purpose of identifying this reaction, three charged tracks should be detected at the same vertex time in CLAS, with no other tracks present. Furthermore, there should be only one photon which has a matching time to this vertex time.

Even though CLAS can detect the K^+ directly, it is still possible to mistakenly identify a π^+ as a K^+ due to the fact that at high momentum their β-values become practically indistinguishable for a given set of kinematics in CLAS.

This would be a major problem were it not for the fact that the Λ^0 peak is easily

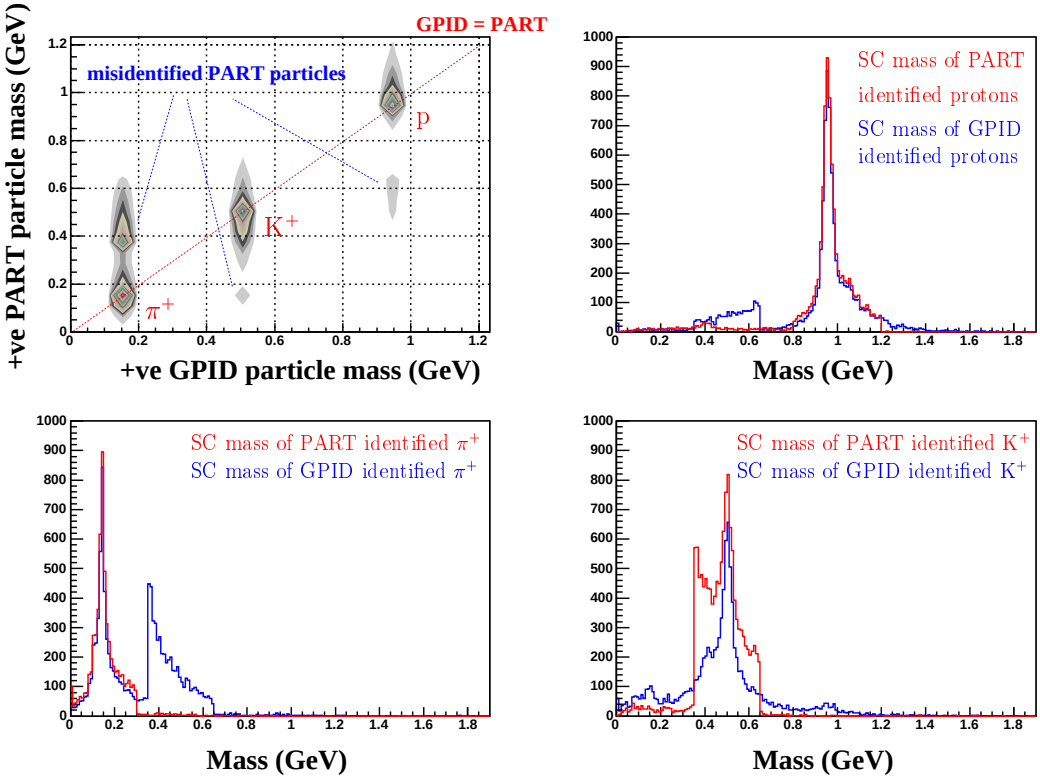

Figure 5.6: *A comparison of the GPID particle identification method versus PART. Top left shows a comparison of the mass deduced from the Time-of-Flight for each method. The other three plots show the relative numbers of pions, kaons and protons, and their Time-of-Flight (SC) mass for each particle ID.*

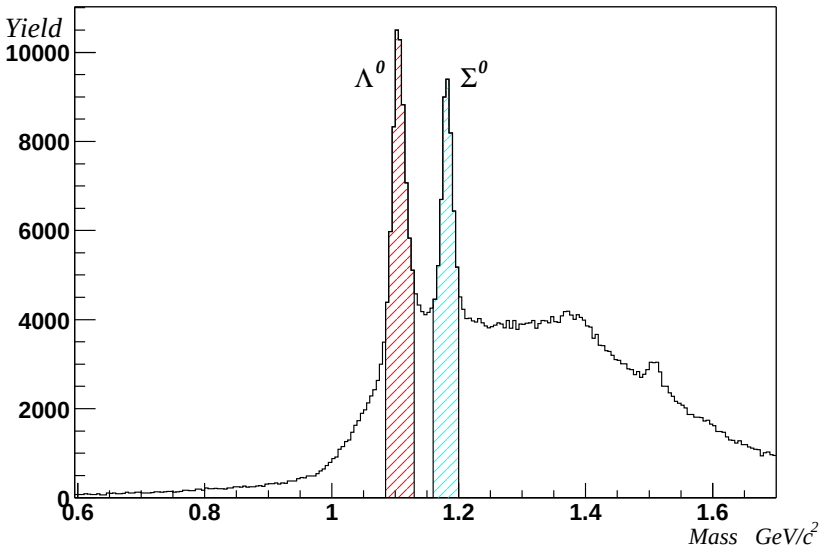

Figure 5.7: *Plot of missing mass from ($\vec{\gamma}$ + p $\rightarrow$ K^+ + X).*

identifiable, and since strangeness must be conserved one can make the assumption that if two of the three charged tracks correspond to a Λ^0 then to a reasonable degree of certainty, the other track must belong to a K^+.

In order to measure how well CLAS identifies the K^+, the opposite logic can apply, in that if the Λ^0 peak has a large background, then this is likely to come from mis-identified pions.

Plotting the missing mass quantity X from

$$\overrightarrow{\gamma} + \mathrm{p} \rightarrow \mathrm{K}^+ + \mathrm{X} \tag{5.6}$$

gives a rough idea of how well the K^+ identification works.

To a large extent, how much background appears in Fig 5.7 underneath the Λ^0 peak depends on how wide the timing gate is made in comparing the photon time from the tagger and the vertex time from the start counter and Time-Of-Flight system. Varying this gate has a noticeable effect on the signal to background ratio. However, the problems in calibrating the photon tagger, which are discussed in Chapter 7, mean that making a very narrow timing gate on the tagger can bias the data set against certain regions of the tagger energy spectrum, especially the region where the polarisation is highest (See Fig 4.10).

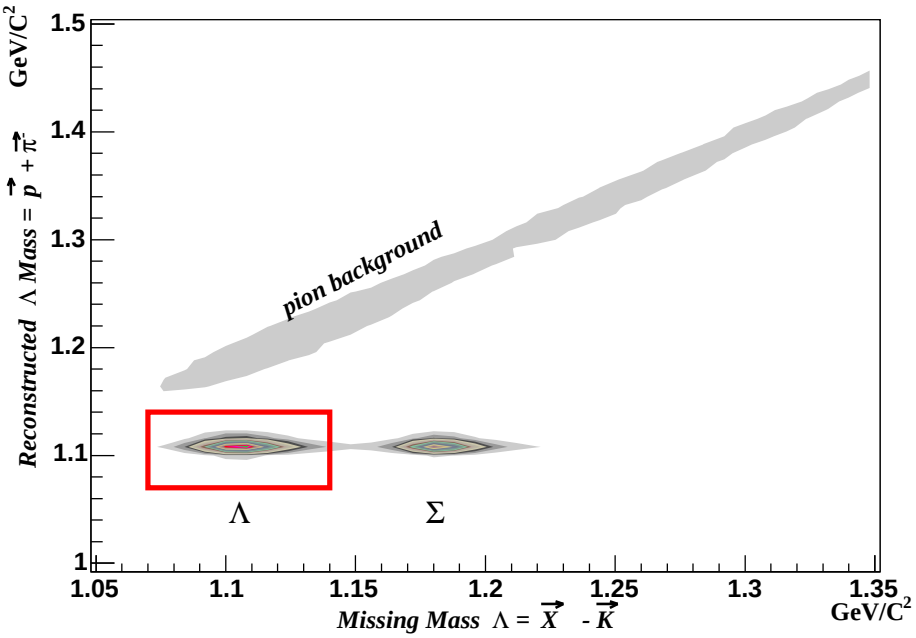

Figure 5.8: *Plot of kinematics of the $K\Lambda^0$ reaction. The box shows the cut made on the kinematics to reduce contamination from the Σ^0.*

In order to resolve this problem, a different approach was used to reduce the background of misidentified kaons. Making a plot of the same quantity X as was shown in Fig 5.7, the quantity of reconstructed Λ^0 particles was plotted on the orthogonal axis as a sum of the detected π^- and proton. This two-dimensional plot seen in Fig 5.8 shows agreement on the position of the Λ^0 peak, but mis-identified pions show as a diagonal band as X increases. This is because the reaction is no longer exclusive if a π^+ is identified as a K^+, and therefore the re-constructed mass of the Λ^0 must increase to account for the extra X quantity that has been detected. In this way, ruling out an unlikely mass for the Λ^0 dramatically decreases the pion background in the reaction signal shown in Fig 5.9. This plot also serves to cut out the contribution from the Σ^0 particle which decays via the same channel as the Λ^0. The Σ^0 decays into a $\Lambda^0 + \pi^+$ with a branching ratio of 99.9%. This means that the diagonal contribution shown in Fig 5.8 is a direct result of the Σ^0 decay.

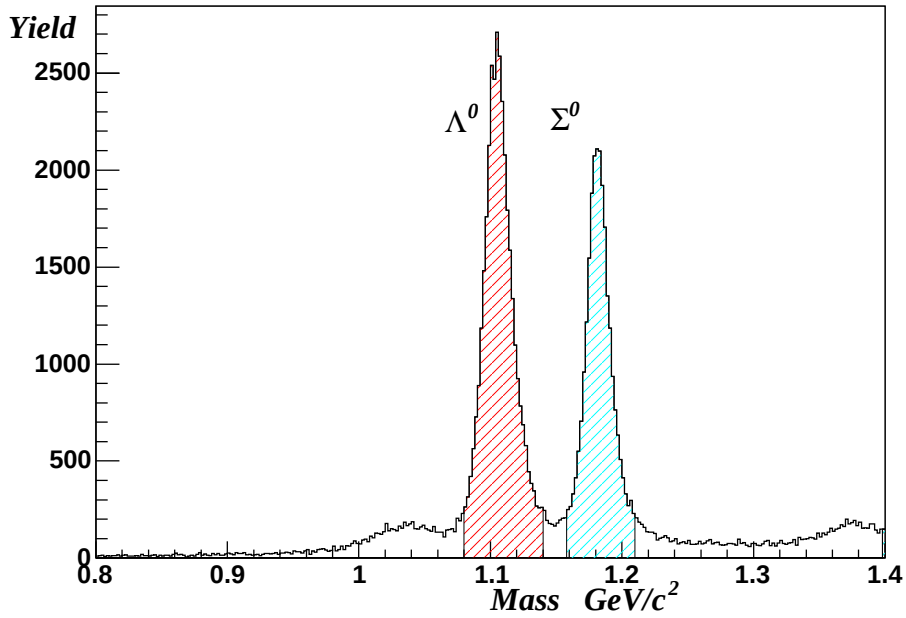

Figure 5.9: *Plot of resulting Λ^0 signal after the horizontal cut is made to eliminate the pion background from Σ^0 decay shown in Fig 5.8.*

5.5 Momentum and Energy Corrections

There are two major effects to take account of when reconstructing the energy and momentum of particles in CLAS. Firstly, particles may hit obstacles in CLAS which could cause them to lose energy, and travelling through the target material, all particles produced will lose a typical amount of energy that can be corrected for. Secondly, if the precise position of the detector components of CLAS are not known, there may be a systematic shift in the the reconstructed momentum of a charged particle track, and this is most likely to come from incomplete knowledge of the geometry and position of the Drift Chambers and the Time-Of-Flight system.

5.5.1 Energy Loss

To address the first problem a software package that takes account of the energy losses of charged particles in the target cell, start counter, supporting structures and beamline was used [91]. This software adjusts the energy and therefore momentum of charged particles depending on where the interaction vertex is reconstructed to intersect with the target cell or beamline. Fig 5.10 shows how this software package affected the

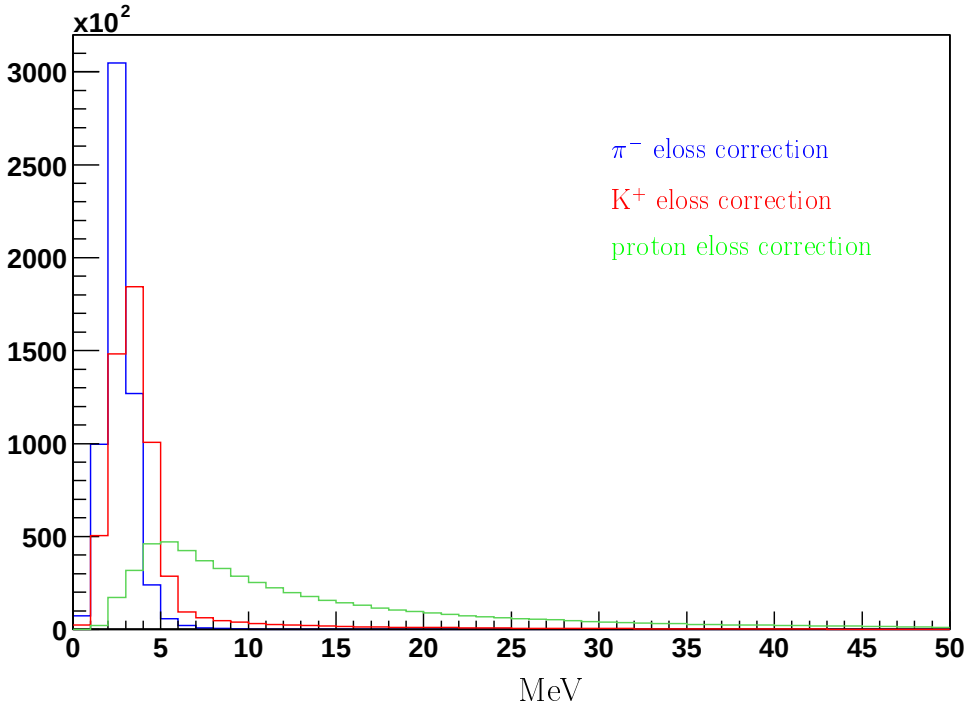

Figure 5.10: *Energy difference of particles after corrections are applied using the eloss software routine [91].*

particles identified using the GPID identification scheme.

5.5.2 Momentum Corrections

When GPID or PART have successfully identified particles, the physics properties can then be examined. However, CLAS does not usually measure the properties of particles in exact agreement with accepted values. There are a number of possible explanations for this: the exact form and strength of the magnetic field is not known precisely in the forward angles of CLAS, each detector component has limits to its resolution, and the actual positions of the various components inside CLAS may not agree exactly with the assumptions made by the reconstruction software about these dimensions.

This problem manifests itself when looking at exclusive events, and when the missing energy and momentum of an exclusive reaction is examined, the leftover quantities that are expected to be zero actually turn out to be non-zero. In Fig 5.11 this non-zero left-over from the exclusive $K^+\Lambda^0$ reaction is clearly visible, and it has a measurable effect on the reconstructed lambda mass, which is an equivalent $20\,\mathrm{MeV/c^2}$ light, as seen in Fig 5.12.

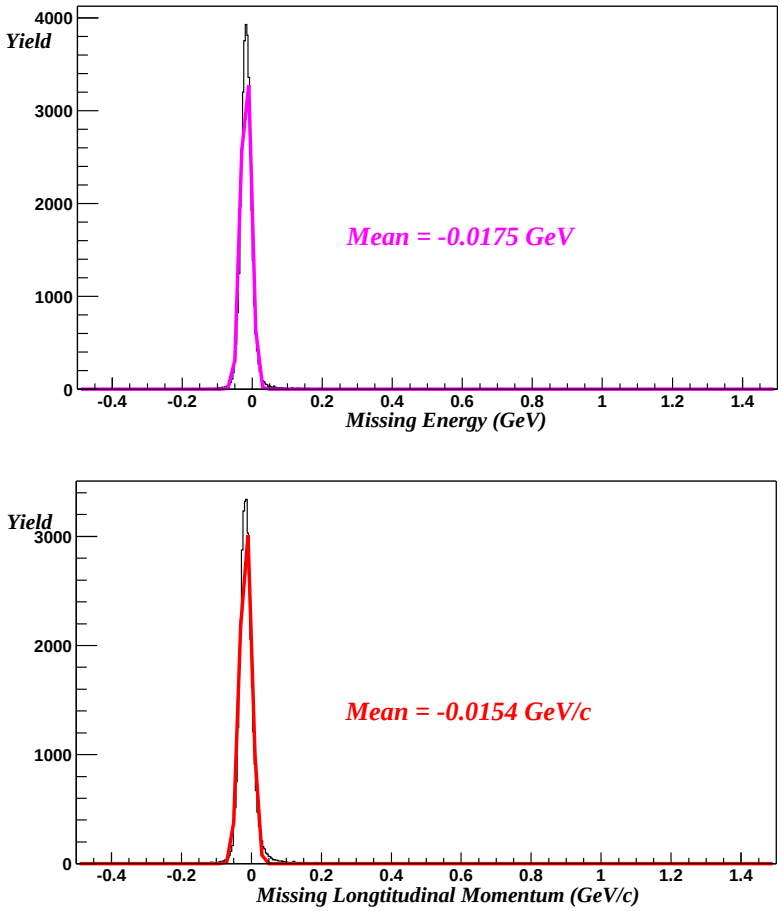

Figure 5.11: *Missing Longtitudinal momentum and Energy of the $K^+\Lambda^0$ reaction. The peaks that correspond to the remaining quantities in CLAS are shown here to be $\sim$ 20 MeV below zero. This effectively means that CLAS will measure a slightly lighter mass for the Λ^0.*

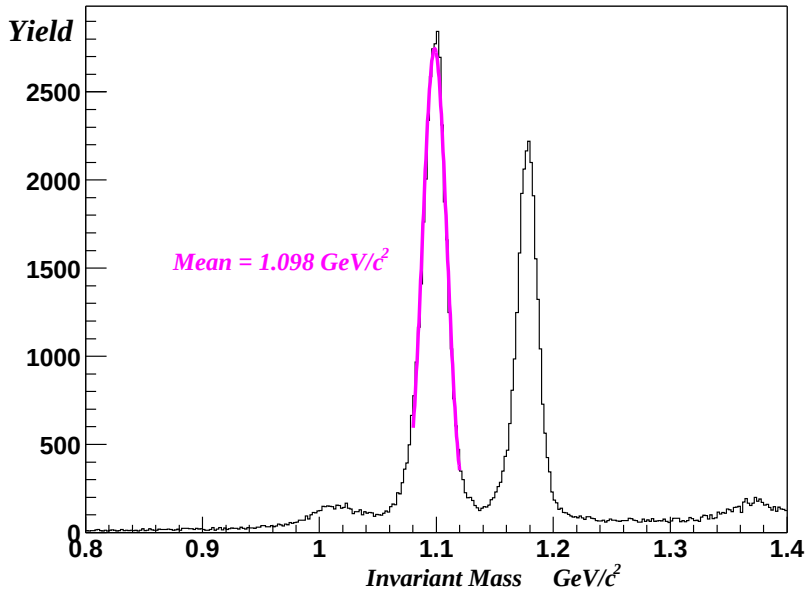

Figure 5.12: *The resulting reconstructed mass of the* Λ^0. *The gaussian fit to the* Λ^0 *peak shows a significant deviation from the accepted value from the Particle Data Group [24] of 1.115 GeV/*c^2.

In any case, on the assumption that variations in the measured energy and momentum of particles detected in CLAS will have a functional dependence on p, $\cos\theta$, and ϕ, it is possible to correct these measurements to agree more closely with accepted values. It is first necessary to have a measurement of a particle or resonance that has a well-known mass and narrow decay width, and this then allows for fits to be made that parameterise this function in terms of p, $\cos\theta$, and ϕ. For G8a, a similar procedure was used to that developed by G6c [92], which involved fitting the momentum and angular dependence of the $\omega\,(780)$, which is reconstructed in CLAS from the $\overrightarrow{\gamma} + \mathrm{p} \rightarrow \pi^+ + \pi^- + \pi^0$ channel.

The functional dependence on p, $\cos\,\theta$,and ϕ can be expressed as follows:

$$
\begin{aligned}
\mathrm{dp} &= \mathrm{F0[i]} + \mathrm{F1[i]}\cos\theta + \mathrm{F2[i]p} + \mathrm{F3[i]}\cos^2\theta + \mathrm{F4[i]p}^2 + \mathrm{F5[i]p}\cos\theta \\
\Delta\mathrm{p} &= \mathrm{p} - \mathrm{dp} \\
\mathrm{p}_{\mathrm{x}}^{\mathrm{new}} &= \Delta\mathrm{p}\,\sin\theta\cos\phi \\
\mathrm{p}_{\mathrm{y}}^{\mathrm{new}} &= \Delta\mathrm{p}\,\sin\theta\sin\phi \\
\mathrm{p}_{\mathrm{z}}^{\mathrm{new}} &= \Delta\mathrm{p}\,\cos\theta
\end{aligned}
$$

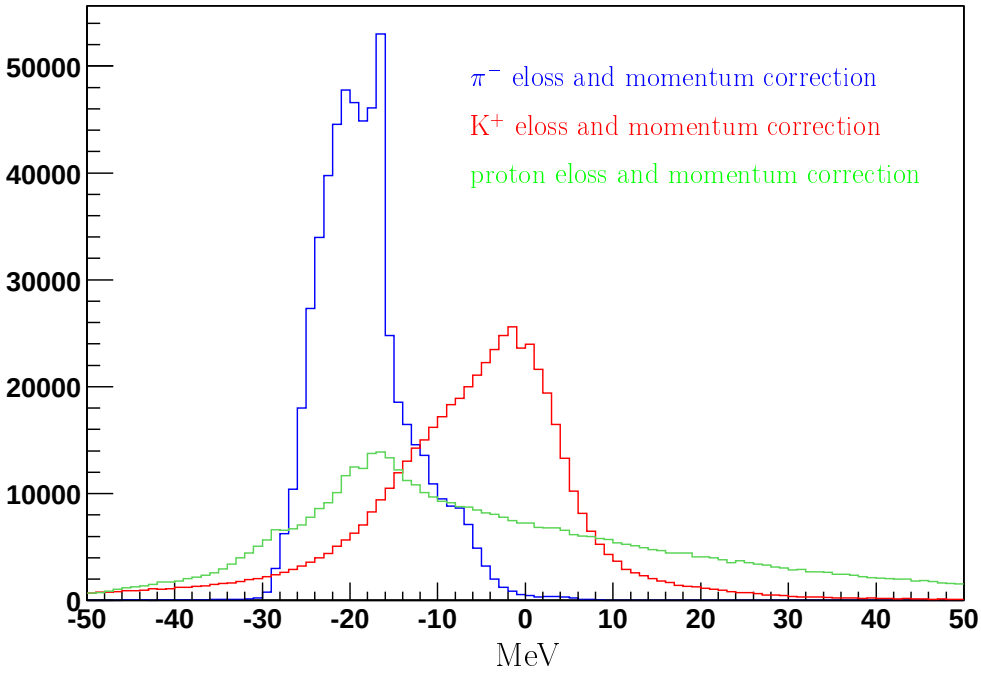

Figure 5.13: *The three particles detected from the $K\Lambda$ reaction after Energy Loss and Momentum Correction procedures have been applied.*

$$E^{new} = \sqrt{\left(M^2 + (p_x^{new})^2 + (p_y^{new})^2 + (p_z^{new})^2\right)} \tag{5.7}$$

Here θ refers to the polar angle of the particle in the lab frame, ϕ is the azimuthal angle, p is the 3-momentum of the particle in the lab frame, and $F0$ to $F6$ are the parameters of the polynomial fitting procedure on the i-th sector. Fig 5.13 shows the result of correcting the momentum of the particles detected in the $K\Lambda$ reaction.

Once these corrections are applied, the missing energy and momentum relating to the $K\Lambda$ channel returns to zero. Figs 5.14 and 5.15 show these quantities along with how the reconstructed Λ^0 mass is affected.

5.6 Particle Mis-identification

In considering the background contribution to the $K\Lambda$ reaction, since a tight restriction is placed on the kinematic separation of the Λ^0 and the Σ^0, the priority is to focus on the particle identification process. For reasons discussed in Chapter 7, the Photon Tagger does not allow the kind of timing cut mentioned in Section 5.2. This rules out the

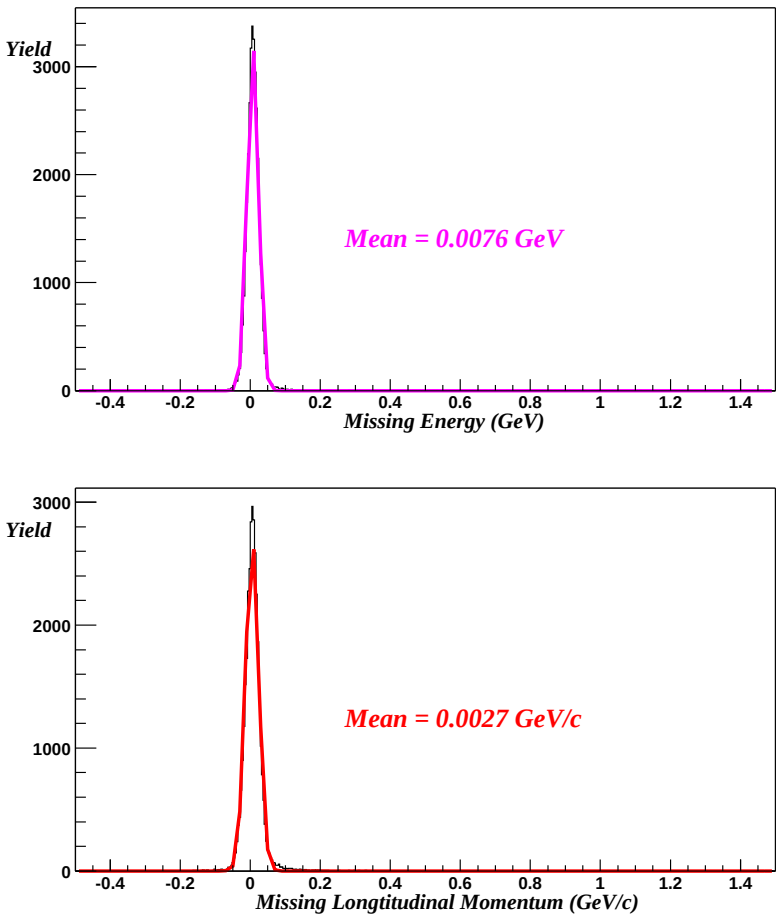

Figure 5.14: *Missing Mass and Momentum after corrections have been applied.*

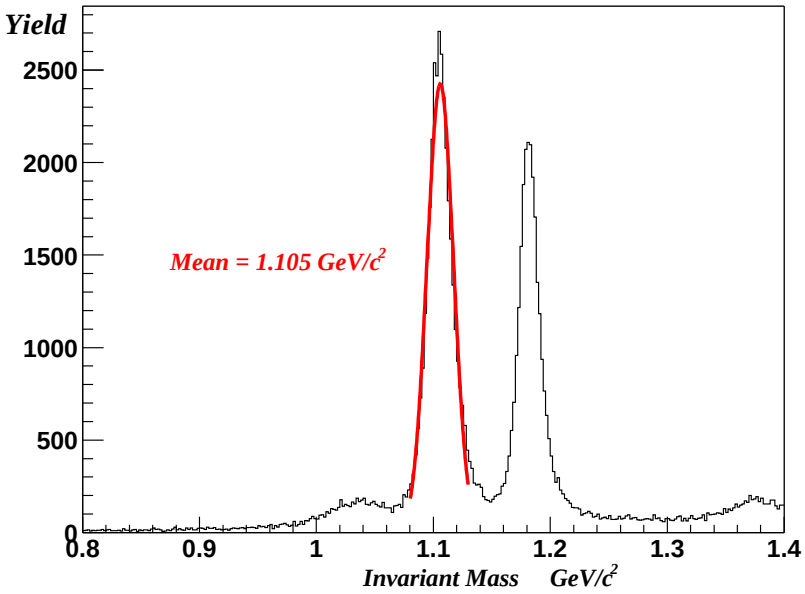

Figure 5.15: Λ^0 *reconstructed mass after correction. This is a clear improvement over Fig 5.12.*

possibility of comparing the performance of the GPID identification scheme in comparison with a method based on the PART bank. One way to evaluate the performance of GPID without an external reference is to see how many particles lie outside an acceptable limit on either side of the expected curve on a β versus momentum plot for each particle of interest. This serves to measure how often the GPID scheme fails to identify a desired particle properly, and Fig 5.16 shows that without the tight cuts described in Section 5.4 applied, there are many particles which have had their β-value adjusted to the best matching particle mass for their track and consequently do not match with a particular particle type. This can be seen in Fig 5.16 as background between the acceptable β limits. These β limits are an estimate designed to take into account the decreasing β resolution at high momentum.

The reason for this failure in the GPID identification method clearly lies in bad timing information. For example if an interaction is believed to be exclusive, the error could come from one of the particles having an incorrect start time. Another example would occur when the wrong time is taken from the Photon Tagger during event reconstruction, effectively giving the wrong energy for the interaction and hence making it seem, incorrectly, to be an exclusive reaction.

If tight cuts are implemented to limit the allowable range of energies and beam

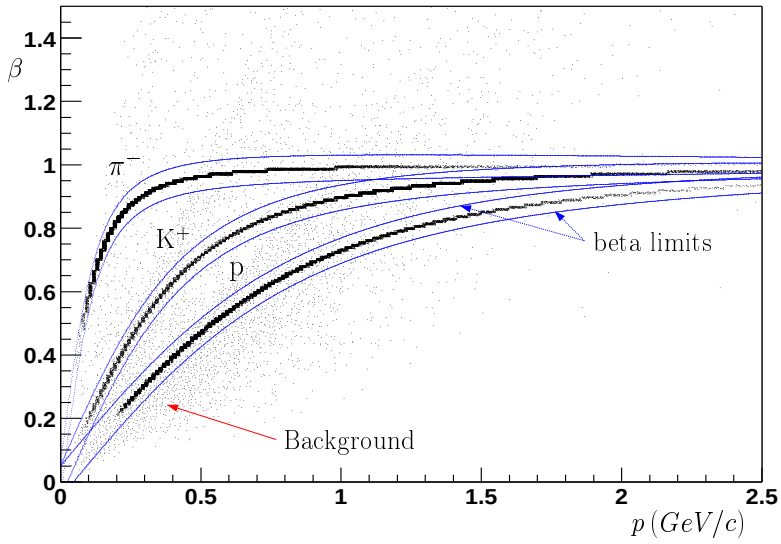

Figure 5.16: *The β versus momentum plot without cuts on events that are not considered for the final analysis. The only restriction on particles here is that there must be at least three particles present and there must be a K^+, a π^- and a proton present.*

conditions that are considered, this effect can be significantly reduced. Fig 5.17 shows the same data, but with tight restrictions imposed. These include the same cuts that are used for the final selection of data to be analysed, and also include restrictions on the movement of the coherent edge of the photon energy distribution from the Tagger. There is markedly less background visible here, although it has not been entirely eliminated. A concern which may arise from Fig 5.17 is that there may be a contribution to the background in the data analysis resulting from the failure of the GPID method.

To address this concern, the β limits shown in Fig 5.17, are enforced in the analysis software. A given particle will be rejected from the analysis if it lies outwith the β limits as shown. This applies to the detection of an exclusive reaction in that all three required particles will be thrown out of the analysis if one fails the test.

Fig 5.18 shows the resulting diagram after these limits on β-value have been imposed. At this point there is no visible background, and a closer investigation into the number of events that constitute each plot shows that the difference in this number caused by GPID failure is of the order of ~0.2%. Table 5.1 shows the results of this investigation in more detail.

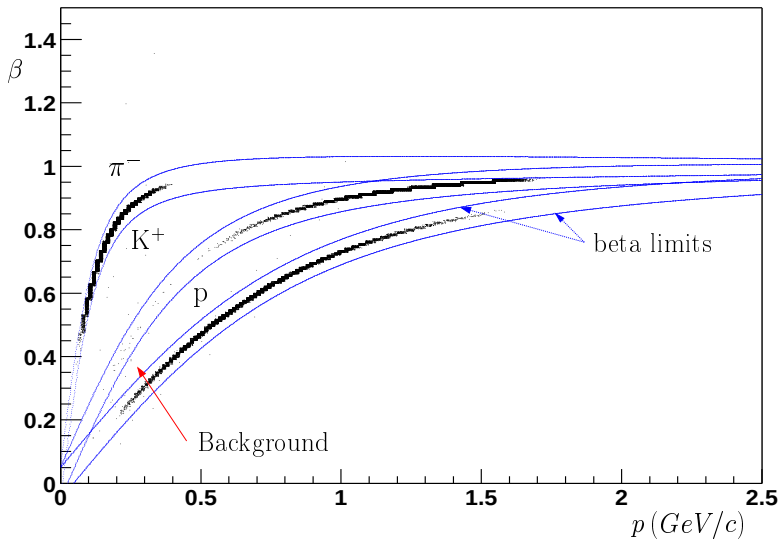

Figure 5.17: *The β versus momentum plot with the final analysis cuts discussed in Section 5.4. Here there is no cut on an acceptable β-value for each particle, and the GPID method fails occasionally.*

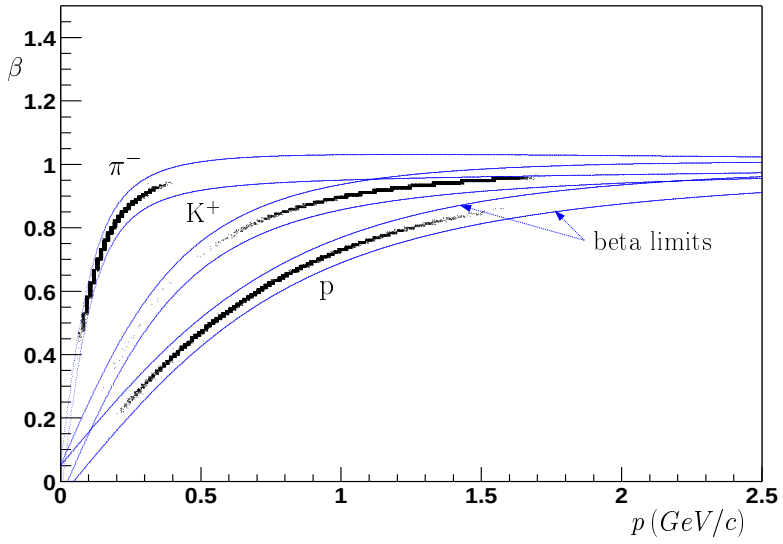

Figure 5.18: *The β versus momentum plot with analysis cuts and a cut on acceptable beta limits for kaons, pions and protons. The background in this plot is practically negligible.*

Type of Cuts	Number of Events
K^+, π^- and proton detected	1717173
As above, plus Λ^0/Σ^0 separation and physics cuts	60408
As above, with β-limits for each particle imposed	60291

Table 5.1: The relative number of events in the Figures described above (Figs 5.16 to 5.18).

5.7 Conclusion

Ultimately the choice between using the GPID method and a method based on the PART bank has not been possible to make during the calibration of the G8a experimental run. Due to faults in the Photon Tagger hardware (discussed in more detail in Chapter 7) it is impossible to make a tight cut in software on the time recorded in the Tagger to reduce accidentals and improve the identification of particles in this way. This has forced the G8a collaborators to use the GPID scheme for all particle identification. For the same reason, it is also difficult to make a systematic study of individual particles in the detector and their PID characteristics. Due to time considerations for this thesis, such work has not been attempted. Essentially the PID for the $K\Lambda$ reaction depends on the reaction itself, in the sense that the reaction must be exclusive. The fact that all three decay particles from this reaction can be identified in CLAS therefore makes it possible to argue that the existence of a missing mass peak equivalent to the mass of the Λ^0 means that a K^+ has indeed been successfully identified.

The main limitation of this method of identifying a reaction is that there is no way of recovering "possible" candidates. For example if two of the three particles required are seen, it is impossible to reliably reconstruct the missing particle, and this limitation significantly reduces the number of events available for analysis. The limitation is also evident for events where the polar angle of the kaon in the detector is relatively large, this means that the Λ^0 is decaying further forward in CLAS than the kaon. For such a case, the π^- decay particle is bent towards the beamline by the polarity of the magnetic field in CLAS. This π^- cannot be detected directly and therefore cannot be reconstructed by the methods described above. Such semi-exclusive interactions must be rejected, and this effect is clearly shown in the final results discussed in Chapter 7.

Chapter 6

Data Analysis

6.1 Introduction

This analysis is carried out by measuring the photon asymmetry Σ of the reaction $\overrightarrow{\gamma} + \mathrm{p} \rightarrow \mathrm{K}^+ + \Lambda^0$, where the reference frame for the measurement is the centre-of-mass frame of the $\mathrm{K}\Lambda$ system, as shown in Fig 5.9.

The main goal of the analysis is to compare with theoretical predictions of the photon asymmetry over as wide a range of θ, ϕ, and $\mathrm{E}_{\overrightarrow{\gamma}}$ as the setup of the G8a experiment will allow.

For the purposes of this thesis, results will be presented showing the photon asymmetry over a photon energy range of $\mathrm{E}_{\overrightarrow{\gamma}} > 1.6\ \mathrm{GeV}\ \mathrm{to}\ \mathrm{E}_{\overrightarrow{\gamma}} < 2.0\ \mathrm{GeV}$, over a range of $\theta^{\ \mathrm{K}^+}_{\mathrm{C.M.}}$ from 20^0 to 130^0 and over the complete azimuthal range of CLAS.

6.2 The $\mathrm{K}\Lambda$ reaction.

As shown in Chapter 4, the $\mathrm{p}\,(\overrightarrow{\gamma},\ \mathrm{K}^+)\,\Lambda$ reaction is easily identified in CLAS. However some important aspects of the detection of this reaction are not described in Chapter 4, such as the angular distribution of the reaction and the average photon energy producing it. These quantities are vital for comparison with theory, and also for accessing the overall measurement of the photon asymmetry.

The threshold centre-of-mass energy for the production of the $\mathrm{K}\Lambda$ system is 0.911 GeV, so with a centre-of-mass energy in excess of $2\,\mathrm{GeV}$ during the G8a run, the angular distribution of the $\mathrm{K}\Lambda$ system is very forward peaked. Fig 6.1 shows the typical distribution for a incident photon energy of $2\,\mathrm{GeV}$ in both the laboratory reference frame and the centre-of-mass reference frame.

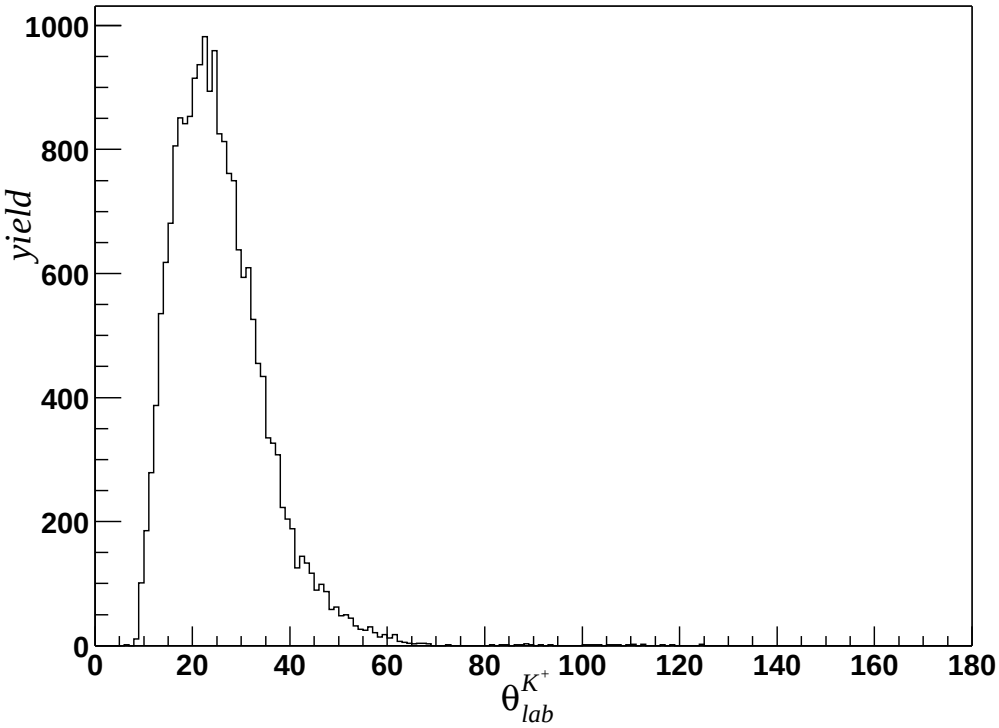

Figure 6.1: *The polar angle distribution of the reaction in the laboratory reference frame at* $1.6 \leq E_{\overline{\gamma}} \leq 2.0$ GeV.
Below is the equivalent distribution shown in the centre of mass frame. The angular bins shown here are used throughout the analysis.

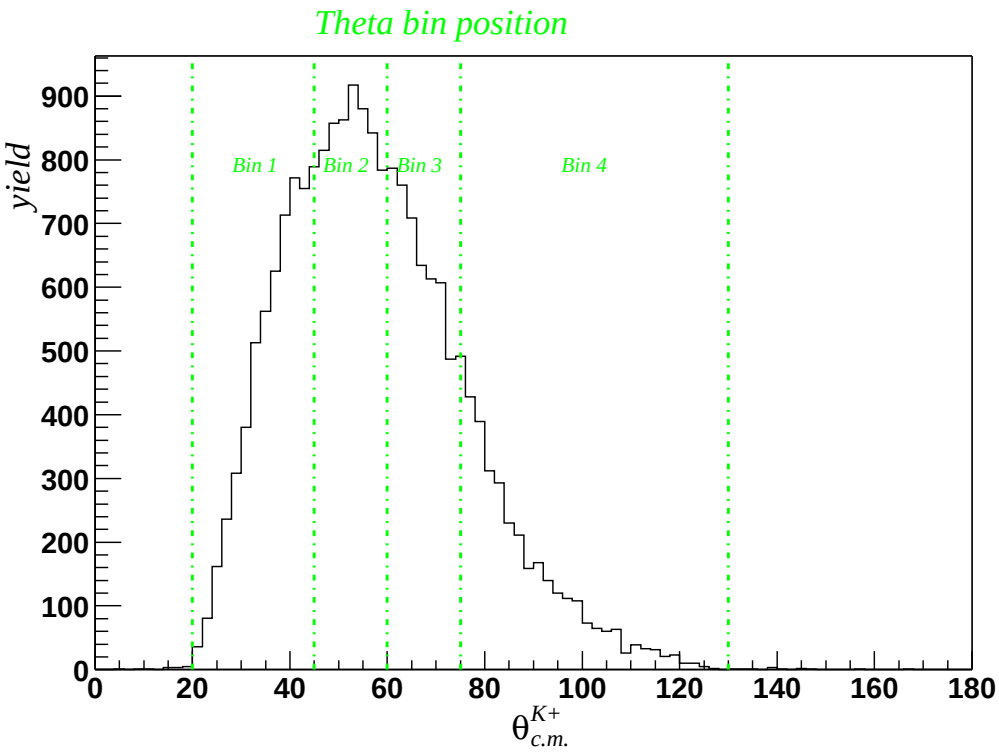

6.3 Acceptance correction issues.

As described in Section 2.6, making a measurement of the photon asymmetry of a reaction in CLAS requires a way of removing or cancelling out those areas inside CLAS where the detectors are not working as efficiently as they should. Any area where the particle yield is abnormally high or low in a given experimental run can bias the parameters used to a fit a cosine 2ϕ function to the data. A natural way to guard against increasing systematic uncertainty in the relationship between the polarised data and unpolarised data set is to have alternate sets of runs, polarised and unpolarised, every day. However as can be seen in Fig 6.3 this was far from the case for the G8a experimental run. Without the safety net of running polarised and unpolarised photon beams under exactly the same experimental conditions, a test of the experimental conditions is required to justify the use of the data as a complete set. This is done in reference to the ρ^0 data set, as explored in Christopher Gordon's thesis [93].

The reason for this is that a lack of statistics in the $K\Lambda$ decay channel renders any analysis of detector stability impractical. Presented in Fig 6.2 is a ratio of the π^+ azimuthal yield produced during a reference run used for calibration purposes, and another run taken 21 days later. Apart from the regions where the acceptance is low due to the presence of the magnetic coils, the acceptance in Fig 6.2 is mostly flat, and this provides an initial basis for the use of the normalisation technique mentioned above.

Fig 6.3 shows an overall plot of the comparative yields of the entire data set compared with specific reference runs, and apart from the amorphous target runs with low statistics, the agreement between the data sets is good, and a consistent chi-squared is also obtained.

This study has also indicated that similar results are obtainable when considering a proton or a π^-, which supports the use of the normalisation method to calculate the Photon Asymmetry. However this method cannot rule out fluctuations in particle yield over a short time, which means there may be transient effects in the detector that would make it more difficult to calculate a reliable cosine 2ϕ.

More importantly, the amount of polarised data significantly outweighs the amount of unpolarised data, so the errors propagated from the amorphous target data set will be the limiting factor in the precision of the photon asymmetry measurement.

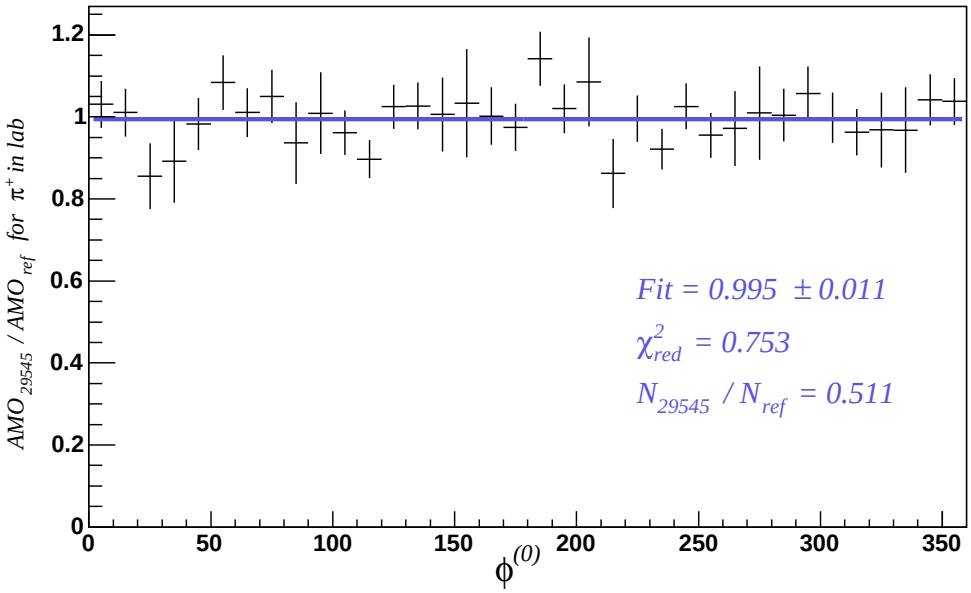

Figure 6.2: *The azimuthal yield of particles from a reference run 29545 is used to normalise another run. If the CLAS detector behaves consistently over the 21 day period between these two runs, a flat straight line should be visible with intercept 1 across the entire azimuthal range of CLAS, except where the presence of the magnetic coils may cause the acceptance to drop to zero.*

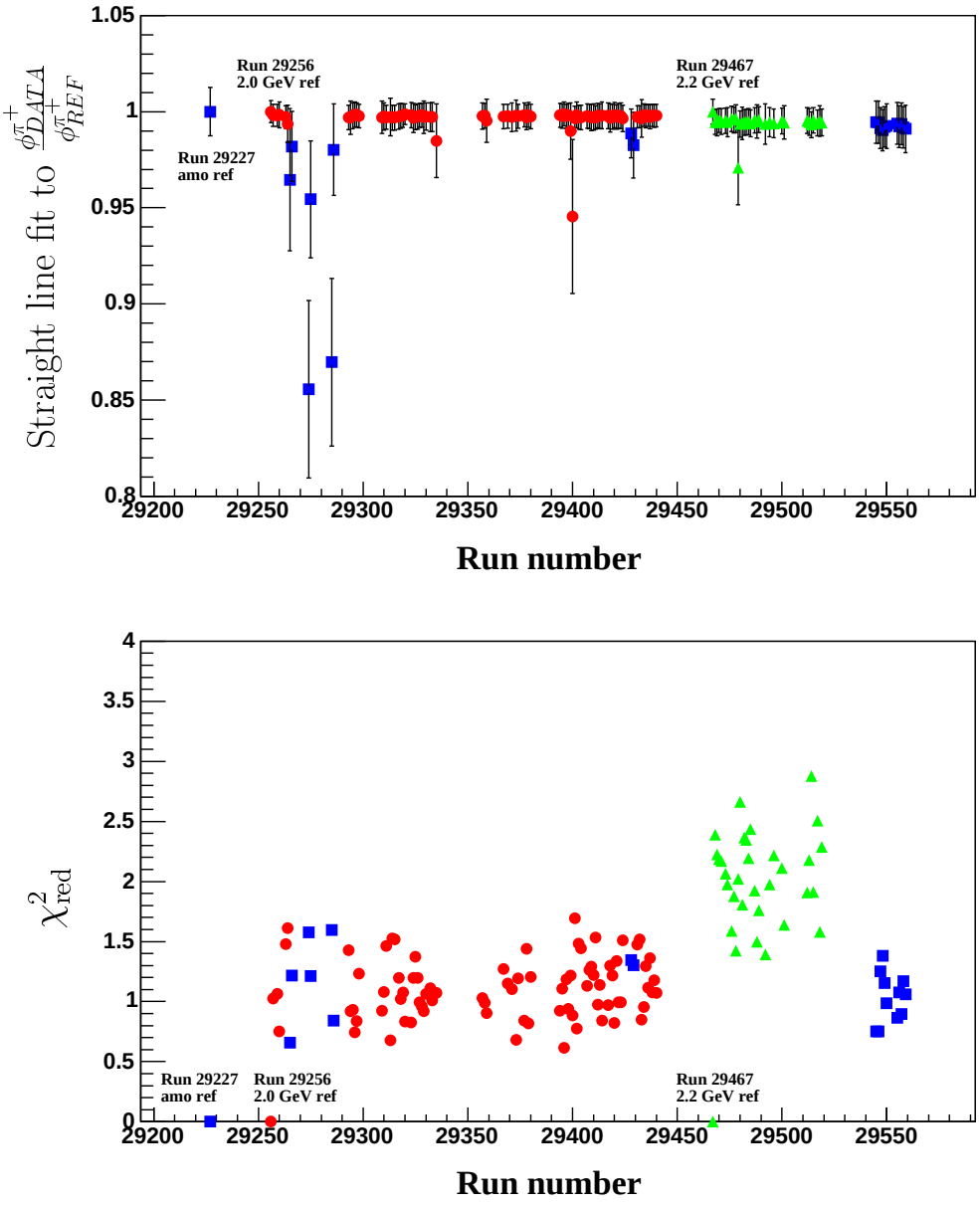

Figure 6.3: *The azimuthal yield of particles of the total G8a data set is here compared with a set of reference runs used in the calibration process. Overall the distribution looks very flat, and an acceptable reduced chi-squared value of* $\chi^2_{red} \simeq 1$ *is obtained, except for the amorphous radiator runs which show* χ^2_{red} *increasing, indicating an increase in statistical error. The blue runs are taken using an amorphous radiator(reference run is 29227), red runs are polarised with the coherent edge at* 2.0 GeV. *(reference is 29256), and green runs have the coherent edge at* 2.2 GeV *(with the reference at 29467).*

6.4 Determination of Photon Asymmetry

The calculation of the photon asymmetry is normally done by measuring the yield of particles both in the plane defined by the electric vector component of the incoming polarised photon, and at right angles to the same plane. In a detector such as CLAS, one can measure the angle of the production plane of the $K^+\Lambda^0$ system in CLAS, and calculate the angle between this plane and the polarisation vector to define the ϕ-angle of the reaction.

Calculating Σ as referred to in Section 2.15,

$$\Sigma = \frac{1}{P_\gamma}\left(\frac{W_\parallel - W_\perp}{W_\parallel + W_\perp}\right) \tag{6.1}$$

where P is the degree of linear polarisation, equivalent to the ratio of linearly polarised photons to the combined polarised and unpolarised photon flux, and $W_{(\mathrm{direction})}$ is the yield of particles in CLAS emerging either parallel or perpendicular to the plane of photon polarisation.

A more direct approach to calculating the photon asymmetry in CLAS is to measure the azimuthal distribution of particles in CLAS and calculate the amplitude directly from a cosine fit to the data. Using linearly polarised photons to induce a reaction has the effect of either increasing or decreasing the yield of particles parallel or anti-parallel to the azimuthal angle of the photon polarisation vector. Hence, the anticipated angular distribution as function of azimuthal angle ϕ is of the form shown in eqn 6.2.

$$W(\phi) = W_0(1 - \alpha\cos 2\phi) \tag{6.2}$$

where α is the amplitude of the cosine distribution which, as shown later, is related to the magnitude of the photon asymmetry. W_0 represents the angular distribution of the amorphous target data set in CLAS, and is expected to have no ϕ-dependence, as shown in Section 6.3, apart from reflecting the systematic deficiencies of the detector e.g. the magnetic coils.

Since the photon asymmetry is then defined as the amplitude of the cosine distribution obtained when the polarised data set is divided by the unpolarised data set, eqn 6.1 can be reduced to an expression dealing with a normalised azimuthal distribution[1], as

[1]A normalised angular distribution here is created by creating suitable bins in ϕ and then dividing the polarised data by the corresponding unpolarised data. The unpolarised data needs to be scaled by a factor according to the number of counts in total that are required to normalise the whole distribution to a value of 1.

This also has the effect of cancelling out the systematic effects of the detector in each bin.

shown in eqn 6.3. It should be noted here that the total yield in the polarised and unpolarised distributions is assumed to be equal. In the case of the G8a experiment this was not the case and the polarised distribution had to be properly scaled to satisfy this condition.

$$\Sigma \cos 2\phi = 1 - \frac{\mathrm{W}(\phi)}{\mathrm{W}_0(\phi)} \tag{6.3}$$

It is then possible to obtain an expression of Σ by considering eqn 2.17. The normalised particle yield will then have a functional dependence on azimuthal angle of the form:

$$\mathrm{W}(\phi) = 1 - \mathrm{P}_\gamma \Sigma \cos 2\phi \tag{6.4}$$

6.5 Addition of orthogonal polarised data.

Due to the limited amount of amorphous data available for this analysis, trying to complete the calculation for all possible values of $\theta^{\mathrm{K}^+}_{\mathrm{C.M.}}$ is not possible due to the large error propagation that comes from scaling up a very limited number of events from the amorphous data at those angles.

Therefore a different method which makes full use of the available statistics is desirable. As mentioned in Section 6.4, the photon asymmetry is essentially a measure of the amplitude of a cosine disturbance in comparison to a flat azimuthal contribution as produced by unpolarised data. If this is always the case whether the photon polarisation is parallel to the y-axis in CLAS for example, or perpendicular to this axis, then by adding together two cosine distributions with a 90^0 phase shift between them it is possible to obtain a unpolarised data set with no azimuthal variation in CLAS. Variations in the degree of linear polarisation must be taken into account for this procedure to work, since the amplitude of the cosine distribution is directly affected by any such change (See Eqn. 6.4).

The process can be more rigorously described as follows:

$$\mathrm{N} = \mathrm{N}_{\mathrm{A}0}(\phi) \tag{6.5}$$

$$\mathrm{N}_\perp(\phi) = \mathrm{N}_{\perp 0}(\phi)[1 + \mathrm{P}_\perp \mathrm{A}_1 \cos 2\phi] \tag{6.6}$$

$$\mathrm{N}_\parallel(\phi) = \mathrm{N}_{\parallel 0}(\phi)\left[1 - \mathrm{P}_\parallel \mathrm{A}_2 \cos 2\phi\right] \tag{6.7}$$

Where N is the yield, and the subscript zero denotes the azimuthal distribution of an

amorphous target or unpolarised data set. These equations reveal how the unpolarised data is considered to have no intrinsic dependence on ϕ in CLAS, but the effect of using polarised photons is to produce a measurable cosine deviation from this flat distribution. Since the cosine amplitudes A_1 and A_2 are known for each data set, and the polarisations $\mathrm{P}_\perp$ and $\mathrm{P}_\parallel$ can also be calculated, a scaling factor can be used to ensure that the polarised contribution to each data set cancels out to create a flat distribution.

$$\mathrm{N_U}\left(\phi\right) = \mathrm{N}_0\left(\phi\right) + \mathrm{N}_\perp\left(\phi\right) + \mathbf{k}\mathrm{N}_\parallel\left(\phi\right) \tag{6.8}$$

The scaling factor $\mathbf{k}$ is key to this whole idea since it allows the addition of these two distinct data sets.

$$\mathbf{k} = \frac{\Sigma \mathrm{N}_\perp\left(\phi\right)\mathrm{P}_\perp}{\Sigma \mathrm{N}_\parallel\left(\phi\right)\mathrm{P}_\parallel} \tag{6.9}$$

Shown in Fig 6.4 is the un-normalised yield from the parallel polarised data set (top), and the perpendicular polarised data set (bottom). The expected cosine 2ϕ modulation is not seen here since the data are dominated by acceptance effects which cancel out when the normalisation procedure is carried out.

Fig 6.5 shows the resulting data set for the second $\theta_{\mathrm{C.M.}}$ bin when the data sets are added together using Eqn 6.8. This data contains the same acceptance variations as the individual data sets, and when it is used to normalise the individual data sets, the cosine 2ϕ modulation becomes evident as seen in Fig 6.6. Table 6.1 shows the appropriate values used to create the unpolarised data set.

Data Set	Entries	Polarisation (av %)
Perp	5716	76.05
Para	400	63.04
Amo	241	0
Unpol.	12612	0

$$\mathbf{k} = \frac{5716(76.05)}{400(63.04)} = 17.24 \pm 1.53$$

Table 6.1: The parameters used in eqns 6.8 and 6.9. These values are quoted for analysis bin 2. The dominant contributing error to **k** is the error from calculating the polarisation. This is discussed in depth in Section 6.7.

It is worthwhile to look at the difference observed between carrying out the procedure of adding together the orthogonally polarised data sets and the more straightforward technique of using amorphous target data to normalise the polarised data set to

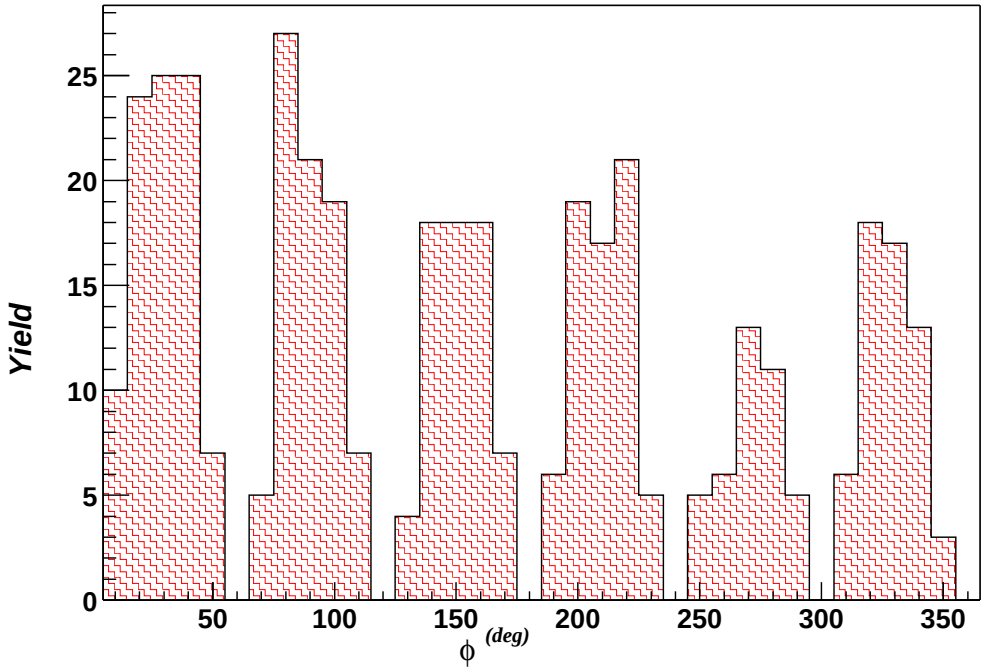

Figure 6.4: *Polarised data set parallel (above) and perpendicular (below) to the floor of Hall B for analysis bin 2. The complete yield of particles passing through analysis cuts is shown here for each data set.*

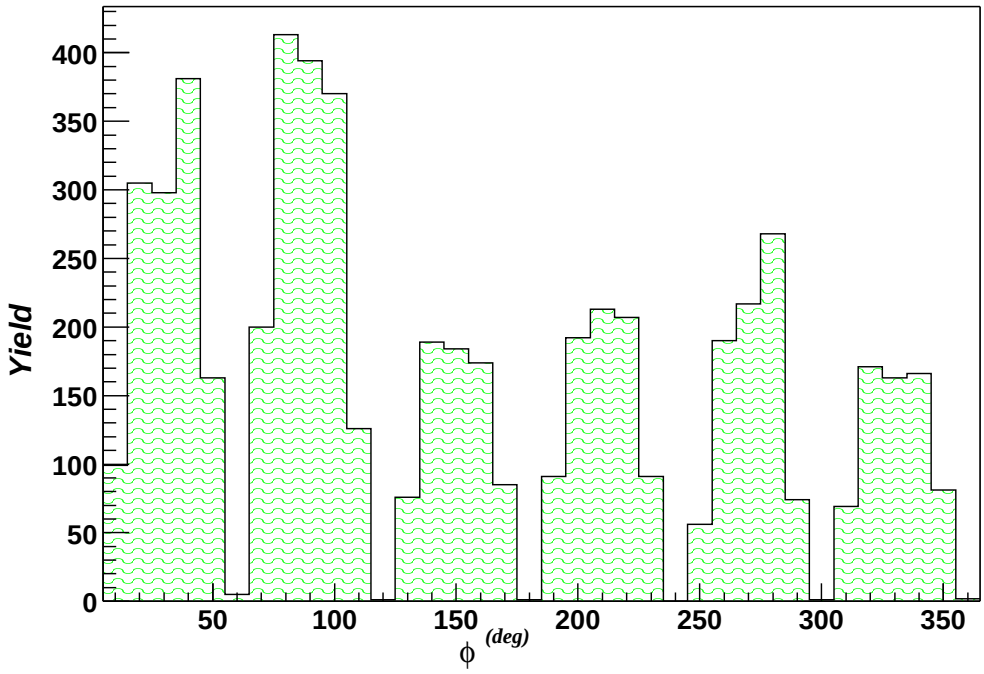

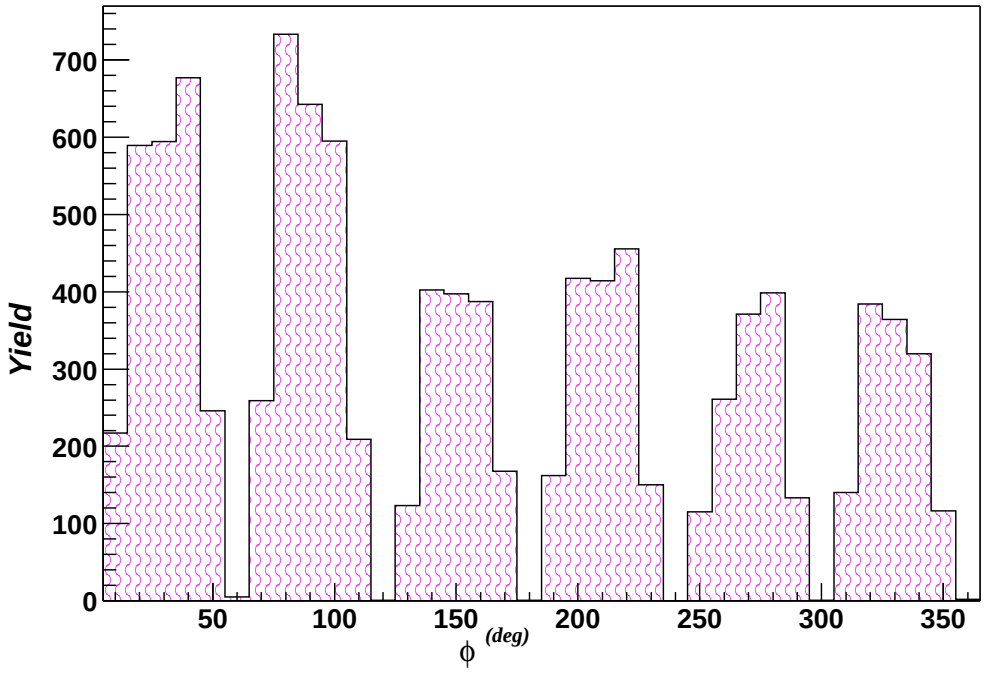

Figure 6.5: *The unpolarised data set created by the process outlined in Eqn 6.8 for analysis bin 2. Here the yield is the sum of the scaled parallel data set and the unscaled perpendicular data set.*

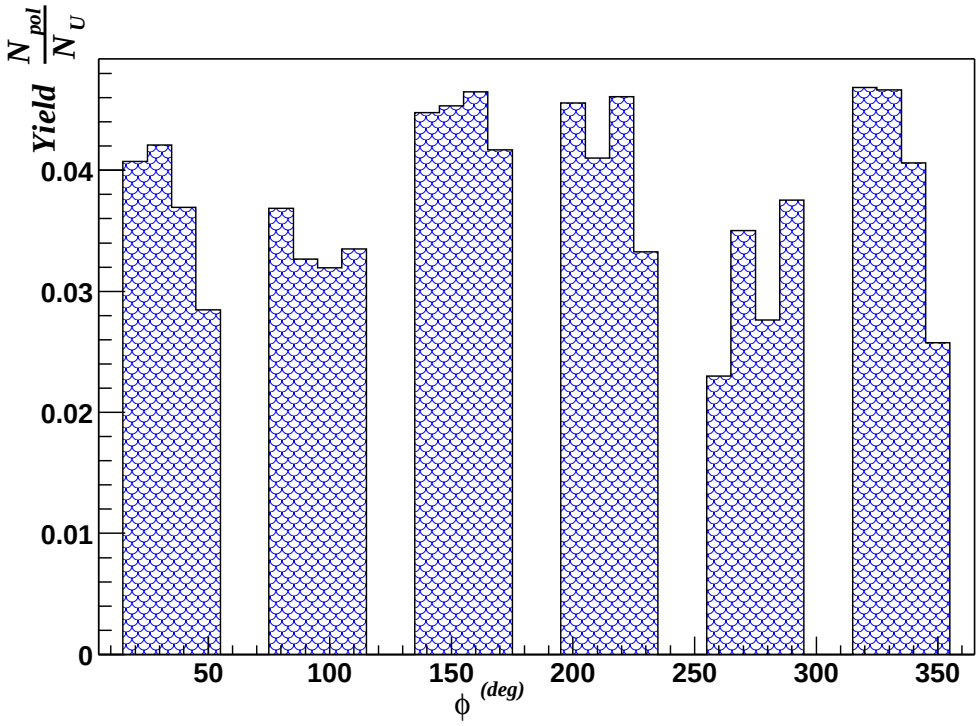

Figure 6.6: *The same data sets as shown in Fig 6.4 when divided by the unpolarised data set. The yield in these plots is the number of entries in Fig 6.4 divided by the number of entries in Fig 6.5. These plots are equivalent to those shown in Fig 6.15, without error bars. The data show a clear 90 degree phase-shift, as expected.*

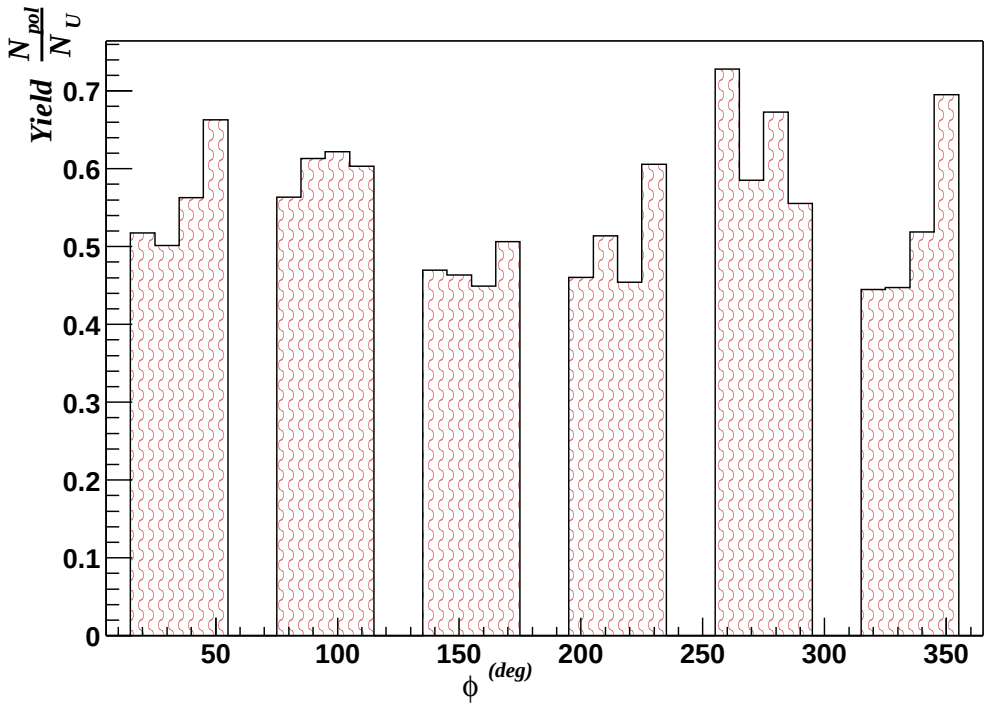

be studied. In the case of the G8a data set, the author found very poor $\cos 2\phi$ fits to the polarised data when normalised using the amorphous target data. In Appendix B a method of visualising the data was employed by the author to understand whether a true polarised signal was being observed, or whether statistical fluctuations caused by the very small quantity of amorphous target data available were dominating the desired signal.

Since a polarised signal will produce a highly symmetric variation over the azimuthal range of CLAS, the author wrote a script to project the azimuthal information into a 3-dimensional cylinder, with the height of the cylinder at a particular place representing the yield of particles in that sector of CLAS. A comparison is carried out in Appendix B between the visual symmetry of the un-normalised and normalised data for each plane of polarisation in analysis bin 2, contrasting also with the two normalisation procedures used.

Although no symmetry is observable when looking at the 3-dimensional plot of the un-normalised data, when the normalisation procedure is carried out, a major difference is seen between the unpolarised normalisation and the amorphous target normalisation. Visually these plots are notably different, and the combination of a significantly low amount of amorphous target data and a lack of symmetry in the resulting normalised distribution seems to indicate that this method is not suitable for reliably extracting the photon asymmetry of the G8a $\mathrm{K}\Lambda$ data set.

6.6 Combining the polarised data sets to measure the photon asymmetry

After the unpolarised data set has been created using the methods described in Section 6.5, the measurement of the photon asymmetry is made by dividing one of the polarised data sets by the unpolarised data set. Eqn 6.10 shows how this may be represented.

$$\Sigma = \frac{1}{\mathrm{P}_\gamma} \cdot \frac{\alpha_\perp}{\alpha_{||} + \alpha_\perp} \tag{6.10}$$

Where α is the magnitude of the amplitude of the cosine 2ϕ distribution measured for one of the polarised data sets. Taking statistical errors into consideration, the statistical error associated with the measurement of Σ is calculated by adding the relevant fractional errors $\sigma\alpha_{direction}$ in quadrature, as shown in eqn 6.11.

$$\sigma\Sigma = \sqrt{\left(\sqrt{(\sigma\alpha_{\parallel})^2 + (\sigma\alpha_{\perp})^2}\right)^2 + (\sigma\alpha_{\perp})^2} \tag{6.11}$$

In the case of the G8a data set, the errors in the scaled parallel data set that goes into creating the unpolarised data set are scaled accordingly, and these end up dominating the total statistical error in the measurement of Σ. One possibility for minimising the statistical error, that arises both from the cosine fit to the data and the size of the statistical errors inherent in each point, is to use a variation on the definition of the photon asymmetry to decrease the relevance of the large statistical errors. The essence of eqn 6.10 is to extract the amplitude of the cosine variation in the polarised data set. One can go a step further by looking at the difference between the data sets, which maximises the size of the amplitude, therefore reducing the weight of the statistical errors for each azimuthal bin. Eqn 6.12 shows the proposed form for this calculation.

$$2\Sigma = \frac{1}{\mathrm{P}_{\gamma}} \cdot \frac{\alpha_{\perp} - \alpha_{\parallel}}{\alpha_{\parallel} + \alpha_{\perp}} \tag{6.12}$$

Here the measured amplitude is twice the size of the proper asymmetry since the separate amplitudes are 90 degrees out of phase with each other, resulting in an effect similar to constructive interference. The results from this method are shown beside the results obtained from dividing a single data set by the created unpolarised data set in Section 6.8.

6.7 Measuring the polarisation of the photon beam.

There are three steps to consider when estimating the polarisation of the photons incident on the target.

1) The Photon Tagger must accurately measure the photon flux from the diamond crystal.

2) The CLAS trigger must accurately classify the photons in the Tagger based on the physical event time.

3) The effect of the collimator must be taken into account. This normally increases the degree of linear polarisation, but the amount is dependent on the photon beam parameters and needs a simulation to quantify this dependence.

To answer the first requirement, the Tagger E-Counter Scalers are read out every 2 seconds, while at the same point in time the EPIC [94] BOS bank gives information on the beamline and goniometer conditions[2].

From this read-out the average flux at the Tagger can be measured, normally with an enhancement at the energy of the coherent photon peak.

The second requirement is met by using the tagger T-Counter TDC output. This is only produced in the event that a good trigger is identified by CLAS, therefore the photon that is measured in the Tagger must have passed through the collimator. Normally this measurement greatly increases the clarity of the peaks with a corresponding reduction in signal to background ratio. In order to account for noise and varying efficiency in the Tagger detector plane, a random background subtraction is performed, followed by a normalisation procedure.

First a plot of the Tagger T-Counter Spectrum is made for a time region well away from the physical event time ($\pm 20\,\mathrm{ns}$). This data is subtracted from the Tagger measurement at the physical trigger time, for both polarised and amorphous target data. This involves dividing through the polarised data from the tagger by an amorphous data set to take care of the varying efficiency. The divided data set is then normalised to a baseline of 100 for the purpose of comparison with simulation. For the third requirement, a simulation based on previous work [56, 95] models the dependence of the collimated beam on various beam line parameters shown in Table 6.2.

This simulation code is called the **anb** code [57], which models the process of coherent bremsstrahlung production in diamond. By calculating the coherent bremsstrahlung photon intensity for a variety of beam parameters (See Table 6.2) and with the effect of a collimator included, the **anb** code produces a calculation of the expected E-Counter Tagger scaler measurement, essentially the uncollimated photon flux. The calculation of the uncollimated spectra takes into account electron scattering from multiple crystal planes in the diamond crystal, and this tends to smudge out and widen the coherent bremsstrahlung peak. When the collimator is included, a simulation of the energy distribution of polarised photons travelling through the collimator is produced. This simulation should agree with the reconstructed tagger information from physical events in CLAS

The procedure for estimating the polarisation then consists of comparing the tagger measurements from (1) and (2) and comparing them with the simulation produced by

[2]EPICs is the Experimental Physics and Industrial Control system. It consists of a set of software applications and libraries designed to interface with read-out hardware, and is the cornerstone of the CLAS electronics slow-control systems.

the **anb** code. Finally the **anb** code generates a table of values that show the polarisation of the tagged photons that make it to the target if the beam conditions match those fed to the simulation. This table contains a row specifying the Tagger Energy and a corresponding row showing the related photon polarisation. The comparison between calculation and experiment is shown in Fig 6.7, and this is the typical plot used to adjust the parameters of the **anb** code.

Since this recipe is specific for particular run conditions, the G8a experiment required numerous polarisation tables to match the widely varying conditions seen during the experiment duration. This occurred as a result of the nature of G8a as a commissioning experiment. Fig 6.13 shows the resulting polarisation distribution obtained from the data which passed the cuts for each analysis bin as illustrated in Section 5.4 and Fig 6.1.

The actual procedure of creating these polarisation tables relied upon comparing the data from the Photon Tagger with the **anb** calculation and determining the best parameters to obtain agreement between calculation and experiment. For a specific run being analysed later, the HEAD[3] BOS bank would be checked in the analysis software and compared with the relevant polarisation table, which would then give the correct polarisation value to a given photon on a run-by-run basis, and also accurate to each read of the EPIC bank, which occurs every 2000 events.

Systematic uncertainties arise due to the following:

1) The aspect of the **anb** code that deals with multiple scattering is unlikely to accurately model the conditions of the experiment, and this is most likely to be caused by inaccuracies in the modelling of multiple crystal plane scattering of the electron beam in the diamond crystal.

2) The Photon Tagger E-Counter Scaler information on the uncollimated coherent bremsstrahlung beam does not agree with the **anb** simulation of the uncollimated polarised photon intensity, which means that the effect of the incoherent contribution and the source of this contribution is not fully accounted for. This leads to the introduction of a scaling factor to at least allow a comparison between the shape of the collimated versus uncollimated photon spectra, which is not completely satisfactory.

[3]Every event has a BOS bank attached when the Data Acquisition system reads out, which specifies exactly the run number, and event number within the run, where the event took place. This is called the HEAD bank, and it also contains information on the type of trigger that took place in CLAS, for example, whether the Tagger Master-OR fired as part of that trigger.

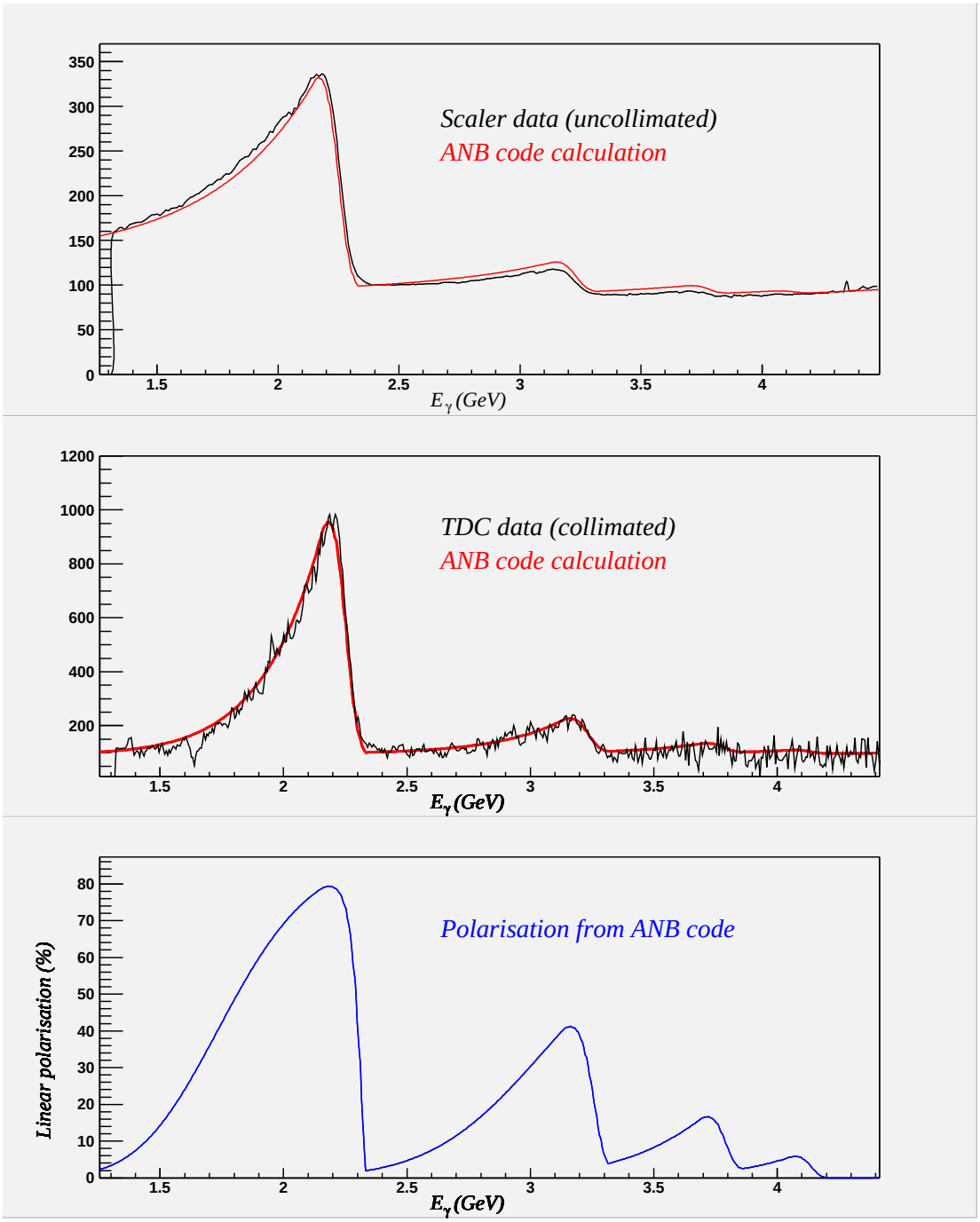

Figure 6.7: *The comparison between Photon Tagger E-Counter Scaler Data and the* **anb** *calculation for uncollimated photon spectrum (top) Comparison between Photon Tagger T-Counter TDC data and the* **anb** *calculation for collimated photon spectrum (middle). The resulting calculated polarisation when a close match is achieved in the two plots above (bottom).*

Parameter	Description	Typical G8a values
Beam Energy	Mean Energy of the incident electron beam	$5734\,\mathrm{MeV}$
Beam Energy Spread	Width of the energy distribution	0
Beam Spot Dimension	Size of the beam spot on the radiator	$Cx_{BeamSize} = 0.045mm$ $Cy_{BeamSize} = 0.045mm$
Beam Divergence	Horizontal and vertical beam divergence measured from crystal	$Cx_{BeamDiv} = 0.040\,mrad$ $Cy_{BeamDiv} = 0.038\,mrad$
Radiator Thickness	measured in nanometres	$C_{thickness} = 0.05m$
Crystal Orientation	Three crystal angles measured in mrad $(\theta_C, \phi_C, \alpha_C)$	$\phi_C = 0.785398\,mrad$. The other angles are measured from the goniometer.
Collimator Geometry	The distance from radiator, length and radius of the collimator	$C_{ColliDist} = 22.7m$ $C_{ColliLen} = 0.3m$ $C_{ColliRad} = 0.7mm$
Type of Incoherent Radiation	Mode of calculating incoherent intensity(Bethe-Heitler,Hubbel): 0 or 1.	1
Number of Lattice Vectors	Number of Crystal Lattice vectors used to calculate coherent bremsstrahlung	10
Atomic Z of Radiator	Number of protons in crystal/amorphous radiator	6 (Carbon)

Table 6.2: Typical parameters used by the **anb** code to calculate the polarisation of uncollimated and collimated photon beams.

6.7.1 The associated error in the polarisation estimate.

In the absence of a direct method of determining the polarisation of the photon beam, a systematic error is inferred from the process used to estimate the polarisation. There are four factors which are deemed to have a significant quantifiable systematic uncertainty, and although the determination of these factors is quite subjective, an upper limit to the systematic uncertainty which propagates to the final result from the polarisation method is determined here.

Error from Photon Tagger E-Counter Plane Since the polarisation tables are based on a comparison with the T-Counter TDC spectrum, it is a valid question to ask if there could be a systematic variation in the energy of the "best" photon from the Tagger inherent in the uncertainty of the position of the hit within the Tagger. One way to determine this uncertainty is to look at the physical photon that caused the hit in the Tagger and move it an integer number of E-Counters up or down the Tagger. This gives information on the accuracy of the comparison between the **anb** calculation and the TDC spectrum used. Shown in Fig 6.8 is a histogram of the mean polarisation for a range of photon energies above and below the "best" photon energy determined from CLAS. The mean polarisation of the "best" photon in this case is 71.16%. However the polarisation varies with the integer stepping of E-Counter bin widths in photon energy. A peak is observed at ~ 1.6 E-bin widths from the energy of the "best" photon, which indicates that there is a systematic uncertainty in the placement of the peak polarisation within one T-Counter energy bin width. If the maximum possible error is considered to be ± 1T-Bin width, the maximum uncertainty is estimated by looking at the polarisation at the maximum in Fig 6.8 and the T-Bin on either side. This gives a systematic uncertainty of $\sim 1.6\%$.

Subjective comparison limits Given the "spikiness" of the TDC Spectra used in comparing to the **anb** calculation, it is possible to use a vary the important parameters within a small range to get an acceptable agreement with the data. There are reasonable extreme limits which can be subjectively set, seen in Fig 6.9, which allow the determination of a systematic uncertainty that may result from variation in the comparison itself. To get some idea of the size of this error the variation in polarisation, obtained from the difference in acceptable parameters used in the **anb** calculation, is scaled by the photon energy distribution from the Tagger. As seen in Fig 6.9, for events where the coherent peak edge position sits at T-Id 95 (within the range of this analysis), a maximum error can be estimated at $\sim$4.6%. Since this is an extreme case based

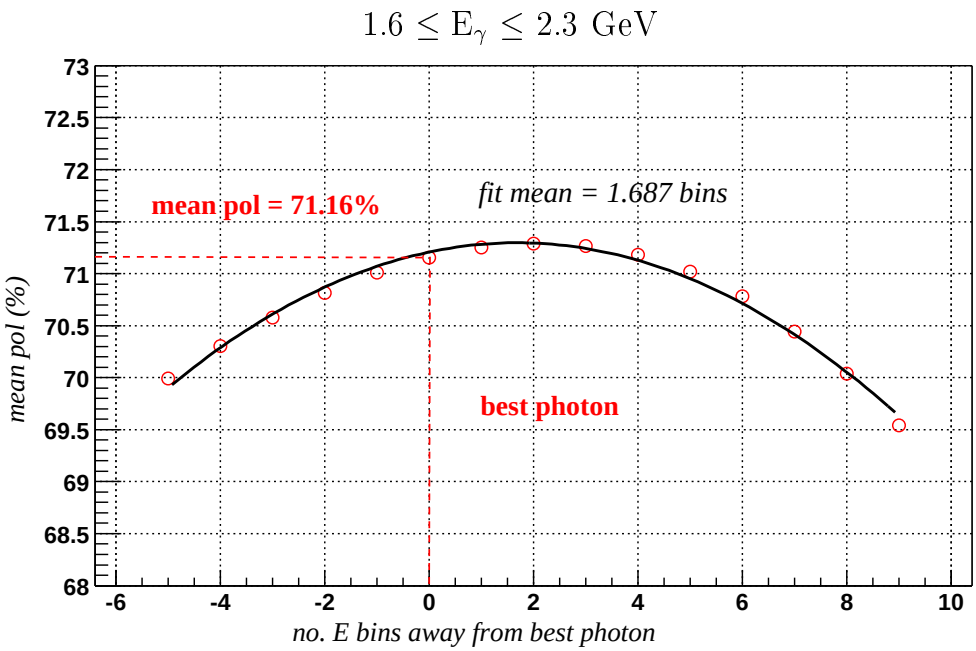

Figure 6.8: *The deviation from the "best" photon polarisation and the maximum calculated polarisation from the* **anb** *code.*

on a random subjective judgement by eye, it is reasonable to assume that the choice of parameters will have a mean value of half of the maximum range, so this gives a systematic error of $\sim$2.3%.

Variation in the height of the Coherent Peak Although the polarisation tables are used as a look-up to determine the polarisation of a photon for a given T-Counter position, there is still variation in the electron beam conditions that causes the height and shape of the coherent peak to vary considerably. This causes the actual polarisation of the photons that cause such events to be reduced. Fig 6.10 shows all the runs where the coherent peak edge was determined to be at T-Id 95 (equivalent to T-Counter 48) by an automated peak fitting routine. It is important to note that this change in coherent peak height can occur over a time period of a few thousand events. Run 29501 in Fig 6.10 shows such a variation where the Tagger TDCs were read out along with the EPICs information over a period of 2000 events, and in this case the data from this readout will be allocated the polarisation value where the coherent peak was much higher, which was the case for the majority for run 29501 and similar for the rest of the data set. This error affects the data sporadically but a maximum overestimation of the polarisation in such a situation is estimated at $\sim$ 5%.

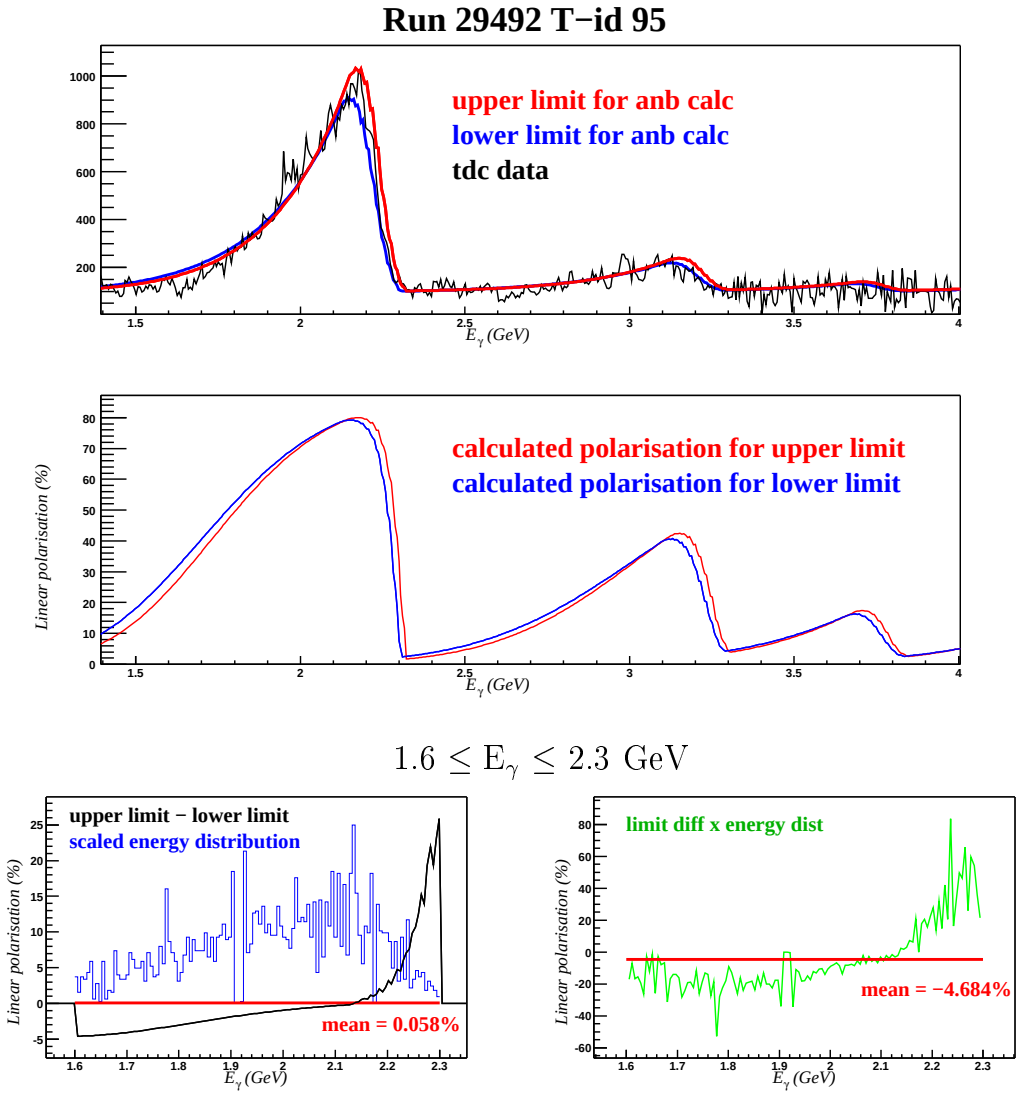

Figure 6.9: *The upper and lower limits for comparison by eye using the* **anb** *code to the data. Bottom left shows the variation of the mean polarisation value(in black) between top and bottom limits used in the* **anb** *code, and the scaled energy distribution(blue) of events that occur when the coherent bremsstrahlung peak is at T-Counter 95 are shown. Bottom Right shows the difference in polarisation multiplied by the scaled energy distribution.*

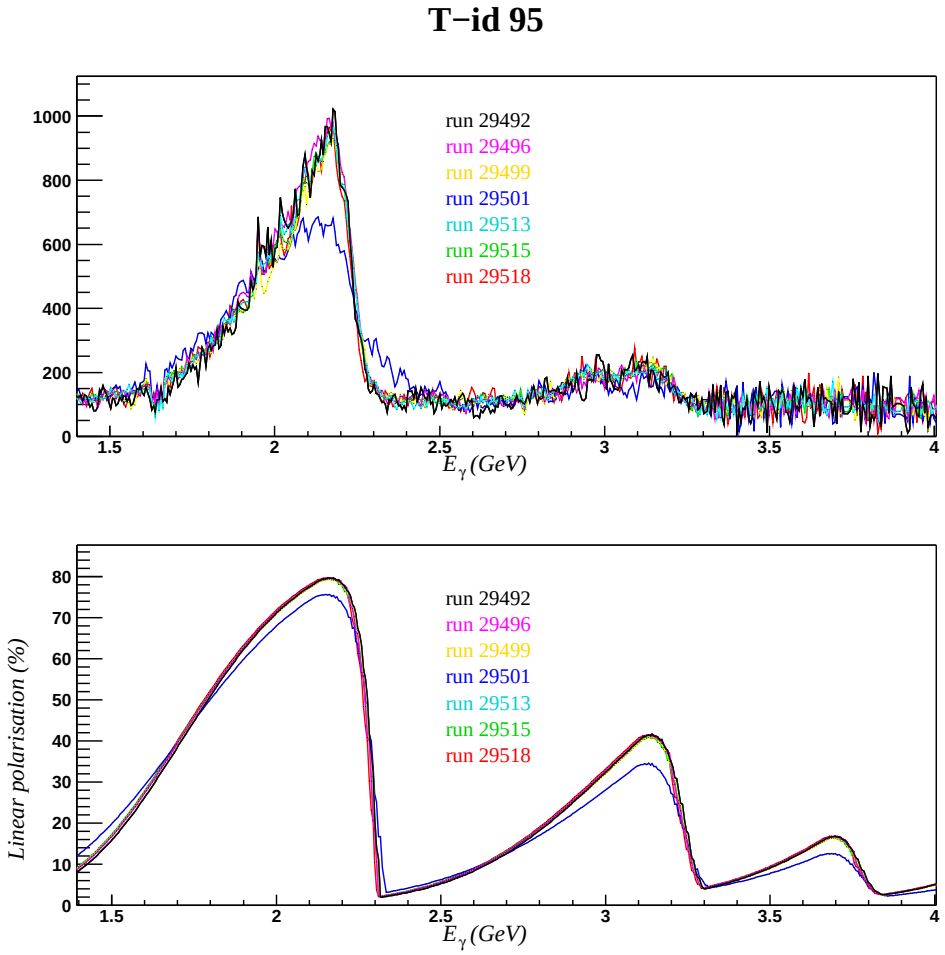

Figure 6.10: *The TDC Spectra where the coherent peak edge is at T-Id 95*

.

Variation in Spectra Normalisation Method The TDC spectra used to compare with calculation are normalised to a baseline of value 100 by considering a region where the polarisation should be zero, then taking the average value of a number of channels and scaling this average value to be 100. The choice of region is important because the statistical fluctuations in the tagger become more pronounced at higher energies due to the low number of counts. When the TDC spectra are normalised by the relevant unpolarised distribution this can have a significant effect on the polarisation. Here a comparison is made between selecting 100 channels at ~ 4GeV, and 40 channels at ~ 2.2GeV (just after the coherent peak). The second method is more stable, especially when dealing with limited statistics as in the case of the parallel polarised data set. However the first method gives a higher value for the maximum polarisation.

The variation in peak height in the TDC spectra is quite pronounced, but since the shape of the distribution is still very similar the polarisation does not vary as much. The systematic variation in the polarisation tables due to this effect is almost negligible when seen in Fig 6.11. However a more detailed analysis in the energy range of interest reveals a maximum effect of $\sim 0.5\%$. The polarisation tables for the perpendicularly polarised data were made using the 4 GeV normalisation routine, while those for the parallel data set used the $\sim 2\,\mathrm{GeV}$ routine.

Conclusion The error from the variation in the height of the coherent peak contributes to the overall systematic error about 10% of the time. Therefore the correction to the measured asymmetry values is $(0.1 * 0.05) = 0.005 = 0.5\%$. This correction is always applied positively to the photon asymmetry measurement since it is a consistent underestimation of the polarisation which leads in turn to an overestimation of Σ.

The other errors add linearly to give a total systematic error due to the calculation of the polarisation of $\sim 4.3\%$.

6.8 Measurement of the photon asymmetry.

In this analysis the data has been passed through cuts to allow only events with a photon energy $1.6 \leq \mathrm{E}_{\vec{\gamma}} \leq 2.0\,\mathrm{GeV}$. In addition, only photons with a measured linear polarisation of greater than 10% pass the analysis cut. This reduces unpolarised background in the polarised signal used for analysis. Using the technique of adding orthogonal polarised data sets, a unpolarised data set is created which is then used to normalise the individual polarised data sets to 1 and cancel out acceptance variations.

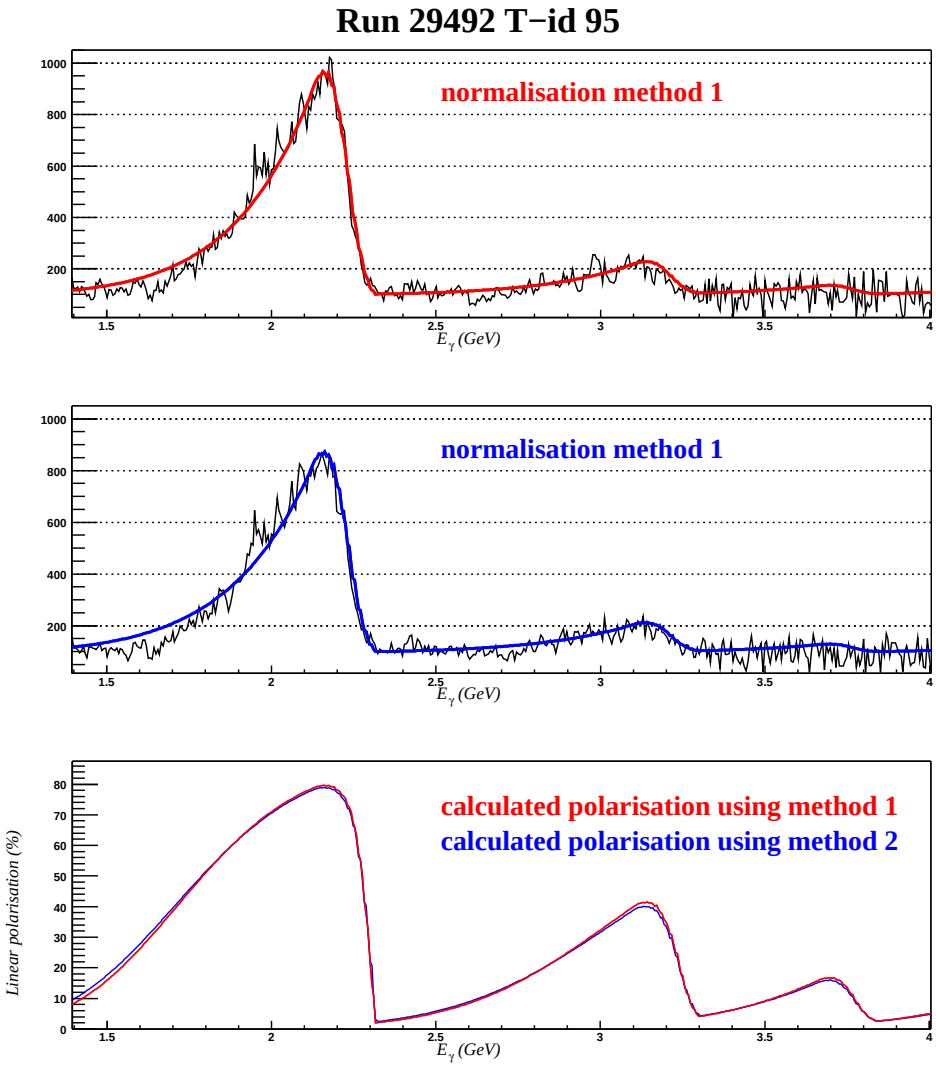

Figure 6.11: *The variation in TDC spectra peak height and polarisation due to differing normalisation methods, shown here when the coherent peak is at T-Id 95.*

Both planes of polarisation are presented here, and although the lack of statistics makes the fit to the parallel data more ambiguous, the comparison between both planes gives confidence that the normalisation technique works properly. Fig 6.12 shows the mean energy in each theta bin of the analysis for both planes of polarisation as well as the amorphous target data. This information is vital to ensure that there is no energy bias between the data sets that could affect the normalisation procedure. The plot shows that there is no significant variation in the mean energy recorded for each analysis bin between the parallel and perpendicularly polarised data sets. The average polarisation for each analysis bin is shown in Fig 6.13, and no significant variation is found over the angular range of the analysis.

Once normalised properly, the cosine 2ϕ distributions are fitted with a parameterisation as shown in eqn 6.13.

$$\mathrm{W}(\phi) \;=\; \mathrm{a}(1 - \frac{\mathrm{b}}{\mathrm{a}}\cos 2\,(\phi + \alpha)) \tag{6.13}$$

The normalised distributions are shown in Figs 6.14 to 6.17, Table 6.3 shows the relevant properties for each analysis bin, and the final fit parameters and results are shown in Table 6.5. In Tables 6.5 and 6.6 the baseline parameter a is fixed to a value of 1, and the phase parameter α is fixed to a value of 4.583^0 based on the results of Chris Gordon's analysis of the photon asymmetry of the ρ^0 [93]. The baseline is fixed due to the lack of statistics making this parameter vary considerably using the $\mathrm{K}\Lambda$ data set. The phase shift is fixed because of the greater number of events in the $\gamma\mathrm{p} \rightarrow \rho^0\mathrm{p}$ reaction during G8a gives a much more accurate measure of the position of the diamond crystal (and therefore the maxima of the cosine 2ϕ distribution detected in CLAS). Figs 6.18 and 6.19 show the resulting cosine 2ϕ fits to the data when following the procedure outlined in Section 6.6 to combine the two complementary data sets, which provides a more accurate measurement in principle.

In Chapter 7 these results will be compared with the latest predictions for the photon asymmetry of the $\mathrm{K}\Lambda$ decay channel calculated with the hadrodynamical model of Janssen [36]. However since the results from the combined data set measurement shows a typically high reduced χ^2 value (shown in Table 6.7), these will not be presented in the final comparison. The combined result shown in Table 6.4 does bear good comparison with the individual measurements from the parallel and perpendicular polarised data sets. This agreement confirms the validity of the approach defined in Section 6.6.

Bin	Perpendicular polarised data	Percentage Polarisation (average)	Parallel polarised data	Percentage Polarisation (average)
1	4987	76.57%	375	63.88
2	5716	76.05%	400	63.04
3	4425	75.62%	279	61.39
4	3060	74.57	198	61.6

Table 6.3: The properties of the analysis procedure. The analysis bins here are as defined in Fig 6.1 and the relevant angles are shown in Table 6.4.

Bin	Perpendicular Σ measurement	Parallel Σ Measurement
1	$0.324 \pm 0.070 \pm 0.014$	$0.328 \pm 0.084 \pm 0.014$
2	$0.212 \pm 0.069 \pm 0.009$	$0.213 \pm 0.084 \pm 0.009$
3	$0.426 \pm 0.077 \pm 0.018$	$0.433 \pm 0.094 \pm 0.019$
4	$0.419 \pm 0.082 \pm 0.018$	$0.393 \pm 0.101 \pm 0.017$

Table 6.4: The results of the photon asymmetry measurement for parallel and perpendicular polarised data sets. Both sets of measurements are presented in the form $\Sigma \pm \sigma_{\mathrm{stat}} \pm \sigma_{\mathrm{sys}}$. Below are shown the equivalent results after combining the data sets as shown in Section 6.6.

Bin	Angle	Combined Σ Measurement
1	$20^0 < \theta < 45^0$	$0.361 \pm 0.036 \pm 0.015$
2	$45^0 \leq \theta < 60^0$	$0.228 \pm 0.034 \pm 0.009$
3	$60^0 \leq \theta < 75^0$	$0.463 \pm 0.039 \pm 0.019$
4	$75^0 \leq \theta < 130^0$	$0.439 \pm 0.042 \pm 0.018$

Bin No.	a $\pm \sigma_{\mathrm{stat}}$	b $\pm \sigma_{\mathrm{stat}}$	$\alpha \pm \sigma_{\mathrm{stat}}$	reduced χ^2
1	1.000	0.248 ± 0.053	4.583	0.93
2	1.000	0.161 ± 0.052	4.583	0.79
3	1.000	0.322 ± 0.058	4.583	1.01
4	1.000	0.312 ± 0.061	4.583	1.95

Table 6.5: Final results and fit parameters from Figs 6.14 to 6.17 for the perpendicularly polarised data set.

Bin No.	a $\pm$ σ_{stat}	b $\pm$ σ_{stat}	α $\pm$ σ_{stat}	reduced χ^2
1	1.000	0.210 ± 0.053	4.583	0.71
2	1.000	0.134 ± 0.053	4.583	0.59
3	1.000	0.266 ± 0.057	4.583	0.69
4	1.000	0.242 ± 0.062	4.583	1.25

Table 6.6: Final results and fit parameters from Figs 6.14 to 6.17 for the parallel polarised data set.

Bin No.	a $\pm$ σ_{stat}	b $\pm$ σ_{stat}	α $\pm$ σ_{stat}	reduced χ^2
1	-0.034 ± 0.040	0.507 ± 0.055	4.583	2.41
2	0.003 ± 0.038	0.317 ± 0.052	4.583	2.58
3	0.072 ± 0.043	0.634 ± 0.059	4.583	2.57
4	0.076 ± 0.045	0.598 ± 0.062	4.583	5.95

Table 6.7: Final results and fit parameters from Figs 6.18 and 6.19 for the combined data set.

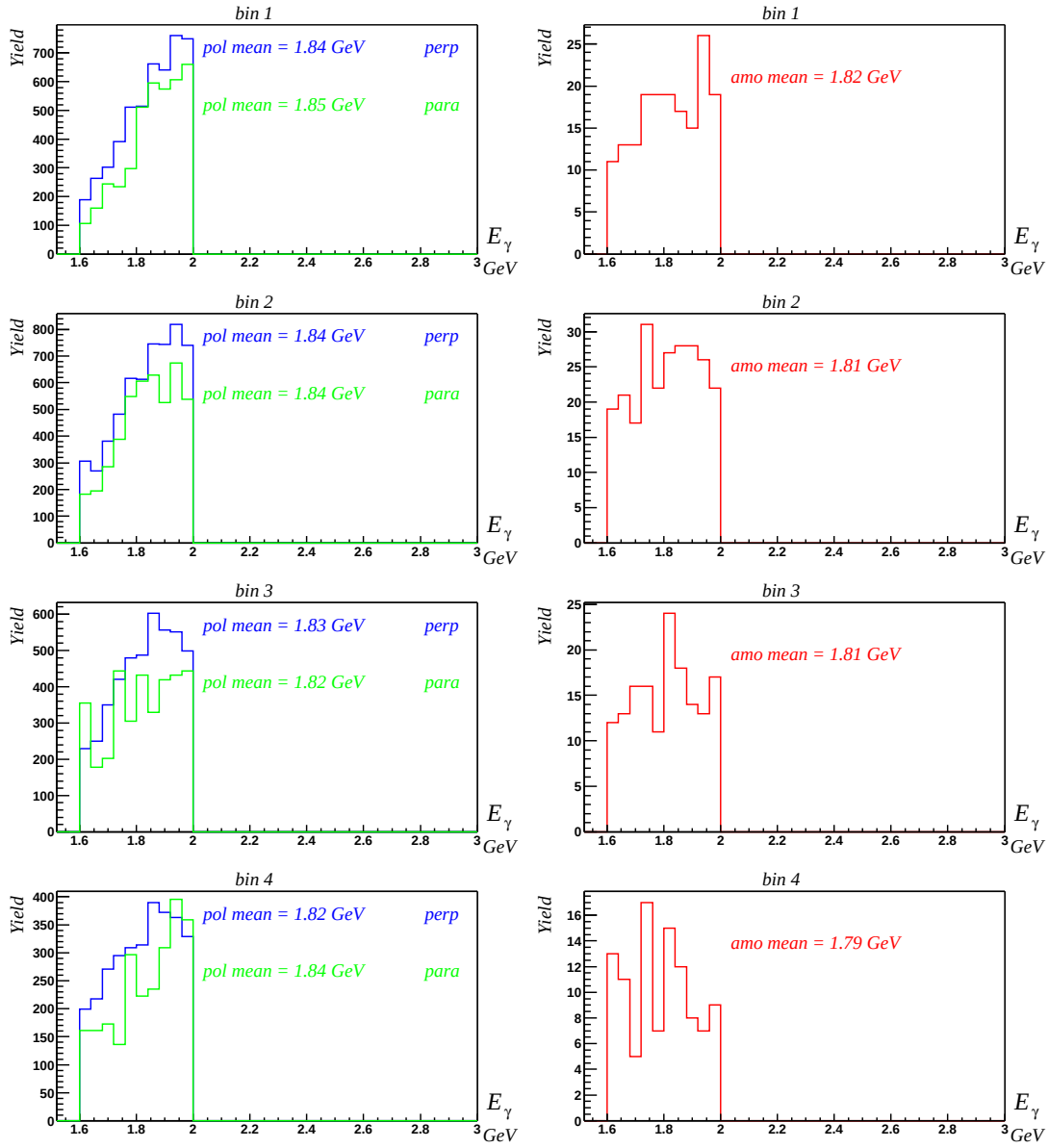

Figure 6.12: *The mean energy for each analysis bin, shown separately for each plane of polarisation as well as amorphous target data.*

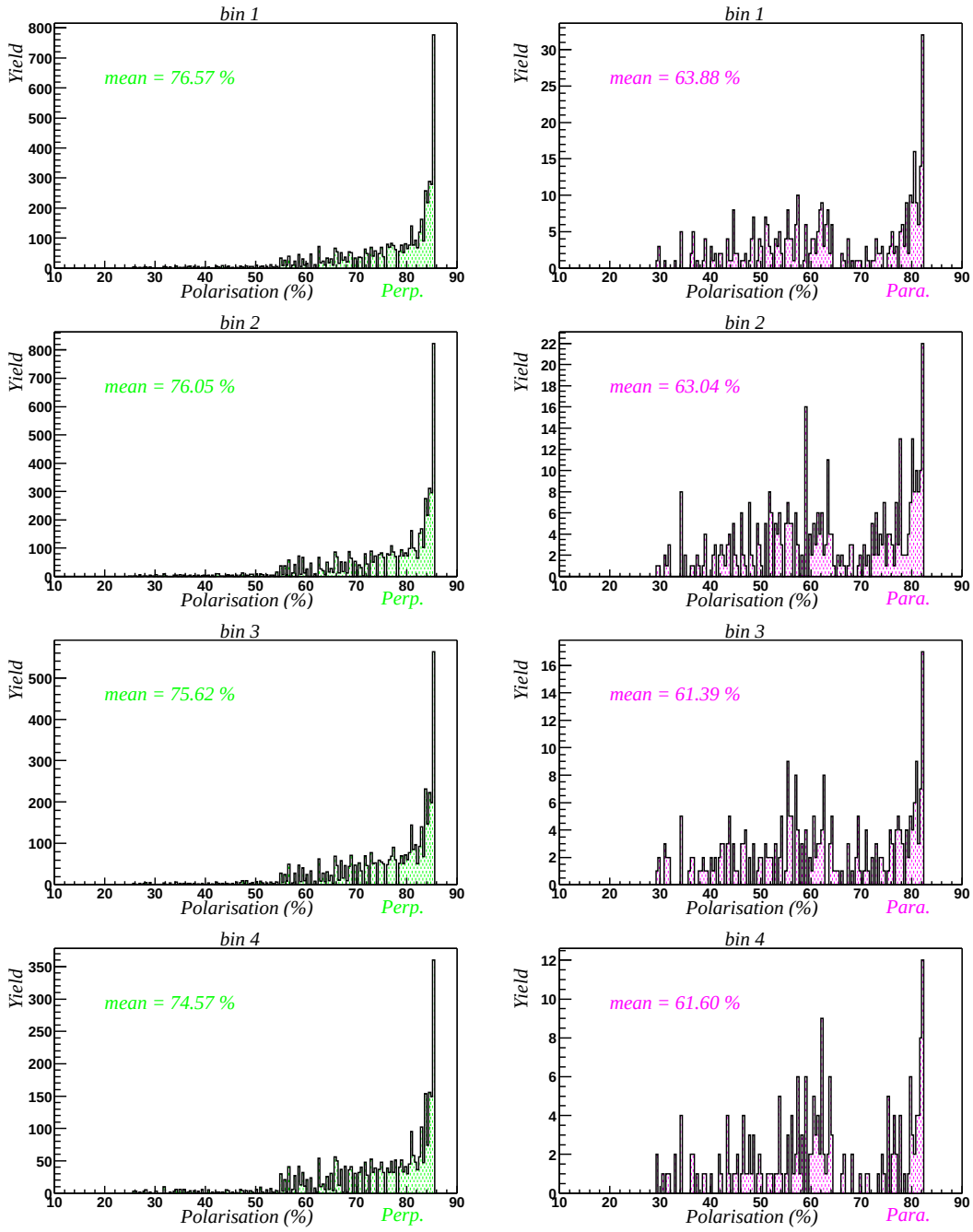

Figure 6.13: *The mean polarisation for each analysis bin, shown separately for the two planes of polarisation.*

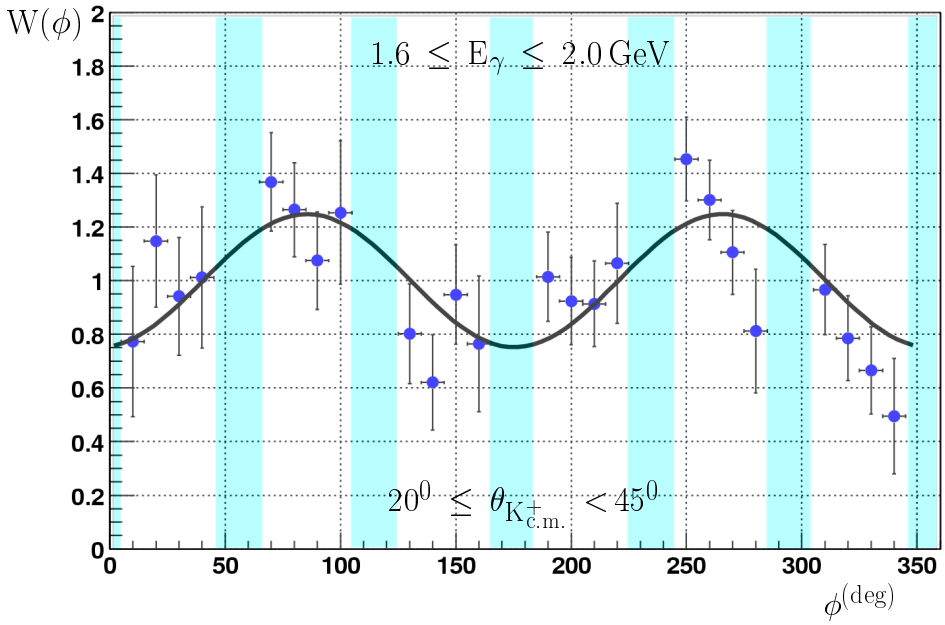

Figure 6.14: *The azimuthal distribution in CLAS, for* $20^0 < \theta_{K^+_{C.M}} < 45^0$. *The blue shaded area shows the regions of no particle acceptance due to the presence of the magnetic coils of CLAS. Top shows the distribution when the* **E***-component of the incident photon beam is perpendicular to the* floor *of Hall B, or the* **x***-axis. Bottom shows the distribution when the* **E***-component is parallel to the* **x***-axis.*

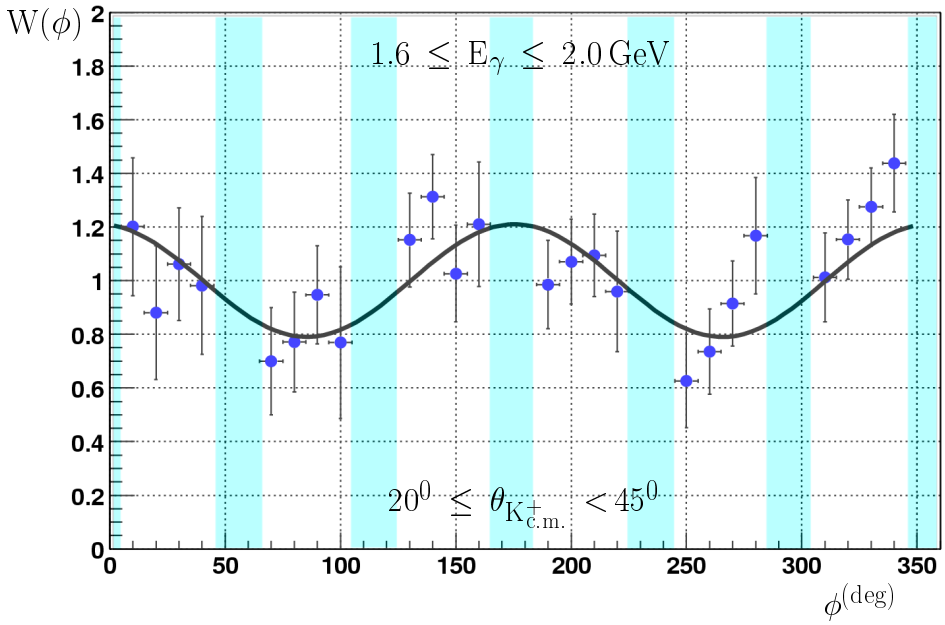

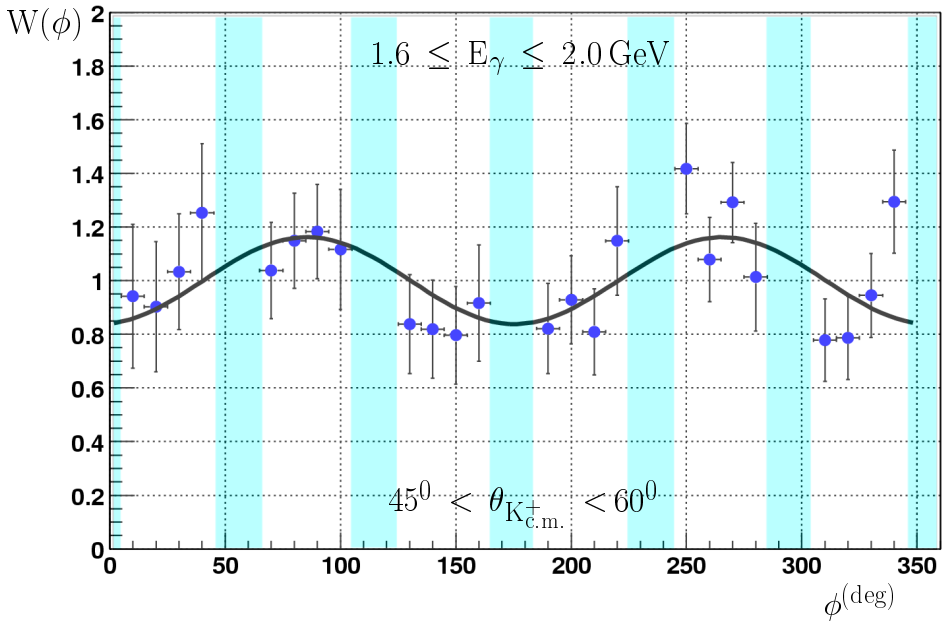

Figure 6.15: *The azimuthal distribution in CLAS, for* $45^0 < \theta_{K^+_{C.M}} < 60^0$. *The blue shaded area shows the regions of no particle acceptance due to the presence of the magnetic coils of CLAS. Top shows the distribution when the* **E***-component of the incident photon beam is perpendicular to the* floor *of Hall B, or the* **x***-axis. Bottom shows the distribution when the* **E***-component is parallel to the* **x***-axis.*

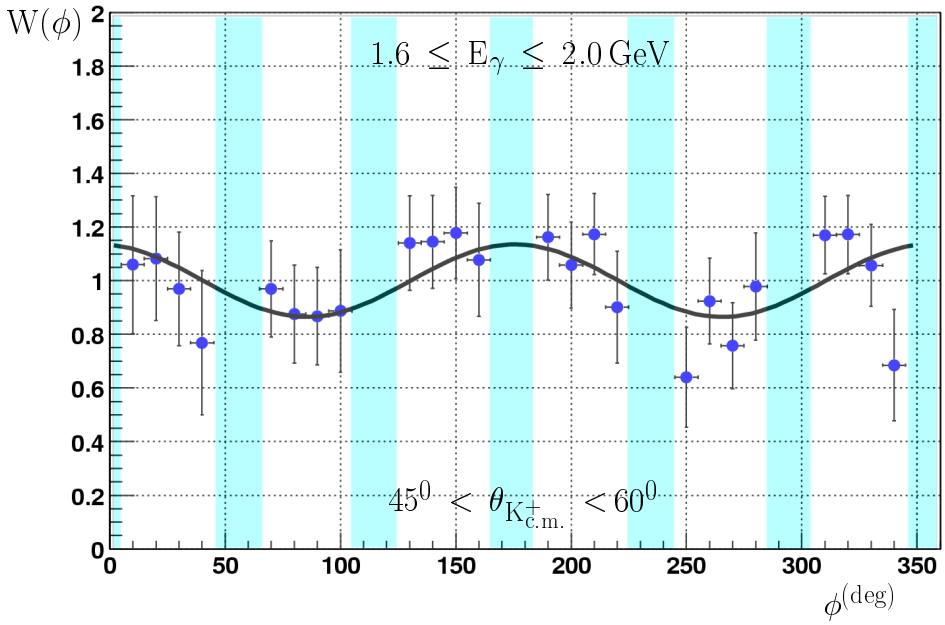

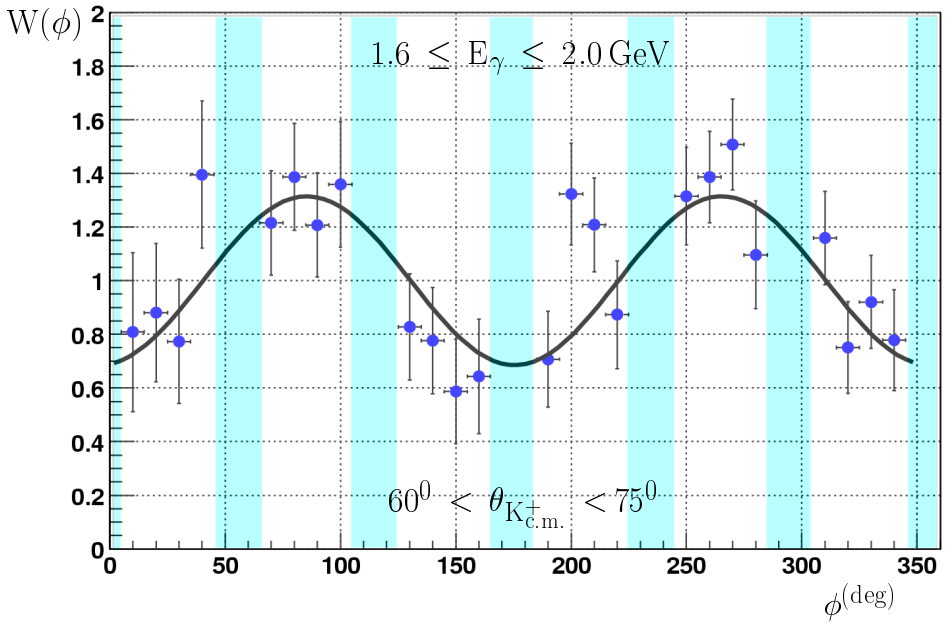

Figure 6.16: *The azimuthal distribution in CLAS, for* $60^0 < \theta_{K^+_{C.M}} < 75^0$. *The blue shaded area shows the regions of no particle acceptance due to the presence of the magnetic coils of CLAS. Top shows the distribution when the* **E***-component of the incident photon beam is perpendicular to the* floor *of Hall B, or the* **x***-axis. Bottom shows the distribution when the* **E***-component is parallel to the* **x***-axis.*

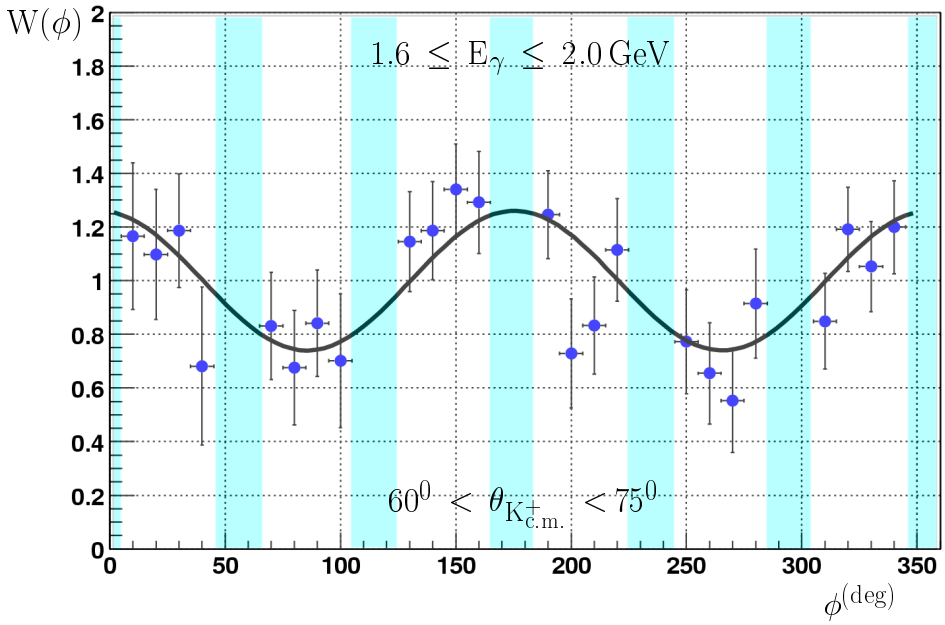

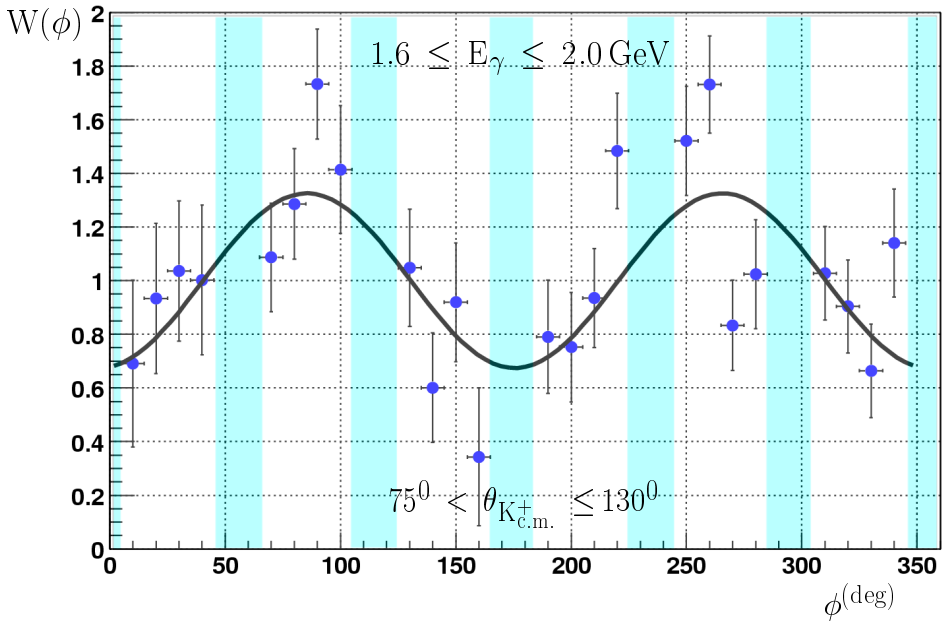

Figure 6.17: *The azimuthal distribution in CLAS, for* $75^0 < \theta_{\mathrm{K^+_{C.M}}} < 130^0$. *The blue shaded area shows the regions of no particle acceptance due to the presence of the magnetic coils of CLAS. Top shows the distribution when the* **E***-component of the incident photon beam is perpendicular to the* floor *of Hall B, or the* **x***-axis. Bottom shows the distribution when the* **E***-component is parallel to the* **x***-axis.*

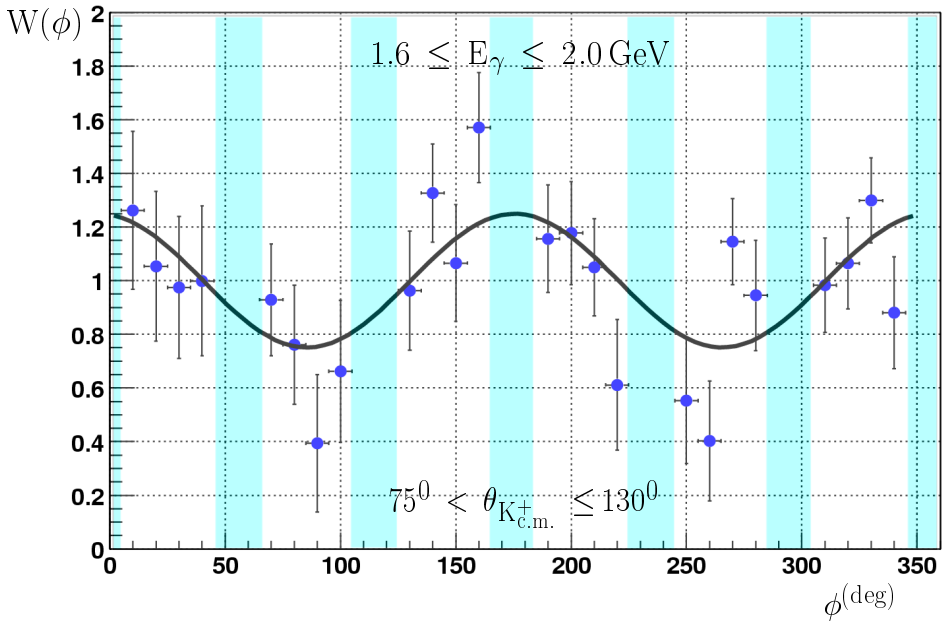

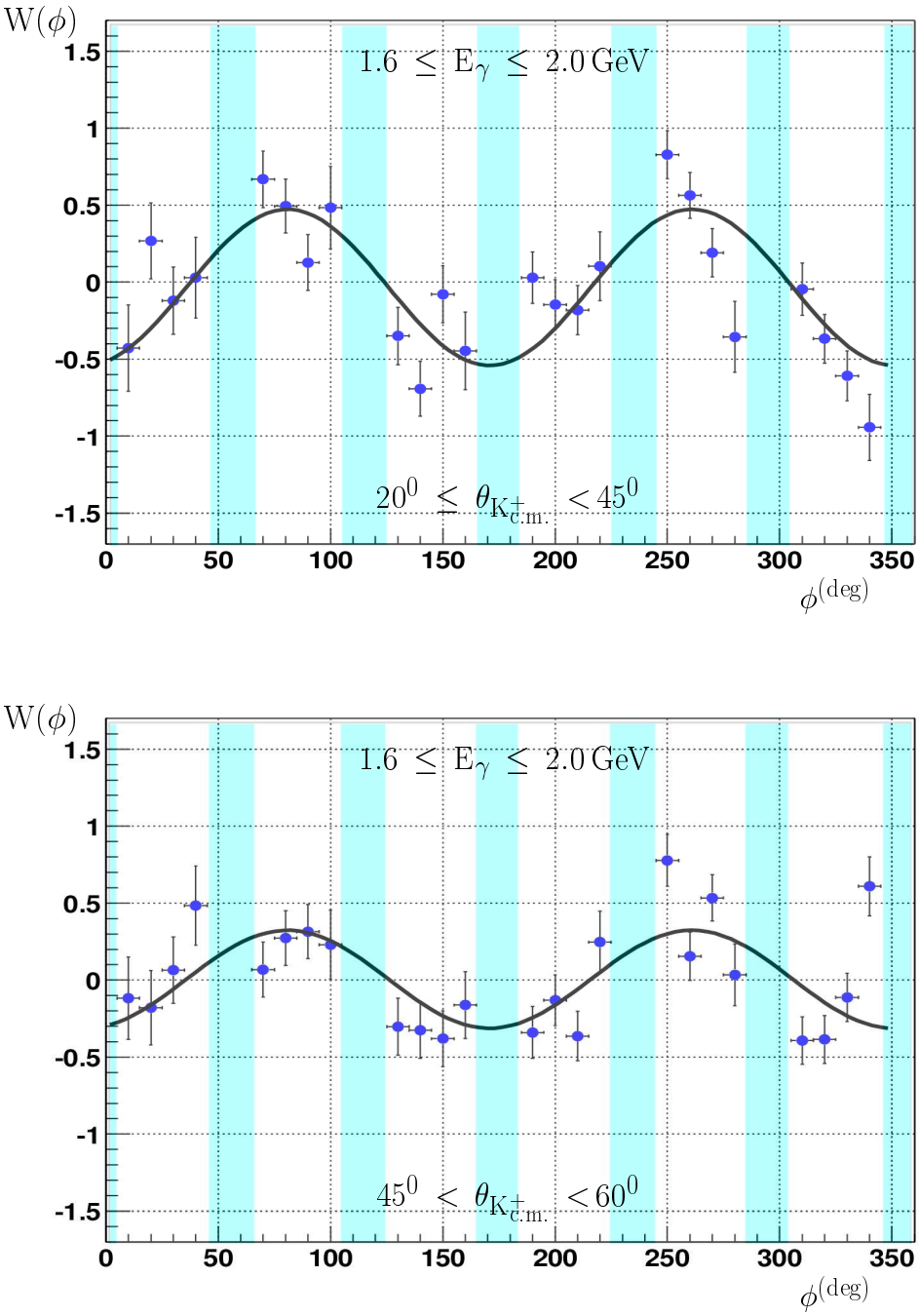

Figure 6.18: *The azimuthal distribution obtained by combining the data sets to amplify the cosine 2ϕ signal, shown here for analysis bins 1 and 2. The blue shaded area shows the regions of no particle acceptance due to the presence of the magnetic coils of CLAS.*

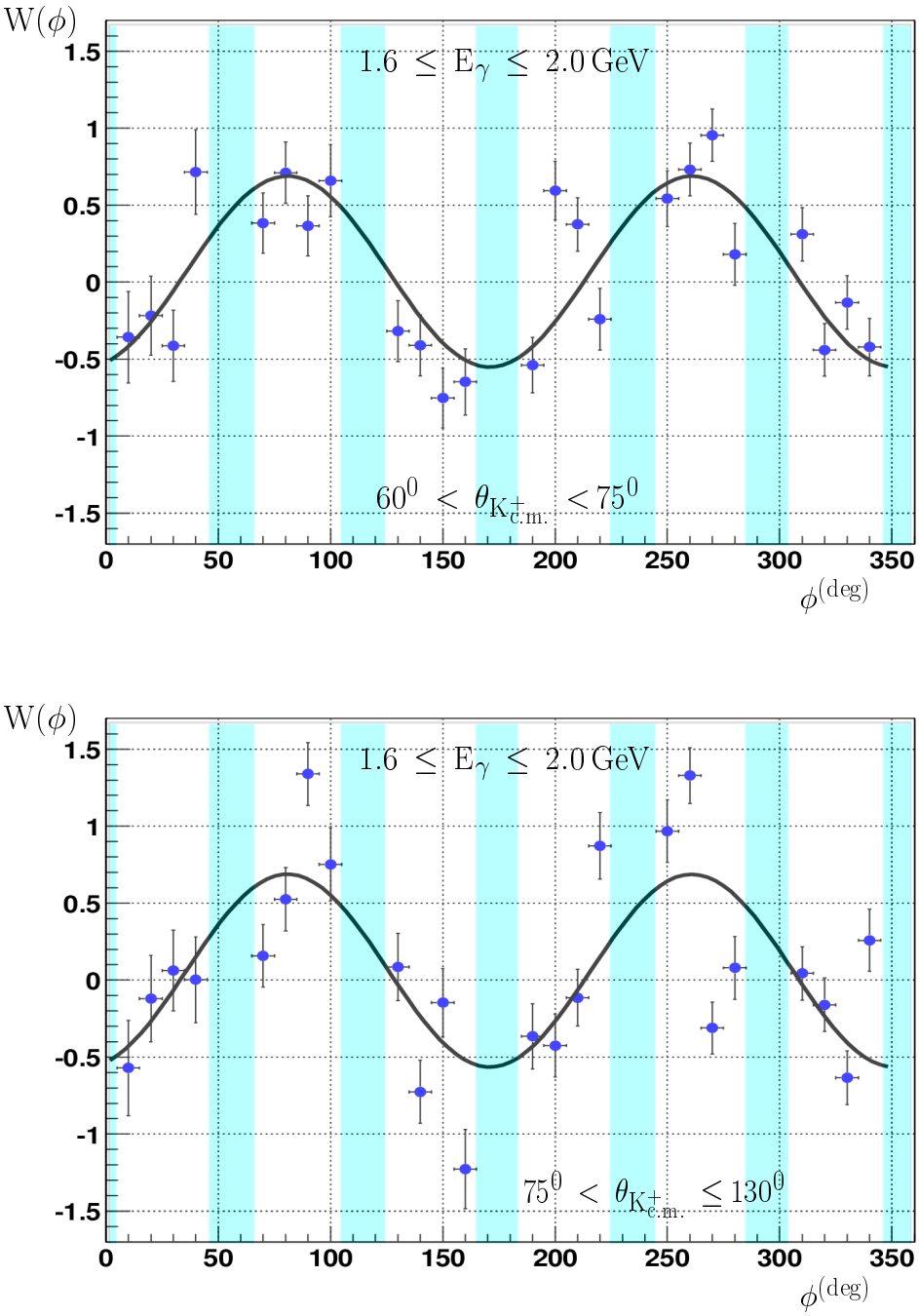

Figure 6.19: *The azimuthal distribution obtained by combining the data sets to amplify the cosine 2ϕ signal, shown here for analysis bins 3 and 4. The blue shaded area shows the regions of no particle acceptance due to the presence of the magnetic coils of CLAS.*

Chapter 7

Discussion of Results and Conclusions

7.1 Results

As a final result, the measurement of the photon asymmetry at a photon energy of $1.6\,\mathrm{GeV} \leq \mathrm{E}_{\overline{\gamma}} \leq 2.0\,\mathrm{GeV}$ is shown in Fig 7.1. The reasons for certain shortcomings in the data set will be discussed below, but the measurements presented in Chapter 6 are still valid and worthwhile for advancing the understanding of the $\gamma\mathrm{p} \rightarrow \mathrm{K}\Lambda$ reaction.

Fig 7.1 shows the dependence of the predicted photon asymmetry on the quantum numbers of the included resonance in the basic model of Janssen et al. [25]. The data points shown clearly indicate a positive asymmetry in the measurable angular range and this would indeed favour the $\mathrm{D}_{13}(1895)$ resonance first postulated by Capstick and Roberts [16], and apparently seen by the SAPHIR [27] group. However, as Section 2.7.1 describes, the usefulness of the genetic algorithm approach developed by Ireland [49] lies in its inherent ability to find the most likely solution for the parameters used in the hadrodynamical model of Janssen et al. [36], and the theoretical curves that are compared to in Fig 7.1 are already being influenced by including the SPring-8 [48] data points which show a definite positive asymmetry at forward angles.

The data presented here indicates that the photon asymmetry stays positive over a wider angular range than first predicted by the model of Janssen et.al, and this should further influence the selection of possible solutions chosen by the genetic algorithm approach.

The recoil polarisation predictions are shown in Fig 7.2, and here they are also influenced by the SPring-8 data for the photon asymmetry, as well as the SAPHIR and CLAS measurements for the differential cross-section and recoil polarisation results. There is limited agreement between the calculations and the data here, but with respect

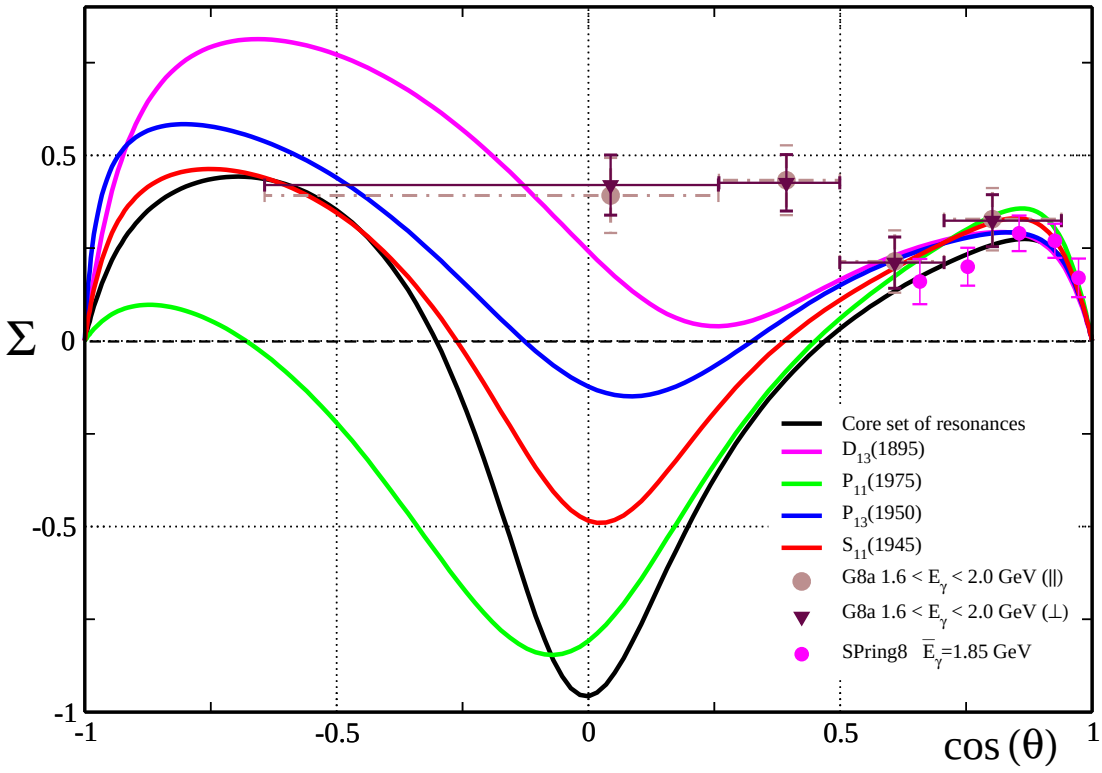

Figure 7.1: *The photon asymmetry measured during the G8a experiment. The core set of resonances used by Janssen et.al [31] is shown here as the black line of calculation. The additional resonances are denoted by coloured lines as shown in the plot legend.*

to the shape and sign of the angular distribution there is some degree of correlation. No one resonance seems to be particularly favoured by experiment. However, it is possible that by restricting the range of solutions further using the G8a data of Fig 7.1, much better agreement between the model predictions of recoil polarisation and the G1c data may be achieved.

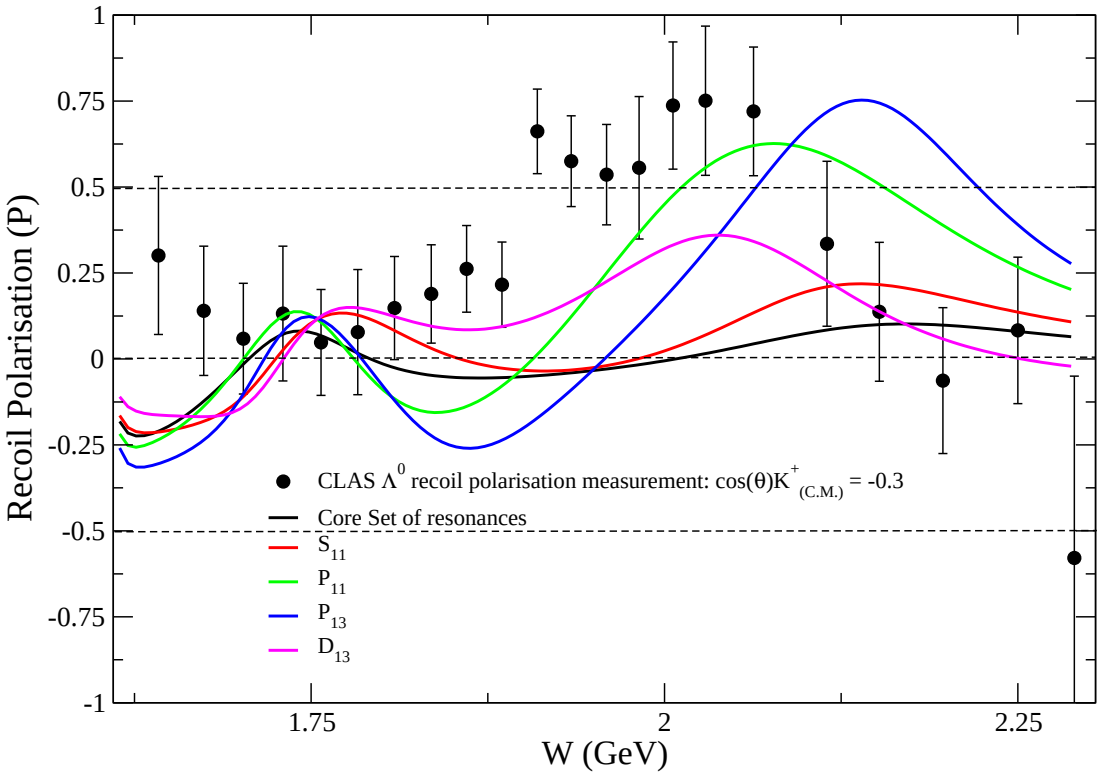

Figure 7.2: *Recoil polarisation calculation by Janssen et al. [31] compared with the CLAS G1c experimental measurement at* $cos(\theta)K^{+}_{(C.M)} = -0.3$. *The predictions made with the core set of resonances are shown by the black line, while the additional resonances are denoted by a coloured line as described in the plot legend.*

7.2 Conclusions

The data used in this thesis has made a significant improvement in the overall understanding of the photon asymmetry for the $K\Lambda$ reaction. With two data points at centre-of mass angles beyond previous measurements, this is a marked improvement,

and also suggests a possible large divergence from the theoretical models already discussed in Chapter 5. There was one crucial limiting factor that emerged during the experimental run. This turned out to be the electronic hardware of the Photon Tagger, in particular the TDCs. Tests carried out [96] indicate that the Tagger operated outside its performance limits due to a number of factors. These factors are either currently being addressed or have already been corrected, and should be regarded as straightforward steps to improve this measurement and similar experiments in the future.

1) A large flux of degraded electrons in certain regions of the tagger hodoscope. At times this could exceed the limit of the photomultiplier tubes that collected the signals, which was ~10 MHz. Above this rate, the response of the PMTs would no longer vary linearly with a proportional increase in electron flux. New tubes have been recently installed in the Tagger which have a higher rate capability, and this will help reduce the effect of high count-rates.

2) The necessity of using the thicker diamond radiator as mentioned in Appendix A.2. The $50\ \mu\mathrm{m}$ diamond produces more multiple scattering that the $20\ \mu\mathrm{m}$ crystal, and this amounts to a higher rate of flux in the tagger in general. This necessity should not be required of future experiments, and higher polarisation with less multiple scattering should reduce the problems encountered in measuring the value of the photon polarisation .

3) The use of a Level 1 Trigger configuration that fired when a single charged particle was detected. This made the effective count-rate in the Photon Tagger very high, and also reduced the relative number of $\mathrm{K}\Lambda$ events. This can be addressed by using a Level 2 trigger to reduce the background unpolarised signal in the Tagger, as well as increasing the relative number of desirable final-state interactions to study.

4) An unidentified hardware problem that made the T-Counter TDCs in the Photon Tagger shift the recorded event time by a random amount. This effectively increased the width of the average Tagger time for good events in CLAS.

As a result of these factors, the number of options open to maximise the data set during the analysis process was reduced. The combination of factors 1,2 and 3 meant that problems arose when analysing the tagger data, especially with regard to estimating

the average polarisation of the photons. However, the time shift described in point 4 above also reduced the effectiveness of the particle identification scheme.

Without a stable time from the tagger for each good event in CLAS, it becomes very difficult to attribute a photon to the kinematics of a detected reaction. It was necessary to require a complete, exclusive reaction in order to eliminate the risk of using a mis-timed photon from the Photon Tagger and thereby introduce errors into the analysis process. This dramatically reduced the statistics of the data set, and gave rise to the further restriction that it was impossible to reconstruct a missing particle reliably in the situation where one of the particles involved in the desired reaction was not detected.

Despite the setbacks that hampered these aspects of the G8a physics analysis, this data set is still able to produce new, valid information on a frontier of intermediate-energy physics which has real potential for furthering experimental understanding in the field. The revealing connections between polarisation observables and the nature of the basic nuclear physics interactions are further strengthened with this type of experiment, and G8a has shown this principle in the setting of Jefferson Lab to be highly successful.

7.3 Future Work

However, the data shown in Fig 7.1 still demonstrate a trend significantly different from the latest calculations made that include the SPring-8 and SAPHIR data sets. This means that future work using linearly polarised photons may be able to resolve decisively which resonances participate in the $\mathrm{K}\Lambda$ photoproduction process. The proposed continuation of this effort at Hall B in Jefferson Lab is the G8b experiment. Using the lessons from G8a, a more in-depth analysis of this trend should be possible. One vital component is a proper Montecarlo simulation using the CLAS GSIM [97] package, adapted for use in CLAS from the FORTRAN simulation package GEANT [98]. Taking proper account of the acceptance in CLAS should allow the extraction of the recoil polarisation from the G8a data set.

Since the Photon Tagger hardware has been significantly improved since the G8a experiment concluded, the problem of statistics and particle identification should become much less severe, and the measurement of the photon asymmetry should be extended over a larger polar angle range in CLAS than is shown in the current work.

The complete experimental description of the $\mathrm{K}\Lambda$ reaction becomes possible when a polarised target is used with a linearly polarised photon beam. This will allow the

measurement of the double-polarisation observables described in Table 2.4. Such an experiment has been proposed and is currently under consideration for running at Jefferson Lab [33].

With this complete description, the genetic algorithm approach should point clearly to the most likely resonance around 1.9 GeV in energy to be involved in the $K\Lambda$ reaction. By taking into account the measured differential cross-section, photon asymmetry, recoil polarisation, target polarisation and double polarisation observables it then becomes possible to establish this whole procedure as a future method for determining the quantum numbers of resonances that contribute to any resonance region reaction. More importantly still, this process may shed some light on the difficult issue of missing resonances, and supply new, high-quality experimental results which will be able to distinguish between the diquark model and the constituent quark model.

Appendix A

Aligning the radiator

A.1 Definition of crystal directions

The radiator is aligned by using the Stonehenge Technique [99], developed in Glasgow, Mainz and Bonn. The target ladder shown in Fig 3.9 is used to mount the crystal, and the degrees of freedom of the goniometer as shown in Fig 3.8 allow scans to be carried out in $(\phi,\ \theta_{\rm v}\,,\ \theta_{\rm h})$.

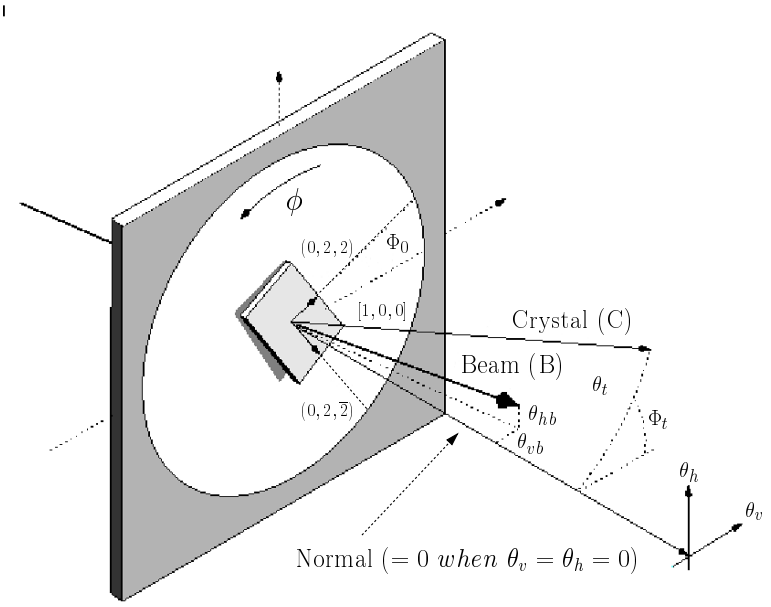

Figure A.1: *The goniometer axes and the crystal axis. All vector notation relates to directions in the diamond unit cell and the Miller Indices represent crystal plane orientation within the unit cell.*

It is standard practice to use the normal to the crystal plane $(1,0,0)$[1] to denote the crystal axis. This axis has the vector direction $[1,0,0]$ and serves as the reference point for aligning the crystal, particularly the planes of interest for coherent bremsstrahlung production. Fig A.1 shows the position of the diamond axes with respect to the goniometer axes, and the crystal planes which are aligned with the beam to produce coherent bremsstrahlung are shown to be orthogonal to the $[1,0,0]$ vector[2]. These crystal planes are oriented with Miller Indices of $(0,2,2)$ and $(0,2,\overline{2})$. The usual notation for the Miller Index of a crystal plane is $\left(\frac{1}{\mathrm{x}},\,\frac{1}{\mathrm{y}},\,\frac{1}{\mathrm{z}}\right)$, where x, y and z are the respective axis intercept points of the crystal plane.

Fig A.2 shows the orientation of the $(1,0,0)$ plane with respect to the primitive unit cell of a typical diamond structure. The primitive unit cell is derived from the smallest repeatable unit that generates the observed lattice structure. In the case of diamond, the primitive unit cell is a face-centred cubic system (fcc) with another fcc system intertwined. Here the second fcc lattice is displaced 1/4 of the primitive unit cell diagonal which allows the tetrahedral diamond structure to emerge as the unit cell is repeated to generate the crystal lattice.

In Fig A.3 the crystal axis plane $(1,0,0)$ is shown with its respective normal, and this time the planes which dominate the scattering process are shown with their relative orientations. This figure is a graphical representation of the structure which the incoming electron beam will produce coherent bremsstrahlung from.

The point of origin from which the calibration scans proceed is the system where $\theta_{\mathrm{h}} = \theta_{\mathrm{v}} = 0$, and although ideally the beam direction would coincide with the crystal axis direction $[1,0,0]$, this cannot be assumed and is frequently found to deviate by some small angles θ_{hb} and θ_{vb}.

The crystal axis will also have some deviation in azimuth and polar angles with respect to the origin, which are denoted as ϕ_{t} and θ_{t} respectively. So the first step in the calibration process is to measure some or all of these angles, which will allow the calculation of the correct values of $(\phi,\,\theta_{\mathrm{v}},\,\theta_{\mathrm{h}})$ to obtain the desired crystal orientation with respect to the electron beam.

[1] This direction is defined in the diamond unit cell.

[2] Crystal planes are denoted by their Miller Indices [58], which are shown in normal brackets. Vector directions and normal vectors to crystal planes are denoted by square brackets.

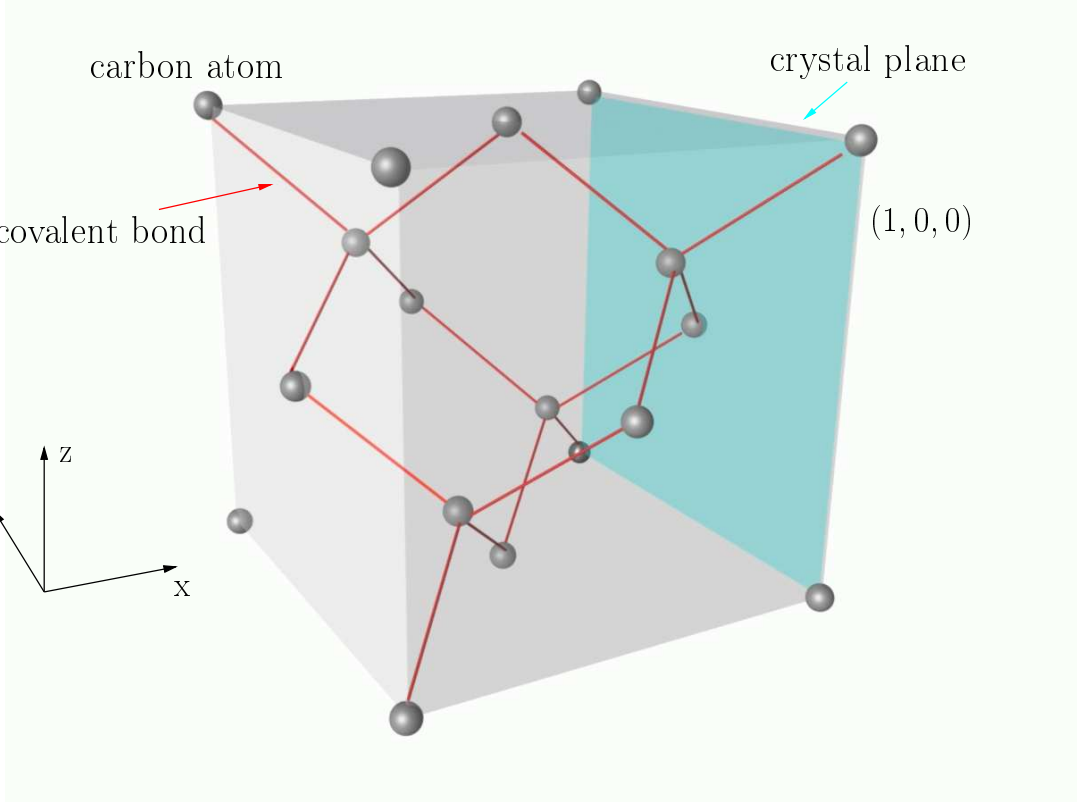

Figure A.2: *The face-centred cubic primitive unit cell of diamond. The crystal plane* **(1,0,0)** *is shown here at the furthest face of the cubic cell from this perspective.*

A.2 The Stonehenge Technique.

Initially the position of the crystal axis is completely unknown, although not usually radically different from the origin of the goniometer. The procedure for determining the crystal axis is to carry out a $h - v$ scan, which is a scan in $\theta_{\mathrm{v}}$and θ_{h}. This is done by making a conical sweep of angular radius θ_s, where $\theta_{\mathrm{v}} = \theta_{\mathrm{s}} \cos(\phi)$ and $\theta_{\mathrm{h}} = \theta_{\mathrm{s}} \sin(\phi)$, and scanning from $0 \leq \phi \leq 2\pi$. For each point in the scan, the photon energy spectrum for the tagger is measured. The coherent bremsstrahlung intensity varies with $(\mathrm{E}_\gamma, \theta_{\mathrm{v}}, \theta_{\mathrm{h}})$ so a three-dimensional plot is required. The parameters of such a plot would be θ_{v} and θ_{h}corresponding to the x and y-axes, with E_γ plotted vertically on the z-axis to make a 3D cylinder as shown in Fig A.4. This plot is made using a simulated photon energy spectrum calculated using the anb code [57]. Where the coherent bremsstrahlung is most intense varies smoothly with θ_{v} and θ_{h} and forms a set of curves on the surface of the cylinder in Fig A.4, shown by the regions in green. These regions are the positions of the coherent peak in the tagger spectrum, and

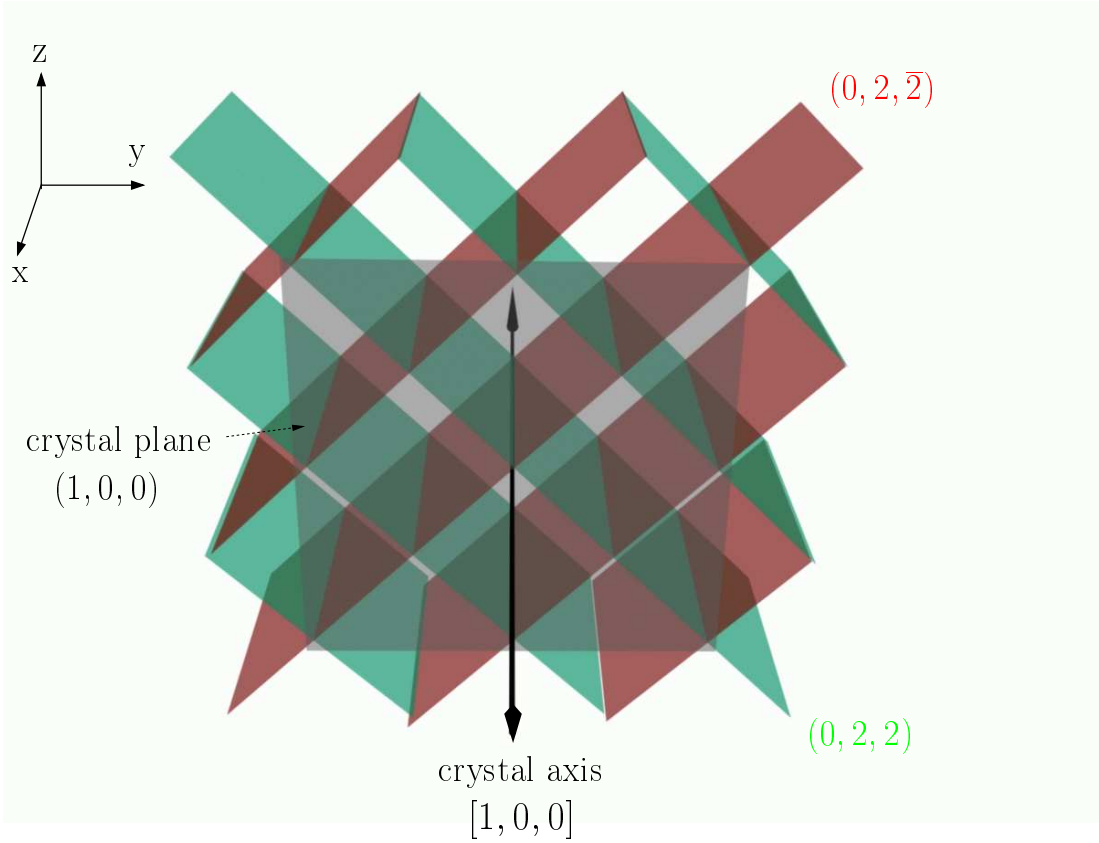

Figure A.3: *The orientation of the crystal axis* [1,0,0] *and the relative dimension of the primitive unit cell to the crystal planes* (0,2,2) *and* (0,2,$\bar{2}$), *shown here in green and red respectively.*

the fourfold symmetry comes from the orthogonal crystal planes $(0, 2, 2)$ and $(0, 2, \overline{2})$. When the crystal axis is aligned with the beam, these planes will form a cross on the projection of the Stonehenge cylinder into two dimensions. Fig A.5 shows a typical Stonehenge plot compressed into two dimensions and the radial width of the circle now represents the photon energy spectrum measured from the photon tagger, increasing with radius.

Using the Stonehenge plot, the position of the coherent peak is extrapolated down to $\mathrm{E}_\gamma = 0$ and a line is drawn, as in Fig A.5, from this point to the corresponding minimum point in the opposite hemisphere of the Stonehenge plot. If the minima produced from the two orthogonal crystal planes are equidistant round the perimeter of the plot, these lines will intersect at the origin of the Stonehenge plot. However, if the crystal is not oriented correctly, the offset in terms of θ_v and θ_h can be calculated by looking at the distance between the intersect point drawn between the minima of the

energy spectrum and the origin of the Stonehenge plot.

For the G8a run, the process is clearly shown in Fig A.6. The initial scan started from a guess at the crystal axis offsets, and the resulting $h - v$ scan can be seen at the top of Fig A.6. Using the $20\ \mu\mathrm{m}$ diamond, this scan was made at an early stage in the experimental run, and the poor quality of the scan is due to the fact that the photon tagger required maintenance at that time. Here the crystal planes clearly are not orthogonal so the crystal axis is not aligned with the beam.

The bottom plot shows the same scan performed on the $20\ \mu\mathrm{m}$ crystal at a later time after the photon tagger had been upgraded, and the fourfold symmetry corresponds exactly with the origin of the Stonehenge plot, indicating that the crystal axis is closely aligned with the beam.

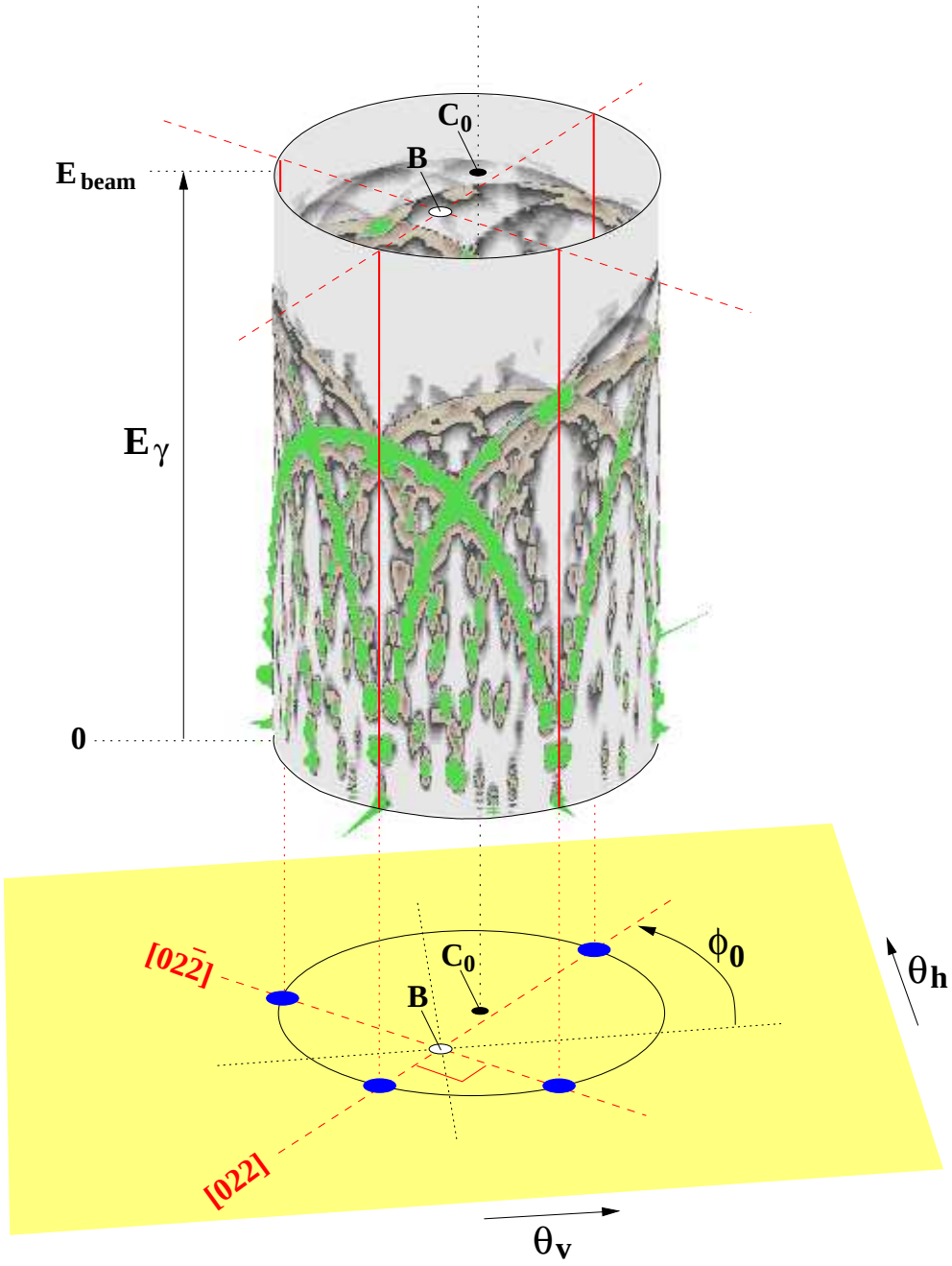

Figure A.4: *The Stonehenge Technique in action. This is a simulated plot of θ_v against θ_h to form a circle, and the height of the cylinder represents the photon energy seen in the tagger. Areas of green show where the coherent peak is positioned in the tagger energy spectrum, so the pattern shows the correlation between coherent edge position and the (θ_v, θ_h) parameters. It is possible to deduce that the crystal is aligned correctly if this relationship between θ_v and θ_h is perfectly symmetric, since this means that the crystal planes* (0,2,2) *and* (0,2,$\bar{2}$) *are in the same position relative to the beam, therefore the beam is aligned with the crystal axis. In the above example, B is the position of the beam and C_0 is the position of the crystal axis, so the crystal is not well-aligned here.*

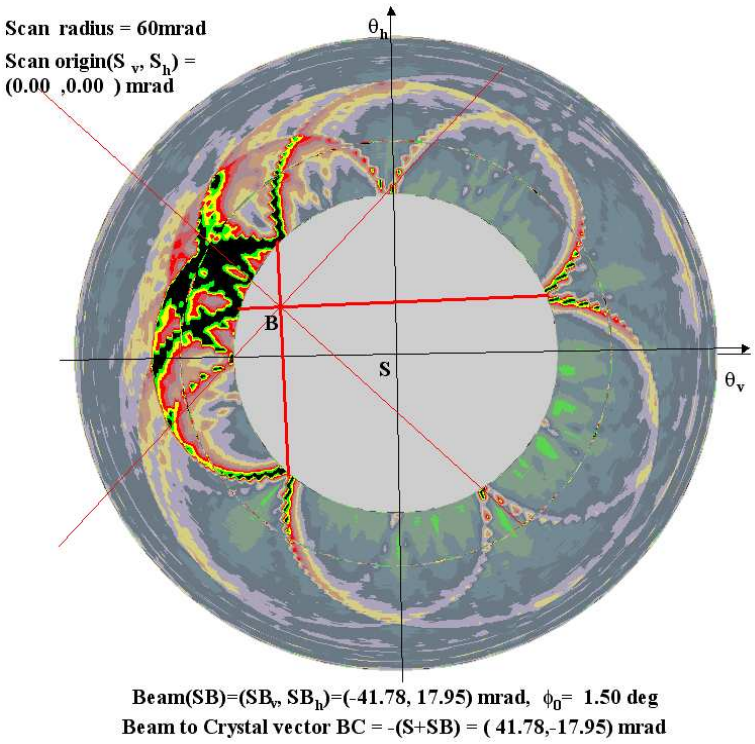

Figure A.5: *The Stonehenge cylinder projected onto two dimensions. The radius of the circle represents the tagged photon energy spectrum obtained from the h-v scan.*

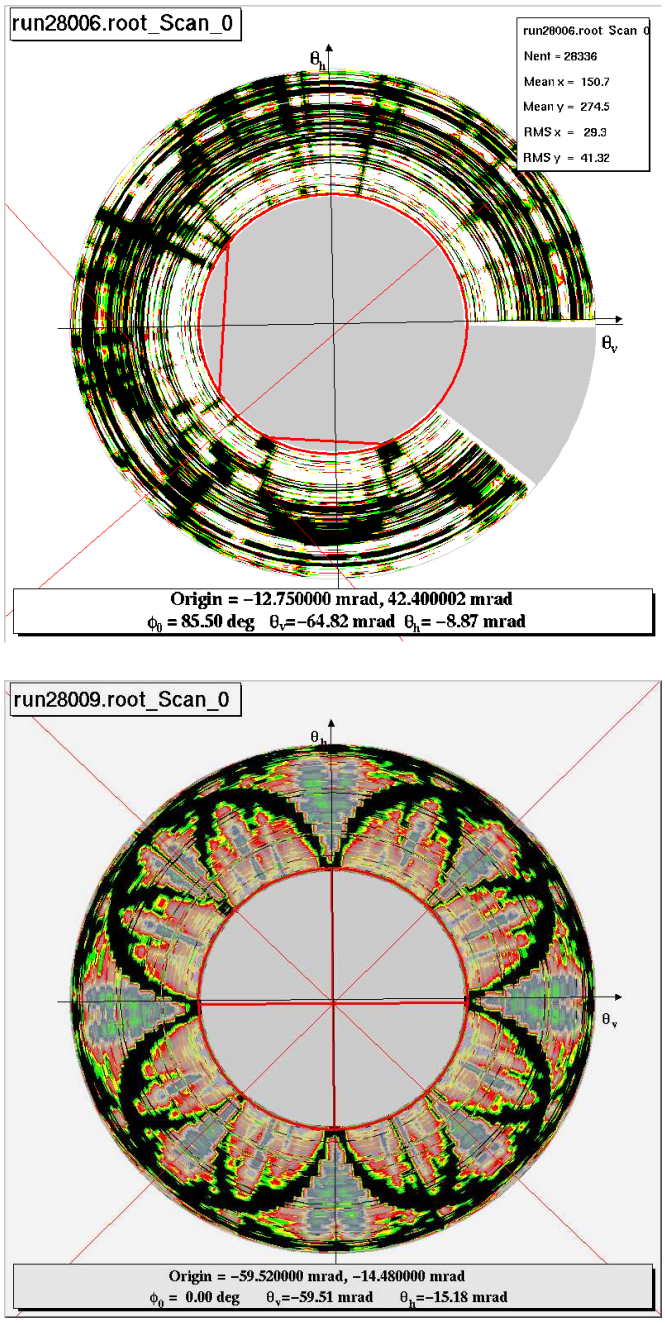

Figure A.6: *The h-v scans performed during the G8a run. Both scans were made during the inital stages of the experiment using the 20 μm diamond. The top scan was made using a starting guess of the crystal offsets, and the bottom scan shows the result when the correct offsets have been calculated. The diagonal lines correspond to the coherent energy minima of the* (0,4,4) *and* (0,4,$\bar{4}$) *crystal planes, and provide further proof of the quality of the crystal alignment.*

Appendix B

Discussion of the state of the $K\Lambda$ data set for G8a

B.1 The G8a data set.

The $K\Lambda$ data set is normally a small fraction of the total experimental yield of charged particles in a typical Hall B experiment at Jefferson Lab. The total number of Level 1 triggers collected in the relevant photon energy range during the G8a experiment registered over 1.8 billion, however the number of $K\Lambda$ events identified using the analysis process outlined in Chapters 4 and 6 was only around 20,000, after cuts had been made.

Allowing for the fact that the cuts are subjectively placed, the low number of events makes a statistical fit to the data very unstable. The results shown in Chapter 6 depend on a process of taking a ratio between two data sets to eliminate systematic errors from the detector system. However, this process is still exposed to statistical variation. The aim of this appendix is to produce a little more proof that the statistical variation in the data sets does not alter the amplitude or sign of the results.

B.2 The perpendicularly polarised data set.

The process outlined in Chapter 6 is followed to attempt to remove systematic errors in the perpendicularly polarised data set. It can be seen from Fig 6.3 that the perpendicular data set outnumbers the amorphous target data set by a factor of 20 to 1. This effectively means that the statistical errors in the amorphous target data set dominate the result when the division process is used. Fig B.1 shows the perpendicular data

set data and the amorphous target data set by which it will be divided. In the case of either a positive or negative photon asymmetry (from the SPring-8 results one would expect a positive asymmetry) there should be a clearly observable bilateral symmetry present in the polarised data that becomes more apparent when the data is divided by the amorphous target data set.

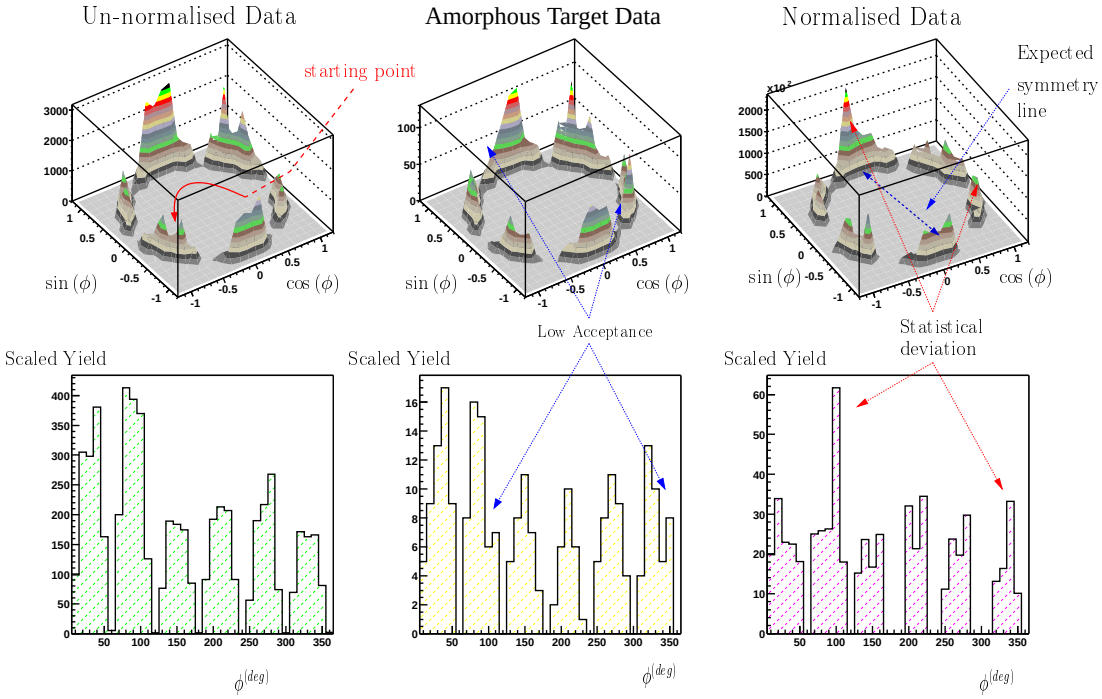

Figure B.1: *A 3-dimensional plot showing the data for perpendicularly polarised photon running in theta bin 2. Left is the un-normalised data set. Centre is the amorphous target data set. Right is the normalised data set.*

The far right plot in Fig B.1 shows the normalised data set with a cosine (2ϕ) variation clearly apparent. This seems fairly unambiguous, although there is evidence of a false peak appearing in the normalised data set at $\phi = 90^0$, which is clearly due to a lack of events at the edge of Sector 4 in CLAS in the amorphous target data set. The point to take from this plot is the possibility of a statistical fluctuation becoming much larger than the systematic error information carried in the amorphous target data set, to the extent that it contaminates the polarised signal that is to be measured.

Fig B.2 shows the same data set when divided by the unpolarised data set described in Section 6.5, and the problem discussed above seems to be dramatically reduced.

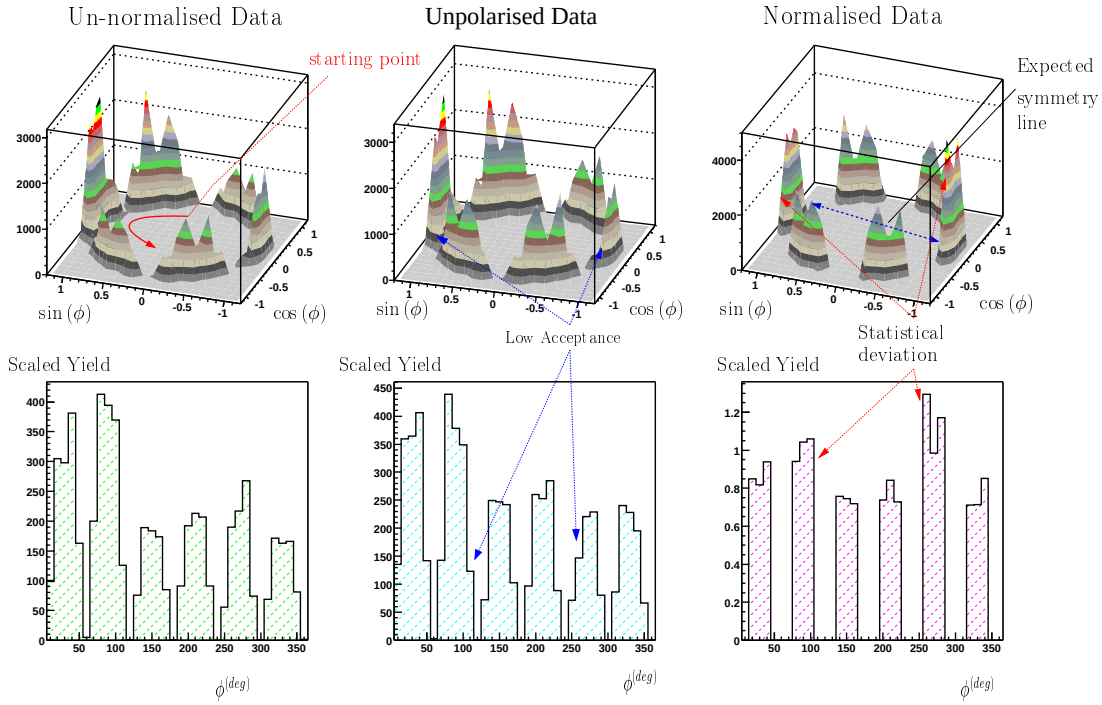

Figure B.2: *A 3-dimensional plot showing the data for perpendicularly polarised photon running in theta bin 2. Left is the un-normalised data set. Centre is the unpolarised data set. Right is the normalised data set.*

B.3 The parallel polarised data set.

In the same way as described above, Fig B.3 shows the parallel polarised data set, the relevant amorphous target data set and the final normalised data set which would be used to measure the photon asymmetry. The amorphous target data set is exactly the same as that used to divide the perpendicular data set since it covers the same angular range in $\theta_{\mathrm{C.M.}}$. This gives rise to the same problem seen in Fig B.1, but it affects the cosine(2ϕ) fit in a different way, shifting the amplitude of the fit, rather than the phase as seen for the perpendicular data set in the section above.

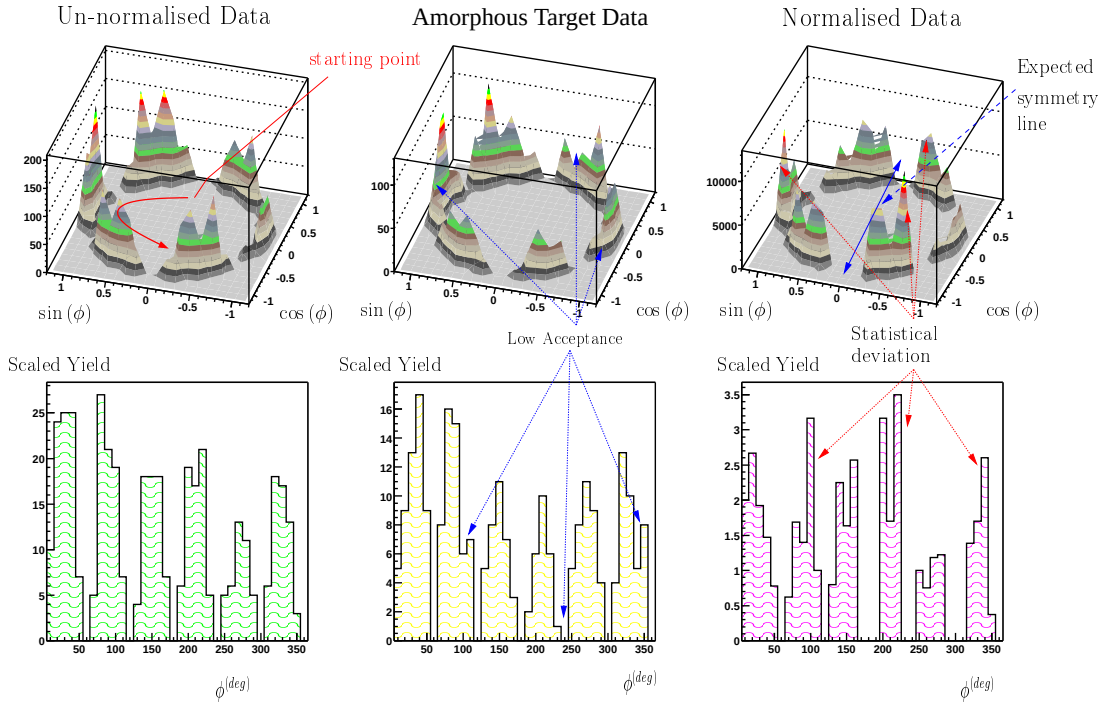

Figure B.3: *A 3-dimensional plot showing the data for parallel polarised photon running in theta bin 2. Left is the un-normalised data set. Centre is the amorphous target data set. Right is the normalised data set.*

If the unpolarised data set is used to normalise this distribution (shown in Fig B.4), not only is the problem of low statistics addressed, but an agreement is reached in the amplitude of the cosine(2ϕ) fit for both planes of polarisation. This indicates that using the method for creating an unpolarised data set as described in Section 6.5, the significant problem of statistical error in the amorphous target data set swamping out the desirable polarised signal is reduced.

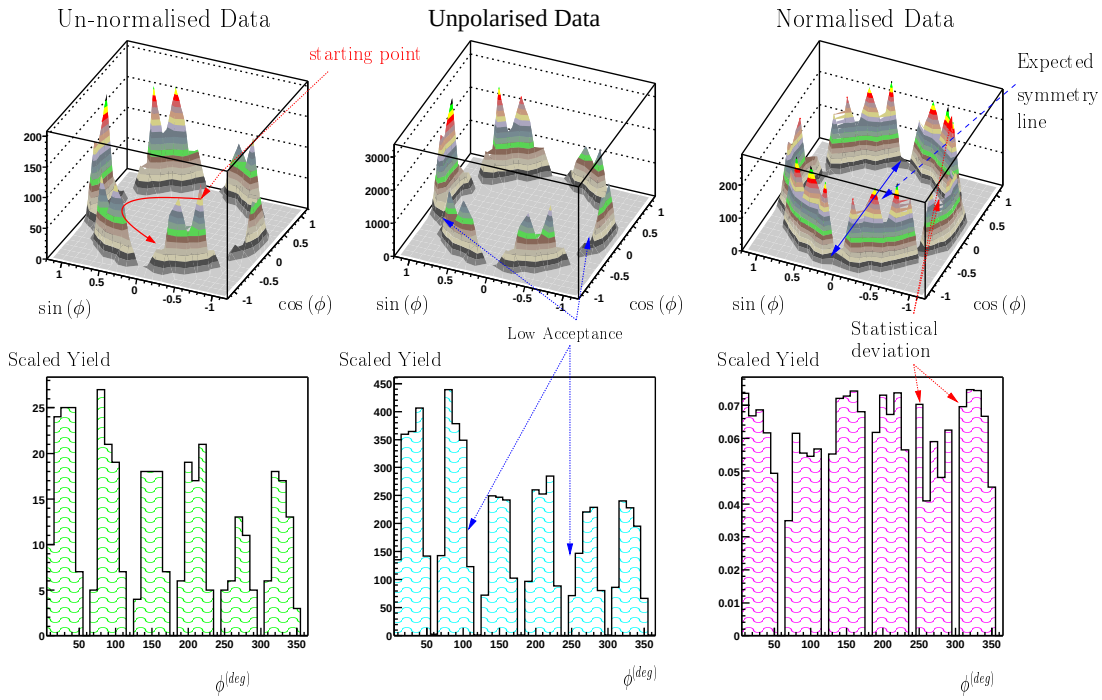

Figure B.4: *A 3-dimensional plot showing the data for parallel polarised photon running in theta bin 2. Left is the un-normalised data set. Centre is the unpolarised data set. Right is the normalised data set.*

Bibliography

[1] E. Rutherford. Phil.Mag.,6th Series, **21**:669, 1911.

[2] D. B. Leinweber. *Visualizations of the QCD vacuum*. http://arxiv.org/ps/hep-lat/0004025, 1999.

[3] R. Koniuk and N. Isgur. Phys. Rev. D., **21**:1868, 1980.

[4] D.B. Lichtenberg, L.J. Tassie, and P.J. Keleman. Phys. Rev., **167**:1535–1542, 1968.

[5] D. B. Lichtenberg. Phys. Rev., **178**:2197, 1969.

[6] R. E. Cutkosky and R. E. Hendrick. Phys. Rev. D., **16**:2902, 1977.

[7] K. H. Hicks. AIP Conf. Proc., **717**:400–404, 2004.

[8] M Karliner and HJ. Lipkin. Phys. Lett., **B575**:249–255, 2003.

[9] R. S. Kaushal, D. Parashar, and A. K. Sisodiya. Phys. Lett., **B600**:215–222, 2004.

[10] S. Capstick and N. Isgur. Phys. Rev. D., **34**:2809, 1986.

[11] C. Bennhold, H. Haberzettl, and T. Mart. Trieste 1999, Perspectives in hadronic physics., pages 328–337, 1999.

[12] C. Bennhold et al. Phys. Rev. C, **C69**:042201, 2000.

[13] *Jefferson Lab Homepage*. http://www.jlab.org.

[14] H. Kamitsubo. Nucl. Instrum. Meth., **A303**:421–434, 1991.

[15] J. Hamilton and B. Tromborg. *Partial Wave Amplitudes and Resonance Poles*. Oxford Clarendon Press, 1972.

[16] S. Capstick and W. Roberts. Phys. Rev. D., **58**:074011, 1998.

[17] P. Cole, J.Connelly, and K. Livingston. *Photoproduction of the ρ Meson from the Proton with Linearly Polarized Photons.* JLab proposal **E-94-109,** 1994.

[18] D. Tedeschi, P. Cole, and J. Mueller. *Photoproduction of ϕ Mesons with Linearly Polarized Photons.* JLab proposal **E-98-109,** 1998.

[19] F. Klein and P. Cole. *Photoproduction of ω Mesons off Protons with Linearly Polarized Photons.* JLab proposal **E-99-013,** 1999.

[20] F. Klein, J. Kellie, and J. C. Sanabria. *Photoproduction of Associated Strangeness using a Linearly Polarized Beam of Photons.***JLab CAA, 2001**.

[21] J. S. Blair and G. F. Chew. Annu. Rev. Nucl. Sci., **v2**:163–404, 1953.

[22] G. Gamow. Z. Phys., **51**:204–212, 1928.

[23] C. P. Forsythe and R. E. Cutkosky. *Z. Phys. C*, 18:219, 1983.

[24] D. E. Groom et al. *Eur. Phys. C*, 15:1, 2000.

[25] S. Janssen and J. Ryckebusch. Prepared for 9th International Conference on the Structure of Baryons (Baryons 2002), Newport News, Virginia, 3-8 Mar 2002.

[26] M. Bockhorst et al. Z. Phys., **C63**:37–47, 1994.

[27] M. Q. Tran et al. Phys. Lett., **B445**:20–26, 1998.

[28] H. Thom. Phys. Rev., **151**:1322, 1966.

[29] R. A. Adelseck, C. Bennhold, and L. E. Wright. Phys. Rev., **C32**:1681–1692, 1985.

[30] R. L. Workman. Phys. Rev., **C32**:2456–2457, 1989.

[31] D. G. Ireland, S. Janssen, and J. Ryckebusch. Nucl. Phys., **A740**:147–167, 2004.

[32] G. O'Reilly S. Strauch, N. Benmouna and I. Strakovsky. *JLab Proposal*. **E-03-105**, 2003.

[33] F.J. Klein, L. Todor and P. Eugenio. *JLab Proposal*. **E-02-112**, 2002.

[34] J. W. C. McNabb et al. Phys. Rev., **C69**:042201, 2004.

[35] K-H. Glander et al. Eur. Phys. J. A, **19**:251–273, 2004.

[36] S. Janssen, D. G. Ireland, and J. Ryckebusch. Phys. Lett., **B562**:51–56, 2003.

[37] S. Mandelstam. Phys. Rev., **112**:1344, 1958.

[38] R. A. Adelseck and B. Saghai. Phys. Rev., **C42**:108–127, 1990.

[39] T. Mart H. Haberzettl, C. Bennhold and T. Feuster. Phys. Rev. C., **58**:40–44, 1998.

[40] J. Cohen. Phys. Rev., **C39**:2285–2294, 1989.

[41] A.W. Thomas and W. Weise. *The structure of the nucleon*. Berlin, Germany: Wiley-VCH (2001).

[42] W. Greiner, J. Reinhardt. *Quantum Electrodynamics*. Springer-Verlag, Berlin (1992).

[43] J.C. David, C. Fayard, G.H. Lamot, and B. Saghai. Phys. Rev., **C53**, 1996.

[44] G. F. Chew, M. L. Goldberger, F. E. Low, and Y. Nambu. Phys. Rev., **106**:1345–1355, 1957.

[45] L. Tiator et al. Few Body Syst. Suppl., **9**:213–218, 1995.

[46] P. J. Bussey et al. Nucl. Phys., **B154**:205, 1979.

[47] T. Hotta. Prog. Theor. Phys. Suppl., **149**:257–263, 2003.

[48] R. G. T. Zegers et al. Phys. Rev. Lett., **91**:092001, 2003.

[49] D. Ireland. J. Phys. G: Nucl. Part. Phys., **26**:157–166, 1999.

[50] C. W. Leemann et al. *Annu. Rev. Nucl. Part. Sci*, 51:413–50, 2001.

[51] C. Hovater et al. **1996**.

[52] B. A. Mecking et al. *Nucl. Inst. Meth. A*, 503:513–553, 2003.

[53] R. T. Jones. JLab internal publication, 1999.

[54] G. Tamas. *Nucl. Phys. News*, 2:411, 1992.

[55] Mainz Microtron, http://www.kph.uni-mainz.de.

[56] U. Timm. *Fortschritte der Physik*, 19:765, 1969.

[57] A. Natter. *ANalytic Bremsstrahlung Code*. http://www.pit.physik.uni-tuebingen.de/grabmayr/software/brems/brems-analytic.html.

[58] H.P. Myers. *Introductory Solid-state Physics*. Taylor & Francis, London (1990).

[59] B. K. Tanner. *X-ray diffration topography*. Pergamon, 1976.

[60] J. Kellie et al. *The Selection of Diamond Radiators for use in Coherent Bremsstrahlung Experiments,* preprint submitted to Elsevier Science 13 June 2002.

[61] W. J. Briscoe et al. *The George Washington University Goniometer*. NSF Major Research Instrumentation, NSF Award 9724489.

[62] D. Sober et al. Nucl. Inst. Meth. A, **440**:263–284, 2000.

[63] A. Freyberger. *Hall B beamline parameters*. Internal JLab document.

[64] P. Cole. *The IPN-Orsay/UTEP Instrumented Collimator.* JLab internal publication, 1999.

[65] S. Christo. *Hall B CryoTarget design.* http://www.jlab.org/∼christo/target_intro.html.

[66] S. Taylor et al. Nucl. Inst. Meth. A, **462**:484, 2001.

[67] M. D. Mestayer et al. Nucl. Inst. Meth. A, **449**:81–111, 2000.

[68] E. S. Smith et al. Nucl. Inst. Meth. A, **432**:265–298, 1999.

[69] G. Adams et al. Nucl. Inst. Meth. A, **465**:414, 2001.

[70] L. C. Smith et al. Nucl. Inst. Meth. A, **460**:239, 2001.

[71] M. Amarian et al. Nucl. Inst. Meth. A, **447**:424, 2000.

[72] D. C. Doughty et al. Nucl. Sci. IEEE Transactions, 39:241–247, 1992.

[73] J. A. Muguira. Master's thesis, Christopher Newport University, 1997.

[74] *CEBAF Online Data Acquisition*. http://coda.jlab.org/.

[75] D. Axmark et al. http://www.mysql.com, since 1980s.

[76] D. Cords et al. *CLAS Event Format with BOS,* CLAS-NOTE **94-012,** 1994.

[77] V. Blobel et al. *The BOS System for CLAS Detector,* Unpublished, 1995.

[78] D. Weygand et al. On CUE at JLab "a1c" is accessible from: **cvs co /packages/utilities/a1**.

[79] C. Gordon, J. Melone and J. C. Sanabria. On CUE at JLab "st dt" is accessible from: **cvs co /packages/utilities/st dt**.

[80] Lohman et al. Nucl. Inst. Meth. A, 343:494, 1994.

[81] E. Anciant et al. CLAS-NOTE **99-004,** 1999.

[82] J.Li. *PhotonTcal, the new tagger calibration program.* CLAS-NOTE **03-004,** 2003.

[83] E. S. Smith et al. *Calibration of the CLAS TOF System,* CLAS-NOTE **99-011,** 1999.

[84] K. S. Krane. *Introductory Nuclear Physics.* John Wiley and Sons, 1988.

[85] CERN (Centre Europeene de Recherche Nucleaire). *P.A.W. Physics Analysis Workstation*. http://paw.web.cern.ch/paw.

[86] D. Lawrence et al. *CLAS Drift Chamber Calibration: Software and Procedures,* CLAS-NOTE **99-018,** 1999.

[87] M. Guillo et al. *EC Time Calibration Procedure For Photon Runs in CLAS,* CLAS-NOTE **01-014,** 2001.

[88] P. Cole and R. Mammei. *G8a active collimator calibration technique,* cole@jlab.org, mammei@jlab.org.

[89] S. Stepanyan L. Elouhadrhiri, V. Burkert and H. Egiyan. *Charged Particle Identification in CLAS.* CLAS-NOTE, **98-004**, 1998.

[90] E. Pasyuk and L. Tudor. *GPID scheme for photon running in CLAS,* Unpublished CLAS-NOTE.

[91] E. Pasyuk. *Energy loss routine on JLab CUE:* **cvs co /packages/eloss**.

[92] J. Li. *Personal correspondence,* liji@jlab.org.

[93] C.I.O. Gordon. PhD thesis, University of Glasgow, 2004.

[94] The EPICS website, http://www.aps.anl.gov/epics/.

[95] H. Uberall. *Phys. Rev.*, 103:1055, 1956.

[96] H. Crannell. *Personal Correspondence,* crannell@jlab.org.

[97] GSIM, http://www.jlab.org/Hall-B/document/gsim/userguide.html.

[98] GEANT, http://wwwasd.web.cern.ch/wwwasd/geant/.

[99] K. Livingston. *The Stonehenge Technique*. Unpublished, to be submitted to Nucl. Inst. Meth. A.